

Experimental analysis and characterization of flow turbulence regarding its effect on fan noise

vorgelegt von

M. Sc.

Luciano Coutinho Caldas

an der Fakultät V - Verkehrs- und Maschinensysteme
der Technischen Universität Berlin
zur Erlangung des akademischen Grades

Doktor der Ingenieurwissenschaften

- Dr.-Ing. -

genehmigte Dissertation

Promotionsausschuss:

Vorsitzender: Prof. Dr.-Ing. Ennes Sarradj

Gutachter: Prof. Dr. rer. nat. Lars Enghardt

Gutachter: Dr. Daniel L. Sutliff

Gutachter: Prof. Dr.-Ing. Dieter Peitsch

Tag der wissenschaftlichen Aussprache: 04. August 2023

Berlin 2023

Abstract

WITH the aim of making aircraft “greener”, researchers are continuously looking for solutions to make airplanes quieter and more efficient. Actual and future aircraft concepts typically rely on highly integrated propulsion systems, aiming on the increase of flight efficiency, what typically leads to higher levels of turbulence ingested by the fan, and consequently the increase of fan noise generation. This work is focused in the understanding of fan noise generation due to distorted inflow. For the experimental investigation a series of measurements were performed in the low-speed aeroacoustic fan rig named CRAFT.

Before experiments with variable inflow distortion may start, a baseline inflow with homogeneous and low-turbulence levels has to be established, as a prerequisite for fan self-noise investigation. This can be achieved by installing an Inflow Control Device (ICD) on the test rig’s inlet. For the CRAFT fan rig an ICD was especially conceived and constructed using flexible honeycomb covered on both sides with a thin wire mesh to ensure maximum turbulence reduction. Variable inflow distortions were generated using perforated plates combined with a honeycomb installed downstream of the inlet bellmouth. The aerodynamic performance of the ICD (baseline) and the inflow distortion tests were assessed by means of hot-wire and total pressure rakes. The fan noise emission was recorded by microphone arrays. A software to estimate turbulence parameters such as turbulence intensity and integral length scale (ILS) from hot-wire data was implemented. A novel technique was developed to estimate these turbulence parameters from the flow downstream of the fan by separating the statistics of the rotor wakes from the background flow.

The ICD established a homogeneous inflow both in terms of turbulence intensity (as low as 0.1%) and the mean flow velocity. The turbulence distribution was characterized both in the inlet and between the fan and the stator section. Three inlet configurations were compared for different fan operating points: Without the ICD, with the ICD, and with ICD and an additional honeycomb installed upstream the fan. Acoustic analyzes revealed a reduction of the fan broadband noise levels and more stable rotor coherent tones with ICD compared to without. A reduction of narrowband components around the blade passing frequencies was also observed and is believed to be associated with the reduction of the low-frequency power content in the turbulence spectrum due to the ICD. These properties were further improved by adding a honeycomb in the duct inlet, with the penalty of a slight increase of the turbulence levels.

The use of perforated plates combined with a honeycomb successfully generated distorted inflow profiles, which are relevant for fan noise investigations. Both the mean velocity profile and the turbulence field were altered by the screens. Acoustic measurements revealed an increase in broadband fan noise emission under distorted inflow conditions. The parametric tests with different levels of distortion allowed the assessment of the parameters that impact on the fan broadband noise generation. Analyzes suggest an approx. linear relationship between the fan broadband sound power emissions in decibels and the average ingested turbulence power. The turbulence profile generated inside the distorted area differs from what is typically seen in boundary layer ingesting fans.

Zusammenfassung

MIT dem Ziel, Flugzeuge insgesamt “grüner” zu machen, suchen Forscher ständig nach Lösungen, leisere und effizientere Flugzeuge zu entwickeln. Aktuelle und zukünftige Konzepte für Flugzeuge basieren in der Regel auf hochintegrierten Antriebssystemen, die auf eine Steigerung der Flugeffizienz abzielen. Eine Folge dieser Integrationslösung ist die Zunahme der Lärmemissionen des Fans, die durch die Aufnahme gestörter (inhomogener) Anströmung verursacht werden. Um die Entstehung von Fanlärm durch gestörte Zuströmung besser zu verstehen, wurde eine Reihe von Messungen in einem aeroakustischen Niedriggeschwindigkeits-Fan-Rig namens CRAFT durchgeführt.

Bevor mit Experimenten von variablen Einlaufstörungen begonnen werden kann, muss eine möglichst gleichmäßige und turbulenzarme Zuströmung in der Einlaufstrecke gewährleistet werden. Voraussetzung für eine ungestörte Untersuchung der Eigengeräuscherzeugungsmechanismen von Fans ist eine Zuströmung mit vernachlässigbarer räumlicher und zeitlicher Inhomogenität. Um eine homogene und turbulenzarme Zuströmung zu gewährleisten, wurde eigens für das CRAFT-Fan Rig ein *Inflow Control Device* (ICD) konzipiert und hergestellt. Der ICD wurde aus einem flexiblen Wabengleichrichter gebaut, welcher beidseitig mit einem dünnen Drahtsieb überzogen ist, um eine maximale Turbulenzreduzierung zu gewährleisten. Die Wirkung des ICDs wurde sowohl aerodynamisch mittels Hitzdraht- und Totaldruck-Messungen als auch durch Erfassung der Fanschallanregung mittels Mikrofonarrays bewertet. Es wurde eine Software zur Verarbeitung von Hitzdrahtdaten implementiert, um Turbulenzparameter wie die Turbulenzintensität und die integrale Längenskala (ILS) zu bewerten. Außerdem wurde ein neuartiges Verfahren entwickelt, um diese Turbulenzparameter aus der Strömung zwischen Rotor und Stator abzuschätzen. Diese auf den Zeitbereich basierende Methode trennt und ermittelt die Turbulenzparameter sowohl der Rotornachläufe als auch der Hintergrundströmung.

Mit dem ICD wurde eine homogene Zuströmung sowohl in Bezug auf die Turbulenzintensität (so niedrig wie 0,1%) als auch auf die mittlere Strömungsgeschwindigkeit festgestellt. Die Turbulenzverteilung wurde sowohl in der Einlaufstrecke als auch zwischen dem Fan und dem Stator über den gesamte Radius charakterisiert. Es wurden drei Einlaufkonfigurationen für verschiedene Betriebspunkte des Fans verglichen: Ohne ICD, mit ICD, und mit ICD und einem zusätzlichen Wabengleichrichter, welcher in der Einlaufstrecke stromauf des Fans eingesetzt wurde. Akustische Analysen ergaben eine Verringerung des breitbandigen Fanlärm und stabilere kohärente Rotortöne aufgrund des ICD

im Vergleich zu ohne ICD. Es wurde auch eine Verringerung der Schmalbandkomponenten im Bereich der Blattfolgefrequenzen beobachtet, die vermutlich mit der Verringerung des tieffrequenten Leistungsanteils im Turbulenzspektrum aufgrund des ICD zusammenhängt. Diese Eigenschaften wurden durch das Hinzufügen eines Wabengleichrichter in der Einlaufstrecke weiter verbessert, allerdings mit dem Nachteil eines leichten Anstiegs der Turbulenzwerte.

Durch die Verwendung von Lochblechen in Kombination mit einem Wabengleichrichter wurden erfolgreich gestörte Zuströmungsprofile erzeugt, die für die Untersuchung der Fanlärmanregung relevant sind. Sowohl das mittlere Geschwindigkeitsprofil als auch das Turbulenzfeld wurden durch die verschiedene Lochblechen verändert. Akustische Messungen ergaben einen bemerkenswerten Anstieg der Breitbandgeräuschpegel aufgrund der gestörten Zuströmung und des Anstiegs der Zuströmturbulenzpegel. Parametrischen Tests mit unterschiedlichen Störungsgraden ermöglichten die Bewertung der Parameter, die sich auf die breitbandige Fanlärmanregung auswirken. Die Analysen ergaben eine annähernd lineare Abhängigkeit zwischen den Schalleistungspegel des Fans in Dezibel und der durchschnittlichen Turbulenzvarianz (oder der turbulenten kinetischen Energie). Das Profil der Turbulenzintensität innerhalb des gestörten Bereichs unterschied sich jedoch von dem, was typischerweise bei Fans mit Grenzschichtansaugung zu beobachten ist.

Dedico esta tese de doutorado aos meus pais Lucia e Henriques, à minha madrina tia Clara (in memoriam), e à minha avó dona Lica (in memoriam).

This thesis is dedicated to my parents Lucia and Henriques, to my late godmother *tia Clara*, and to my late grandma *dona Lica*.

Acknowledgments

THIS work was only possible because of the effort put by Prof. Dr. Lars Enghardt and Dr. Ulf Tapken from the DLR, Engine Acoustics Department in Berlin, Germany. I am very grateful to their effort that through the cooperation DLR-DAAD made this study financially doable. A special thank to Dr. Ulf Tapken who supervised my work throughout these years, and believed in my potential not only to accomplish the expected work, but who also believed I could learn German.

The present work counts in the support of many people. Starting with the design of the inflow control device (ICD), which demanded several meetings with direct and indirect support from many colleagues. I am immensely grateful for the support of everyone involved somehow in this project. For those involved in the initial phase of design: Dr. Henri Siller, Dr. Robert Meyer, Dr. Wolfram Hage, Dr. Robert Jaron, Dr. Ulf Tapken, Maximilian Behn, and Dr. Benjamin Pardowitz. As the project moved towards construction, the support from the colleagues Angelo Rudolphi, Sebastian Kruck and Oliver Klose was vital for the successful construction of the ICD. Indeed my lack of expertise and experience in the construction of such special device was filled with the insights and better ideas from these colleagues. The precision mechanical skills of Sebastian Kruck made possible the “as perfect as possible” construction of the CRAFT ICD. All test preparations relied on the support of these colleagues, whose dedication makes science and experiments possible.

The measurement team within the project AGATA3S was often composed by Lukas Klähn, Dr. Robert Meyer, Angelo Rudolphi, and me. The insights from Maximilian and Lukas regarding acoustic analysis and general signal processing were also very helpful. When the analyses deepened into the turbulence field the support from Dr. Carolin Kissner and Dr. Robert Meyer were extremely helpful for the better understanding of turbulence properties. The chats with Dr. Lionel Hirschberg on dealing with thesis writing and general theme were also fruitful. Indeed, I acknowledge not only all the colleagues from the Engine Acoustics department of the DLR in Berlin, but also the colleagues from other departments who were involved in project AGATA3S. Thanks to my friends who patiently helped on reviewing parts of this thesis: Dr. Alana Zülke, Bernardo Martinez Rocamora Jr., and Paula Wesselmann.

An unconventional thanks go to Sergei Cobra and all people responsible for the production of the Brazilian radio program *8 em ponto* (8 o'clock sharp) from the radio station *Cultura FM Brasil*. Radio is still an amazing broadcast media which connects people somehow in a different way. Since the beginning of the Covid-19 pandemic, listening to this program

from Berlin made quite a difference on shortening the distance and keeping in contact with Brazil, my homeland.

Finally, I would like to acknowledge the thousands of anonymous individuals who have coded for open-source projects for free. It is due to their efforts that scientific work with powerful tools is possible and available to everyone.

“... Today I understand my father well. A man must travel. On his own, not through stories, pictures, books or television. He must travel with his own eyes and his own feet, to understand what is his own, so one day he can plant his own trees and appreciate them. So he can feel the cold in order to appreciate the warmth. And the other way around, feel the distance and lack of shelter, to be happy under his own roof. A man must travel to unknown places to him so he can lose the arrogance that makes us see the world the way we imagine it, instead of how it simply is, that makes us teachers and doctors of what we have not seen, whereas we should be students and simply go see it.”

free translation extracted from the book: *Mar sem fim*,
“Endless sea” - Amyr Klink

“... Hoje entendo bem o meu pai. Um homem precisa viajar. Por sua conta, não por meio de histórias, imagens, livros ou tv. Precisa viajar por si, com os seus olhos e pés, para entender o que é seu. Para um dia plantar as suas próprias árvores e dar-lhes valor. Conhecer o frio para desfrutar do calor. E o oposto. Sentir a distância e o desabrigo para estar bem sob o próprio teto. Um homem precisa viajar para lugares que não conhece para quebrar essa arrogância que nos faz ver o mundo como o imaginamos, e não simplesmente como é; que nos faz professores e doutores do que não vimos, quando deveríamos ser alunos, e simplesmente ir ver.”

Original version: “*Mar sem fim*” - Amyr Klink

Contents

1. Introduction and Objectives	1
1.1. Aircraft noise	1
1.2. Fan noise generation	3
1.3. Future aircraft concepts: towards lower noise emissions and higher flight efficiency	4
1.4. Objectives and approach of this thesis	6
1.5. Literature review	8
1.5.1. Impact of turbulence ingestion on fan aerodynamics	8
1.5.2. Impact of inflow distortion ingestion on fan aerodynamics	9
1.5.3. Fan noise generation due to turbulence ingestion or distorted inflow	10
1.5.4. Estimation of relevant turbulence parameters	15
1.5.5. Design and construction of an ICD	19
1.5.6. Impact of ICD on the inflow aerodynamics and on the fan noise generation	21
1.6. Novel contribution of this thesis	24
1.7. Thesis overview	25
2. Literature review on fundamental turbulence	27
2.1. Review of fundamental turbulence definitions	27
2.2. Coordinates system	31
2.3. Fundamental turbulence parameters	32
2.3.1. The integral length scale (ILS) Λ	32
2.3.2. Dissipation scale or microscale λ	35
2.3.3. Reynolds stresses	37
2.3.4. Turbulence intensity	37
2.4. Homogeneous and isotropic turbulence velocity spectrum models	38
2.4.1. The two-parameters von Kármán spectrum model	38
2.4.2. The three-parameters Bullen spectrum model	39
2.4.3. Test case: Turbulence velocity spectrum	39
2.4.4. Test case: Estimation of the dissipation microscale λ	40
3. Hot-wire data analysis techniques: extraction of flow turbulence parameters	43
3.1. Noise reduction techniques	43
3.1.1. Low-frequency disturbance removal	43
3.1.2. Cyclostationary technique for the removal of rotor coherent components	45

Contents

3.1.3.	Use of accelerometer signal to remove rotor coherent components . . .	46
3.2.	Turbulence integral length scale (ILS) estimators	49
3.2.1.	Integral length scale estimation according to the definition	50
3.2.2.	Integral length scale estimation under the Taylor assumption	50
3.2.3.	Integral length scale estimation under the homogeneous and iso- tropic turbulence (HIT) assumption	51
3.2.4.	L-1 norm synthetic spectrum fit	51
3.2.5.	L-1 norm synthetic spectrum fit with constraint	52
3.3.	Turbulence intensity estimators	53
3.3.1.	Estimation via variance	53
3.3.2.	Estimation via power spectral density	53
3.4.	Separation of rotor wake and background turbulence parameters	54
3.4.1.	Necessary coordinate system change	55
3.4.2.	Novel technique to separate turbulence parameters of rotor wakes from the background flow	57
3.4.3.	Cyclostationary spectral analysis	68
3.4.4.	Test of the new method	69
4.	DLR-CRAFT aeroacoustic fan test facility	75
4.1.	Design and construction of the CRAFT Inflow control device (ICD)	77
4.1.1.	Design of the CRAFT ICD	77
4.1.2.	Construction of the ICD	78
4.2.	Aerodynamic instrumentation	81
4.2.1.	Essential aerodynamic instrumentation for the adjustment of fan operating point	81
4.2.2.	Pressure rakes	82
4.2.3.	Hot-wire instrumentation	83
4.3.	Acoustic instrumentation	84
5.	Baseline characterization of the CRAFT test rig.	85
5.1.	Fan performance map	85
5.2.	Inlet aerodynamics	86
5.2.1.	Velocity flow profile at plane E1	86
5.2.2.	Turbulence intensity analysis at plane E1 - Spatial homogeneity as- sessment	87
5.2.3.	Radial profile of the turbulence intensity and integral length scale at plane E3	88
5.2.4.	Deeper analysis of the low-frequency turbulence mechanisms	92
5.2.5.	Turbulence spectral assessment at plane E3	96
5.2.6.	Radial profile of the Reynolds number based on the dissipation length scale (Taylor microscale) at plane E3	98
5.2.7.	Turbulence isotropy assessment at plane E3	99
5.2.8.	Impact of the ICD ribs on the inflow turbulence	100

5.3. Interstage turbulence characterization at plane E5	105
5.3.1. Impact of the ICD on the turbulence field at plane E5	105
5.3.2. Impact of the fan flow coefficient on the turbulence field for a constant fan speed	109
5.4. Inlet acoustic analyses	115
6. Measurements with variable fan inflow distortion	123
6.1. Test rig configuration for inflow distortion (boundary layer ingestion - BLI) experiments	124
6.2. Test cases measured	126
6.3. Fan operation point adjustment	127
6.4. Aerodynamic and acoustic instrumentation	128
6.5. Aerodynamic analyses	129
6.5.1. Velocity distribution profile	131
6.5.2. Boundary layer profile	132
6.5.3. Reynolds Stresses	133
6.5.4. Turbulence intensity and integral length scale	135
6.6. Fan acoustic analyses	136
6.6.1. Overall SPL levels vs fan flow coefficient ϕ	137
6.6.2. R1.2 microphone ring array spectra vs angular position	138
6.6.3. Sound power levels: Combined axial and azimuthal sensor array technique - CAAS	140
6.6.4. Overall sound power levels vs fan flow coefficient ϕ	143
6.6.5. Overall sound power levels trends: correlation with extrapolated aerodynamic data	144
6.7. Representativeness of the distortion profile generated	146
6.8. Overall correlation among turbulence parameters	148
7. Conclusions	149
8. Recommendations for further research	153
A. Appendix	165
A.1. General aerodynamic equations	165
A.2. Fan aerodynamic parameters	166
A.2.1. Total Temperature	166
A.2.2. Total Pressure Ratio	167
A.2.3. Corrected mass flow	167
A.2.4. Corrected fan speed	168

1. Introduction and Objectives

1.1. Aircraft noise

WHEN flying, civil airplanes are loud. Increasing attention has been given to this problem in the past decades due to the rising demand for flights combined with the expansion of towns towards airports (Envia (2018)). Aircraft noise can be classified into airframe noise and propulsion noise, according to its generating mechanism/origin. Fig. 1.1 illustrates the major noise sources in a modern civil aircraft. The relative contribution levels of each source indicated in this figure to the overall noise emission may vary depending on the aircraft and on the flight condition.

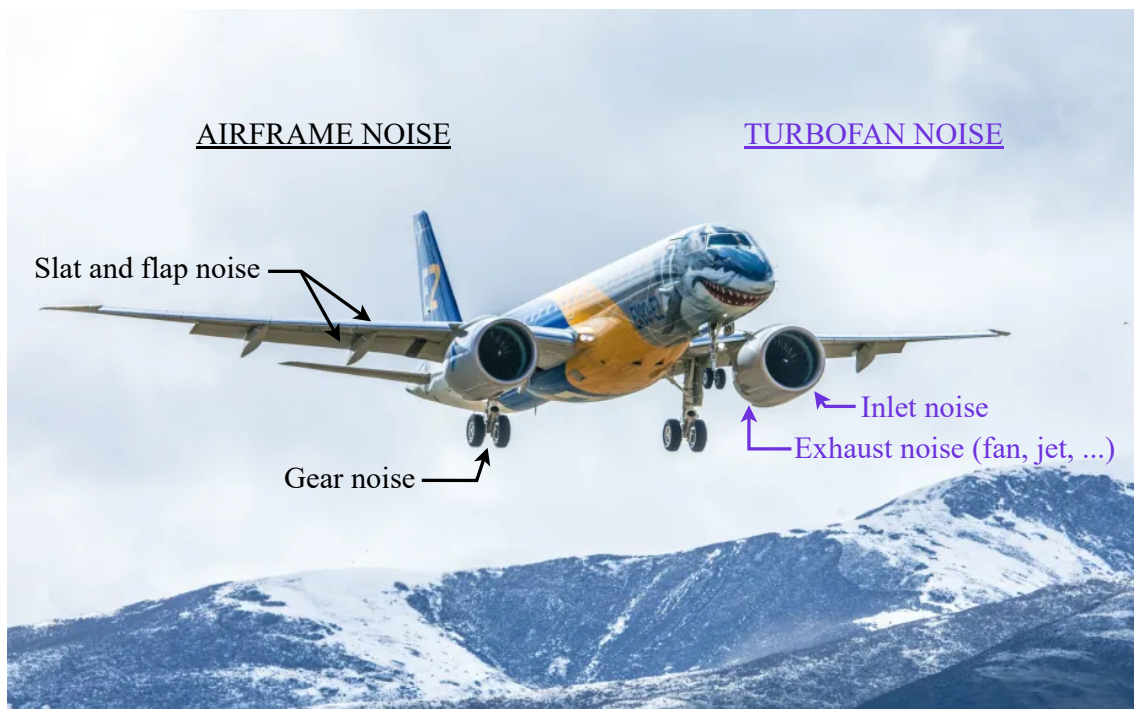


Figure 1.1.: Major sources of in-flight aircraft noise. Photograph extracted from Schuurman (2022).

The relative contribution of each main noise source of a civil aircraft for the flight conditions takeoff and approach is depicted in Fig. 1.2. These results were extracted from Bertsch et al. (2015) and refer to a simulation based on an aircraft similar to an Airbus A319. Details about the simulation method can be found in Bertsch (2013). The airframe noise is composed by the contribution of landing gear, high lift devices (slat and flap),

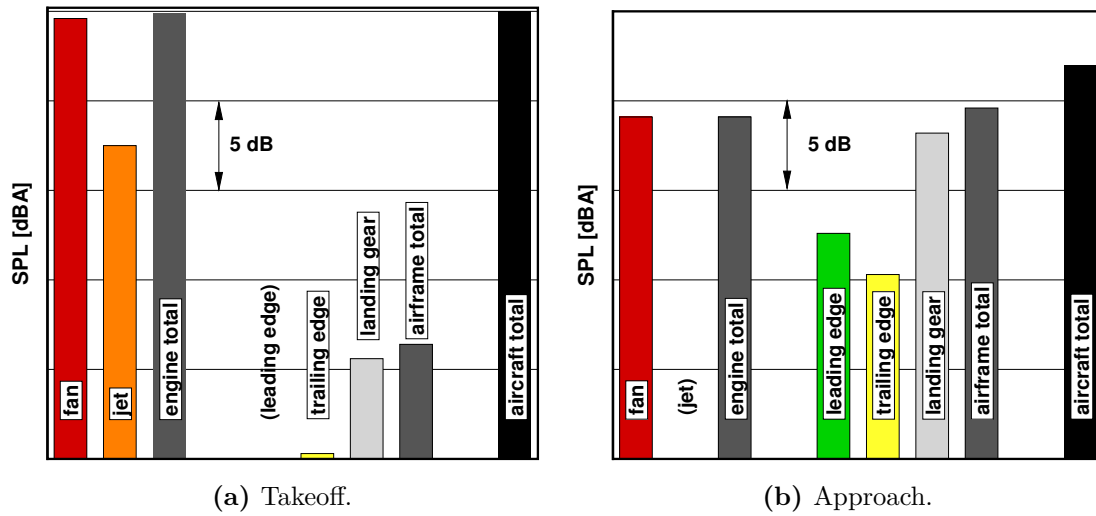


Figure 1.2.: Typical noise source breakdown of an airplane configuration similar to an Airbus A319 for two operating conditions. Figures extracted from Bertsch et al. (2015) and cordially shared by the Authors.

nacelles, etc. In this figure engine noise source is divided into fan and jet. For both flight conditions the noise produced by the engines is comparable to the total aircraft noise emissions. For the takeoff configuration, the engines are the major source of noise generation. The fan stage (composed of a set of blades, typically what is first observed when looking at an aircraft engine from the front, and the outlet guide vanes) generates noise which propagates in both directions of the engine (inlet and outlet), as indicated in Fig. 1.1. Jet noise is generated at the engine exhaust due to the turbulent mixing of the engine exhaust with the relatively lower velocity free-stream flow ('ambient air').

In view that the engines are one critical source of noise of an aircraft, it is therefore logical to focus on the improvement of this component, aiming on overall lower noise emissions. Since the introduction and the widespread use of turbofan engines, the continuous increase in their bypass ratio (BPR), and further technological advances, an overall aircraft noise reduction of around 20 dB has already been achieved (ACARE (2010) and Dron (2008)). The bypass ratio of a turbofan engine is defined as the ratio between the mass flow rate of that bypass the core engine to the mass flow rate entering it. The continuous development of more efficient and quieter engines established the trend of increasing both the fan diameter and the BPR. One of the most recent step in engine technology development was the introduction of a gearbox in the engine to allow lower rotational speeds of the fan, compared to the low-pressure compressor/turbine stage, and to the high-pressure compressor/turbine stage. As consequence, bigger fan diameters can be used, allowing lower jet velocity in the exhaust, reducing significantly the noise generation of the latter. The breakdown noise mechanisms in a turbofan engine is described in the next section. To give the reader an idea of a few modern civil aircraft engines with state-of-the-art technology (to the time this thesis was written) it can be listed: The PW1000G family, a geared

UHBR (Ultra-High Bypass Ratio) turbofan engine equipping airplanes like the Embraer E-Jet E2 family (as in Fig. 1.1) and the Airbus A320neo family. This engine has (for the bigger version) 2.06 m in diameter, a BPR of 12.5:1, and generates a takeoff thrust of 110–160 kN. The CFM International LEAP, a UHBR turbofan engine equipping airplanes like the Airbus A320neo family and the Boeing 737 MAX, uses twin-spool technology (two concentric shafts that rotate at different speeds) instead of a gearbox to allow the fan and the other stages to rotate at different speeds. This engine has (for the bigger version) 1.98 m in diameter, a BPR of 11:1, and generates a takeoff thrust of about 141 kN.

1.2. Fan noise generation

Fan noise can be considered as a combination of tonal and broadband noise. The former, due to the interaction of the periodic rotating wakes generated by the fan blades with the flow and rigid bodies, occurs at the so called blade passing frequency (BPF) and its harmonics. The BPF is a function of the fan speed and blade count. Its fundamental frequency is given by $f_{BPF} = \eta \cdot B/60$, where η is the fan speed in revolutions per minute (RPM) and B is the rotor blade count. The higher harmonic orders of this frequency, that means, the two, three, four, etc., times this fundamental frequency, are typically found in the fan noise spectrum. The broadband component has by definition a continuous distribution over a broad range of frequencies, governed by a non-deterministic stochastic process.

The different fan noise generation mechanisms can be divided into two groups (under homogeneous inflow condition): (1) Rotor coherent components: Tonal noise generated by the fan falls into this group. The periodic fan wakes interact with the stator vanes exciting tones at harmonics of the fan speed. This mechanism is fully coherent with the fan rotational speed. (2) Rotor incoherent components: In general, broadband aerodynamically induced noise belongs to this second group. Its generation mechanisms are intrinsically caused by turbulence and its interaction with rigid surfaces such as fan blades and stator vanes (D. Hanson (2001)).

Fig. 1.3 gives a good picture of the main aerodynamic mechanisms in a turbofan engine associated to the excitation of noise sources. In an ideal working condition, where the inflow ingested by the fan has minimum distortion and turbulence levels, also known as the flight condition, the fan noise emission is the lowest possible. Under this condition, in Fig. 1.3 the two sources: Upstream turbulence and distortion are negligible. The other sources of turbulence generation highlighted in this figure are present under the flight condition and contribute to the generation of broadband noise. These sources of turbulence faced by the fan rotor blades under this condition are the boundary layer turbulence at the duct wall and on the spinner (Glegg (1993)). Further turbulence is added in the flow downstream of the fan: the fan wakes due to the boundary layer over

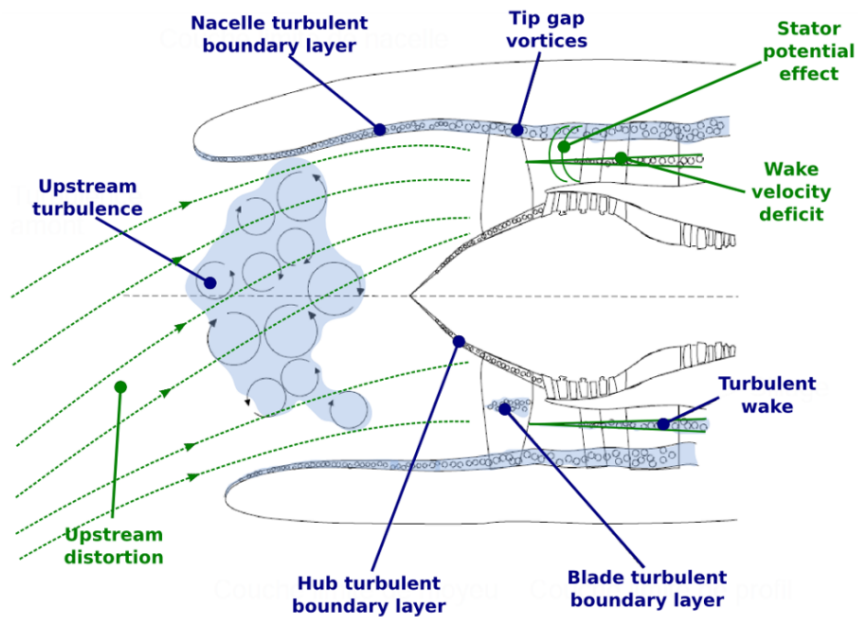


Figure 1.3.: Breakdown of noise sources in a turbofan engine. Figure extracted from S. Moreau (2019).

the fan blades, the tip gap vortices generated due to the gap between duct wall and rotor blades, and the further development of both hub and duct wall boundary layers.

For the understanding of fan noise generation mechanisms, besides the geometry of the fan stage, a detailed characterization of the mean and turbulence flow is necessary. Under distorted inflow condition, additional noise is generated by a fan. The detailed description of the importance of flow turbulence characterization for the understanding and modelling of fan noise generation, as well as the impact of inflow distortion and turbulence ingestion in fan noise emissions will be covered in the next sections.

1.3. Future aircraft concepts: towards lower noise emissions and higher flight efficiency

Alongside with the development of more efficient engines, different concepts have been proposed in terms of aircraft fuselage design with the aim of increasing flight efficiency. A rather established concept which is continuously under investigation with growing attention in face of the current environmental scenario is the boundary layer ingestion (BLI) aircraft concept, an example of highly integrated propulsion. The simple idea that the aircraft's fuselage low-momentum boundary layer can be ingested and re-energized by the engines, reducing in consequence aircraft drag, has been envisaged for decades.

Fig. 1.4 illustrates a BLI aircraft concept proposed within the DLR project AGATA3S (Tapken et al. (2022)). The aerodynamic drag reduction in BLI concepts can achieve a

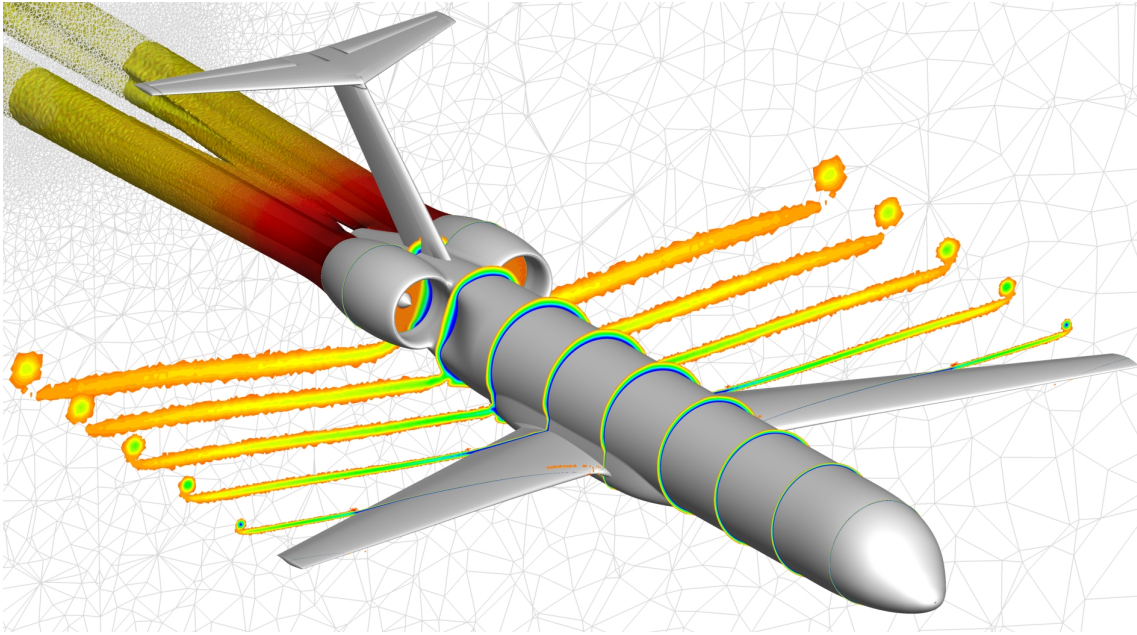


Figure 1.4.: Example of a boundary layer ingesting (BLI) concept alongside with a CFD result. Colors represent qualitatively different levels of velocity deficit generated by the airplane. The engines are highly integrated in the fuselage. This concept was proposed within the DLR project AGATA3S (Tapken et al. (2022)). The CFD analysis was performed by Andreas Vinz from the Institute of Aerodynamics and Flow Technology, Department of Transport Aircraft of DLR.

reduction of up to 15% in fuel consumption compared with conventional concepts (Greitzer et al. (2010) and Madani and Hynes (2009)). The penalty faced by this approach is, however, the loss of performance encountered by the engines, which builds a typical trade-off problem: in order to achieve a positive efficiency net balance, the benefit on drag reduction has to compensate the engine performance loss. In a BLI aircraft design as shown in Fig. 1.4, different than as depicted in Fig. 1.1, the engines are mounted podded into the aft fuselage. In traditional aircraft design on the other hand, as in Fig. 1.1, engines are mounted underneath the wings with enough distance to the fuselage, avoiding any flow distortion or turbulence ingestion due to flow interaction to the aircraft fuselage. Few other examples of BLI aircraft concepts can also be mentioned: A blended wing body concept was assessed by Thomas et al. (2012), the NASA D8 Subsonic Transport Concept reported by I. A. Clark et al. (2018), and a compiled analysis of few configurations reported by Menegozzo and Benini (2020).

The aerodynamic performance loss faced by engines due to BLI is by no means a novelty. Alongside with several researches which aimed on the assessment of the aerodynamic impact of inflow distortion on fan/compressor performance, such as: Gunn and Hall (2014, 2019), Perovic et al. (2019) and Plas et al. (2007), much less effort has been taken, so far, to assess the BLI impact on fan acoustics. As discussed in more details in the next sections, the ingestion of additional turbulence and distorted mean flow by an turbofan

engine generates additional noise. Fig. 1.5 illustrates the problem of fuselage boundary layer ingestion regarding turbulence ingestion. The aircraft's fuselage and engine nacelle is illustrated in blue. The engine is sketched in gray. In red is sketched the region affected by the wall boundary-layer turbulence. In the airplane fuselage side, besides the thicker turbulent boundary layer ingested by one side of the engine, depending on the fuselage design, fuselage flow separation might also occur in a region of adverse pressure gradient. The implication of this all is not only a higher degree of turbulence ingested by the fan, but also a non-axisymmetric distribution of the velocity profile and turbulence distribution at the fan inlet.

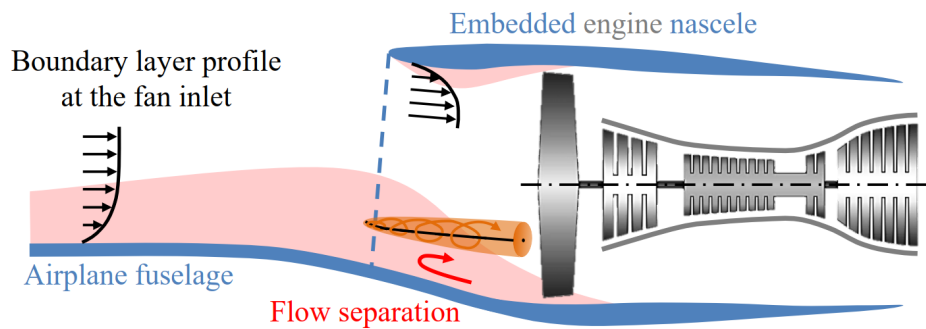


Figure 1.5.: Ingestion of turbulence by a BLI engine. Figure extracted from Tapken (2016).

With the aim of better understanding the inflow distortion impact on fan propulsion systems a DLR project named AGATA3S was started, as reported by Tapken (2016) and Tapken et al. (2022). Within this project, the aerodynamic, aeroelastic, structural mechanic, and aeroacoustic impact on a realistic transonic fan is investigated. Within the branch of aeroacoustics, the current thesis is focused on the inflow aerodynamic characterization under distorted and non-distorted inflow conditions regarding its impact on a low-speed fan. In the frame of the AGATA3S project, measurements were performed both in a transonic fan (Tapken et al. (2022) and Meyer et al. (2022)) as well as in a subsonic fan. To fulfill the experimental data need regarding the subsonic fan, several measurement campaigns were conducted in the newly built low-speed DLR fan test rig named CRAFT (Tapken et al. (2021b) and Tapken et al. (2021a)). The work presented in this thesis refers to the low-speed fan rig.

1.4. Objectives and approach of this thesis

The CRAFT test rig was designed and developed for the detailed study of fan aerodynamic sound generation mechanisms in a laboratory environment, which requires, among others, the minimization of non-representative noise generation components (such as installation and operating conditions, ground vortex ingestion, etc.) and clean inflow conditions for measuring representative turbulence intensities and turbulent length scales.

In a laboratory environment, very special care must be taken regarding the fan inflow properties. The establishment of an ideal environment (turbulence- and distortion-free) is nearly impossible. However, with the state-of-the-art knowledge, the closest to this can be achievable by using an Inflow Control Device - ICD (also referred to Turbulence Control Screen - TCS) placed in front of the inlet of a fan test rig. This device aims on breaking down turbulence structures as well as homogenizing the inflow. Roughly speaking, the turbulence large eddies are broken down into small eddies which dissipate due to viscosity when traveling further downstream. The pressure drop along its surface helps homogenizing the flow over its whole surface. An ICD typically consists of a combination of honeycomb and metal screens built in a precisely engineered shape. The ICD allows the establishment of a baseline condition, where turbulence levels are as low as possible, and the mean flow speed is constant and homogeneous over the duct cross-section.

Once the baseline and clean configuration is established, measurements with distorted inflow may start. For the investigation of fan noise due to inflow distortion in a laboratory environment, different types of flow distortions have to be reproduced in the fan inlet. With the parametric control of distortion parameters such as: mean velocity distribution, turbulence intensity and lengthscales distribution, the impact of the variation of each these parameters shall be assessed and correlated with the fan noise captured by microphone arrays.

With that said, the first goal of this work was to design and construct an inlet composed of a bell-mouth and an ICD for the newly built CRAFT fan rig.

The second goal was to assess the aerodynamic flow-field both at the fan inlet and at the interstage section of the fan stage (between fan and stator vanes). This assessment was performed with the help of extensive aerodynamic measurements by means of pressure rakes and hot-wire anemometry. Three different inlet configurations were assessed. The impact of the new ICD was assessed in both axial positions (inlet and downstream the fan), with focus on its impact on the turbulence flow field. The fan noise emissions were also captured by microphone arrays and correlated with the different inflow conditions.

The third goal was the investigation of fan noise and inflow aerodynamic properties under distorted inflow conditions. For this purpose, the inlet of the CRAFT test rig was especially designed to allow the insertion of predefined distortion devices. Tests with variable inflow distortion were performed and aerodynamic parameters were correlated to the acoustic fan noise emissions.

The fourth and last goal of this work was to develop a reliable data reduction software to extract relevant turbulence parameters, such as: turbulent kinetic energy (TKE) (or equivalently the turbulence intensity) and integral length scale (ILS), to highlight a few. As mentioned previously, these parameters are of crucial importance for the understanding of the fan noise generation mechanisms. Besides that, in order to feed the growing demand

in the departments group working with numeric simulations and semi-empiric models for fan noise predictions (Klähn et al. (2022c) and A. Moreau (2017)), these flow turbulence parameters were expected as boundary conditions for simulations.

1.5. Literature review

The continuous demand for more efficient and quieter airplanes has met in current times critical levels in view of the pressure to reduce the aircraft noise and CO₂ emissions, or even, moving towards net zero carbon emissions. The introduction of Ultra-High Bypass Ratio and geared turbofan engines in modern aircraft contributed one step further to the reduction of both fuel consumption and noise level emissions. However, because of the increasingly growing in engine diameter, fitting these big engines underneath traditional aircraft wings can be challenging due to clearance (distance to wing, fuselage, ground, etc) and other issues (Cousins (2004), Kantola and Warren (1978) and Conrad and McAulay (1955)). Among them, one of relevance is the engine ground clearance, which has become smaller (tighter), what favors the ingestion of ground vortex and further distortions due to the engine - ground interaction (Cousins (2004)).

This section gives an overview of the state-of-the-art knowledge and tools that this thesis is based on. The literature review is grouped according to the four goals of this thesis as described in the last section. According to the needs, a deeper review will be given in the next chapters. Complementary to this survey, a review on fundamental turbulence is found in Chapter 2.

1.5.1. Impact of turbulence ingestion on fan aerodynamics

In order to better understand the impact of turbulence on fan aerodynamics, it is useful to take a step back and firstly discuss its impact on airfoil aerodynamics. The turbulence intensity, the integral length scale, and the Reynolds number play an important role on the characteristics of the airfoil's boundary layer. Some key impacts can be listed as follows:

1. *Boundary layer transition from laminar to turbulent:* Aerodynamic and aeroacoustic characteristic of airfoils are intrinsically connected and dependent on its boundary layer properties. As Denton (1993) states, loss in turbomachines is defined in terms of entropy increase, and one important source of entropy rise is due to the boundary layer. The transition position is mainly influenced by the pressure distribution, Reynolds number, turbulence intensity, and naturally by the airfoil geometry. The Reynolds number based on the airfoil chord length and streamwise flow velocity has a direct impact not only on the boundary layer transition point, but also on the characteristics of the laminar separation bubble (Zhang et al. (2020)). Both the increase in Reynolds number and free-stream turbulence intensity moves the

transition point upstream towards the leading edge of the airfoil (Butlera et al. (2001)) and reduces the size of the laminar separation bubble (Zhang et al. (2020)). According to Butlera et al. (2001), the integral length scale does not impact the boundary layer transition point. Mayle et al. (1997) stated “Transition in a laminar boundary layer begins at the first position along the surface where isolated spots of turbulence are formed, and the main effect of free-stream turbulence is to generate and amplify the laminar fluctuations in the boundary layer upstream of this position. Where these fluctuations attain a critical value, turbulent spots form and transition begins.”

2. *Heat transfer*: Moss and Oldfield (1992) confirmed other previous work in that the heat transfer between airfoil and fluid is a function of the streamwise turbulence intensity and integral length scale in gas turbine experiments. Mayle et al. (1997) also discussed the effects of free-stream turbulence and integral length scale on laminar heat transfer in gas turbines. They highlighted the importance of not only the turbulence intensity, but also the Reynolds number based on the dissipation length scales Re_λ on the heat transfer. One important conclusion from this work was that all length scales of the turbulence field are related through Re_λ . Thus, if T_u and Re_λ are known, λ and all length scales, including the integral length scale Λ , are known. Butlera et al. (2001) observed that the increase in turbulence intensity leads to an increase in stagnation heat transfer in a low-pressure turbine setup.
3. *Stall margin and lift*: Zhang et al. (2020) observed for a NACA0012 airfoil at small angle of attack and under high freestream turbulence intensity levels a minor decrease in lift. On the other hand, at pre-stall angle of attack the lift was increased and stall was delayed.

1.5.2. Impact of inflow distortion ingestion on fan aerodynamics

Not necessarily linked to the ingestion of additional turbulence, the ingestion of distorted inflow in terms of mean velocity profile leads to a fan performance loss. As mentioned earlier in this chapter, several researches have investigated the impact of inflow distortion ingestion by fans or compressors. Among them, three are to be highlighted:

Gunn and Hall (2014) compared experimental and CFD results regarding the aerodynamic effect of BLI in a low-speed fan rig. Plus, a transonic configuration was also simulated and the results were contrasted with the low-speed fan rig. The inflow distortion was generated with the help of a 3D-printed perforated plate with heterogeneous porosity. The aerodynamic field was assessed up- and downstream the fan with the help of a five-hole pressure probe. They found out that the inflow exhibits three-dimensional characteristics, i.e., measurements revealed circumferential and radial components variation in the flow field. Furthermore, for the configuration tested, additional loss was generated by flow

separation of the outer casing boundary layer due to a loading peak at the rotor tip. For both simulated and lab tested configurations, the overall stage efficiency was reduced by 1-2% relative to operation with clean and uniform inflow.

Lucas et al. (2014) performed aerodynamic tests with a modified JT15D-1 turbofan engine (fan diameter: 533 mm, max. speed: 16,000 RPM, inlet Mach number: 0.43). The distorted inflow profile was generated with the help of layered metal screens aimed to reproduced a specific pressure profile. The major findings were a 15.5% reduction in stream thrust and a 14% increase in thrust specific fuel consumption when the engine was tested with inflow distortion. Furthermore, the distortion resulted in an increase of 24% in the mass-averaged entropy production along the fan flow path, compared to the non-distorted configuration Plas et al. (2007). In these works, it is highlighted the importance of a integrated airframe/inlet/engine design to mitigate losses in the entire system.

1.5.3. Fan noise generation due to turbulence ingestion or distorted inflow

The subject of understanding and modelling noise generation mechanisms in fans and airfoils due to the interaction with turbulence received growing attention for around seventy years. One of the early studies was done by Sharland (1964), who proposed a theory and experiments with an isolated plate and a model fan to estimate the noise generation due to its interaction with flow turbulence. One important finding of this work was that the broadband noise generation originates from the lift fluctuations on the fan blades, arising from the vortex shedding at their trailing edge. The interaction of large scale turbulence present in the inflow will also set up additional lift fluctuations, which in turn leads to additional noise generation.

Amiet (1975) calculated the sound radiated from an airfoil due to its interaction with the upstream inflow turbulence. For the developed model, among other parameters, the turbulence spectrum is used as input parameter for the broadband noise generation predictions. In this work (and commonly found) the von Kármán spectrum is used. Due simplifications, these two works assumed homogeneous and isotropic turbulence (HIT), which in a few words, assumes that the turbulence eddies and the fluctuation intensity are identical independent of the direction. The turbulence spectrum model used has a direct impact in the predicted noise generation spectrum. For example, Santos et al. (2021) investigated the impact of the modification of the von Kármán spectrum on the predicted noise emissions of a single airfoil by taking into consideration the turbulence dissipation range in the turbulence spectrum. As consequence, lower levels in the higher frequency-band of the predicted noise spectrum of a single airfoil was observed. More details about basic aspects on turbulence, the HIT, among others will be given in Chapter 2.

Succeeding investigations revealed that in static engine test conditions, the turbulence eddies present in the atmosphere are elongated at the inlet when ingested by the engine.

Therefore the isotropic turbulence assumption does not hold valid. D. B. Hanson (1974) reported a few static engine experiments with the aim on investigating the fan noise generation due to atmospheric turbulence. The fan noise generation model based on blade-loading proposed in this work includes the assumption of flow anisotropy. This model is based on the fact that the elongated eddies interacting with the rotating blades cause a train of lift pulses, which repeat at the fan rotational frequency. This can be physically understood as the chopping of long eddies (correlated structures) by consecutive blades. Relevant for this interaction is the relation between eddy sizes, flow speed, and blade chord length. The interaction of long eddies with the fan blades causes partially coherent blade loading, which in turn leads to partially coherent or narrowband random noise generation. This effect is observed in the harmonics of the BPF, which are broadened or commonly referred to “haystacking” effect, as illustrated in orange in the lower graph in Fig. 1.6. A detailed description of this figure will be given in the following. The energy lost from these narrowband components due to the pulse position modulation was associated to the generation of broadband fan noise. The pulse amplitude modulation to the fan blades interaction with the turbulence eddies cause additional fan broadband noise generation.

Fig. 1.6 gives the reader a qualitative picture of a typical fan noise spectral shape under ideal and distortion ingestion conditions. In this figure, on the top-right a fan rotor / stator stage is sketched. The plot on the top left-hand side shows the average normalized streamwise velocity profile U/U_∞ as a function of the radial position upstream of the fan. The blue curve represents an ideal scenario of uniform inflow velocity, i.e. no wall boundary layer, perfect constant flow velocity profile. The green curve illustrates a distorted inflow velocity profile (typical of a BLI fan) as well as the wall boundary layer. The middle plot shows a generic streamwise turbulence intensity profile $\sqrt{u^2}/U_\infty$ as a function of the radial position. The blue curve represents an ideal, turbulence-free scenario (no turbulence in the free-flow or in the wall boundary layer). The red curve illustrates an example of distorted inflow (similar to a BLI fan), where the non-symmetric wall boundary layer is ingested by the fan. The bottom plot displays a typical noise spectrum of a turbofan engine. The blue graph depicts the fan noise emissions under the ideal conditions as described above (uniform average axial flow velocity and turbulence free). In the noise spectrum, both the broadband and the tone components are visible. The broadband and tone levels are lower than in the red curve, the BPF tones are sharp and no additional narrowband components (“haystacking”) are observed around them.

The fan noise emission under distorted inflow is illustrated by the red/orange/green curve. The increase in the broadband levels (red curve) is due to the ingestion of turbulence, as shown on the top-mid plot by the red curve. The green dots in the noise spectrum illustrate the increase in the tone levels due to the non-homogeneous mean flow profile (as the green curve on the top-left plot). Finally, the narrowband components (“haystacking”) around the BPF tones in the noise spectrum (in orange) are due to the ingestion of large and coherent eddies, or lengthscales (D. B. Hanson (1974) and U. Ganz et al. (1998)). For

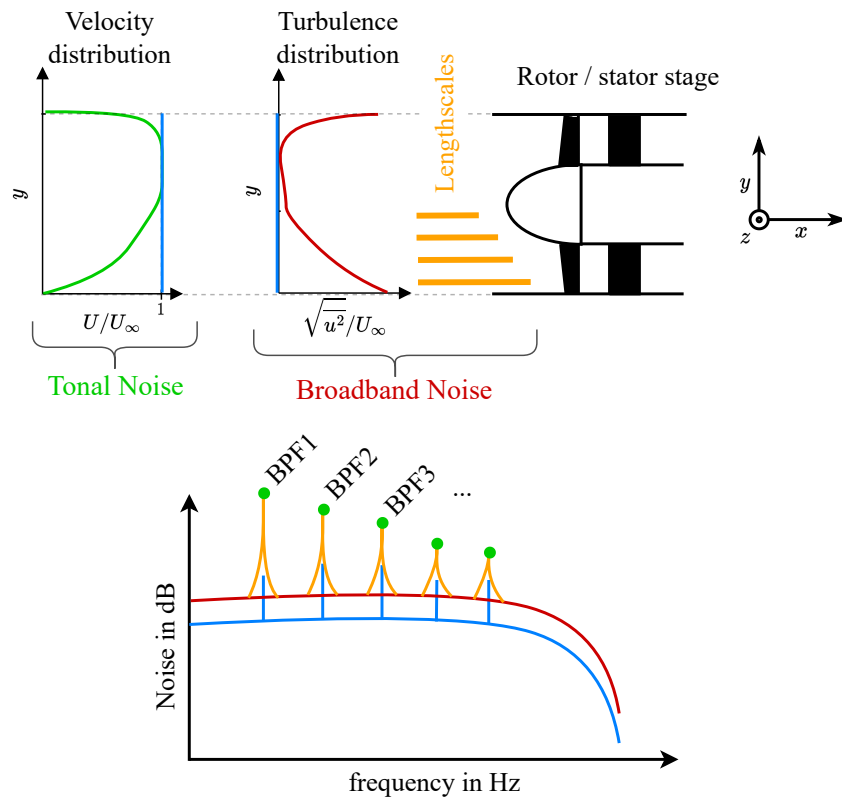


Figure 1.6.: Illustration of the impact of inflow distortion on the fan noise spectrum.

this source of noise, the length of the eddies is important, as the interaction of a coherent eddy with multiple blades is a prerequisite.

One remarkable observation in D. B. Hanson (1974) is the outcome of an experiment performed with the insertion of a cylinder ($0.054D$ in diameter by $0.22D$ in height) between a fan (diameter $D = 1.4$ meters) and its inlet. The fan rig was mounted outdoors for static tests. Pressure transducers were installed on one fan blade to evaluate the intensity of the pressure fluctuations due to the cylinder wake, compared to the atmospheric turbulence ingestion. The analysis of the pressure signal recorded on the fan blade revealed as expected the one-per-rev pressure fluctuation due to the cylinder wake. However, the ingested disturbances from the atmosphere were almost as large as the cylinder wake disturbance, although the ambient wind was only 3.2 km/h. This experiment demonstrated the magnitude of the atmospheric turbulence in the pressure fluctuations experienced by the fan blades.

A comprehensive theory of fan tone noise was proposed by U. W. Ganz (1980). In this work special attention was given to the modelling of the free-stream turbulence. The rapid distortion theory was used to provide all the one-dimensional turbulence spectra of the flow downstream the inlet contraction, considering then the deformation of the atmosphere turbulence eddies. The turbulence upstream the contraction was considered isotropic. One important outcome of this work was that the difference in fan tone noise

generation between static and flight conditions due to atmospheric turbulence is mainly because of the difference in turbulence intensity involved in the fan tone noise generation. However, the difference in spectral shape due to the different turbulence scale energy distribution plays an important role. In static tests, the inflow contraction results in three main impacts in the turbulence field: (1) large initial lengthscale (low-frequency turbulence power); (2) large increase in the power of the transverse turbulence component; and (3) large streamwise integral length scale at the fan face. At flight condition the turbulence power at large wavenumbers (high-frequency) decreases with altitude due to the nearly constant turbulence power and the increase of the large scales with altitude. In other words, the power in the turbulence spectrum shifts towards the low-frequency band of the spectrum with the increase in flight altitude, remaining, however, the overall spectrum power nearly constant. Complementary to these findings, Majumdar and Peake (1998) demonstrated the different impact of static and flight tests in the turbulence integral length scale and how they impact fan noise generation. The integral length scale was found to be a key parameter to understand fan tonal noise generation.

Kobayashi and J. Groeneweg (1980) investigated the impact of inflow distortion in terms of mean velocity profile on the fan tone noise generation. The periodic movement of the rotor blades subjected to a non-homogeneous mean flow generate extra tonal noise. The model developed uses as input, among others, the aerodynamic modal structure computed from the distorted inflow profile. The radial and circumferential distortion shapes are obtained from the Fourier-Bessel components, which represent each individual distortion mode, similar to a mode decomposition. The contribution of each individual aerodynamic mode and the generated acoustic mode is then computed. For instance, a test reported with a Gaussian circumferential distortion profile generates circumferential acoustic mode content corresponding to the circumferential Fourier harmonic content associated with the aerodynamic distortion. Moreover, the flow non-homogeneity effects the rotor wakes and thus the noise sources resulting from the rotor-stator interaction. Highlighted in this work was, however, that each generated acoustic mode is subject to a coupling constraint. Because of the way the dipole sources are generated on the fan blades, some modes are effective on generating acoustic mode power, whereas others are not. The experimental assessment of the impact of distorted mean velocity profile on the fan tonal noise generation is, however, not straight-forward. The presence of a pressure gradient in the inflow profile is itself a fundamental mechanism of turbulence generation. As consequence, the generation of different distortion profiles with negligible levels of turbulence might be challenging, and therefore, hard to isolate the effects of distortion mean velocity profile from the ingestion of additional turbulence.

The specific problem of fan noise generation due to the ingestion of an asymmetric and thicker boundary layer as depicted in Fig. 1.5 involves the combination of the two phenomena described above: the ingestion of a non-homogeneous mean inflow profile and additional and non-homogeneous turbulence distribution. Non-homogeneous in this context

means in the extent of the 2D distribution throughout the duct cross-section. Generally speaking, the thickening of the boundary layer enlarges the region with high turbulence content. The thicker the boundary layer is, the more turbulence is ingested by then fan, which is translated in an increase in the broadband levels proportional to the increase of the turbulence levels.

An important experiment setup for the understanding of open propeller noise generation due to boundary layer ingestion is the Benchmark ‘3rd fundamental test case - FC3’. Which consisted of a 10-bladed, 457 mm diameter open rotor operating inside the test section of a wind-tunnel, partially immersed in a planar boundary layer, as reported by Wisda (2015) and Murray et al. (2018) at Virginia Tech and exhibited in Fig. 1.7. The rotor distance to the wind-tunnel wall was carefully adjusted depending on the thickness of the wall boundary layer ingested by the rotor. The rotor advanced ratio was adjusted based on the ratio of the wind-tunnel free-stream speed and the rotor blade tip speed. The noise emissions were captured by microphones placed outside the test section, behind sound-transparent Kevlar wall. Measurements with hot-wire probes mounted on a rotor blade revealed an abrupt increase in blade angle of attack when the rotor blade travels inside the ingested wall boundary layer, suggesting reverse flow in this region. The “haystacking” generation due to BLI was investigated and correlated with the various advanced ratio tested. They found that for low advanced ratios, the haystacks narrowed, became more symmetric, and increased in number. The narrowing of the haystacks was associated to the increase in correlation between turbulence eddies and its interaction with the rotor blades.

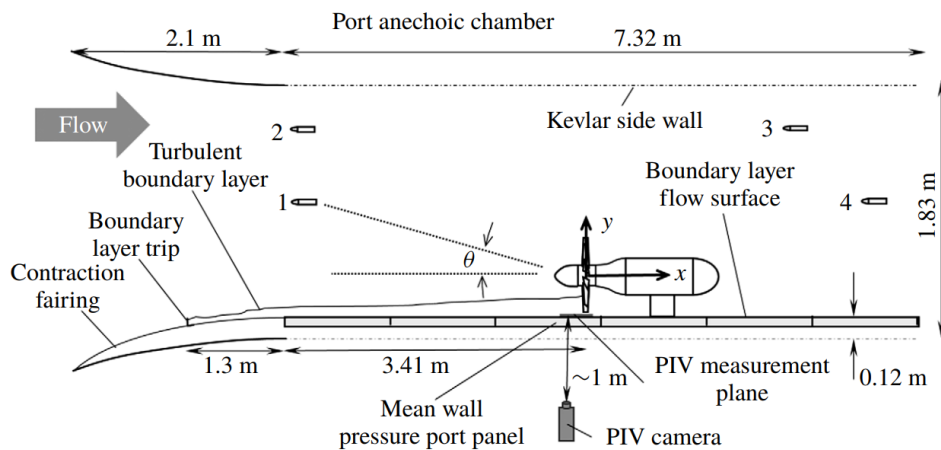


Figure 1.7.: Detailed schematic of the wind-tunnel test setup with a propeller ingesting wall boundary layer. Figure extracted from Murray et al. (2018).

Gonzalez-Martino and Casalino (2019) performed large eddy simulation (LES) using lattice-Boltzmann solver in order to predict the noise levels generated for this same test setup. The Reynolds stresses profile of the planar boundary layer obtained from the simulations matches fairly well the measurements, which is a crucial step for an accurate noise gen-

eration prediction. The authors highlight that the haystacks around the BPF tones are very significant for specific operating points.

More recently, Staggat (2021) developed a model based on the noise prediction physical-based analytical tool PropNoise (A. Moreau (2017)) for the prediction of broadband noise emission in open rotors and ducted fans. The different noise generation mechanisms and the dependence on the turbulence parameters on the noise generation prediction are described. Key turbulence parameters for the noise prediction modelling are the 2D cross-section distribution of the: mean flow speed, turbulence intensity, and integral length scale. The present work has great overlap with this last mentioned thesis, although Staggat (2021) worked with the development of analytical tools for the investigation of fan noise generation due to BLI, the present work is focused in the experimental assessment of fan noise generation under similar circumstances.

1.5.4. Estimation of relevant turbulence parameters

The importance of the assessment of turbulence parameters for the understanding and prediction of fan noise generation mechanisms have already been discussed. Key parameters are typically the turbulence intensity, the integral length scale and the mean flow velocity. The typical need of only these parameters is because of the use of turbulence models for the simplification of the problem. One turbulence model widely used in turbomachinery applications is the von Kármán. However, if no simplifications are made, or no modelling is used, more information from the turbulence field is necessary. As stated by Mayle et al. (1997) “...the effects of turbulence can only be explained when the full spectrum of turbulence is known”. Another important outcome from this work was that once the turbulence intensity and the Reynolds number based on the dissipation lengthscale are known, then all the turbulence lengthscales can be determined.

Parameters such as turbulence intensity, integral length scale, and dissipation length scale have their equations well defined in the literature (Pope (2000) and Hinze and B. J. Clark (1975)). The problem in the estimation of these parameters arises due to the fact that, especially for the two length scales and the turbulence spectral shape, statistic tools are necessary for their estimation, due to the strong stochastic, non-deterministic behaviour of turbulence and the lack of mathematical tools to fully describe it. In addition to that, disturbance that may be present in turbulence measurements. To give a few examples of distortions in turbulence measurements, Mark (1981) reported the problem of disturbance in the low-frequency band of the turbulence spectrum, i.e., additional power content found in this frequency band. The origin of this phenomenon was associated to “wind gusts” and does not have necessarily to do with turbulence. Nevertheless, it is a physical phenomenon related to the atmosphere which was captured by the measurement instruments and not artifacts due to the measurement technique itself. The negative impact of this disturbance

is that the estimation of the integral length scale, as will be carefully shown in Chapters 2 and 3, is directly dependent on the low-frequency band power of the turbulence spectrum. If distortions are present in this frequency band, errors in the estimation of this length scale is encountered.

Karlos et al. (2021) reported the problem of probe vibration during hot-wire anemometry measurements. Contamination in the turbulence spectrum such as tones and narrow-band components were observed due to this problem. The impact of this kind of contamination is that e.g. higher turbulence levels were observed by the instruments than the real levels present in the measured turbulence field. Karlos et al. (2021) proposed a technique based on the signal measured by accelerometers installed in the anemometer probe to reduce the contamination in the turbulence spectrum.

In view of the importance of turbulence parameter estimation in this thesis, Chapter 3 is completely dedicated to the issue of estimating the relevant turbulence parameters. Different estimators are covered, depending on the assumption that can be made about the turbulence field measured. Also important for the understanding and prediction of fan noise generation mechanisms is the turbulence characterization of the stage downstream the fan and upstream the OGV (Output Guide Vanes), called interstage. In this region the periodic wakes generated by the rotor blades have to be characterized and discerned from the background flow. Signal processing techniques are required for the separation of turbulence parameters from these two domains. The following section covers a literature survey on this problem.

Separation of turbulence information of rotor wakes from background flow

Evans (1975) analyzed hot-wire data from a compressor rig measured downstream the moving blades. A relevant observation from this work was that the free-stream turbulence levels are lowest near the compressor design point, and increase with decreasing flow coefficient as the compressor operation point moves towards stall condition. This study was one of the pioneers on removing the periodic component of the mean velocity distribution due to the rotor wakes for the correct estimation of the turbulence intensity. It was also observed that turbulent components from the velocity signal become more important than the periodic fluctuations of the mean velocity, when the compressor operating point changes towards stall.

Camp and Shin (1995) performed a series of measurements in three different multistage compressors. Hot-wire measurements were performed downstream of one of the rotors of a multi-stage compressor. For more details about the measurement procedure please consult the reference. For one compressor configuration the hot-wire was traversed both in radial and circumferential directions, covering two vane passages. In order to suppress the harmonic components arising from the periodic rotor wakes, they proposed estimating

the turbulence intensity by transforming the data into the frequency domain by a discrete Fourier transform, setting the BPF tones to zero, and in turn transforming the spectrum back to time domain. The integral length scale was obtained by the multiplying the Fourier transformed series by its complex conjugate, transforming it back to time domain in order to obtain the auto-correlation function. This function was then integrated giving the equivalent ILS of the signal. This approach allows removing the power due to the periodicity of the rotor wakes from the turbulence power spectrum, however, only providing the average parameters (turbulence intensity and ILS) of the respective measurement data.

Lewalle and Ashpis. (2004) used the Wavelet technique to assess spatial and frequency resolution from the turbulence data measured downstream a rotating fan. The unsteady velocity signals from hot-wire measurements were segmented in data blocks with size equivalent to a blade passage. The blade passage is defined as the geometric angle between two neighbouring blades. The data blocks were averaged in the time domain delivering the average velocity profile of a rotor blade wake. The wavelet transform was then applied into this smoothed signal. Each element from the wavelet spectrum was multiplied by its respective frequency in order to obtain the energy spectrum $f.E(f)$, where f stands for the frequency and $E(f)$ for the wavelet spectrum. The maximum of this energy spectrum is associated with the dominant turbulence scale in the flow, which is not the same as the turbulence integral length scale, since the formulations for each procedure are different from each other. However, the results are correlated. Under Taylor's hypothesis (Pope (2000) and Hinze and B. J. Clark (1975)) and the HIT assumption, for $Re > 300$ the ratio of the integral scale and the calculated dominant scale lies at approx. 0.75.

The Wavelet technique is performed into the time-averaged velocity signal, which is equivalent to the coherent component resulted from a cyclostationary analysis, as described in Section 3.4.2. The averaging procedure in time domain leads to a loss of the turbulence information of the signal. In our understanding, what remains is the average shape of the rotor blade wake. The wavelet spectrum will have a shape dependent on the slope of the averaged wake velocity profile, not due to the turbulence properties themselves. In our opinion, a potentially better approach could be done by applying the wavelet technique either on the incoherent part of the signal resulted from a cyclostationary analysis, or directly on the resampled signal. After that the wavelet spectrum of each data block can be averaged for every blade passage. This approach is similar to a Welch power spectrum density estimator (Kay (1993) and Percival and Walden (1993)), but instead of using a discrete Fourier transform, the Wavelet transform shall be used. In this way, the frequency properties of the signal is averaged out over every blade passage, and not the time domain properties.

Jurdic et al. (2009) used techniques based on the cyclostationarity property of the turbulence signals combined with the Wigner-Ville (Giannakis et al. (1998) and Antoni (2007))

spectrum to detect cyclic-periodic properties of the turbulence spectrum. The authors demonstrated the ability of the technique on estimating the cyclic turbulence spectrum related to the periodic rotor wakes, and the turbulence spectrum of the background flow. With these two spectra the turbulence parameters of each domain could be successfully retrieved. One potential drawback of this approach is the cross-interference that might be experienced in the estimation of the Wigner–Ville spectrum (Antoni (2007)). Despite the complexity of its implementation, the technique performs properly with experimental data. One particular issue reported in this work regarding the over estimation of the ILS is due to high power content in the low-frequency band of the turbulence spectrum. This sort of phenomenon is believed to not be turbulence related and can be filtered out from the turbulence spectrum by applying specific techniques as described in Mark (1981) and Caldas et al. (2021b).

Maunus et al. (2013) processed data from the SDT NASA test bed (Envia (2002)). They observed that the ILS increases from hub to tip. Furthermore, these scales are larger for an axial position further downstream compared to one closer to the fan. They stated that, as previously reported by Podboy et al. (2003), this is due to the thickening of the wakes, as they are convected with the stream. Maunus et al. (2013) argued, it is impossible to calculate passagewise distributions of the integral length scale with only hot-wire measurements. Instead, they estimated this length scale as a function of the root-mean-square velocity (in the streamwise direction), the mean energy dissipation rate per unit mass ϵ , and a Reynolds number dependent constant C_ϵ . With the help of this formulation, the ILS could be estimated for the entire rotor passage. Results were compared with several RANS CFD simulations. The distribution of the ILS estimated from hot-wire data compared with several CFD was quite disparate and hard to draw any conclusion about possible trends.

Odier et al. (2018) analyzed hot-wire data obtained downstream the fan and the stator vanes of real turbofan engine (DGEN380). Results were compared with LES numerical computation. A separation of rotor wake and background turbulence was not performed in this study. A spatial distribution of the turbulence integral time scale as well as turbulence intensity are shown for experimental and simulation data.

Another possibility to estimate the turbulence parameters of rotor blade wakes is by using empiric methods. One to be cited is described by A. Moreau (2017). The estimation of the integral length scale is made based on the shape of the wake mean velocity. That means, no turbulence data is necessary, instead, the mean velocity profile of the wakes is used with help of some calibration factors to estimate the ILS. This method is particularly helpful for estimating turbulence parameters from simulation data, in the case when only the average profile of the flow downstream the fan is available.

1.5.5. Design and construction of an ICD

The use of an ICD mounted on the inlet of a fan test rig is widely used since decades for fan acoustic measurements. The use of honeycombs combined with wire meshes is well-known and largely used for wind tunnel applications for turbulence reduction (Cattafesta et al. (2010)). In a conventional wind-tunnel, a combination of honeycomb and screens is placed inside the settling chamber, where the flow speed is lower compared to the test section. The section where these devices are installed is rather flat, which facilitates the installation of honeycomb panels, which are intrinsically stiff. However, the inlet of a ducted fan test rig consists of a bell-mouth and the flow control device must be incorporated onto that. The solution commonly found is to build a flow straightener roughly in a shape of a half sphere to account for the three-dimensional inlet flow. Different designs are proposed in the literature, such as using flexible honeycombs with ribs as structure (see Pochkin and Khaletskiy (2014) and Loew et al. (2006)), self-supported flexible honeycombs without rib structure (see Schulz and Köhler (2011), Köhler (2012) and Sturm (2015)) or even flat panels arranged in a geodesic shape (see Ganz (Mar. 31, 1981) and D. L. Sutliff (2018)).

Existing ICD designs were reviewed with the goal of developing an optimal design for the CRAFT test bed based on the gained experiences. Despite the number of ICD variants found in the literature, their performances are often not clearly reported neither in terms of the impact on fan noise due to inflow turbulence reduction, nor as a full assessment of the flow turbulence properties, or regarding the flow homogeneity established by the ICD. Some examples of existing ICDs are shown in Fig. 1.8. A careful description of a compact ICD design and manufacturing was given by Homyak et al. (1983). In this approach, flexible honeycombs were used together with thin ribs as structure. No screen was added. They observed a few extra high order acoustic modes at the blade passing frequency (BPF) originating from the interaction of the rotor with the wakes of the ribs. These modes were, however, considered insignificant due to the low amplitude levels. To avoid this problem the number of ribs can be chosen based on the fan blade count in a way that mostly cut-off modes are excited. Following the same design, Pochkin and Khaletskiy (2014) reported a great reduction of the BPF tones measured in the far-field, besides a slight reduction of broadband noise due to the ICD.

ICDs for the fan test rigs at NASA Glenn (D. L. Sutliff (2018) and D. Sutliff (2019), Fig. 1.8f), École Centrale de Lyon (Pestana et al. (2017)) and the outdoor test bed from Boeing (Ganz (Mar. 31, 1981), Fig. 1.8e), all have geodesic shape. But no reference was found regarding their impact on fan noise generation. The geodesic shape has *a priori* the advantage of having no periodic structural ribs. Therefore, no associated wakes are introduced in the flow. However, such a design and construction is highly complex. The connection of adjacent honeycombs must be perfect, otherwise, any gap between two panels would allow a preferable path for the flow (lower pressure path), leading to flow non-homogeneity and turbulence generation. Moreover, a frame should be constructed

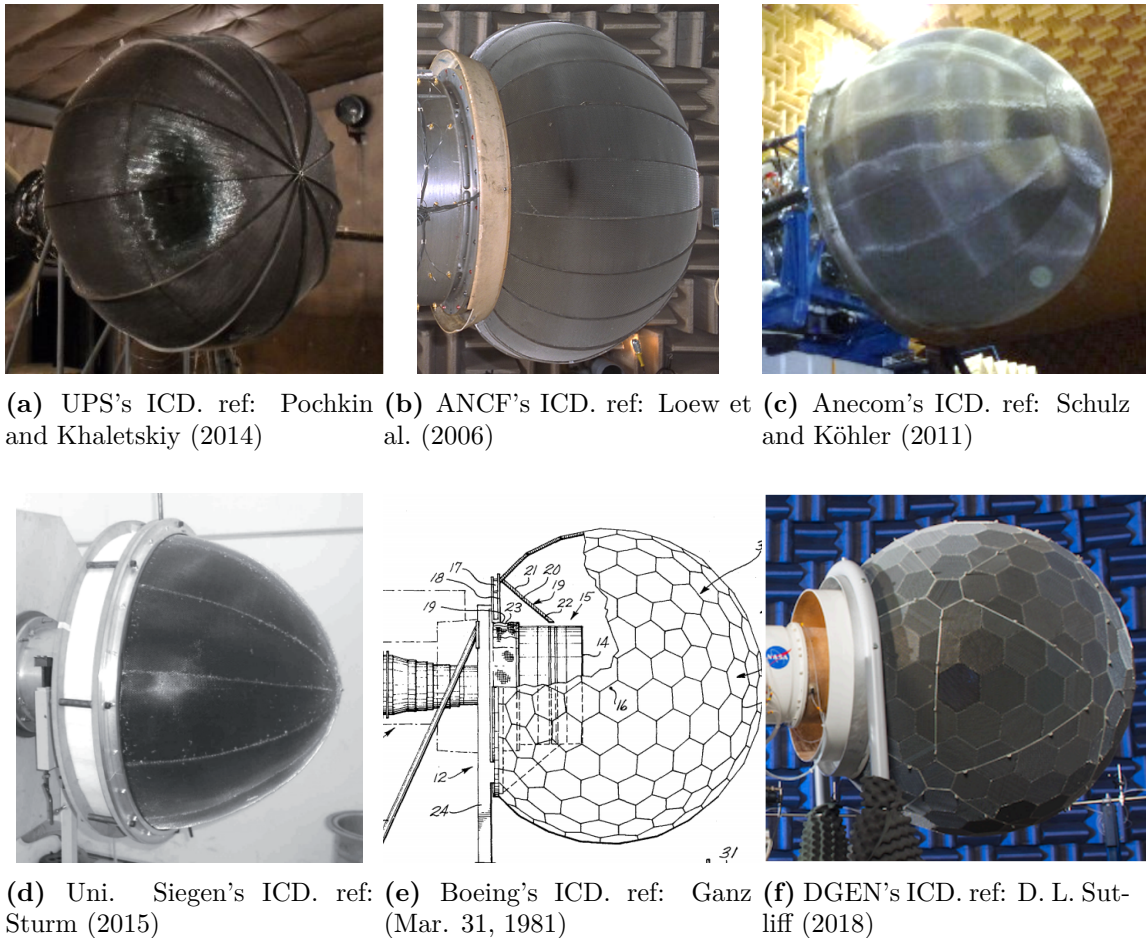


Figure 1.8.: Different ICD geometries collected from the literature.

to support the honeycomb panels, which would have to be precisely cut to fit at each individual position.

The solution found by Sturm (2015) and Sturm and Carolus (2013), as in Fig. 1.8d, uses flexible honeycomb material without structural ribs. In fact, due to the small ICD diameter (approx. 1 m) and low mass flow, no big structural forces are found on this ICD. The honeycomb panels are connected together with thin wires. Four segments of wire mesh are placed downstream, directly onto the honeycomb, forming a half hemisphere shape. A significant reduction of turbulence and fan noise levels was determined for this configuration. However, turbulence measurements revealed a cross-shape characteristic (Sturm (2015)), which is likely due to the overlap of the mesh segments. Although the ICD seems to be cost-efficient and delivers good performance, the observed effect should be avoided for the present ICD design.

The ICD of Anecom AeroTest (Schulz and Köhler (2011) and Köhler (2012)), shown in Fig. 1.8c, is based on flexible stainless-steel honeycombs spot-welded together without structural ribs. A thin wire mesh is also spot-welded on both sides of the ICD. A perfect round shape is achieved with no flat panels or ribs. For this reason and based on the

report of Grizewski et al. (2021), we believe that this is one of the best solutions in terms of homogeneous and low-turbulence inflow so far achieved. However, this design might be one of the most expensive, based for example on the price of stainless-steel honeycomb and manufacturing complexities.

1.5.6. Impact of ICD on the inflow aerodynamics and on the fan noise generation

As discussed in the last section, a fair number of ICD variants can be found in the literature. Important to highlight is that, the ICD has to be designed for each specific engine/fan, as a dependence on the mass-flow, fan diameter, etc. Different ICD sizes have different impact in the inflow aerodynamics for a same engine under test, as reported by Mcardie et al. (1980). Notwithstanding the ICD size, the type of materials used also play an important role on its aerodynamic performance. One example is whether wire meshes are used combined with honeycombs or not.

Mcardie et al. (1980) reported static tests with a turbofan engine for flight simulation. Four ICD's consisted of honeycomb and screen, with overall size ranging from 1.6 to 4 fan diameters, with different shapes and fabrication method were tested. At subsonic fan tip speed the acoustic transmission loss was negligible for all ICD's tested. Transmission loss was found, however, at supersonic fan tip speed for the smallest ICD. Far-field microphones measurements revealed for all ICD's tested significant reduction of the BPF tones. The smallest ICD introduced propagating modes, which are believed to be due to the ICD structural struts. Pressure transducers mounted on the fan blades confirmed that all ICD's tested removed the unsteady inflow disturbances and their harmonics. Distortions capture when the ICD was installed was related to the test setup, such as engine struts, and the ICD structural support itself.

Rogers and U. Ganz (1980) assessed two different aircraft turbofan engines operating in outdoor static tests with and without ICD. Static pressure measurements performed at different circumferential and axial positions showed no difference comparing test cases with and without ICD. Total pressure probe traversed in the fan inlet captured the boundary layer mean velocity profile and also revealed no impact due to the ICD. Pressure transducers installed on a rotor blade of both engines showed a noticeable reduction in the broadband fluctuations of the pressure comparing the cases with against without ICD. For one specific engine, higher content of broadband pressure level fluctuations was recorded for static tests with ICD when compared to the flight test. Pressure transducers were also mounted on one fan exit vane leading edge. A substantial reduction in the harmonic amplitude was observed between 1BPF, 2BPF, and 3BPF. The reason for that was attributed to the lower level of higher harmonic content in the rotor wakes as a result of wake merging due to the ICD.

Hot-wire anemometry measurements in the inlet of both engines confirmed the strong reduction of the turbulence levels, leading to an overall reduction in the turbulence spectrum levels. The authors showed the similarities of the turbulence spectral shape from hot-wire data measured at the engine inlet during static tests compared to turbulence data measured at flight. Indeed, in both cases the turbulence spectra is characterized by a large inertial subrange, typical for large scale turbulence fields. Turbulence levels of 0.6% for all velocity components were found for the flight test case. Another outcome from this work was that, for static tests, the inflow field for the case without ICD is dominated by airflow distortions related to the test facility itself, rather than atmospheric turbulence, and therefore the crucial importance of the ICD.

Kobayashi and Torisaki (1986) reported the aerodynamic performance of ten small scale ICD's mounted on the inlet of a test rig. For these preliminary tests, the fan stage was removed from the test rig and a blower was connected to the rig to establish air flow through the ICD under test. A combination of several different materials were tested, among different honeycomb sizes, combined or not with wire meshes or perforated plates. They observed that the honeycomb combined with wire mesh is the most effective combination for turbulence reduction. Furthermore, an additional wire mesh installed downstream of a honeycomb reduced the low-frequency band of the turbulence spectrum by more than 4 dB, compared to the case of a honeycomb alone. The use of wire mesh was found important especially in the reduction of the longitudinal turbulence generated but not suppressed by a honeycomb. With the new findings and experience gained, a full-scale ICD was built for an outdoor turbofan engine test rig. A geodesic shape, half sphere, and 4 m in diameter was chosen, equivalent to 3.5 times the fan inlet diameter. Each element of the geodesic was composed of: a frame member, a perforated plate with 51% OA covering each element's outer side, honeycomb of 6.3 mm cell size by 41 mm depth (length/cell-size ratio $L/D = 6.5$), and a 20 wire mesh screen in the inner side.

Inlet measurements in a turbofan engine showed a reduction of the turbulence intensity for the axial velocity component from levels in the range of 2-3% to 1.3%, comparing the cases without to with ICD, respectively. The turbulence intensity reduction of the circumferential component was found in the range of approx. 2.8-4% to 1.5%. Also shown in this study with the help of hot-wire measurements in several circumferential positions is that the ICD established not only lower turbulence levels for both velocity components, but a homogenization along the circumferential direction regarding the turbulence levels was found. A reduction factor of two in the turbulence axial lengthscale due to ICD compared to tests without ICD was reported. Furthermore, tests without ICD revealed a $\pm 1\%$ variation of the fan rotational speed, whereas with ICD this number dropped to as low as $\pm 0.1\%$. The authors associated this improvement with the strong reduction of inflow distortion due to the ICD.

Acoustic measurements were performed with a forward far-field 45 m radius arc micro-

phones. A maximum of 20 dB tone reduction for the 1BPF was found at a position roughly perpendicular to the engine axis when comparing tests with to without ICD. The microphone aligned with the engine axis virtually did not recorded any level difference for this tone. The acoustic transmission loss of the ICD was found to be less than 1.0 dB.

Cocking and Ginder (1977) reported tests with two transonic fans. A 2.03 m diameter ICD was mounted at the rig's inlet. The ICD was built with self-supporting honeycombs, without struts or wire meshes. Hot-wire measurements revealed a reduction of the turbulence intensity and length scales both inside the wall boundary layer and in the main stream, due to the ICD. Acoustic measurements were performed with a forward far-field arc of microphones. A substantial reduction of both 1BPF and 2BPF tones for both fans was observed. No extra interaction tone was captured due to a possible fan-ICD aerodynamic interaction. The broadband noise levels were hardly affected by the ICD. The authors argued that this is consistent "with the view that the self noise of the rotor is the main contributor rather than sources excited by inflow disturbances."

Grizewski et al. (2021) analyzed the impact of an ICD on the transonic fan noise generation with the help of the cyclostationary technique. The ICD tested is made out of honeycomb covered on both sides by a thin wire mesh, as reported in Köhler (2012). Tests were performed in the transonic fan at AneCom aerotest rig. Acoustic measurement with a mode detection microphone ring and forward far-field arc microphones were analyzed. For subsonic fan speeds, a consistent BPF tone reduction was found when the ICD was installed. A reduction in other fan-coherent sources such as tones present in the frequency band between BPF's was also observed. No visual difference was observed in the broadband spectrum comparing the cases with and without ICD. By performing a cyclostationary analysis, the level of the four first BPFs were analyzed in terms of rotor locked and fluctuating components. The coherent components outputted from the cyclostationary analysis (rotor locked) is associated with the fan-periodic sources, such as stationary distortions that might be present in the inflow (e.g. wake from sensors) or the rotor locked sources themselves. The fluctuating components are associated to non-stationary and stochastic sources, such as turbulence ingestion. A significant reduction in the fluctuating contribution of the four BPFs was observed due to the ICD. This impact was more significant for the 1BPF and progressively lower for the higher BPF harmonics. The rotor locked component did not change considerably comparing the two cases with and without ICD. The authors concluded that the BPF tone amplitude reduction due to the use of an ICD is due to the reduction in the fluctuating component present in each tone.

Data analyzed from far-field microphones suggests that the use of the ICD influenced the radiation of 1BPF and 2BPF. Peaks in the radiation pattern of these two tones were shifted forward when the ICD was installed. For lower subsonic fan speeds, a modal analysis showed that the Tyler-Sofrin interaction modes were stabilized and most of the power was concentrated in relatively few modes when the ICD was installed. For tests

without ICD, however, power was spread out into neighboring mode orders of the Tyler-Sofrin modes. The cause of that was associated to the refraction effects when the acoustic waves propagate through non-uniform flow.

Sturm and Carolus (2013) researched the impact of the ingestion of large inflow distortions in fan noise generation. One objective of this work was to evaluate current standards for acoustic measurement of industrial fans, which require, among others, an undisturbed volume (room, or plenum) upstream of the fan. One main take away from this study was that the standard requirement for fan acoustic measurements proved to be insufficient to eliminate the impact of fan noise generation due to inflow distortion ingestion. Tests were performed with and without an ICD mounted at the fan inlet inside a semi-anechoic chamber meeting the ISO 13347 for fan acoustic measurements. Results revealed a notorious BPF tone reduction due to the ICD, besides also a small reduction in broadband levels. They argued that the large scale flow structures in the plenum, although associated to small flow velocities, are responsible for velocity non-homogeneity in the fan inflow profile. This is the reason for the presence of tones at the BPF produced when the rotor was tested isolated (without OGV). Solutions for the reduction of inflow distortion in indoor fan tests, according to this study, could be a very large room, where the fan intake is placed in. However, this solution is in most cases impractical. On the other hand, the most feasible solution is the use of an ICD mounted on the inlet of the fan rig.

1.6. Novel contribution of this thesis

The main contribution of this thesis is in the comprehensive analyses and characterization of the turbulence parameters and their correlation to the fan noise generation. A summary of the novel discoveries and developments that this thesis added to the scientific community is listed as follows:

- Characterization of the in-house built ICD impact on the turbulence field of the fan inflow. Turbulence spectra were analyzed for several different radial positions in the flow, alongside with a few important turbulence parameters such as turbulence intensity and integral length scale. The impact of the ICD was compared to the case without ICD and with the ICD plus an additional honeycomb installed inside the inlet channel upstream the fan.
- The low-frequency power content in the turbulence spectra was assessed, as well as the impact of the ICD in this turbulence frequency band. The possible correlation of its impact on the fan noise generation is proposed.
- The turbulent wakes of the ribs used in the ICD were measured and analyzed.

- A novel technique based in time domain to separate the turbulence statistical information of the fan blade wakes from the background flow was developed and detailed. This technique allows retrieving turbulence parameters from the fan wakes and background flow.
- The impact of the ICD in the fan wakes turbulence field was assessed with the help of the new tool. This allowed the characterization of the turbulence parameters of the rotor wakes and in the background flow for each inlet configuration.
- Experimental characterization of distorted inflow generated by perforated plates in terms of the aerodynamic and turbulence field, and its impact on fan noise generation.

Most of the findings of this thesis have been published in different conferences Caldas et al. (2019a,b), Caldas et al. (2021a), Caldas et al. (2022a) and Klähn et al. (2022a) and journals: Caldas et al. (2021b), Caldas et al. (2022b) and Caldas and Meyer (2023). Chapters or sections that are based in publications are properly assigned with the associated

1.7. Thesis overview

This thesis is organized as follows:

- Chapter 2 introduces the literature review on fundamental turbulence, with focus in the view of turbulence as a multi-scale problem.
- Chapter 3 describes all techniques used to analyze turbulence data measured by hot-wire anemometry. Emphasis is given in the extraction of turbulence parameters such as turbulence intensity and integral length scale. The novel technique proposed to deal with hot-wire data measured downstream a rotating fan is detailed. This technique separates and characterizes both the turbulence statistics of the periodic rotor wakes and the background flow.
- Chapter 4 details the CRAFT fan test rig used for aerodynamic and acoustic measurements, as well as the associated instrumentation. The design and construction of the new ICD is also reported in this chapter.
- Chapter 5 provides an aerodynamic and acoustic assessment of the CRAFT fan rig regarding its baseline configuration. Aerodynamic measurements performed at two measurement planes in the inlet and one downstream the fan are analyzed. In order to assess the impact of the new ICD in both flow aerodynamics and fan noise emissions, in total three inlet configurations were tested: Without ICD, with ICD, and with ICD and an additional honeycomb installed inside the inlet duct. This last

test case proved to be relevant due to the modification of the turbulence field and fan noise signature caused by this additional honeycomb.

- Chapter 6 assesses the impact of distorted inflow in both the fan noise emissions and in the inflow aerodynamics. Four distorted inflow setups plus a baseline case were analyzed. Aerodynamic and acoustic measurements at the fan inlet were performed and discussed.
- Chapter 7 draws an overall conclusion of all analyzes and techniques implemented. Focus is given in the characterization of the turbulence flow field, the impact and correlation of inflow distortion on fan noise emissions.
- Chapter 8 concludes this thesis with recommendations for future work.

2. Literature review on fundamental turbulence

THIS chapter gives an overview of basic turbulence definitions and the description of turbulence as a multiple length scale problem. Also, an introduction of a few important turbulence parameters, typically used in turbulence modelling and correlated with aerodynamic noise generation is given. This chapter is complementary to the literature survey on the impact of turbulence on the acoustic and aerodynamic of turbomachinery reviewed in Chapter 1. This chapter is partially based on the authors publications Caldas et al. (2021b,a).

2.1. Review of fundamental turbulence definitions

Turbulence is a complex, interdisciplinary, and vast field of investigation. It can be observed in anyone's daily life in several forms. For example, by looking up into the sky and observing the clouds shape, or wind blowing through trees, or even in a cup of hot coffee. However, when watching the waves in the ocean, or in a lake, they should not be confused with turbulence. An exception holds when waves brake in the shore, which is the moment when the potential energy in the wave is converted into turbulent kinetic energy through vorticity. Wave breaking typically occurs when the wave amplitude reaches the point that the crest of the wave overturns. This is dependent on the relation of the wave amplitude and water depth. A deeper analysis of the brake of waves will be skipped. Important to highlight is: TURBULENT FLOWS ARE ALWAYS DISSIPATIVE¹. If there is no continuous external input source of energy for the continuous generation of the turbulence, the motion will decay. According to Tennekes and Lumley (1972), the major distinction between random waves and turbulence is that waves are essentially nondissipative (though they often are dispersive²) and irrotational³, while turbulence is essentially dissipative and always exhibits high levels of fluctuating vorticity. In the words of Tennekes and Lumley (1972) "The random vorticity fluctuations that characterize turbulence could not maintain themselves if the velocity fluctuations were two dimensional, since as important vorticity-maintenance mechanism known as vortex stretching is absent in a two-dimensional flow. In turbulence, the equations do not give the entire story, differently as for two-dimensional waves."

¹Dissipation is the process of gradually disappearing or losing energy.

²Disperse is the spreading of something across a large area, conserving however the overall energy.

³Irrotational flows have zero vorticity, or net rate of change of angular velocity in all directions is zero, or the curl of the velocity vector is zero.

Books on turbulence traditionally show pretty pictures of turbulence as a matter of illustration. This thesis is not an exception. Fig. 2.1 shows a collection of frames extracted from a video recording of a freshly brewed cup of coffee. The cup was stationary on a table during the footage. It happens that when the coffee is still hot, the temperature difference between the liquid and the room induces heat transfer and the coffee cools down. Due to the temperature gradient and the convection phenomenon turbulence is induced in the fluid. The oil extracted from the coffee powder lies on the top as a thin layer, which helps for this visualization of turbulence.

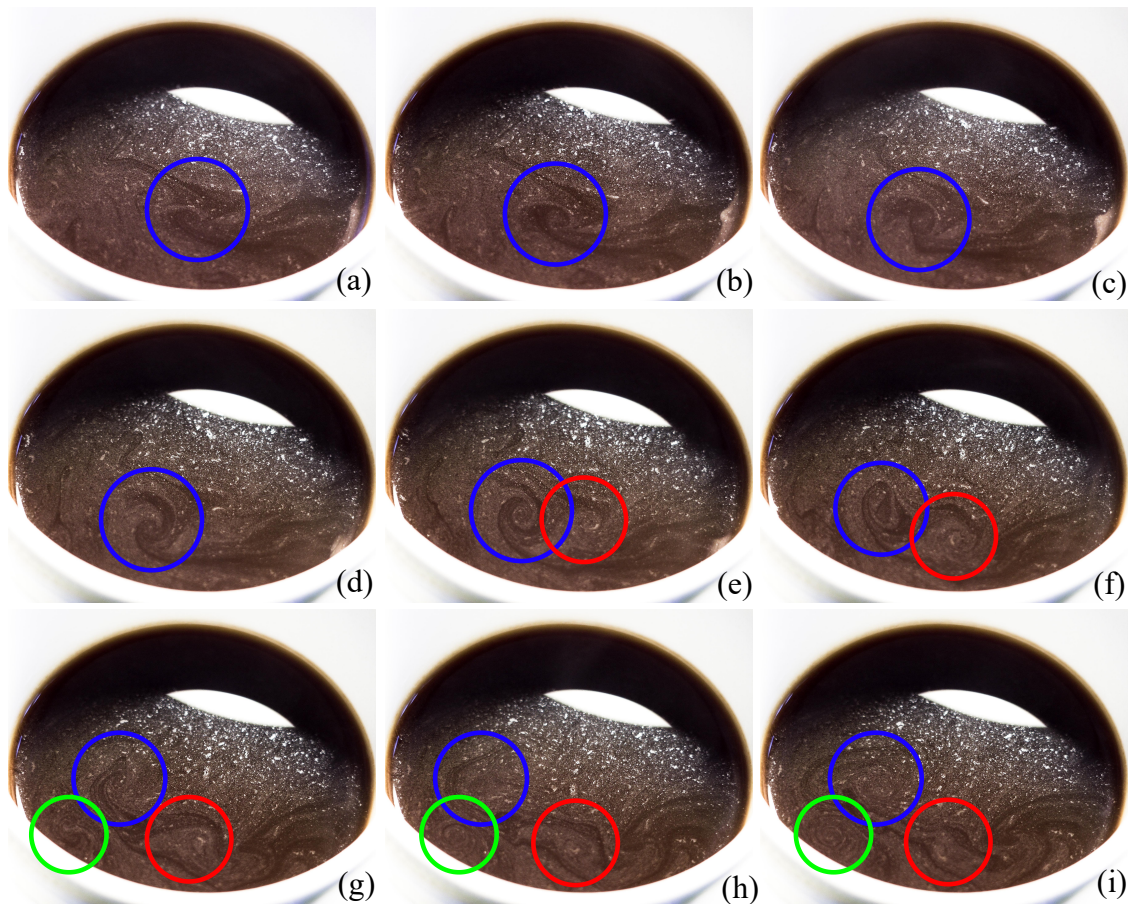


Figure 2.1.: Turbulence in a cup of coffee induced by heat transfer.

Fig. 2.1 shows each frame with one or more circles plotted around the induced vortices. The blue circle shows the first vortex formed. As it starts to spin, quickly a second vortex is generated (red circle in frames (e) and (f)) which interestingly spins with the same orientation, i.e., not counter-rotating. Soon, this interaction leads to a stretching of these eddies and a new interaction takes place with an eddy close to the wall (green circle in frame (g)). In frame (i) the vortex highlighted by the blue circle is very much dissipated and now the one close to the wall proceeds to spin. This process of new eddies formation and breaking down continues until the heat transfer between the liquid and the room is not enough anymore to induce movement in the fluid. From this point the fluid viscosity

is too high to allow weak heat transfer inducing turbulence. Experiments like this can easily be repeated and observed by anyone.

This thesis is strongly focused on the analysis of experimental data and therefore several measurement campaigns were needed to feed the necessary input data. The words from Professor Julius Sumner Miller (extracted from his lessons available in Sumner Miller (1969)) describe well how research with experiments is like:

“Experiments demonstrations never fail.
For nature to do, what you want her want to do,
you must make some very special,
meet some very special requirements.
If they are not met absolutely precisely,
nature will not show what you want her to show,
she will do something else.
So if the experiment did not succeed in an earlier case,
we will try it again,
but we are forced to think of why didn't it work before.”

Back to the introduction to turbulence. According to Hinze and B. J. Clark (1975) and Tennekes and Lumley (1972): “TURBULENCE IS A MULTIPLE LENGTH SCALE PROBLEM. Scales are bounded from above (large scales) by the dimensions of the flow-field and bounded from below (small scales) by the diffusive action of molecular viscosity. That is the reason spectral analyses of turbulent motions are so useful”. That is, in a turbulent flow-field a broad range of turbulent structures are present, ranging from big to small scales. When however, the turbulence is found in the so called “equilibrium”, the big structures break down into smaller ones. The energy of big scales is transferred to smaller ones, and so forth. This process keeps going up to a limit, when the scales are so small, that due to viscosity their kinetic energy transforms into thermal energy. This process is called the energy cascade. Richardson (1922) described the cascade process in a turbulent field poetically as

“Big whorls have little whorls,
Which feed on their velocity;
And little whorls have lesser whorls,
And so on to viscosity”

Fig. 2.2 illustrates qualitatively, how this cascade process works. The turbulence generation, or the injection of energy \mathcal{P} in the turbulence field, takes place through the large eddies. This is illustrated by the blue circles in the region called “Energy-containing range”. Hinze and B. J. Clark (1975) stated “As Taylor and Von Kármán have stated in their definition, turbulence can be generated by friction forces at fixed walls (flow through

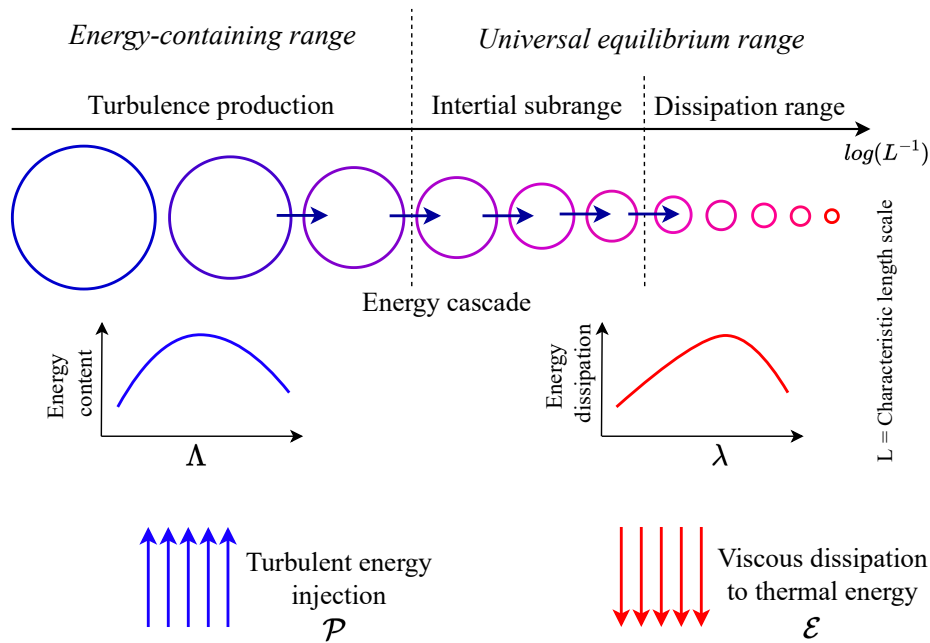


Figure 2.2.: Illustration of the turbulence energy cascade. The two length scales Λ and λ referred to the energy content and dissipation eddies, respectively, are indicated.

conduits, flow past bodies) or by the flow of layers with different velocities past or over one another. There is a distinct difference between the kinds of turbulence generated in the two ways. Therefore it is convenient to indicate turbulence generated and continuously affected by fixed walls by the designation ‘wall turbulence’ and to indicate turbulence in the absence of walls by ‘free turbulence’, the generally accepted term.”

According to Kolmogorov’s second hypothesis, there exists a subrange, in which negligible energy dissipation occurs and the transfer of energy by inertia forces is the dominant process. This range is called the inertial subrange and is illustrated in Fig. 2.2 as the purple eddies in the center of the cascade. The blue arrows indicate the energy transfer from big eddies into smaller eddies. The energy cascade is finally fully described with the introduction of the dissipation range. In this range of length scales, the eddies are small and the dissipation of energy is principally due to the conversion (or dissipation) of kinetic energy into thermal energy (heat). According to Kolmogorov’s universal equilibrium theory, the dissipation rate per unit mass ε (m^2/s^3) and the kinematic viscosity ν (m^2/s) govern this small-scale motion (Ting (2016) and Kolmogorov (1941)).

The modelling of turbulence is by no means straight-forward. Indeed, due to its strong non-deterministic behavior, the complete modelling is simply impossible. The use of statistic tools allows the extraction of useful information from turbulence data. Tennekes and Lumley (1972) argued “...turbulence theory suffers from the absence of sufficiently powerful mathematical methods. This lack of tools makes all theoretical approaches to problems in turbulence trial-and-error affairs”.

The next sections will introduce a special type of turbulence called isotropic, and a few turbulence parameters important for this study.

Homogeneous and isotropic turbulence (HIT)

The meaning of homogeneous and isotropic turbulence (HIT) can be understood as the name suggests. A brief definition according to Wikipedia¹ refers homogeneous to that the statistical properties are invariant under arbitrary translations of the coordinate axes. That means, independently of where in a defined spatial domain, the statistical properties are constant. Isotropy is when the statistical properties are invariant over a full rotation group, which includes rotations and reflections of the coordinate axes. This is commonly understand as the no preference for directions. The statistical properties are the same independently of the direction of a given coordinate system.

Hinze and B. J. Clark (1975) stated: “Usually the condition of isotropy is defined, rather briefly, by the invariance under rotation of the coordinate system and under reflection with respect to the coordinate planes of the statistically averaged properties of the turbulence.” A more precise definition is given by Batchelor (1953): “In isotropic turbulence the joint-probability distribution of the velocities at any arbitrarily chosen n points in space is invariant under arbitrary rotations of the configuration as formed by the n points and by the various direction vectors, and under reflection of the configuration with respect to any plane”.

Due to the complexity of turbulence modelling and analysis, in some cases the simplification by assumption of isotropy is the only way of making modeling possible. A deeper analysis of HIT is, however, outside the extension of this present study. Instead, flow isotropy is assessed by the ratio of the integral length scale of both longitudinal and transverse (radial and circumferential) velocity components, as well as the ratio of the turbulence intensity of these components, as documented by Roach (1987).

2.2. Coordinates system

The coordinates system nomenclature used is as shown in Fig. 2.3. Virtually all literature references work with (x, y, z) Cartesian system. As this study is focused on turbomachinery, i.e. measurements are referred to in-duct, the cylindrical coordinates are referred to as (u, v, w) , i.e. the axial, radial, and circumferential axes, respectively.

¹https://en.wikipedia.org/wiki/Homogeneous_isotropic_turbulence

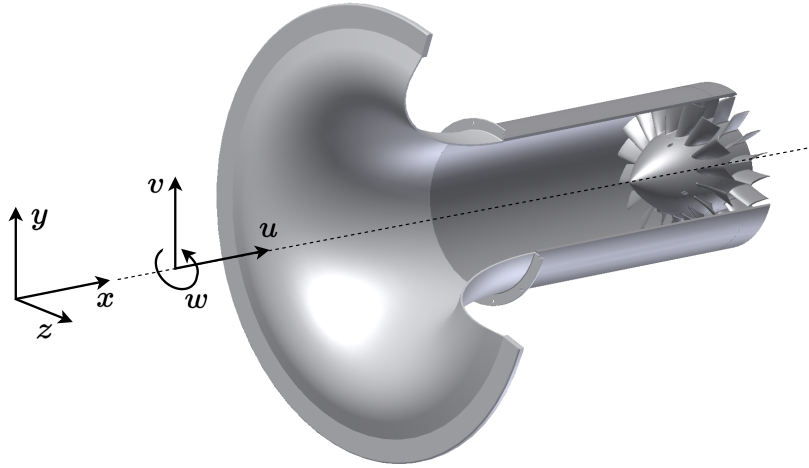


Figure 2.3.: Coordinate system notation.

2.3. Fundamental turbulence parameters

2.3.1. The integral length scale (ILS) Λ

The turbulence integral length scale is a mathematically well defined measure of length scale. It belongs to the group of big scales in a turbulent field and can be seen roughly as the most energetic eddy size in a given turbulence field. The integral length scale is computed as the integral of the spatial velocity correlation function in a given axis. For the x-axis it is computed as follows:

$$\Lambda_x = \int_0^{\infty} \rho_{uu}(r) dr, \quad (2.3.1)$$

where $\rho_{uu}(r)$ is the normalized spatial crosscorrelation function between two points distanced by r in the axial direction \vec{x} of the axial velocity component $u(t)$. Eq. 2.3.1 computes the ILS in the axial x direction, however its formulation is similar for the other axes y and z . If, for example, hot-wire anemometry is used in order to determine the spatial correlation defined in Eq. 2.3.1 from experimental data, simultaneous measurements from two hot-wire probes are required and their distance apart has to be varied. Due to physical constraints, this kind of measurement is seldom adopted, or even not possible to be performed. For instance, two hot-wire probes cannot be placed downstream of another, as the one downstream would measure the turbulence generated by the one mounted upstream, invalidating the measurement. This approach might be feasible for simulation data or turbulence measurement technique based on spatial measurement such as PIV (Grant (1997)).

Typically, the spatial correlation is alternatively estimated utilizing the temporal autocorrelation from a single hot-wire probe by assuming Taylor's hypothesis (Hinze and B. J. Clark (1975)), also referred to as the "frozen-turbulence" assumption. Under this assump-

tion, the integral length scale is estimated from the integral time scale:

$$\Lambda_x = \tau_x U_0, \quad (2.3.2)$$

where U_0 refers to the average streamwise flow speed, τ_x is the integral time scale in the x direction and it is calculated via:

$$\tau_x = \int_0^\infty r_{uu}(\tau) d\tau. \quad (2.3.3)$$

The temporal normalized autocorrelation function $r_{uu}(\tau)$ is computed from the unsteady velocity signal in axial direction $u(t)$:

$$r_{uu}(\tau) = \frac{\overline{u(t)u(t-\tau)}}{\overline{u^2}} = \frac{R_{uu}(\tau)}{R_{uu}(0)}. \quad (2.3.4)$$

The overbar refers to the time-averaged value. $R_{uu}(\tau)$ is the temporal autocorrelation as a function of the time lag τ . The integral length scale for the other velocity components is calculated in the same way by replacing the axial velocity signal $u(t)$ with their associated velocity signals: $v(t)$ for the radial component and $w(t)$ for the circumferential component.

From another perspective, the autocorrelation function can be estimated by the inverse Fourier transform of the power spectral density function (PSD) $S_{uu}(f)$ of the unsteady velocity $u(t)$:

$$r_{uu}(\tau) = \frac{1}{\overline{u^2}} \int_{-\infty}^{\infty} S_{uu}(f) e^{j2\pi f\tau} df. \quad (2.3.5)$$

It is known from the Parseval Theorem (Percival and Walden (1993)) that:

$$R_{uu}(0) = \int_{-\infty}^{\infty} S_{uu}(f) df, \quad (2.3.6a)$$

and

$$S_{uu}(0) = \int_{-\infty}^{\infty} R_{uu}(\tau) d\tau, \quad (2.3.6b)$$

and therefore, the integral time scale can be calculated by:

$$\tau_x = \frac{S_{uu}(0)}{2\overline{u^2}}, \quad (2.3.7)$$

where

$$\overline{u^2} = \int_{-\infty}^{\infty} S_{uu}(f) df. \quad (2.3.8)$$

By assuming Taylor's hypothesis, we finally obtain, for all three components:

$$\Lambda_x = \tau_x U_0 = \frac{S_{uu}(0)U_0}{2u^2}, \quad (2.3.9a)$$

$$\Lambda_y = \tau_y U_0 = \frac{S_{vv}(0)U_0}{2v^2}, \text{ and} \quad (2.3.9b)$$

$$\Lambda_z = \tau_z U_0 = \frac{S_{ww}(0)U_0}{2w^2}. \quad (2.3.9c)$$

It is worth mentioning that in duct measurements the velocity components are referred to in cylindrical coordinates. The integral length scales then become: Λ_u , Λ_v , and Λ_w referring to the axial, radial and circumferential components, respectively.

Integral length scale under the hypothesis of homogeneous and isotropic turbulence (HIT)

Under the HIT assumption, the velocity components are referred to as only streamwise (with the flow direction) and transverse (perpendicular to the flow direction), other than to the three components: axial, radial and circumferential. In this case both the radial and circumferential components are transverse to the streamwise component, and are modelled by one turbulence spectrum. Typically, the nomenclature uses the suffix 1 for the streamwise component, and 2 for the transverse component. Table 2.3.1 compiles the different nomenclature used.

Λ_u	Turbulence ILS in axial direction. No HIT assumption.
Λ_v	Turbulence ILS in radial direction. No HIT assumption.
Λ_w	Turbulence ILS in circumferential direction. No HIT assumption.
Λ_1	Turbulence ILS of the longitudinal velocity component. HIT is assumed.
Λ_2	Turbulence ILS of the transverse velocity component. HIT is assumed.

Table 2.3.1.: The different nomenclature for the turbulence integral length scale (ILS) used.

If the HIT assumption is met, then $\Lambda_v = \Lambda_w = \Lambda_u/2$ and $\Lambda = \Lambda_1 = \Lambda_2$.

In order to assess the integral length scale under the HIT assumption, the power spectral density of the streamwise velocity component, according to Roach (1987), can be described by:

$$\frac{4\overline{u^2}\Lambda}{S_{11}(f)U_0} = 1 + \left(\frac{2\pi f\Lambda}{U_0} \right)^2. \quad (2.3.10)$$

This formulation is based on the assumption that the temporal autocorrelation follows a negative exponential shape.

By definition, under the HIT hypothesis the turbulence has no direction preference. As a consequence, $\overline{u^2} = \overline{v^2}$, and one integral length scale Λ plus the mean flow velocity U_0 fully describe the turbulence field. By setting $f = 0$ in Eq. 2.3.10, the integral length scale is obtained as:

$$\Lambda_1 = \left[\frac{S_{11}(f)U_0}{4\overline{u^2}} \right]_{f \rightarrow 0}, \quad (2.3.11)$$

while for the transverse velocity component it is given by:

$$\Lambda_2 = \left[\frac{S_{22}(f)U_0}{2\overline{v^2}} \right]_{f \rightarrow 0}. \quad (2.3.12)$$

At this point, attuned readers might ask themselves, why equations 2.3.9 and 2.3.11 are the same, except for the factor 2 dividing the former, and the factor 4 dividing the latter. In fact, the PSD at $f = 0$ has a different meaning than the nearby frequency bins $f \rightarrow 0$. The first is associated to the Root Mean Square (RMS) of the signal. Another way to see it is as the integral of the autocorrelation function, as introduced by Eq. 2.3.6b. The latter, however, is essentially an average power of the low-frequency band of the turbulence PSD. This fact is (from the authors' understanding) not modeled by synthetic turbulence models under HIT assumption, although observed on measured turbulence data.

2.3.2. Dissipation scale or microscale λ

The dissipation-scale (or microscale, or Taylor microscale, or only turbulence length scale) λ may be considered as a measure of the average dimensions of the eddies, which are mainly responsible for the dissipation of turbulent energy into heat due to viscosity. Or as stated by Phillips et al. (2022), “it represents the end of fluids properties and onset of dissipative processes”. One importance of this length scale is that the Reynolds number based on this scale, Re_λ , also often only referred to as the turbulence Reynolds number, dictates the whole characteristics of a given turbulence field (Mayle et al. (1997)). Most of research in turbulence, as well as equations governing its physics, are valid for a certain range of this Reynolds number. Authors typically state “... at a sufficient high Reynolds number ...”, meaning that the statements given hold only for high enough Re_λ , which is why the description of this length scale is of such importance. By definition (Roach (1987)), the streamwise micro-scale λ_u is given by:

$$\frac{1}{\lambda_u^2} = -\frac{1}{2U_0^2} \left\{ \frac{\partial^2 r_{uu}(\tau)}{\partial \tau^2} \right\}_{\tau=0}. \quad (2.3.13)$$

This formulation relies on the second derivative of the normalized autocorrelation function for no time delay $\tau = 0$. As shown in the next chapter, the autocorrelation function of

the turbulence velocity signal is often problematic to work with. Instead, it is preferred to work with the power spectral density of the turbulence velocity.

If the turbulence can be considered fully homogeneous and isotropic, the determination of this length scale can be obtained directly from the turbulence velocity power spectral density:

$$\frac{1}{\lambda_u^2} = \frac{2\pi^2}{U_0^2 u^2} \int_{-\infty}^{\infty} f^2 S_{uu}(f) df, \quad (2.3.14)$$

and for the other velocity components it holds $\lambda_r \equiv \lambda_w \equiv \lambda_u/\sqrt{2}$. Note that some authors such as Roach (1987) consider the velocity power spectrum as single sided spectrum, and therefore in his work the integral is bounded by $[0, +\infty)$. However, if the double sided spectrum is computed, then the integral is bounded by $(-\infty, +\infty)$.

One problem that arises from Eq. 2.3.14 is the convergence of the integral. The term f^2 multiplying the turbulence velocity spectrum inside the integral weights the high-frequency band of the spectrum. This naturally makes sense, as the microscale are associated with small eddies, which have high-frequency. If for example a synthetic spectrum is used for the calculation of λ , the convergence of Eq. 2.3.14 depends on the roll-off rate of the spectrum. This is explained in more detail in Section 2.4. And a few examples of how this equation converges as a function of the frequency band used are given in Section 2.4.4.

Following Ting (2016), another way to compute the dissipative scale under the HIT assumption is as a function of the dissipation rate ε , the kinematic viscosity ν , and the velocity variance $\overline{u^2}$:

$$\lambda_u^2 = 30 \overline{u^2} \frac{\nu}{\varepsilon}. \quad (2.3.15)$$

If the flow is however anisotropic, Eq. 2.3.15 can be approximated by:

$$\lambda_u^2 \approx 10(\overline{u^2} + \overline{v^2} + \overline{w^2}) \frac{\nu}{\varepsilon}, \quad (2.3.16)$$

which reduces to Eq. 2.3.15, if all variances are identical.

The Reynolds number based on the dissipation microscale λ and on the RMS of the velocity fluctuations $\sqrt{\overline{u^2}}$ can finally be estimated by:

$$\text{Re}_\lambda = \frac{\lambda \sqrt{\overline{u^2}}}{\nu}. \quad (2.3.17)$$

McMurtry (2001) highlighted the historical significance of this length scale as well as that it was the first length scale derived to describe a given turbulence field. For a given fluid kinematic viscosity ν , the Reynolds number is proportional to the turbulence dissipation microscale and to the RMS of the velocity fluctuations. Large Reynolds numbers typically mean large values of turbulence intensity and large dissipation microscale, what can be understood as a high energetic turbulent flow. Mydlarski and Zellman (1996) roughly defined weak turbulence as $\text{Re}_\lambda < 100$ and strong turbulence as $\text{Re}_\lambda > 200$. It was also

showed in this study the roll-off of a turbulence spectrum dependence (in some degree) on the Reynolds number.

2.3.3. Reynolds stresses

The Reynolds stresses play a crucial role in equations that govern turbulent flows, such as in the momentum conservation equation (Pope (2000)). In this equation, the Reynolds stresses account for the momentum transfer by the fluctuating velocity field (turbulence). A deep analysis of its meaning is however outside the scope of this study.

The Reynolds stresses are also computed with the help of the auto- and cross-power spectral density of each velocity component. The shear stress is computed as:

$$\overline{uv} = \int_{-\infty}^{\infty} S_{uv}(f)df, \quad (2.3.18)$$

where $S_{uv}(f)$ stands for the cross-PSD of the signals $u(t)$ and $v(t)$. In this case, the axial and radial velocity components are used. However, the same holds for the other components. The normalized shear Reynolds stress is finally obtained by:

$$\frac{\overline{uv}}{U_0^2}. \quad (2.3.19)$$

The normal Reynolds stresses are computed using each velocity component individually. The axial, radial and circumferential normal stresses are computed respectively by: $\overline{u^2}/U_0^2$, $\overline{v^2}/U_0^2$, and $\overline{w^2}/U_0^2$.

2.3.4. Turbulence intensity

The turbulence intensity according to Hinze and B. J. Clark (1975) and Roach (1987) for all three velocity components are obtained by:

$$\begin{aligned} T_u &= \frac{u_{rms}}{U_0} = \frac{\sqrt{\overline{u^2}}}{U_0}, \\ T_v &= \frac{v_{rms}}{U_0} = \frac{\sqrt{\overline{v^2}}}{U_0}, \text{ and} \\ T_w &= \frac{w_{rms}}{U_0} = \frac{\sqrt{\overline{w^2}}}{U_0}, \end{aligned} \quad (2.3.20)$$

where often $\overline{u^2}$ is obtained from Eq. 2.3.8. More detail on alternatives to compute the signal variance is given in the next chapter. The turbulence intensity is essentially the square root of each normal Reynolds stress. If the HIT condition is met, then $T_u = T_v = T_w$, that implies also that $\overline{u^2} = \overline{v^2} = \overline{w^2}$.

For the turbulence intensity calculation, the mean velocity U_0 in this work is considered the local velocity, opposed to the free-stream velocity U_∞ , as sometimes observed in other works. The same holds for the Reynolds stress calculation.

2.4. Homogeneous and isotropic turbulence velocity spectrum models

2.4.1. The two-parameters von Kármán spectrum model

A turbulence model commonly adopted in the literature of turbomachinery is the von Kármán model. The two-dimensional energy spectra of the longitudinal (streamwise) and transverse velocity components are described following Hinze and B. J. Clark (1975) and Wohlbrandt (2017) as:

$$E_{11}(\hat{k}_n) = \frac{\overline{u^2}\Lambda}{\pi} \frac{1}{(1 + \hat{k}_n^2)^{5/6}}, \quad (2.4.1a)$$

$$E_{22}(\hat{k}_n) = \frac{\overline{u^2}\Lambda}{2\pi} \frac{1 + \frac{8}{3}\hat{k}_n^2}{(1 + \hat{k}_n^2)^{11/6}}, \quad (2.4.1b)$$

where the subscripts 11 and 22 refer to the longitudinal and transverse velocity components, respectively. \hat{k}_n is the normalized wave-number given by:

$$\hat{k}_n = \hat{k}(f, n, \Lambda, U_0) = \frac{2\pi f}{U_0 k_e(n, \Lambda)}, \quad (2.4.2)$$

where

$$k_e(n, \Lambda) = \frac{\sqrt{\pi}\Gamma(n + 1/2)}{\Lambda\Gamma(n)}. \quad (2.4.3)$$

$\Gamma(n)$ stands for the Gamma function of order n . For the von Kármán spectrum, n has to be set to 1/3. The turbulence velocity PSD is then defined by:

$$S_{ii}(f) = \frac{4\pi}{U_0} E_{ii}\left(\hat{k}_n = \frac{2\pi f}{U_0 k_e(n, \Lambda)}\right), \quad (2.4.4)$$

where the subscript ii refers to the respective velocity component.

A relevant exercise is to substitute the von Kármán turbulence velocity equations into Eq. 2.3.9 in order to obtain the integral length scale for every velocity component. For the streamwise velocity component, the following holds:

$$\Lambda_u = \frac{S_{uu}(0)U_0}{2\overline{u^2}} = \left(\frac{4\pi}{U_0} \frac{\overline{u^2}\Lambda}{\pi}\right) \frac{U_0}{2\overline{u^2}} = 2\Lambda, \quad (2.4.5)$$

whereas for the transverse velocity component the integral length scale follows:

$$\Lambda_v = \frac{S_{vv}(0)U_0}{2\overline{v^2}} = \left(\frac{4\pi}{U_0} \frac{\overline{v^2}\Lambda}{2\pi}\right) \frac{U_0}{2\overline{v^2}} = \Lambda. \quad (2.4.6)$$

In other words, a single integral length scale Λ is used to model the synthetic turbulence spectrum of both velocity components. However, if Eq. 2.3.9 is used to compute the turbulence integral length scale of each velocity component spectrum, we conclude that $\Lambda = \Lambda_v = \Lambda_u/2$, which agrees with the previous statements and is found in the references (Roach (1987) and Pope (2000)). In this regard, care must be taken when computing and comparing the integral length scale using different equations and assumptions. As just stated, there is a factor of two in the computation of the streamwise integral length scale, if Eq. 2.3.9a or Eq. 2.3.11 is used. Both results are naturally correct, however they have different meanings.

2.4.2. The three-parameters Bullen spectrum model

The Bullen spectrum model (Mark (1982a) and Mark (1982b)) can be seen as a generalization of the von Kármán spectrum, where the spectral slope towards high frequencies can be set by the parameter n . When $n = 1/3$, the Bullen spectrum becomes identical to the von Kármán spectrum.

$$E_{11}(\hat{k}_n) = \frac{\overline{u^2}\Lambda}{\pi} \frac{1}{(1 + \hat{k}_n^2)^{n+1/2}}, \quad (2.4.7a)$$

$$E_{22}(\hat{k}_n) = \frac{\overline{u^2}\Lambda}{2\pi} \frac{1 + 2(n+1)\hat{k}_n^2}{(1 + \hat{k}_n^2)^{n+3/2}}. \quad (2.4.7b)$$

2.4.3. Test case: Turbulence velocity spectrum

Fig. 2.4 displays a test case for both synthetic spectrum models, along with both transverse and longitudinal velocity components. Non-normalized and normalized plots are shown. The Bullen spectrum is displayed with the two examples of slope coefficients $n = 1$ and $n = 3$. In these two examples, the Bullen spectra experience a steeper slope at high frequencies in contrast to the von Kármán spectrum.

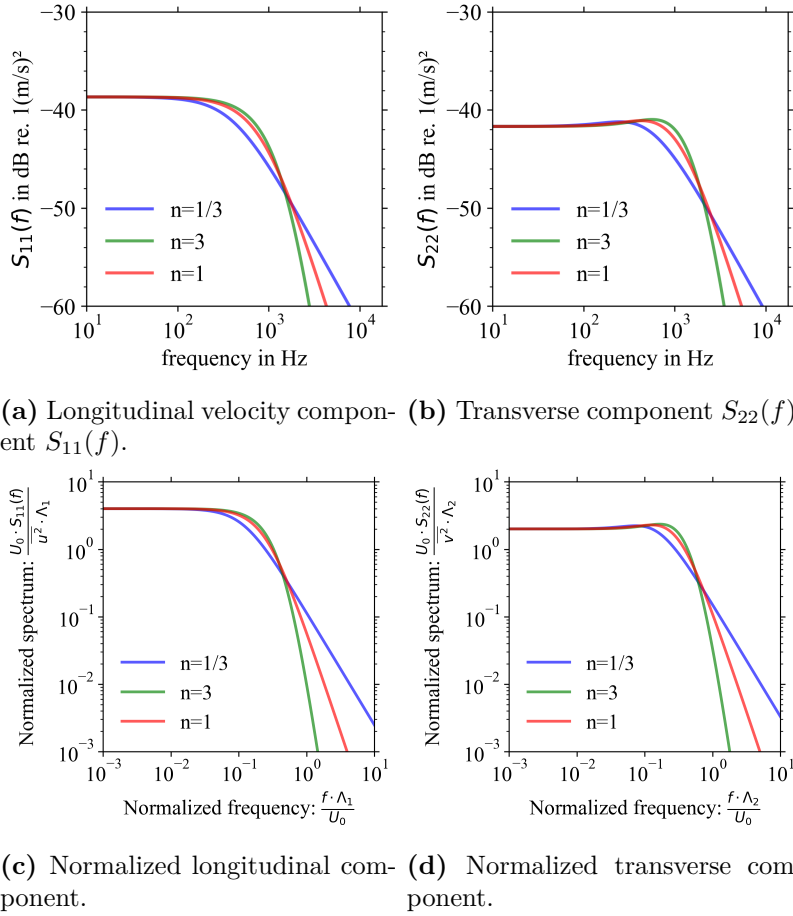


Figure 2.4.: Synthetic turbulence power spectral density using the Bullen and von Kármán models. Parameters used: $U_0 = 34$ m/s, $T_u = T_v = 1\%$, $\Lambda = 10$ mm.

2.4.4. Test case: Estimation of the dissipation microscale λ

In order to evaluate the convergence of Eq. 2.3.14 as a function of the frequency bandwidth used to compute this integral, two test cases are proposed. For the first test, the synthetic turbulence velocity spectra von Kármán and Bullen are selected with the same coefficient n as in the previous section, $n=1/3$, 1, and 3, respectively. The other turbulence parameters such as the free-stream velocity, turbulence intensity, and integral length scale were also varied in order to assess their impact on the convergence of Eq. 2.3.14. Fig. 2.5 shows the results of each coefficient n and the aerodynamic parameters used. The free-stream velocity is shown as the Mach number, where the speed of sound was considered to be 340 m/s.

As we can observe, for the von Kármán spectrum in Fig. 2.5a, the curves start to converge only for very high-frequency of approx. $f > 200$ kHz. The reason for this is essentially that neither the von Kármán spectrum nor the Bullen spectrum model the dissipation range of the turbulence velocity spectrum (Santos et al. (2021) and Pope (2000)). However, for the

von Kármán spectrum this problem is more accentuated, as the roll-off of the spectrum is less steep than the Bullen spectra in this example for $n=1$ and $n=3$.

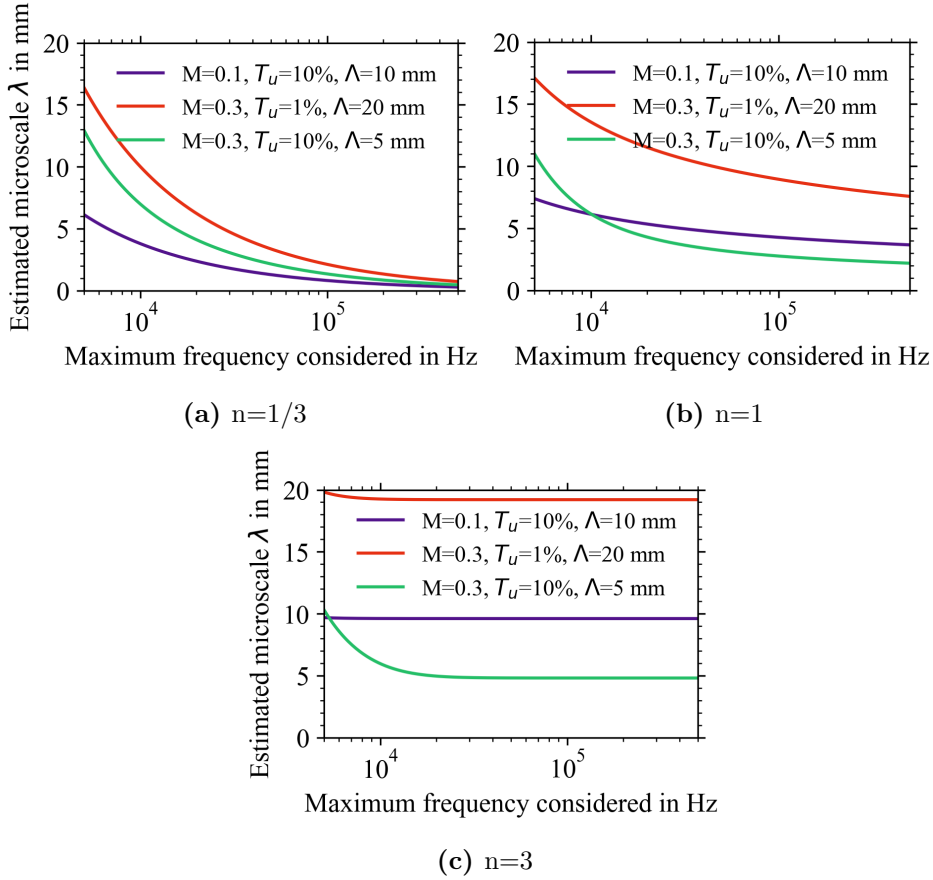
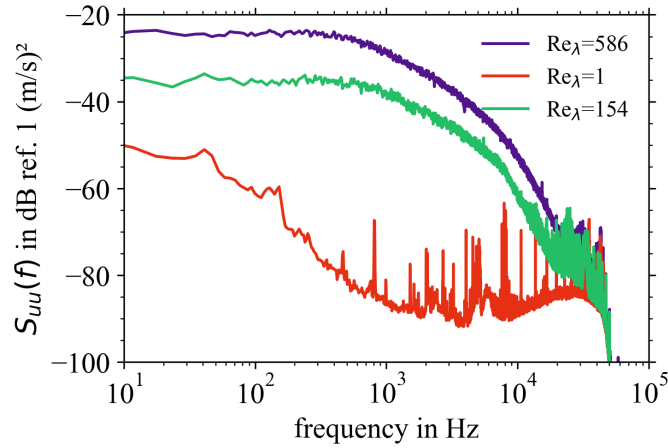


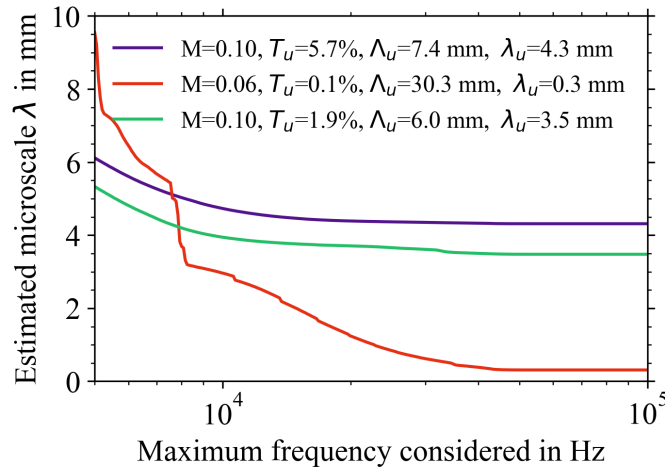
Figure 2.5.: Convergence test for the estimation of the dissipation microscale λ with synthetic turbulence model as a function of the frequency band considered to compute the integral.

A second test with experimental data was conducted and the results are shown in Fig. 2.6. Details about the instrumentation and experimental setup are given in the next chapters and are not relevant for now. Fig. 2.6a depicts the streamwise velocity spectra of three different measurements. Different flow velocities and turbulence intensities were measured. The estimated turbulence parameters respective to each test case are shown in Fig. 2.6b in the label box. The integral length scale was calculated under the HIT assumption using Eq. 2.3.11. The purple and green curve refer to two relatively high turbulence intensity measurement points (5.7% and 1.9%, respectively) and the axial flow speed of Mach = 0.1.

The dissipation scale was computed again using Eq. 2.3.14. In Fig. 2.6b, we see that for these two data sets the estimation of the microscale roughly converges for $f \approx 20 \text{ kHz}$. However, for the red curve, an odd behaviour is observed and the convergence is found only for $f > 40 \text{ kHz}$. Note the very low turbulence levels for this test case of 0.1%. A closer look in the red spectrum in Fig. 2.6a reveals that for $f > 2 \text{ kHz}$ the roll-off of



(a) Turbulence spectra of the streamwise velocity component.



(b) Convergence of the microscale estimation.

Figure 2.6.: Convergence test of the dissipation microscale λ with experimental data.

this turbulence spectrum does not take place anymore, and it seems that a noise floor is reached at around -90 dB, which is extremely low. It is likely for this test point that the $f > 2$ kHz frequency band contains more noise than turbulence information. In circumstances like this, the computation of the dissipation microscale can be erratic. If we set the bandwidth to 5 kHz in this case, then $\lambda_u \approx 9$ mm. The Reynolds number, previously estimated to $Re_\lambda = 1$, corresponds now to $Re_\lambda \approx 30$, differing by a factor of 30.

3. Hot-wire data analysis techniques: extraction of flow turbulence parameters

THIS chapter describes all signal processing techniques used to condition hot-wire data, filter them when necessary, and estimate desired turbulence parameters. In the previous chapter, the theoretical definition of the relevant turbulence parameters were introduced. In the present chapter, it is described how statistic tools can be used to estimated these parameters. Section 3.1 describes different techniques used to deal with a few typical sources of disturbance present in a turbulence signal. Sections 3.2 and 3.3 deal with the integral length scale and turbulence intensity estimators. As shown, depending on the assumptions that can be made about the measured turbulence field, several options are available regarding different estimators. Finally, Section 3.4 presents the turbulence analysis in the interstage of a rotor-stator stage, i.e. the turbulence data measured directly downstream of a rotating fan. A novel technique is introduced to separate turbulence information of the periodic rotor wakes from the background flow along with a few exemplary results. This chapter is partially based on the publications Caldas et al. (2021b,a), Caldas et al. (2022a) and Caldas and Meyer (2023).

3.1. Noise reduction techniques

This section describes three different techniques to filter present distortions from a turbulence signal. In this work, distortion is meant to be any component that is not related to turbulence. A few examples of distortion can listed: electromagnetic interference in the sensors and/or cables, vibration of the sensors, influence of strong acoustic modes in the sensors.

3.1.1. Low-frequency disturbance removal

The problem of disturbance in the low-frequency band of the turbulence spectrum was first reported by Mark (1981). In that work, a hot-wire probe was fixed onto an airplane wing and flight turbulence data were recorded. The investigation of the autocorrelation function of the hot-wire data revealed the presence of a low-frequency component in the signals. The autocorrelation function had a faster and a slower decaying regime. By looking at the turbulence power spectral density function, this is seen as a monotonous and almost linear roll-off, roughly similar to a typical $1/f$ noise spectrum curve (Keshner (1982)).

Further investigation concluded that this disturbance had a non-Gaussian distribution, which was interpreted as “wind gusts”, i.e., slow oscillations in the velocity signals, and is not originated from turbulence. In our study, after analyzing a reasonable large hot-wire data set recorded in the inlet of turbo-machines, we observed a similar phenomenon depending on the test configuration.

Mark (1981) described this event as the superposition of two random processes: A low-frequency process (or slow oscillations, associated with “wind gusts”) and a process of higher frequency (fast oscillation), associated to turbulence. Mathematically, it can be described by:

$$\begin{aligned} w(t) &= w_s(t) + w_f(t) \\ &= w_s(t) + \sigma_f(t)z(t), \end{aligned} \tag{3.1.1}$$

where $\sigma_f(t)z(t) \geq 0$, $\mathbb{E}\{z(t)\} = \overline{z(t)} = 0$ and $\mathbb{E}\{z^2(t)\} = \overline{z^2(t)} = 1$. In Equation 3.1.1, $w(t)$ refers to the measured signal, $w_s(t)$ to the “slow” (low-frequency) component, and $w_f(t)$ to the “fast” one. Mark (1981) assumes that $z(t)$ is a Gaussian stationary process and that $\sigma_f(t)$ is a stationary random process. Furthermore, $\sigma_f(t)z(t) \geq 0$, $\sigma_f(t)$ is not necessarily a Gaussian process. Crucial for this analysis is the assumption that $w_s(t)$ and $w_f(t)$ are statistically independent. Thus, the autocorrelation and the PSD can be assessed by:

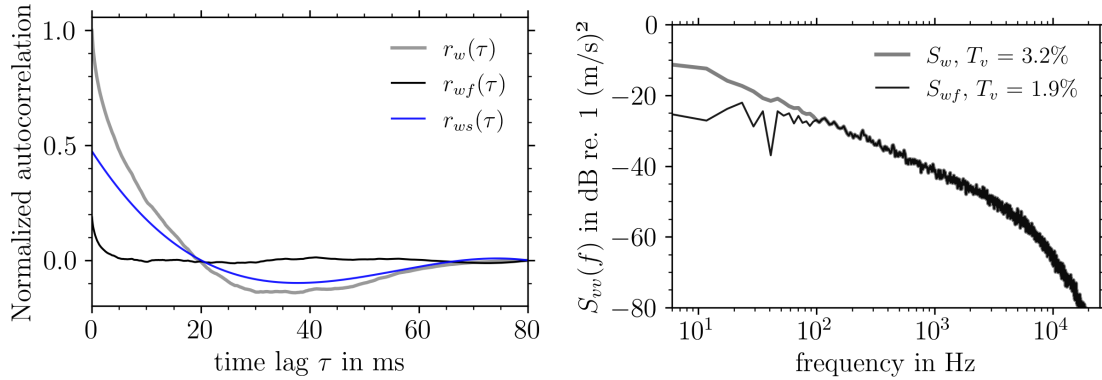
$$R_w(\tau) = R_{w_s}(\tau) + R_{w_f}(\tau), \tag{3.1.2}$$

and

$$S_w(f) = S_{w_s}(f) + S_{w_f}(f). \tag{3.1.3}$$

By following the guidelines suggested by Mark (1981), the “slow-component” of the autocorrelation function $R_{w_s}(\tau)$ can be interpolated by a polynomial of order 2 or 3. As shown by Keshner (1982), the autocorrelation function of a $1/f$ system has roughly a linear shape with a negative slope. This is similar to what is observed for turbulence of type “slow-component”. Fig. 3.1a shows an example of the interpolation using experimental hot-wire data. These data were measured at the inlet of the fan rig investigated in this thesis. More details about the test rig and instrumentation will be described in the next chapters. In this figure, the autocorrelation function is normalized by the zero lag value, often called the autocorrelation coefficient. Note that this result agrees with the observations from Mark (1981).

$R_{w_s}(\tau)$ (blue curve) represents the outcome of a polynomial interpolation of order 3 to $R_w(\tau)$. The black curve refers to $R_{w_f}(\tau)$. The difference in falling time of the black curve “fast-components” and the blue curve “slow-component” is evident in Fig. 3.1a. Fig. 3.1b shows the PSD of each component’s raw signal ($S_{vv}(f) = S_w(f)$) and the turbulence resultant component $S_{w_f}(f)$. The radial velocity component was selected for this example.



(a) Normalized autocorrelation function and fit-polynomial interpolation. (b) PSD before and after the low-frequency disturbance removal.

Figure 3.1.: Low-frequency disturbance removal technique test with hot-wire data.

The turbulence intensity of each PSD is shown in the labels. The raw data has $T_v = 3.2\%$, whereas after the use of the described technique this intensity dropped to $T_v = 1.9\%$, which is almost half of the intensity, or one-fourth of the remaining power. For this test case, roughly three-fourths of the power of the signal is concentrated in the frequency band of $f < 100$ Hz. It is not believed to be turbulence related, but instead, to represent low-frequency oscillations in the flow.

The technique described was incorporated into the proposed signal processing chain. However, it is used only for measurement data sets that are affected by low-frequency distortions, that means, when the typical spectral shape described in this section is observed in the low-frequency band of the turbulence PSD.

3.1.2. Cyclostationary technique for the removal of rotor coherent components

For hot-wire measurement data that includes with rotor coherent components such as BPF tones or vibrations induced by the test rig, a cyclostationary analysis is a useful technique to separate cyclic components from the stochastic process (Martinez et al. (2018), Antoni (2009) and Behn et al. (2018)). In order to perform this analysis, the unsteady velocity signals have to be resampled to give an exact number of samples per revolution N_{rev} . This is performed with the help of a 1 pulse-per-revolution shaft trigger signal. For convenience, the signals are organized as a 2D matrix with dimensions $n \times k$, where $n = 0, 1, \dots, N_{rev} - 1$ is the sample position related to the angular position of the fan. $k = 0, 1, \dots, K - 1$ is the k^{th} revolution of the fan:

$$u[n, k] \triangleq u\left(t = \frac{n + kN_{rev}}{f_s}\right), \quad (3.1.4)$$

where f_s is the sampling frequency.

The coherent part of the signal - CyS1 (often the tones present in the PSD) can be calculated by

$$\bar{u}[n] = \text{CyS1}\{u[n, k]\} = \frac{1}{K} \sum_{k=0}^{K-1} u[n, k], \quad (3.1.5)$$

whereas the incoherent part of the signal - CyS2 (turbulent information) is obtained by:

$$\tilde{u}[n, k] = \text{CyS2}\{u[n, k]\} = u[n, k] - \bar{u}[n], \quad \text{for } k = 0, 1, \dots, K - 1. \quad (3.1.6)$$

k refers to the k^{th} revolution of the fan. Another way to visualize the CyS2 signal is not as a vector in time, but instead as a $\theta \times k$ matrix, which corresponds to a collection of time series vectors corresponding to each k^{th} revolution of the fan.

If, for example, turbulence data from a clean flow is analyzed, the rotor-coherent part of the signal CyS1 $\bar{u}[n]$ should have ideally no power. This is because turbulence has stochastic nature, as discussed in the previous chapter, and therefore, no periodic components associated with the fan angular speed are expected to be present in the flow. However, in cases where vibrations or any periodic process coming from the rotor is present, this part of the signal (understood in this work as distortion) will be found in the CyS1 component. On the other hand, the turbulence data, the rotor-incoherent part of the signal $\tilde{u}[n, k]$ should, under distortion-free conditions, be equal to $u[n, k]$. In the case of rotor-coherent components present in the signal $u[n, k]$, $\tilde{u}[n, k]$ is expected to be free from them.

A sample test case with hot-wire data measured in a fan rig inlet is shown in Fig. 3.2. The dataset used for this test is the same as published by Caldas et al. (2021b). These data were collected within the frame of the TurboNoiseBB project in the ACAT1 Transonic fan. More information regarding the test rig and operation condition can be found in this reference and will be skipped for simplicity here. Raw data and the CyS2 cyclostationary component are shown. The frequency resolution used for this analysis was set equal to 14 Hz. We can observe a successful tone removal for this dataset resulting from the cyclostationary analysis. Important to mention is the difference in turbulence intensity of the three signals. Due to the presence of tones, the raw signal carried by a factor of more than two times higher turbulence intensity compared to the CyS2 signal, where tones are virtually absent. In terms of power, this is equivalent to approx. five times more power in the raw signal, compared to the CyS2 component. Distortions are still observed in this spectrum for $f > 4 \text{ kHz}$, which are not rotor-coherent. For this type of interference, the cyclostationary technique was not effective.

3.1.3. Use of accelerometer signal to remove rotor coherent components

If a hot-wire probe subjected to vibration possesses an accelerometer sensor mounted onto its body, it is possible to use the vibration signal measured by this sensor in order to

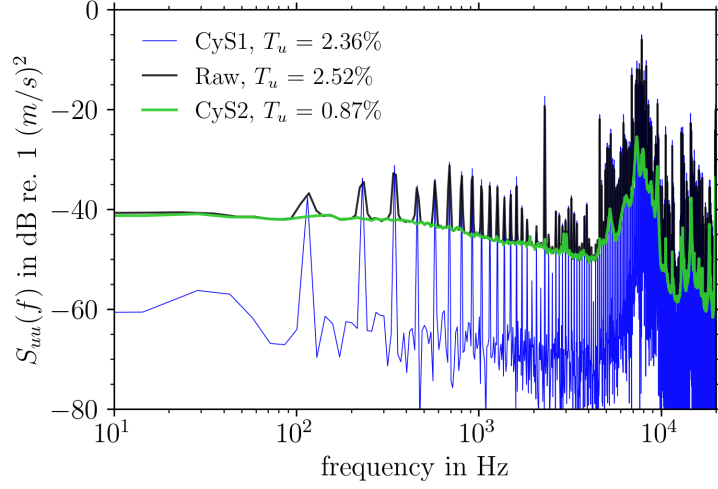


Figure 3.2.: Raw spectrum compared to the coherent (CyS1) and incoherent (CyS2) parts of the signal. The turbulence intensity of each signal is indicated in the label box.

remove components in the velocity signals due to vibration. A similar work has been done by Karlos et al. (2021).

Consider that the output signal measured by the hot-wire $u(t)$ can be decomposed as

$$u(t) = u_{\text{turb}}(t) + u_{\text{vib}}(t), \quad (3.1.7)$$

where $u_{\text{turb}}(t)$ stands for turbulence velocity fluctuations and $u_{\text{vib}}(t)$ for the contamination induced by the vibration of the hot-wire probe captured by the wire elements. Fig. 3.3 shows a block diagram with each signal component. $u_{\text{acc}}(t)$ is the vibration measured by the accelerometer. This signal is translated into distortion of the hot-wires signals by an unknown transfer function of the hot-wire probe system $H_{hw}(z)$, the Z-transform of a linear time-invariant system. This transfer function is obtained in the frequency domain by setting $z = j2\pi f$, where $j = \sqrt{-1}$.

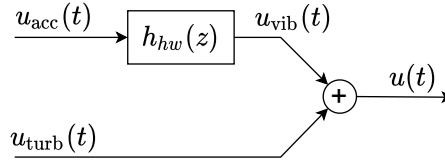


Figure 3.3.: Block diagram of the signal constituents in the measured turbulence data.

Assuming that both signals are uncorrelated, we obtain from Eq. 3.1.7:

$$S_{uu}(f) = S_{u_t u_t}(f) + S_{u_v u_v}(f). \quad (3.1.8)$$

$S_{u_t u_t}(f)$ is the PSD of the turbulence fluctuations which we are interested in. $S_{uu}(f)$ is the PSD of the output signal from the hot-wire measurement. $S_{u_v u_v}(f)$ is the PSD of the

signal measured by the hot-wire induced by the vibration, which we do not know. The latter can be indirectly estimated based on the signals from the accelerometers fixed in the hot-wire probe by

$$S_{u_v u_v}(f) = |H_{hw}(f)|^2 S_{u_a u_a}(f), \quad (3.1.9)$$

where $H_{hw}(f)$ is the hot-wire transfer function in the frequency domain. From another perspective this transfer function can be estimated from the signals of the accelerometer and hot-wire by

$$H_{hw}(f) = \frac{S_{uu_a}(f)}{S_{u_a u_a}(f)}. \quad (3.1.10)$$

The coherence function between hot-wire signal $u(t)$ and accelerometer signal $u_{acc}(t)$ is given by

$$\gamma_{u_a u}^2(f) = \frac{|S_{u_a u}(f)|^2}{S_{u_a u_a}(f) S_{uu}(f)} \quad (3.1.11)$$

Finally, by rearranging Eq. 3.1.8 with eqs. 3.1.11, 3.1.10 and 3.1.9 we obtain

$$\begin{aligned} S_{u_t u_t}(f) &= S_{uu}(f) - S_{u_v u_v}(f) \\ &= S_{uu}(f) - |H_{hw}(f)|^2 S_{u_a u_a}(f) \\ &= S_{uu}(f) - \frac{S_{uu_a}^2(f)}{S_{u_a u_a}^2(f)} S_{u_a u_a}(f) \\ &= S_{uu}(f) - \gamma_{u_a u}^2(f) S_{uu}(f) \\ &= [1 - \gamma_{u_a u}^2(f)] S_{uu}(f) \end{aligned} \quad (3.1.12)$$

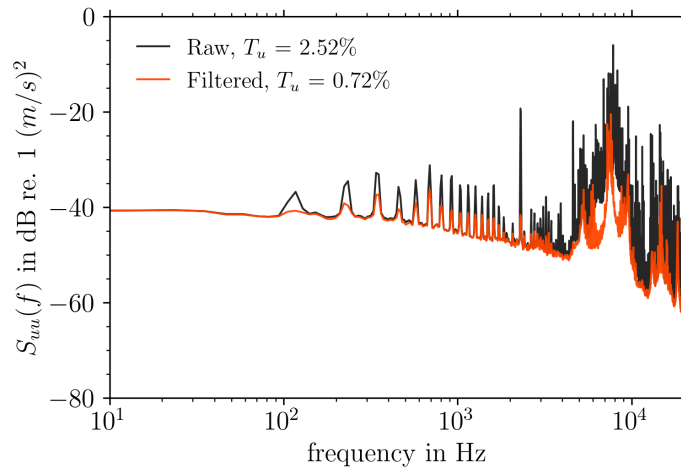


Figure 3.4.: Raw spectrum compared to the filtered signal using the accelerometer signal. The turbulence intensity of each signal is indicated in the label box.

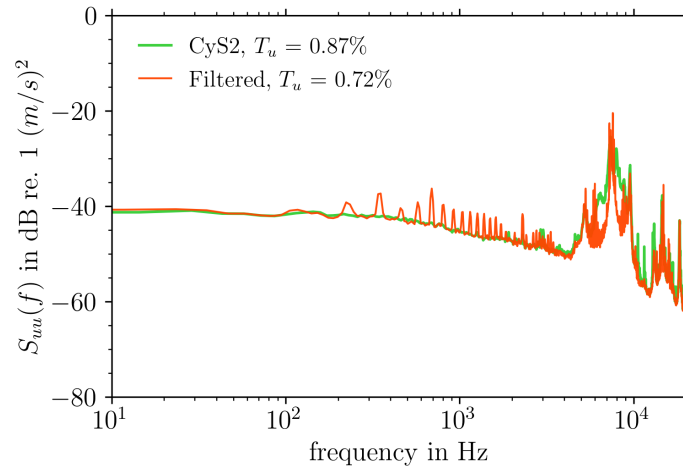


Figure 3.5.: Comparison of results obtained with the cyclostationary technique against filtered using the accelerometer signal. The turbulence intensity of each signal is indicated in the label box.

Fig. 3.4 shows the result of the technique tested with the same data set as shown in Fig. 3.2. In this case, the tones were only partially removed from the raw data, showing less effectiveness than the cyclostationary technique. However, this approach was more effective to remove distortions present in the frequency band of $f > 4 \text{ kHz}$ of the spectrum.

Finally, Fig. 3.5 compares how different both methods performed with contaminated data: one based on a cyclostationary technique and the other using the transfer function of an accelerometer sensor. The turbulence intensity of the former is slightly higher than the latter. This is probably due to the better capacity of removing distortions in the frequency band from approx. 4 kHz to 10 kHz . In this test, the ability of the cyclostationary analysis to remove tones from the signal is superior to the filtering using an accelerometer.

3.2. Turbulence integral length scale (ILS) estimators

This section describes several estimation approaches of the turbulence integral length scale from an unsteady velocity time signal. The order they are introduced refers from the most general (no assumption about the turbulence field) to the most specific case (i.e., the assumption of homogeneous and isotropic turbulence). Sections from 3.2.1 to 3.2.3 refer to estimators found in the literature. These estimators work well, if the data set is distortion-free, i.e. has a good signal-to-noise ratio (SNR). All these estimators are highly sensitive to the power in the low-frequency band of the turbulence PSD. In general, additional power due to distortions (non-turbulence related, as shown in Section 3.1.1) in this frequency band leads to an overestimation of the ILS. The precise estimation of the turbulence power from the measurement data has also an impact on the estimation of the ILS. If tones or other types of distortion which are not expected to be turbulence

related are present in the signal, for example as shown in the sections 3.1.2 and 3.1.3, this will lead to an underestimation of the ILS. Whether a distortion leads to an over- or underestimation of the ILS will become clearer by introducing the equations of different estimators.

Sections 3.2.4 and 3.2.5 report two new approaches proposed for the estimation of the ILS. They are based on the fit of a synthetic turbulence PSD to the estimated turbulence PSD from measured data. This technique is suited for highly contaminated data with low SNR, where strong distortions arise in the signal, such as presented in the sections 3.1.2 and 3.1.3. They are well documented in the reference Caldas et al. (2021b).

3.2.1. Integral length scale estimation according to the definition

According to the definition, the ILS shall be obtained by means of the spatial autocorrelation function of the turbulence field $\rho(r)$ as a function of the spatial distance r :

$$\Lambda = \int_0^{\infty} \rho(r) dr. \quad (2.3.1 \text{ revisited})$$

As mentioned in Chapter 1, this approach is seldom used due to experimental restrictions.

3.2.2. Integral length scale estimation under the Taylor assumption

This approach is also called “frozen turbulence”. Under this circumstance, the spatial autocorrelation function is assumed to be a function of the temporal autocorrelation unsteady velocity signal. The use of Eq. 2.3.9

$$\Lambda = \tau U_0 = \frac{S_{uu}(0)U_0}{2u^2} \quad (2.3.9 \text{ revisited})$$

provides an estimation of the ILS from a velocity signal that e.g. could originate from a hot-wire measurement. The advantage of this approach is that no assumption about turbulence isotropy or a turbulence model is taken. The biggest drawback of this method is, however, its lack robustness in terms of the variance of this estimator.

Mark (1982b) showed that if Eq. 2.3.9 is used for the estimation of the ILS using $S_{uu}(0)$ estimated from the periodogram, it follows that the coefficient of variation of this estimator (Eq. 2.3.9) will asymptotically approach $\sqrt{2}$ as the record length becomes arbitrary large. Just a single bin of the turbulence PSD $S_{uu}(f)$ is used as input into the equation, more specifically: $S_{uu}(0)$. Spectral estimation is still a vast topic of research. The value of a single spectral bin from an estimated power spectral density can vary depending, for example, on the type of data window used, the window length, the type of estimator

technique. More information can be found in Kay (1993) and Percival and Walden (1993). Therefore, despite of the advantages mentioned in favor of this approach, care must be taken regarding the estimation of the turbulence PSD.

In order to improve the statistical performance of this estimator, as also suggested by Mark (1982b), instead of using a single frequency of the turbulence PSD, several bins shall be used and averaged. By doing this, the coefficient of variation of the estimator tends to zero, if the chosen record is large enough. In order to do this, however, assumptions about the turbulence field shall be taken.

3.2.3. Integral length scale estimation under the homogeneous and isotropic turbulence (HIT) assumption

The HIT assumption allows us to use a much more robust estimator than the one shown in Section 3.2.2. Instead of using a single frequency bin value from the turbulence PSD, under the HIT assumption the average of the PSD is taken from its low-frequency band. For the longitudinal velocity component, the ILS can be estimated via:

$$\Lambda_1 = \frac{U_0}{4u^2\Delta f} \int_0^{\Delta f} S_{uu}(f)df, \quad (3.2.1)$$

where Δf is the frequency band used to average the PSD. Values to be used depend on the frequency band of the PSD, where it starts to roll-off. Typical chosen values in this work are in the range $80 \text{ Hz} < \Delta f < 200 \text{ Hz}$. The ILS can also be obtained from the transverse velocity component PSD as:

$$\Lambda_2 = \frac{U_0}{2v^2\Delta f} \int_0^{\Delta f} S_{vv}(f)df. \quad (3.2.2)$$

In Eq. 3.2.2, the radial velocity component v is used for illustration, but the circumferential component w could also be used in the same way. The robustness of this estimator is considerably higher than the one discussed in the last section, suffering less influence from the spectral estimation parameters. Different window sizes were tested to assess the impact on the output integral length scale. Results were presented by Caldas et al. (2021b) revealing a weak dependence on the variation of this parameter.

3.2.4. L-1 norm synthetic spectrum fit

The principle of the fit technique is to adjust a synthetic turbulence PSD model based on a few parameters in order to match the estimated PSD of the experimental data. An appropriate turbulence spectrum model has to be selected based on the characteristics of the flow field. In this study, as shown in Section 2.4, the Bullen and the von Kármán turbulence spectra are chosen. These models are constrained by the HIT assumption.

The validity of the HIT assumption can be proven by assessing eventual differences in the spectra fits of both velocity components. If different values for turbulence intensity and/or integral length scale are obtained for the two velocity components, the flow is potentially anisotropic at the measurement position observed.

The adjustment of parameters of a synthetic turbulence problem is expressed by the following optimization problem:

$$\underset{\overline{u^2}, \Lambda_1, n \in \mathbb{R}}{\operatorname{argmin}} \quad \|S(f) - S_{11}(f, \overline{u^2}, \Lambda_1, n, U_0)\|_1, \quad (3.2.3)$$

where $S(f)$ is the estimated PSD of the experimental data. If the low-frequency distortion removal technique is used, then its outcome, the “ S_{wf} spectrum”, is used as input. The synthetic turbulence spectrum $S_{11}(f, \overline{u^2}, \Lambda_1, n, U_0)$ (in this case the longitudinal component as assigned with the suffix 11, but it is analogously obtained for the transverse component 22) is a function of the frequency f , the signal variance $\overline{u^2}$, integral length scale Λ_1 , roll-off exponent n , and the mean longitudinal velocity U_0 , respectively. If the Bullen model is selected, the optimal n is automatically adjusted. Otherwise, for the von Kármán model n is fixed to $1/3$.

Note that the L1-norm was selected in this formulation. Indeed, the selection of the norm for the objective criterion is another critical step of this minimization problem. Aiming the minimization of the residual power, the L2-norm is often used for a typical least-squared-fit (LSF) problem. However, in this work, the L1-norm is rather used in order to give a more significant weight on the broadband part of the signal, and to reduce the importance of eventual points distanced from the synthetic spectrum. A classical example would be tonal components. These are known to be not related to turbulence (Hinze and B. J. Clark (1975) and Pope (2000)). The use of the L1-norm provides robustness for the technique against tonal components, which can be present in turbo-machinery data as shown in Section 3.1 (Meyer et al. (2019, 2015) and Meillard et al. (2013)). If tones are not removed from the PSD, this could lead to strong discrepancies in the estimated turbulence intensity (or equivalently the TKE).

3.2.5. L-1 norm synthetic spectrum fit with constraint

The difference between this fit technique and the previous one is that a constraint is added to the minimization problem. The new formulation is addressed as follows:

$$\begin{aligned} & \underset{\overline{u^2}, \Lambda_1, n \in \mathbb{R}}{\operatorname{argmin}} \quad \|S(f) - S_{11}(f, \overline{u^2}, \Lambda_1, n, U_0)\|_1 \\ & \text{subject to } \Lambda_1 = \left[\frac{S(f)U_0}{4u^2} \right]_{f \rightarrow 0} = \frac{U_0}{4u^2 \Delta f} \int_0^{\Delta f} S(f)df, \end{aligned} \quad (3.2.4)$$

i.e., the variables $\overline{u^2}$ and Λ_1 now meet a physical restriction governed by Equation 2.3.11. This constraint reduces the numbers of degrees of freedom of this optimization problem by one, as the variable Λ_1 is now a function of the variable $\overline{u^2}$, U_0 , and the average of $S(f)$ in the frequency range Δf . The constraint can make the method more stable, i.e., helping on finding the solution of the problem, in particular when the input data set is strongly contaminated with noise.

3.3. Turbulence intensity estimators

As previously defined in Section 2.3.4, the turbulence intensity is a function of the unsteady velocity signal power and the mean value of the flow velocity.

$$T_u = \frac{\sqrt{\overline{u^2}}}{U_0}, \quad (2.3.20 \text{ revisited})$$

where U_0 defines in this work the local mean velocity. Some other works use the free-stream U_∞ instead. The estimation of the power of $u(t)$: $\overline{u^2}$ can be performed in different ways. In this work, two of them are described in the following sections.

3.3.1. Estimation via variance

The physical meaning of the variance of a signal is indeed the power of this signal. The variance estimator is widely used in statistics and is given by

$$\overline{u^2} = \text{Var}\{u(t)\} = \mathbb{E}\{u(t)^2\} - \mathbb{E}\{u(t)\}^2. \quad (3.3.1)$$

N.B.: For a turbulence signal $\mathbb{E}\{u(t)\} = 0$.

3.3.2. Estimation via power spectral density

Another option to estimate the power of the signal by integrating its PSD as follows:

$$\overline{u^2} = \int_{-\infty}^{\infty} S_{uu}(f) df, \quad (3.3.2)$$

where $S_{uu}(f)$ stands for the PSD of the signal $u(t)$. Two advantages of this formulation are worth mentioning: The first is the extra robustness achieved by estimating the PSD of $u(t)$. Different techniques and data windows are available and can be chosen depending of the origin of the signal. The Welch method is typically preferred as a way of reducing the estimator bias. By averaging the discrete Fourier transform of several data blocks the contribution of non-stationary components are reduced. The second is the possibility of filtering the signal in the frequency domain. The limits of the integral can be set in

order to avoid undesired frequency bands. In cases where distortions appear in the signal for high-frequency bands, they could be easily removed by not integrating the PSD in the respective frequency band. Avoiding the very low-frequency band of PSD could be necessary, as well as shown in Section 3.1.1. Important to consider is that the signal has to be stationary, so that by using the Welch estimator technique, the mean and variance of the signal must be constant through all data segments. It will be shown in the next chapters that with low-frequency distortion present in a given signal, the statement of stationarity does not hold anymore. As a consequence, the power estimated using this method is dependent on the data block size selected.

3.4. Separation of rotor wake and background turbulence parameters

This section describes the estimation of turbulence parameters from data measured downstream of a rotating fan. The signal processing techniques necessary are more complex than in a free-stream field, e.g. upstream the fan. The literature review of relevant references found regarding the extraction of turbulence information from unsteady data measured downstream of a rotating fan was as introduced in Section 1.5.4. To the best of the author's knowledge, the only existing method to separate rotor wakes and background flow turbulence parameters and spectral information from hot-wire data measured downstream a rotor is the one presented by Jurdic et al. (2009) and described in Section 1.5.4. Different from this method, the new method proposed is based in the time domain and use windows to separate the parts of the turbulence signal corresponding to the rotor wake from the background flow. The duration and position in time of these windows are determined based on the cyclic variance of the turbulence signal, that means, the power of the signal as a function of the circumferential position. A threshold separates the two regions: low-variance is associated to the background flow, whereas high-variance to the rotor wakes. The proposed technique searches automatically the position and size of the data windows and separates both domains: rotor wakes and background flow. Overall, the proposed method can be applied to any signal to separate two superimposed processes, where one is cyclostationary and the other stationary. The requirement is that the processes have to have discernible variance.

The following sections describe the novel technique proposed to separate the rotor wake from the background turbulence statistics. After that, a brief description of a second technique found in the literature contrasts the results obtained. This section is partially based on the publication Caldas et al. (2022a).

3.4.1. Necessary coordinate system change

Typically, the data from a hot-wire measurement are referenced to the machine coordinates, i.e. the velocity signals are referenced to the axial $U(t)$, radial $V(t)$, and tangential $W(t)$ directions, as depicted in Fig. 3.6. Due to the swirl introduced by the fan in the flow, the streamwise velocity component in the plane behind the fan is not aligned with the axial line. As turbulence has to be modeled in terms of streamwise and transverse velocity components, a coordinate transformation must be performed.

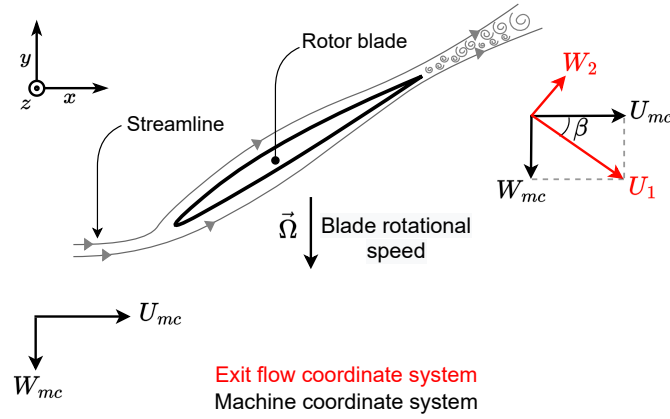


Figure 3.6.: Coordinate system used in the interstage section.

The new reference frame for turbulence analysis considers the main streamwise velocity component $U_1(t)$ and its respective transverse component $W_2(t)$, also known as the upwash velocity component. This last has by definition zero mean, as the streamwise component $U_1(t)$ already consists of the vector sum $\vec{U}_1 = \vec{U}_{mc} + \vec{W}_{mc}$. $W_2(t)$ consists essentially of the cyclic velocity fluctuations and the stochastic fluctuation component. As previously introduced, the index “1” stands for the streamwise component, whereas the index “2” indicates the transverse component. The exit flow angle in the rotor blade trailing edge β is calculated by:

$$\beta = \arctan\left(\frac{\overline{W}_{mc}}{\overline{U}_{mc}}\right), \quad (3.4.1)$$

where

$$\begin{aligned} U_{mc}(t) &= \overline{U}_{mc} + u(t) \\ W_{mc}(t) &= \overline{W}_{mc} + w(t), \end{aligned} \quad (3.4.2)$$

with

$$\overline{U}_{mc} = \mathbb{E}\{U_{mc}(t)\} = \lim_{T \rightarrow \infty} \frac{1}{T} \int_0^T U_{mc}(t) dt, \quad (3.4.3)$$

where the operator $\mathbb{E}\{\cdot\}$ denotes the expectation value. $u(t)$ and $w(t)$ refer to the zero mean fluctuations component of each respective velocity component. \overline{W}_{mc} is obtained identically as \overline{U}_{mc} and therefore omitted for simplicity here. Organizing the variables in a matrix form and with the help of a coordinate transformation matrix we obtain:

$$\begin{bmatrix} U_1(t) \\ W_2(t) \end{bmatrix} = \begin{bmatrix} \cos \beta & \sin \beta \\ -\sin \beta & \cos \beta \end{bmatrix} \begin{bmatrix} U_{mc}(t) \\ W_{mc}(t) \end{bmatrix}, \quad (3.4.4)$$

and therefore

$$\begin{aligned} U_1(t) &= U_0 + u_1(t), \\ W_2(t) &= w_2(t), \\ \overline{U_1} &= U_0, \\ \overline{W_2} &= 0, \\ U_0^2 &= \overline{W_{mc}^2} + \overline{U_{mc}^2}. \end{aligned} \quad (3.4.5)$$

To illustrate these velocity components, Fig. 3.7 shows velocity signals measured downstream a rotating fan using hot-wire anemometry. More detail about the instrumentation capability is given in the next chapters. The blade wakes are clearly seen in the periodic valleys of each signal, in total 11 wakes are plotted. The black curve (axial direction) and red curve (circumferential direction) velocity components refer to the original machine coordinate system. The flow exit angle for this measurement point can be calculated by the resulting vector using the mean velocities displayed in the plot. For this case, with the help of Eq. 3.4.1, $\beta = 27^\circ$. The results velocity signals obtained from the coordinate system change are the longitudinal component, in blue, and the transverse component, in green. Note that $\overline{W_2} = 0 \text{ m/s}$, as this is a transverse velocity component (perpendicular to the flow) but all the turbulent information is still present in the signal, i.e. $\overline{w^2_{22}} > 0 \text{ m}^2/\text{s}^2$.

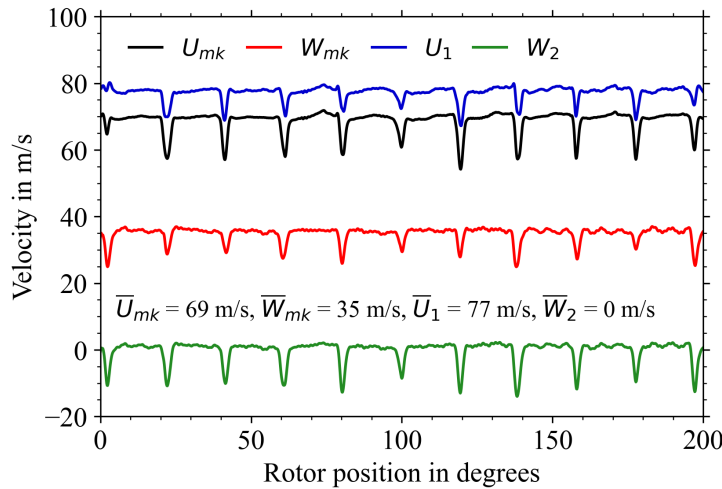


Figure 3.7.: Example of velocity signals measured downstream of the rotor. The black and red curves are in machine coordinates. The blue and green curves are the velocities in the new coordinates system. The mean values of each component are shown in the plot.

3.4.2. Novel technique to separate turbulence parameters of rotor wakes from the background flow

The newly implemented technique in this work is based on the separation of the rotor wake turbulence signal from the background turbulence signal. One way to look at this problem is by assuming that the hot-wire measured velocity is a superimposition of two different processes. The periodic wakes coming from the rotor blades overlap the background flow, resulting in a cyclostationary signal. The rotor wake turbulence is characterized by high turbulence intensity levels, whereas the background flow by much lower levels. The technique developed is based on separating the two processes by tapering the hot-wire data using suitable data windows. Fig. 3.8 sketches the presented idea. On the left-hand side, a synthetic turbulence signal is shown. The blue- and red-hatched areas show the borders dividing the two processes.

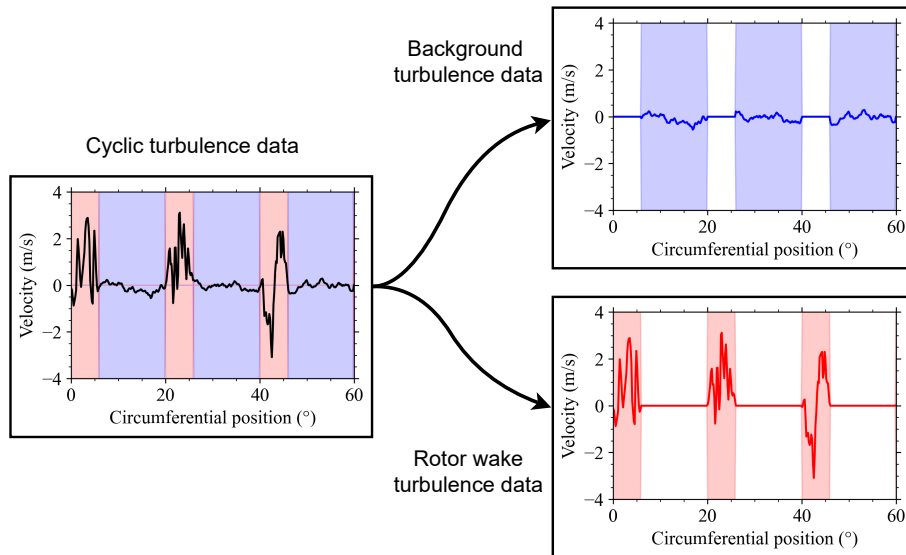


Figure 3.8.: Sketch of how the rotor wake - background turbulence separation technique works. The signals shown were obtained synthetically and represent only the turbulent fluctuations of each signal. The periodic mean fluctuations of the rotor wakes are not included in this signal.

In order to analyze the rotor wake signal, the region of the signal between the wakes (blue hatch, in the left-hand side plot in Fig. 3.8), referred to the background turbulence is multiplied by zero. The result is shown on the bottom-right-hand side of this figure. This allows us to analyze the statistics corresponding to the wakes only. On the other hand, in order to investigate the background turbulence, the region of the signal corresponding to the rotor wakes are similarly multiplied by zero, as in the top-right-hand side of this figure. Evidently power loss is faced by the use of these tapers, which is later corrected. Step by step, the technique is described as follows:

1. *Performing a cyclostationary analysis:* The cyclostationary tool is used to separate

the periodic velocity signal from the turbulence fluctuations. The signals $u_1(t)$ and $w_2(t)$ are already resampled and have an exact number of samples per revolution N_{rev} . For convenience, the signals are organized as a 2D matrix with dimensions $n \times k$, where $n = 0, 1, \dots, N_{rev} - 1$ is the sample position related to the angular position of the fan. $k = 0, 1, \dots, K - 1$ is the k^{th} revolution of the fan.

$$u_1(n, k) \triangleq u_1\left(\frac{nk}{f_s} + kT\right), \quad (3.4.6)$$

where T is the fan rotation period $T = 60/\eta$ in seconds, and η is the fan speed in RPM (revolutions per minute).

The cyclic mean of the velocity signal, which can also be seen as the coherent part of the signal (CyS1 - when performing a cyclostationary analysis) can be calculated by:

$$\bar{u}_1(n) = \text{CyS1}\{u_1(n, k)\} = \frac{1}{K} \sum_{k=0}^{K-1} u_1(n, k). \quad (3.4.7)$$

On the other hand, the incoherent part of the signal - CyS2 (turbulent information) resulting from the cyclostationary analysis is obtained by:

$$\begin{aligned} u'_1(n, k) &= \text{CyS2}\{u_1(n, k)\} \\ &= u_1(n, k) - \bar{u}_1(n) \quad \text{for } k = 0, 1, \dots, K - 1, \end{aligned} \quad (3.4.8)$$

where k refers to the k^{th} revolution of the fan. The best way to observe the CyS2 signal is not as a vector in time, but instead as a $N_{rev} \times k$ matrix, which corresponds to a collection of time series vectors allocated to each k^{th} revolution of the fan. Fig. 3.9 shows a representation of each of these velocity constituents. The blue curve represents the overall mean flow speed U_0 . The black curve stands for the cyclic average $\bar{u}_1(t)$ added by the total mean speed U_0 , where a typical blade wake shape is shown. The red curve illustrates $U_1(t)$ that is the sum of the stochastic oscillations $u'_1(t)$, the cyclic mean value $\bar{u}_1(t)$, and the overall mean U_0 . The CyS2 component of the signal is represented by $u'_1(t)$ as the difference between the black and red curves.

2. Calculation of the cyclic-variance of the signal:

The cyclic-variance refers to the variance of the turbulence as a function of the angular position. It can be easily calculated from $u'_1(n, k)$ by:

$$\begin{aligned} \text{Var}\{u_1(n, k)\} &= \bar{u}_1^2(n, k) - \bar{u}_1^2(n) \\ &= \frac{1}{K} \sum_{k=0}^{K-1} \left(u'_1(n, k)\right)^2. \end{aligned} \quad (3.4.9)$$

An example of a signal measured in the interstage of a fan is shown in Fig. 3.10. The

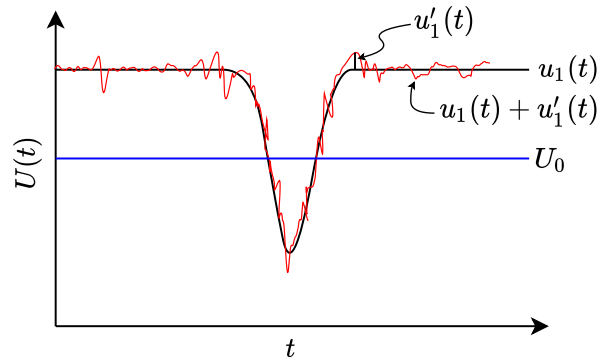


Figure 3.9.: Sketch of each constituent of an unsteady velocity signal measured downstream of a rotating fan.

further illustrations also refer to this data set. Details about the test rig will be given in the upcoming section. In this figure three fan revolutions $K = 3$ and three blade passages data, $\theta = 60^\circ$ or equivalently $n = 3N_b$, are shown. That means, the samples per blade passage are given by $N_b = N_{rev}/B = 113.8$ samples, for $N_{rev} = 2048$. The black curve at the back of this plot refers to the cyclic-variance of the streamwise velocity component. The grey curves are instantaneous snapshots of the $u_1'(n, k)$ signal for $k = 3$ fan revolutions.

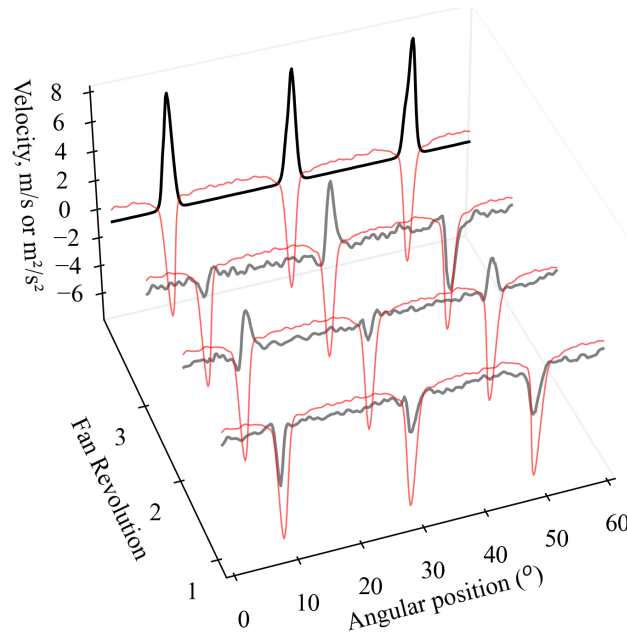
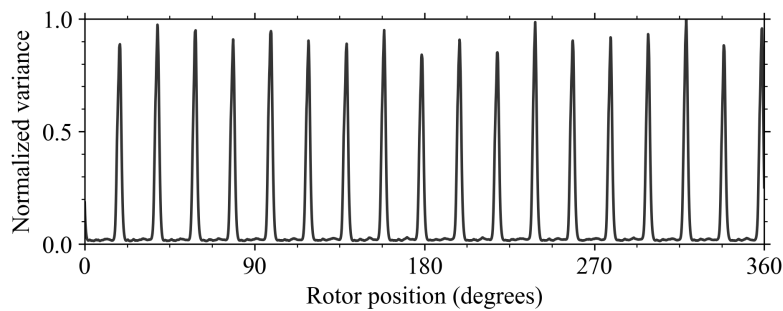


Figure 3.10.: Snapshot of the turbulence fluctuation signal $u_1'(n, k)$ for $k = 3$ fan revolutions in gray in m/s . Three blade passages are shown. The black curve shows the cyclic variance of $u_1(n, k)$ in m^2/s^2 . The red curves show the periodic velocity mean $\bar{u}_1(n)$ in m/s .

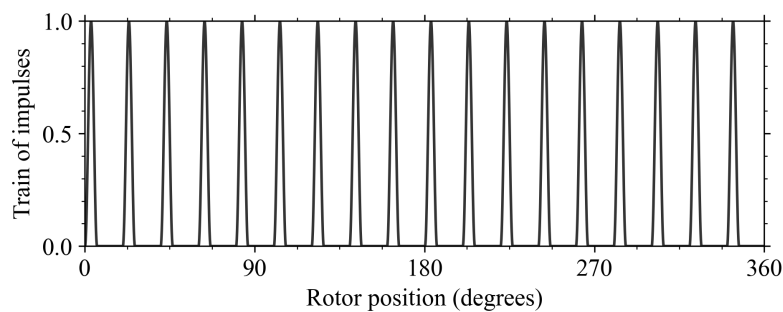
3. *Finding the center of the rotor wakes:* Once the cyclic-variance is calculated, it is

necessary to determine where the center of the wakes lies. In other words, as in Fig. 3.10, regarding the black curve, how many samples separate the beginning of the signal $n = 0$ from the first peak of the cyclic variance signal, understood as the center of one rotor wake. The algorithm assumes that all wakes are equally spaced. In Fig. 3.11 the top plot shows an example of a cyclic-variance normalized by its maximum value.

In order to find the center of the wakes, a train containing $B = 18$ impulses shaped with a Hann (see refs. Kay (1993) and Percival and Walden (1993)) window is created first. The Hann window is used as an impulse shape just for simplicity. Other impulse shapes could be used too. The window width is initially set to 30% of the width of a blade passage. The bottom plot in Fig. 3.11 portrays how this train of impulses signal looks like. In this example, the first pulse is roughly at the first position $\theta = 0^\circ$ or equivalently $n = 0$.



(a) Normalized cyclic-variance as a function of rotor position.



(b) Train of $B = 18$ equally spaced impulses. The impulses that were used have the Hann window shape.

Figure 3.11.: Signals to be compared in order to find the rotor position.

The method works by multiplying the train of impulses (Fig. 3.11b) by the cyclic-variance signal (Fig. 3.11a), summing up the resulting signal, and storing the output value. The train of impulses is then cyclic-shifted by one sample, and the same procedure is repeated. The algorithm performs this search N_b times, corresponding to one blade passage. This process can be mathematically described as follows:

Firstly, one sample passage impulse $h(n, L)$ is defined by:

$$h(n, L) = \begin{cases} \text{Hann}(n) & \text{for } n = 0, 1, \dots, L - 1 \\ 0 & \text{for } n = L, \dots, N_b - 1, \end{cases} \quad (3.4.10)$$

where L is the width of the impulse itself initially set as $L = 0.3N_b$. The train of impulses $I(n, n_\alpha, L)$ is defined as:

$$I(n, n_\alpha, L) = h(n_b, L)z^{-n_\alpha} \quad (3.4.11)$$

$$n_b = \text{mod}(n, N_b).$$

The symbol z^{-1} used from the Z-transform ($z = j\omega$, and $j = \sqrt{-1}$) denotes the unit delay operator defined by $z^{-1}y(n) = y(n - 1)$.

Finally, a cost function $f(n_\alpha)$ is defined as a function of the sample shift n_α applied to the train of impulses and multiplied with the cyclic-variance signal:

$$f(n_\alpha) = \sum_{n=0}^{N_{rev}} \text{var}\{u_1(n, k)\}I(n, n_\alpha, L), \quad (3.4.12)$$

and the sample corresponding to the distance from the beginning of the signal and the first wake center $n_{\alpha,c}$ is obtained by:

$$n_{\alpha,c} = \underset{n_\alpha \in [0, N_b]}{\text{argmax}} f(n_\alpha). \quad (3.4.13)$$

Typically, the cost function has a shape similar to a Gaussian curve. An example of this curve obtained from the signals shown in Fig. 3.11 is shown in Fig. 3.12. The x-axis refers to a rotor blade passage position, whereas the y-axis is the cost function normalized by its maximum.

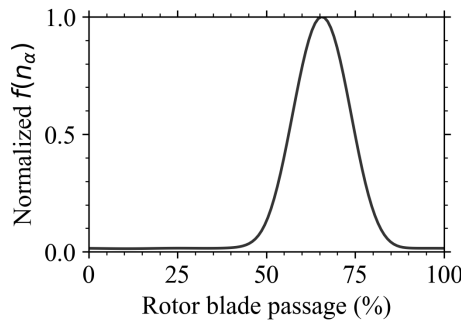


Figure 3.12.: Example of the cost function $f(n_\alpha)$ evaluated for the whole blade passage: $0 \leq n_\alpha \leq N_b$.

The advantage of this technique over, for example, searching for the peak in the cyclic-variance signal, is the robustness introduced. This technique searches the

strongest coherent structure with B equally spaced peaks. Any other structure, even with higher amplitude than the rotor wakes would not bias the result. The only situation that can lead to deviation in the results is when a structure with an integer multiple of B peaks stronger than the rotor wakes is present in the signal. One example is the region close to the rotor blade tip. In this region, as shown later, tip vortices are present, which have a structure with B equally spaced peaks with a power higher than the blade wakes themselves. This problem can be overcome by a technique discussed in the upcoming sections.

4. *Estimation of the average wakes amplitude:*

Once the position of the maxima in the cyclic-variance vector is found, the average of these maximums is computed. This is made by averaging n_{avg} samples around the maxima of each blade passage. The default used in this work is $n_{avg} = 3\%$ of N_b samples around the center of each rotor wake. In our case ($N_{rev} = 2048$), this gives 3 samples. In other words, the average amplitude \bar{A}_{u1} of the peaks in the signal $\text{var}\{u_1(n, k)\}$ is obtained by:

$$\bar{A}_{u1} = \sum_{n=0}^{N_{rev}-1} \text{var}\{u_1(n, k)\} I_2(n, n_{\alpha, c}, n_{avg}), \quad (3.4.14)$$

$$\bar{A}_{u1} = \frac{1}{n_{avg}B} \sum_{n=0}^{N_{rev}-1} \left[\text{var}\{u_1(n, k)\} \sum_{m=n_{\alpha, c}-(n_{avg}-1)/2}^{n_{\alpha, c}+(n_{avg}-1)/2} \delta(\text{mod}(n, N_b) - m) \right], \quad (3.4.15)$$

where $\delta(n)$ is the Dirac-delta defined by:

$$\delta(n) = \begin{cases} 1 & \text{for } n = 0 \\ 0 & \text{elsewhith.} \end{cases} \quad (3.4.16)$$

Eq. 3.4.15 does not seem straight-forward to understand, but, what it does is to average the n_{avg} samples around each peak in the signal $\text{var}\{u_1(n, k)\}$ spaced by N_b .

5. *Estimation of the width of the wakes:* The width of the wakes L_w in samples is estimated by varying the width L of each impulse in the train of impulses $I(n, n_{\alpha}, L)$ and comparing it to the cyclic-variance signal $\text{var}\{u_1(n, k)\}$. A cost function $g(L)$

of the impulse width L is defined as:

$$g(L) = \sum_{n=0}^{N_{rev}-1} \|\bar{A}_{u1}I(n, n_{\alpha,c}, L) - \text{var}\{u_1(n, k)\}\| \quad (3.4.17)$$

$$L_w = \underset{L \in [0, N_b]}{\text{argmin}} g(L)$$

where $\|\cdot\|$ is the absolute value operator. In other words, the optimal impulse width L_w is found, when the width of the impulses in $\bar{A}_{u1}I(n, n_{\alpha,c}, L)$ gets as close as possible to the ones in the variance signal $\text{var}\{u_1(n, k)\}$, which results in a local minimum in this absolute difference. Fig. 3.13 shows how the cost function $g(L)$ behaves as a function of L . In this plot, L is represented as a percentage of the rotor blade passage, as a way of normalizing the axis. In this case, the minimum value is found at approx. 33% of the blade passage. The width of the blade wakes $w_{w,k}$ is finally computed based on the train of impulses $I(n, n_{\alpha,c}, L_w)$ and a threshold value. $w_{w,k}$ is assumed to be the width of $h(n, L)^2$ in samples, when its amplitude drops by a specified threshold value relative to its maximum amplitude. In this work, this threshold is typically set between 90% - 95%.

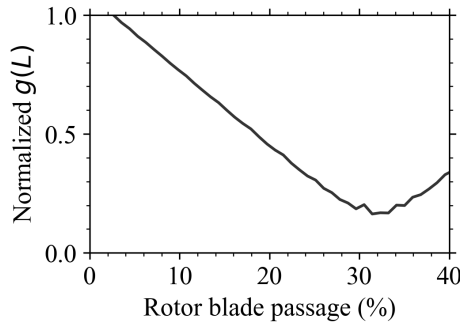


Figure 3.13.: Example of the cost function $g(L)$ evaluated for 40% of a blade passage: $0 \leq L \leq 0.4N_b$.

6. *Generating the data tapers:* Once the center of the rotor wakes is known, as well as their width, the data tapers can be created in order to separate the rotor wake and the background turbulence data from $u'_1(n, k)$. Two types of tapers need to be created: one with a smooth window, for example, a Hann window, to tape the data and avoid spectral leakage, and later estimate the power spectral density; and another taper with a rectangular window. The latter is used to compute the original power present in the region delimited by the first window, and in turn to correct the power loss introduced by the Hann windowing and the zeros between the windows. The N_{rev} long data tapers are defined as follows: The unsteady data is separated into blade wake signal $u_{1,w}(t)$ and background flow signal $u_{1,b}(t)$, where $t = nT_s$ and $T_s = 1/f_s$ is the sampling time. The separation is done by applying a suitable

window in order to set the values corresponding to the field outside of the region of interest to zero. Similar to step 2 of this series of steps, two windows are generated in order to separate both signals. The window $H_w(n)$ is used to isolate $u_{1,w}(t)$, whereas $H_b(n)$ isolates $u_{1,b}(t)$. The rotor wake smoothing taper $H_w(n)$ is calculated as follows:

$$H_w(n) = h_w(n_b, w_w)z^{-n\alpha},$$

$$h_w(n, w_w) = \begin{cases} \text{Hann}(n) & \text{for } n = 0, 1, \dots, w_w - 1 \\ 0 & \text{for } n = w_w, \dots, N_b - 1, \end{cases} \quad (3.4.18)$$

whereas for the background turbulence taper $H_b(n)$ holds:

$$H_b(n) = h_b(n_b, w_w)z^{-n\alpha},$$

$$h_b(n, w_w) = \begin{cases} 0 & \text{for } n = 0, 1, \dots, w_w - 1 \\ \text{Hann}(n) & \text{for } n = w_w, \dots, N_b - 1, \end{cases} \quad (3.4.19)$$

$n_b = \text{mod}(n, N_b)$. The rectangular windows $R_w(n)$ and $R_b(n)$ are obtained similarly by:

$$R_w(n) = \text{rect}_w(n_b, w_w)z^{-n\alpha},$$

$$\text{rect}_w(n, w_w) = \begin{cases} 1 & \text{for } n = 0, 1, \dots, w_w - 1 \\ 0 & \text{for } n = w_w, \dots, N_b - 1, \end{cases} \quad (3.4.20)$$

whereas for the background turbulence it holds:

$$R_b(n) = \text{rect}_b(n_b, w_w)z^{-n\alpha},$$

$$\text{rect}_b(n, w_w) = \begin{cases} 0 & \text{for } n = 0, 1, \dots, w_w - 1 \\ 1 & \text{for } n = w_w, \dots, N_b - 1. \end{cases} \quad (3.4.21)$$

7. *Separating background and wake data:* With the tapers available, the separated signals are obtained by:

$$u'_{1,w}(n) = H_w(\text{mod}(n, N_{rev}))u'_1(\text{mod}(n, N_{rev}), k),$$

$$u'_{1,b}(n) = H_b(\text{mod}(n, N_{rev}))u'_1(\text{mod}(n, N_{rev}), k), \quad (3.4.22)$$

$$k = \lfloor \frac{n}{N_{rev}} \rfloor,$$

where k is obtained by the integer division of n by N_{rev} with the operator $\lfloor \cdot \rfloor$. $u'_{1,w}$ stands for the rotor wake signal and $u'_{1,b}$ for the background turbulence signal. At this stage, the signals can be arranged back into vectors instead of a matrix. With the signals now separated, it is necessary to correct their energy loss due to tapering.

8. *Computing the original energy of each component:* The original (lossless) power of the rotor wake signal σ_w^2 and the background turbulence signal σ_b^2 , respectively, are calculated by:

$$\sigma_w^2 = \frac{1}{w_w BK} \sum_{n=0}^{N_{rev}-1} \sum_{k=0}^{K-1} [R_w(n)u'_1(n, k)]^2, \quad (3.4.23)$$

and similarly, for the background turbulence:

$$\sigma_b^2 = \frac{1}{w_b BK} \sum_{n=0}^{N_{rev}-1} \sum_{k=0}^{K-1} [R_b(n)u'_1(n, k)]^2 \quad (3.4.24)$$

as both are already zero-mean signals.

9. *Computing the power spectral density:* The biased power spectral density (power loss not yet corrected) of the rotor wakes is obtained by $\hat{S}_{11,w}(f_n)$:

$$\hat{S}_{11,w}(f_n) = [\mathcal{F}\{u'_{1,w}(n)\}]^2, \quad (3.4.25)$$

where $\mathcal{F}\{\cdot\}$ stands for the discrete Fourier transform, and f_n is the discrete frequency bin. For simplicity, the power spectral density estimation is in this text expressed as the squared value of the Fourier transform of the signal. However, in practice, the Welch method (Kay (1993) and Percival and Walden (1993)) should be used to improve estimation performance. The bias of the power spectral density can be corrected as follows:

$$S_{11,w}(f_n) = \sigma_w^2 \frac{\hat{S}_{11,w}(f_n)}{\Delta f_n \sum_{f_n} \hat{S}_{11,w}(f_n)}. \quad (3.4.26)$$

The dividing term in this equation is essentially the power of the spectrum $\hat{S}_{11,w}(f_n)$. This division normalizes the spectrum so that its power is equal to unity. Δf_n stands for the discrete frequency resolution. Afterwards, the normalized spectrum is corrected with the term σ_w^2 to adjust it to the correct power. The power spectral density of the background turbulence $S_{11,b}(f_n)$ is obtained in the same way by:

$$\begin{aligned} \hat{S}_{11,b}(f_n) &= [\mathcal{F}\{u'_{1,b}(n)\}]^2, \\ S_{11,b}(f_n) &= \sigma_b^2 \frac{\hat{S}_{11,b}(f_n)}{\Delta f_n \sum_{f_n} \hat{S}_{11,b}(f_n)}. \end{aligned} \quad (3.4.27)$$

For the other transverse velocity components such as the w_2 , the data tapers used are the same as chosen for the u_1 component. Step 1 needs to be repeated in order to obtain the cyclostationary components. After that, the steps 2 to 6 are skipped, jumping straight to steps 7, 8 and 9.

10. *Estimating turbulence parameters from the PSD:* After the estimation of the PSD of each spatial domain, the turbulence parameters of interest (i.e., turbulence intensity and integral length scale) need to be estimated. The turbulence intensity is estimated by:

$$T_x = \frac{\sqrt{\sigma_x^2}}{U_0}, \quad (3.4.28)$$

where σ_x^2 is the variance of the signal and U_0 the mean longitudinal velocity at the chosen measurement position.

The turbulence integral length scale is estimated from the output PSD of the velocity signal S_{xx} . This is done under the Taylor assumption and, as discussed in Section 3.2, different approaches can be used. In this work, the HIT assumption is taken in order to use a more robust estimator. For the longitudinal velocity component, Eq. 3.2.1 is used, whereas for the transverse component, Eq. 3.2.2 is used.

11. *Increasing the robustness of the algorithm:* Not always is the turbulence data behind a rotor clean from secondary flow phenomena. A typical example is observed from turbulence measurement data in regions close to the rotor blade tip. In this radial position, the effect of tip vortex is expected to be present in the measured data. This is due to the flow leakage in the gap between the blade and the duct wall. The cyclic-variance of the turbulence fluctuations in this region (tip vortex) is often higher than the variance of the rotor wakes themselves. Fig. 3.14 shows an example of a measurement point at a radial position corresponding to 95% of the blade span, i.e. 4 mm away from the duct wall. In this figure, the peaks with the variance of about $7.5 \text{ m}^2/\text{s}^2$ are due to the blade wakes, whereas the strong peaks with variance $> 30 \text{ m}^2/\text{s}^2$ are due to the blade tip vortex.

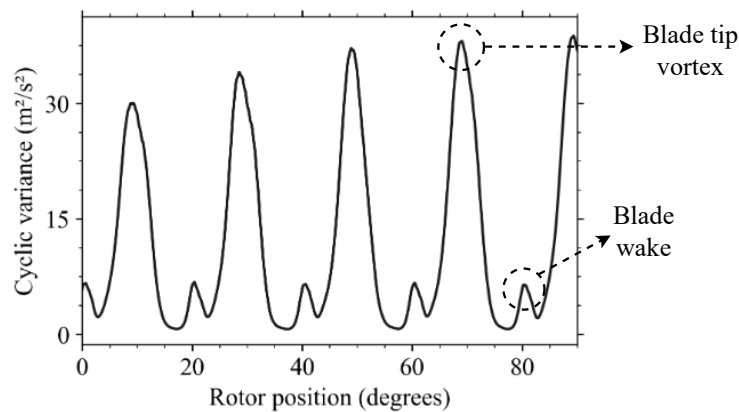


Figure 3.14.: Cyclic-variance at the radial position corresponding to 95% of the blade span, i.e. 4 mm away from the duct wall. 4.5 blade passages are shown. The peaks associated to the blade tip vortices and blade wakes are indicated.

If the presented algorithm is applied to the same dataset as shown in Fig. 3.14, the peaks associated with the tip vortex will be detectable as the blade wakes. Even

though the tip vortex is generated by the blades, it is not considered as part of the blade wake, instead, it is a phenomenon apart. In this work, all flow fluctuations that are not considered as blade wakes are classified as background turbulence.

In order to guide the algorithm to not detect the tip vortex as blade wakes, the following is done: for a set of radial measurement positions ranging from blade tip to the blade root, the algorithm has to start the wake detection at a radial position close to the blade mid-span, where the flow is often clean and free of secondary effects. By knowing the position of the wakes with respect to the trigger signal, and their width, the algorithm can move to the next radial position in the direction of the blade tip (duct wall), and afterwards to the blade root (hub). The position of the wakes and their width with respect to the previously processed radial position have to be within a range pre-defined by the user. This works as constraints for the algorithm. For example, we assume that for a given radial position the first blade wake was detected at 20° and the angle difference allowed between radial positions is set to 1.5° , the wake position of the next radial measurement position shall be scanned and found only in the range of $20 \pm 1.5^\circ$. This procedure is based on the physics of the flow itself, as the blade wake position in the data from a radial position cannot be found several degrees apart from the previously measured radial position.

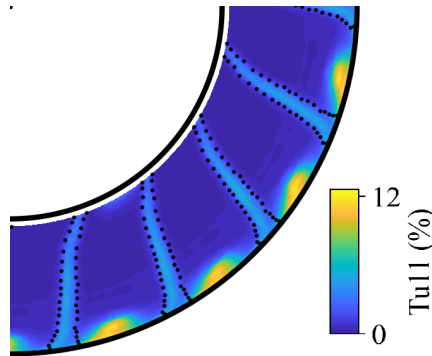


Figure 3.15.: Turbulence intensity distribution for the longitudinal velocity component. The tip vortices have the highest turbulent fluctuations. The wake areas detected automatically are shown delimited by the black dots.

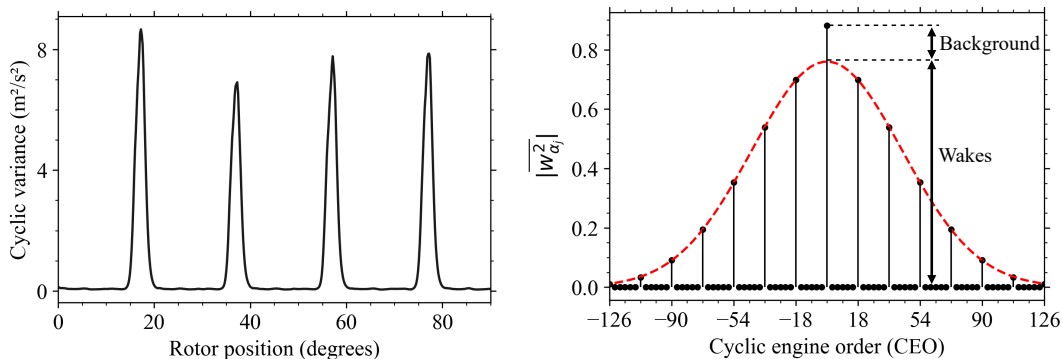
An exemplary result that shows the detected wake region and the blade tip vortex is depicted in Fig. 3.15. The black dots represent the borders between what is considered rotor wake and background flow. This figure shows the turbulence intensity distribution of the longitudinal velocity component as a function of radial and circumferential positions. The fan operating point for this measurement is: $\eta_c = 4500$ RPM, $\phi = 0.33$.

3.4.3. Cyclostationary spectral analysis

The technique briefly introduced in this section is based on the guidelines provided by Jurdic et al. (2009). With this method, the turbulence intensity of the rotor wakes and the background flow can be estimated. This method is based on the Fourier transform of the cyclic variance signal $\text{var}\{u_1(n, k)\} = \overline{u_1^2(n)}$:

$$\overline{w_{\alpha_j}^2} = \overline{w(\alpha_j)^2} = \mathcal{F}\left\{\overline{u_1^2(n)}\right\}^2, \quad (3.4.29)$$

where α_j represents the cyclic engine order (CEO) as an equivalent frequency domain of the time step from the cyclic variance signal. Fig. 3.16 shows an example using hot-wire data from the CRAFT test rig. As the number of rotor blades is equal to $B = 18$, the periodic power distribution is found at cyclic frequencies harmonics of B , compare Fig. 3.16b, in black points. At $CEO = 0$, the respective value is related to the total power of the signal itself. In other words, this is a sum of the contributions of the periodic components (wakes) and the non-periodic (background) signals, as indicated in Fig. 3.16b. As discussed by Jurdic et al. (2009), the shape of the cyclic wakes variance is similar to a Gaussian (bell) curve. Indeed, the Fourier transform of a Gaussian curve is another Gaussian curve. In Fig. 3.16b, the red-dashed curve is a fit of a Gaussian (let's say $\mathcal{G}(\alpha_j)$) curve to the harmonics of B components. In this example we see a good agreement between $\overline{w_{\alpha_j}^2}$ at the harmonic components of B and the Gaussian curve. One requirement for this technique to work properly is that the cyclic-variance curve needs to be a periodic composition of Gaussian curves. If this requirement is not met, deviations are found, as the extraction of each variance contribution (rotor wakes and background flow) depends on the interpolation of a Gaussian curve, see Fig. 3.16b. As shown later, this is often the case in regions close to the outer casing, where blade tip-vortices are found. Another circumstance is when the fan operates with high loading. In this condition, the rotor wakes are more asymmetric and deviate more from a Gaussian shape, which is a symmetric curve.



(a) Cyclic variance of the longitudinal velocity component. Four blade passages are shown. (b) Fourier transform of the cyclic variance (black) and a Gaussian fit (red-dashed).

Figure 3.16.: Cyclic variance analysis.

The variance (power) of the background turbulence is then obtained with the help of the function $\overline{w(\alpha_j)^2}$ and the Gaussian fit $\mathcal{G}(\alpha_j)$ by:

$$\sigma_b^2 = \overline{w(0)^2} - \mathcal{G}(0), \quad (3.4.30)$$

which is the difference of both curves calculated at $\alpha_j = 0$. The power of the wakes is thus obtained by:

$$\sigma_w^2 = \sum_{k=-\infty}^{+\infty} \overline{w(kB)^2} - \sigma_b^2, \quad (3.4.31)$$

where B is the number of the rotor blades. In this work, k is typically set to 20.

3.4.4. Test of the new method

In order to test the new method, synthetic data were generated by low-pass filtering a white noise signal with an amplitude adjusted to provide the desired equivalent turbulence intensity. The flow speed was set to 50 *m/s*. This parameter was necessary for the turbulence modeling and turbulence intensity calculation. For both rotor wakes and background flow signals, a $n = 1$ order linear time-invariant (LTI) filter of Butter-worth type was selected. Its attenuation of 3 dB per decade is slightly higher than the slope of a von Kármán spectrum, as it will be shown. The signal corresponding to the rotor wake $u_w(t)$ was generated using $\text{var}\{u_w(t)\} = 1.6 \text{ m}^2/\text{s}^2$. The equivalent turbulence intensity is $Tu = 2.6\%$. A window was used to provide a smooth transition from the background flow (low variance) to the wake region (high variance), as observed in experimental data. In this work, the square root of the Hann window was chosen.

The width of the wakes N_b was set to equivalently 30% of a blade passage, or $0.3 \cdot 20^\circ = 6^\circ$. The signal corresponding to the background flow $u_b(t)$ was generated using: $\text{var}\{u_b(t)\} = 0.021 \text{ m}^2/\text{s}^2$ producing a turbulence intensity of $Tu = 0.3\%$. The cut-off frequency f_c of the low-pass filter was set, so that the fitted von Kármán spectrum (the fit technique is as described in Caldas et al. (2021b)) delivers the desired integral length scale. For $u_w(t)$, f_c was set at 3.6 *kHz*, producing $\Lambda = 4 \text{ mm}$. Hence, for $u_b(t)$, $f_c = 1.6 \text{ kHz}$, which resulted in $\Lambda = 10 \text{ mm}$. These are typical values observed from measured data. Fig. 3.17 shows the three PSD generated for the test. The fitted von Kármán spectrum is also shown as dotted lines. Fig. 3.18 shows a block diagram of the process to generate synthetic data. Finally, Table 3.4.1 resumes the parameters from the generated synthetic data, as well as the estimated parameters using the techniques described in sections 3.4.2 and 3.4.3. We see from this table that the new technique performed surprisingly well on detecting the turbulence parameters from the mixed signals. The cyclostationary technique performed also reasonably well, however, from this test results, it seems that the latter tends to underestimate the levels.

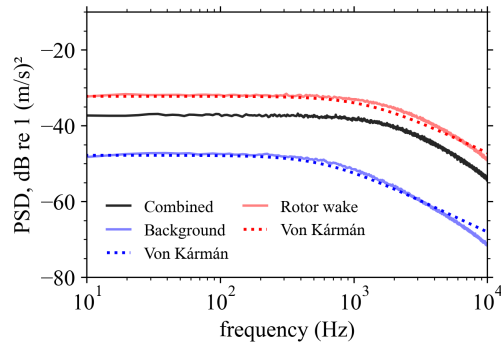


Figure 3.17.: PSD of both synthetic signals generated with the help of a low-pass filter. The dotted lines show the respective adjusted von Kármán spectrum. The black curve represents the spectrum of the mixed signals.

	Generated	Detected	
		New technique	Cyclostationary
Wake T_u (%)	2.65	2.65	2.1
Wake Λ_1 (mm)	4.30	4.30	-
Background T_u (%)	0.29	0.30	0.26
Background Λ_1 (mm)	9.40	9.30	-

Table 3.4.1.: Turbulence parameters created and obtained for the test case with synthetic data.

Test with experimental data

A second test was conducted with experimental data to prove the capability of the new method to separate the turbulence PSD of the rotor wakes from the background flow. Details about the fan operating point, test rig, and instrumentation are skipped for convenience. Fig. 3.19 shows the output spectra for two different radial measurement positions. In fact, these results refer to the same dataset as used in Fig. 3.15. The estimated PSD of the raw longitudinal velocity signal is shown in black. The blue curve refers to the estimated PSD of the background flow, whereas the red of the rotor wakes. As expected, tones associated with the periodic rotor wakes are observed in both plots in the black curve (raw signal).

Fig. 3.19a refers to a measurement position close to the fan outer casing, where tip vortices are observed in the signals. At this radial position, most of the power present in the velocity signal is due to the blade tip vortices, not to the rotor wakes. This can also be observed in Fig. 3.15 as spatial distribution of the turbulence intensity, and in Fig. 3.14 with the help of the cyclic variance function. For this reason, the blue (background flow) and black (total signal) curves almost overlap, confirming that the majority of the power is concentrated in the area between the rotor wakes. It is worth mentioning, that the background curve in this example is tone-free, as the periodic components were previously removed from this signal, which proves the ability of the technique to successfully retrieve the background

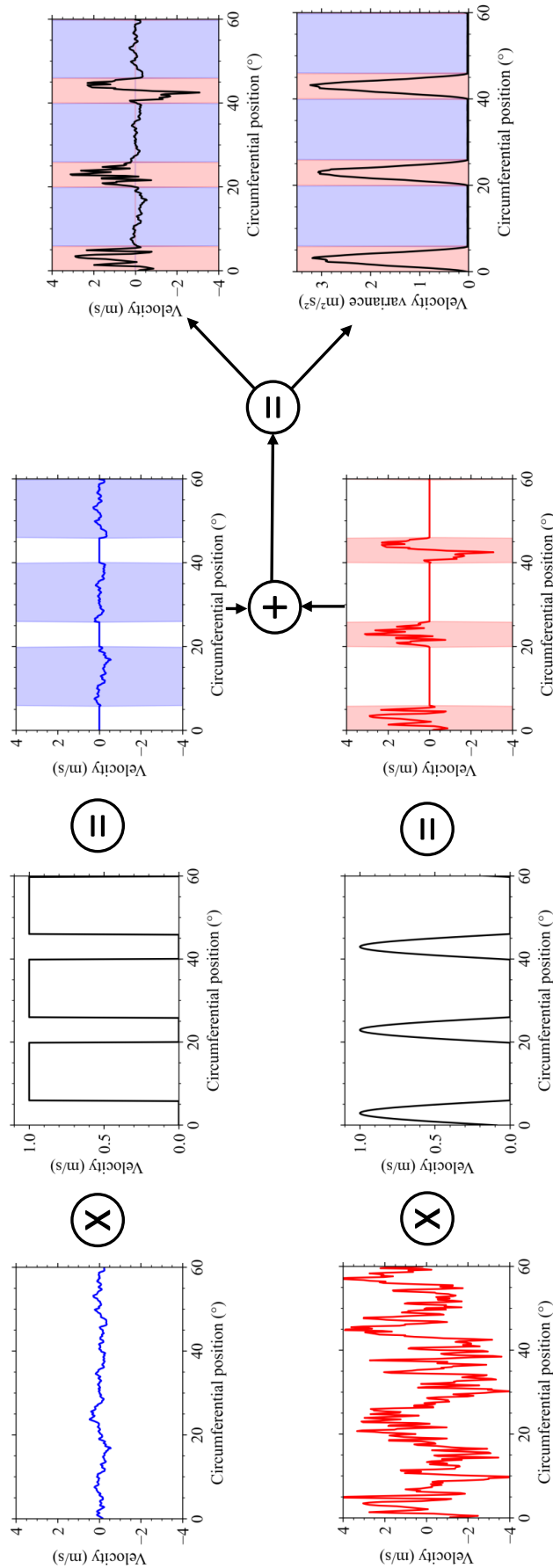
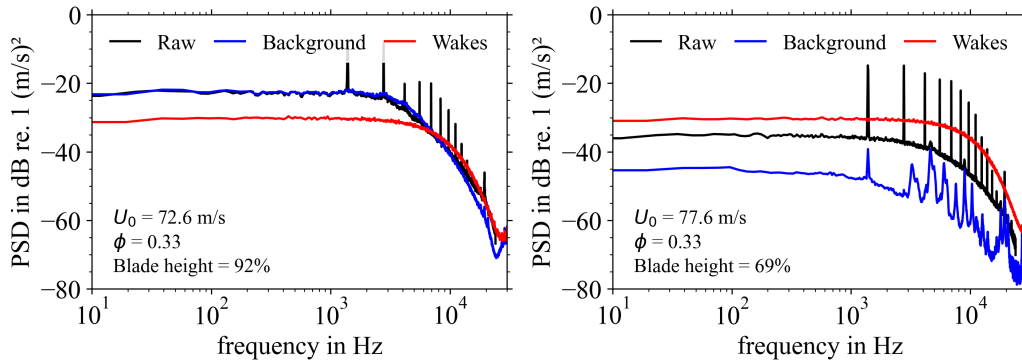


Figure 3.18.: Block diagram of the synthetic generation algorithm of an equivalent turbulent field behind a rotor. A snapshot of the signals corresponding to the passage of three rotor blades (60° for a 18-bladed rotor) is illustrated. On the top is the background flow signal $u_b(t)$ in blue, whereas on the bottom the blade wake signal $u_w(t)$ in red. The resulting mixed signal is plotted both as instantaneous velocity signal as well as its variance.



(a) Measurement position close to the outer casing, where tip vortex leakage is found. (b) Measurement position away from the outer casing and closer to the blade mid-span, where the flow is free from disturbances.

Figure 3.19.: PSD of the longitudinal velocity component of the raw signal (black), separated blade wakes (red), and background flow (blue). Results for two radial positions are shown.

flow turbulence information.

Fig. 3.19b refers to a measurement position closer to the mid blade-span. At this measurement position, the turbulence is dominated by the rotor wakes. For that reason, the red curve (wake turbulence) has more power than the raw signal, as the latter contains only a fraction of the power content of the former. The low background flow turbulence levels are confirmed by the low level of the blue curve.

Finally, Table 3.4.2 displays the turbulence parameters (turbulence intensity and integral length scale) of the rotor wakes and background flow estimated for these two measurement positions. Results refer to the longitudinal velocity component. The results of the newly proposed method (Section 3.4.2) is compared with the results of the cyclostationary technique (Section 3.4.3). We observe for the measurement position at 92% of the blade height (region where tip vortices are found) that the turbulence intensity detected with the cyclostationary technique is very high: 36% for the wake region and 16.6% for the background flow. These values are not realistic and do not agree with the numbers observed in Fig. 3.15, where we see that the turbulence levels are lower than 12%. In contrast, the new technique estimated numbers that seem plausible. At this measurement position, the background turbulence levels are found to be higher than the rotor wakes levels (6.6% versus 3.4%), what seems plausible due to the tip vortex. For the measurement point at 69% of the blade height, both techniques led to very similar values. In fact, the background turbulence values detected were identical for both techniques. In this region, no flow distortion is present, and the cyclic variance signal seems similar to the example shown in Fig. 3.16. More comments on the aerodynamic analysis are given in the next chapters.

	92% of blade height		69% of blade height	
	New technique	Cyclo.	New technique	Cyclo.
Wake T_u (%)	3.42	36	3.56	4.1
Wake Λ_1 (mm)	2.50	-	2.20	-
Background T_u (%)	6.65	16.6	0.47	0.47
Background Λ_1 (mm)	4.20	-	4.11	-

Table 3.4.2.: Turbulence parameters detected from experimental data. The newly proposed method is contrasted against the cyclostationary technique. Results refer to the longitudinal velocity component.

4. DLR-CRAFT aeroacoustic fan test facility

CRAFT (Co-/ Counter Rotating Acoustic Fan Test rig) is a low-speed fan test rig especially designed for aeroacoustic and aerodynamic studies. The fan stage consists of a 18-bladed rotor and a 21-vaned stator. The test rig can achieve fan speeds up to 4500 RPM. For the baseline rotor/stator configuration this produces a flow speed equivalent of 0.14 Mach number in the inlet and 0.48 Mach at the blade tips. This produces a rotor blade Reynolds number of about 500,000 at 70% of the blade height. The duct has a constant inner diameter of 453.6 mm. One important aerodynamic parameter that is related to the fan operating point is the flow coefficient ϕ , defined as the ratio of the axial and fan tip velocities:

$$\phi = \frac{M_{ax}}{M_{tip}} = \frac{\bar{U}}{U_{tip}} = \frac{\bar{U}}{2\pi\omega R}. \quad (\text{A.1.3 revisited})$$

The different fan flow coefficients are adjusted by changing the axial flow speed with the help of a conic throttle at the duct exhaust. This is done by adjusting the throttles axial position, which alters the pressure drop at this location. As a consequence, it changes the fan pressure ratio and the axial flow speed. The various mass flows associated with different flow coefficients are computed in its corrected form by

$$\dot{m} = \rho \int_0^{2\pi} \int_0^R U(r, \theta) r dr d\theta, \quad (\text{A.1.1 revisited})$$

allowing for constant and comparable axial Mach flow speeds, when testing in different configurations, with different room temperatures and ambient pressures.

For every measurement, the fan speed is adjusted to the corrected fan speed according to:

$$\eta_c = \eta \sqrt{\frac{T_{ref}}{T_t}}. \quad (\text{A.2.17 revisited})$$

This correction is made in order to compensate mainly for temperature changes among different measurement days. The corrected fan speed guarantees a constant tip Mach number based on a reference condition. This condition is typically defined at standard sea level: $T_{ref} = 288.15 K$ and $p_{ref} = 101,325 Pa$. The detailed formulation of how to compute the corrected fan speed η_c based on the actual fan speed η is provided in Appendix A. Due to its modular construction, measurements can be performed at several axial and circumferential positions. A photograph of the test rig is shown in Fig. 4.1.

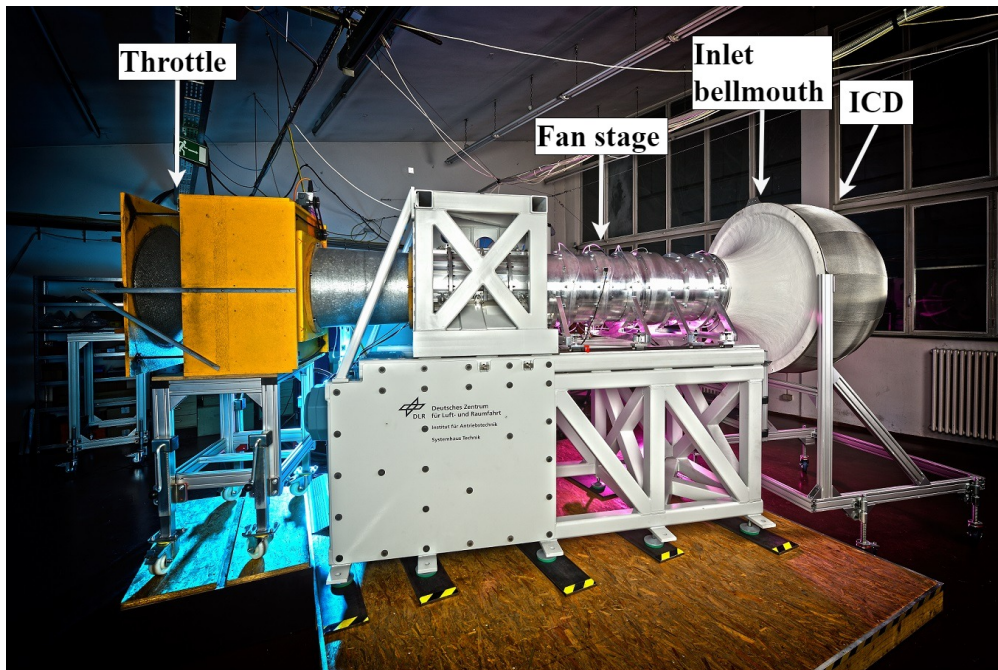


Figure 4.1.: Photograph side view of the CRAFT test facility.

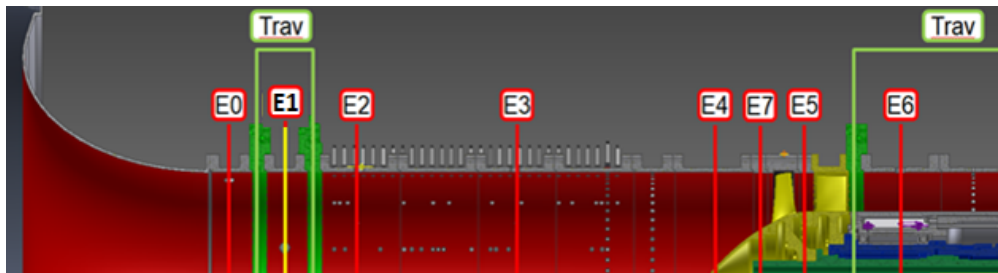


Figure 4.2.: CRAFT cross-section and the seven aerodynamic measurement planes highlighted, from E0 to E7.

A view of the cross-section of the CRAFT rig along with all aerodynamic measurement planes is depicted in Fig. 4.2. A more detailed view with several relevant dimensions is found in Fig. 4.3. On the left-hand side, the inflow control device (ICD) and bellmouth defines the rig inlet. The ICD assures homogeneous flow and low turbulence level at the duct inlet. The ICD was in-house designed and constructed specifically for the CRAFT test rig. Its design, construction and assessment are described in detail by Caldas et al. (2022b) and in the next sections.

For the configuration with inflow distortion, the inflow distortion screens combined with a honeycomb straightener is positioned downstream of the bellmouth, at plane E1. This honeycomb is made out of stainless steel with 25.4 mm (1") depth, a hexagonal cell size of 6.25 mm (1/4"), and a wall thickness of 0.2 mm. It works both as a structural device to support the distortion screen and to keep the streamlines parallel, reducing the flow three-dimensionality induced by the screen. The section containing the distortion screen

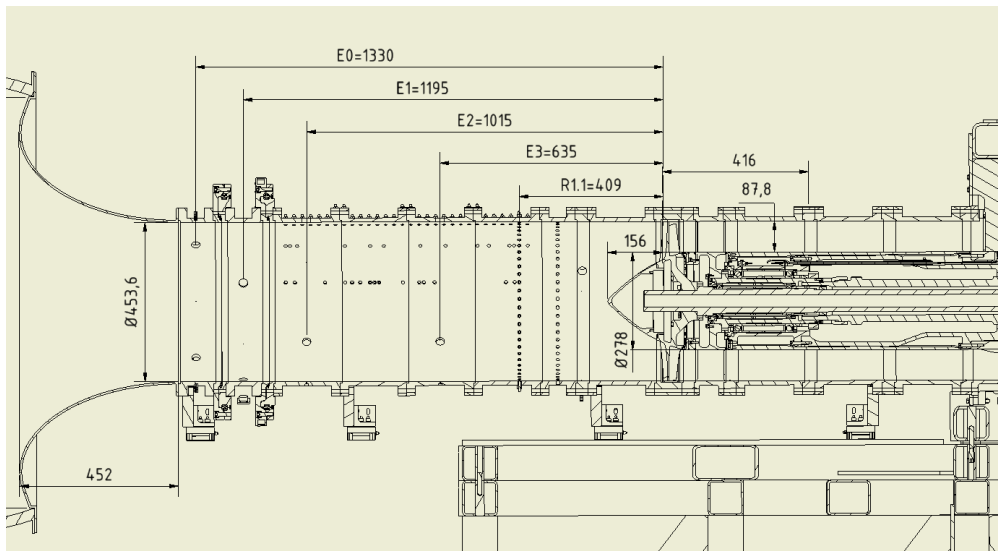


Figure 4.3.: CAD drawing of the test rig. The relevant distances and dimensions are indicated in the drawing, as well as the distance of each aerodynamic measurement plane to the tip rotor leading edge. The dimensions given are in millimeters.

and honeycomb is mounted in a circumferential traverse, allowing it to rotate over 360° . A more detailed description of the test rig, possible instrumentation and analysis capabilities are given by Tapken et al. (2021b) and Tapken et al. (2021a).

4.1. Design and construction of the CRAFT Inflow control device (ICD)

This section describes the steps taken for the design, conception, and construction of the CRAFT ICD and is based on the publications Caldas et al. (2022b, 2019b). A thorough ICD performance assessment regarding its impact on the flow aerodynamics and fan noise emissions is given in Chapter 5.

4.1.1. Design of the CRAFT ICD

As discussed in Caldas et al. (2019b) in the early stages of the CRAFT ICD design, the ICD diameter shall be in the range of 2 to 5 times of the fan diameter. The exact value depends on the maximum flow speed acceptable through the ICD. If we select a mesh with a wire diameter of 0.25 mm operating only in the subcritical regime ($Re < 50$ based on wire diameter, where Re stands for the Reynolds number), which is typically found in the literature (see Cattafesta et al. (2010), Kulkarni et al. (2011), Sturm and Carolus (2013) and Groth and Johansson (1988)), this leads to a maximum flow speed of 3 m/s through the ICD surface.

The maximum mass flow through the ICD is dictated by the fan used in the test rig. The CRAFT test rig was designed to operate with a rotor-stator or a rotor-rotor configuration

mounted in a 453.6 mm diameter duct. For the rotor-stator configuration (baseline), the maximum mass flow expected is $\dot{m} = 9.3$ kg/s at $\eta = 4500$ RPM, resulting in a fan pressure ratio of $PR = 1.025$. The design point for this configuration is at $\eta = 4500$ RPM producing $\dot{m} = 7.3$ kg/s and $PR = 1.036$. The rotor-rotor configuration, however, should achieve a maximum flow rate of $\dot{m} = 11$ kg/s at $\eta = 4500/4000$ RPM (first and second rotor, respectively), and $PR = 1.025$. As the ICD was designed to be used with both rotor set configurations, a maximum operation mass flow of $\dot{m} = 11$ kg/s was therefore selected.

With the bellmouth flare angle set to 70° , an ICD with 1.25 m in diameter meets these requirements, keeping the flow speed through the ICD below 3 m/s. The bell-mouth flare is the tangential straight prolongation of the inlet ellipse, used to adjust the bell-mouth size to the ICD and provide a mechanical connection. This size leads to a ratio between ICD and fan diameter of 2.8, which is within the recommended range. The process for selecting the ICD design was guided primarily by the following requirements: (1) optimal impact on the flow; (2) cost of manufacture; and (3) ease of manufacture (the manufacturing should be possible at the DLR workshop).

Based upon that, the solution adopting flexible aluminium honeycomb (approx. 3.2 mm cell size and 30 mm depth) using 0.5 mm thick stainless-steel ribs as structure was chosen. A thin stainless-steel wire mesh with dimensions of 1.00 mm x 0.25 mm covers the outer side of the ICD, whereas a 0.75 mm x 0.25 mm one its inner side. The number of segments was set to 13. The chosen rib number minimizes the potential generation of modes due to the interaction of the rib wakes with the rotor. The baseline rotor-stator configuration of the CRAFT test rig is a 18-bladed rotor ($B = 18$) and 21-vaned stator ($V = 21$). According to the Tyler-Sofrin theory of interaction modes (Tyler and Sofrin (1962)), the first order rib-rotor interaction mode is the $m = -18 + 13 = -5$, which is a cut-off mode at 4500 RPM fan speed. Indeed, under standard conditions, $\eta = 4500$ RPM, $\phi = 0.40$ and inlet Mach number of $M = 0.11$, the mode $(m, n) = \pm(5, 0)$ becomes cut-on for $f > 1.51$ kHz. Furthermore, for higher BPF harmonics, the interaction modes can be clearly distinguished from the rotor-stator interaction modes. A sketch of the ICD design is depicted in Fig. 4.4.

4.1.2. Construction of the ICD

The honeycomb panels were sliced into segments in a shape similar to the meridian lines of a sphere by a water jet CNC machine, as shown in Fig. 4.5a. The design of these segments is not a trivial step. A 2D plate needs to be bent and deformed into a 3D shape. A software was used to approximate the 2D cut shape from the 3D model shown in Fig. 4.4. The 3D slices come easily from a hemisphere equally sliced into 13 segments. The

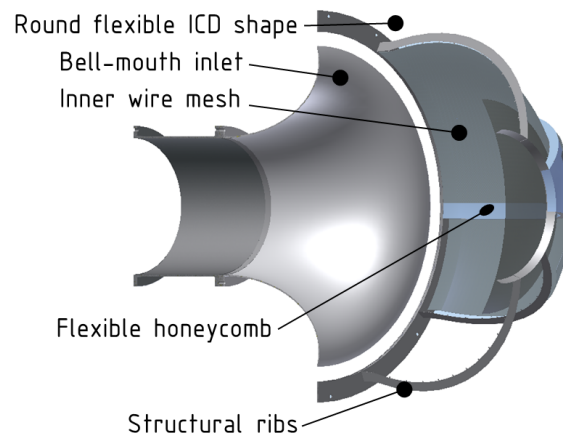


Figure 4.4.: Sketch of the new bellmouth and flexible ICD shape.

cut shape had to be very precise, otherwise, gaps between honeycomb segments and ribs would appear. A few trial and error cuts were necessary to get the right shape.

With the help of a wooden mold and screws to hold each segment in place, the flexible honeycomb panels were glued together on the thin ribs, shown in Fig. 4.5b. In Fig. 4.5c five segments are already glued together. At some points of each segment, the honeycomb sides do not touch completely the ribs (upper and lower sides). Instead of parallel, a “V” contact is observed between the honeycomb and the rib, reducing the contact area. This gap is seen only from the outer side and was filled with epoxy glue. This solution provides not only more structural stiffness but also avoids secondary flow moving through any eventual gap between honeycomb and rib.

After the gluing process, the wire mesh could be spot-welded on the ribs. Fig. 4.5d shows how the mesh was stretched and held firmly in place with the help of screws and pads. Fig. 4.5e shows one side already with wire mesh welded on the rib and trimmed off. The other side would still receive a layer of wire mesh. In Fig. 4.5f a whole segment is covered by a wire mesh already welded, and ready to be trimmed. With this approach, there was no wire mesh overlap. This reduces the risk of generating extra flow non-homogeneity, as discussed in Section 1.5.5.

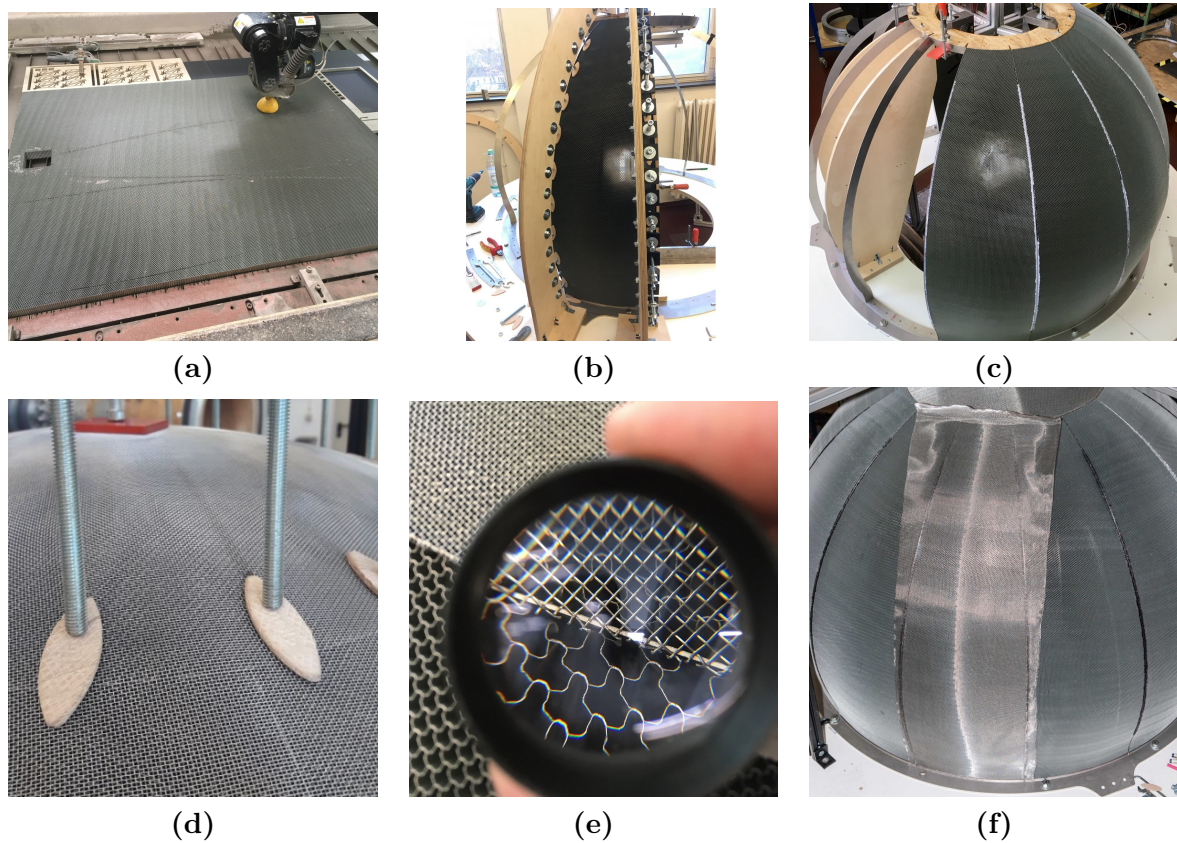


Figure 4.5.: Chronology of the ICD construction: (a): Honeycomb segments were water jet cut. (b): Segment held in place with the help of a mold and screws. (c): Few honeycomb segments glued together. (d): Wire mesh placed and held in position ready for spot-welding. (e): Quality inspection; wire-mesh already spot-welded on one side and excess mesh trimmed off. (f): Full segment covered with wire-mesh, spot-welded, ready to be trimmed.

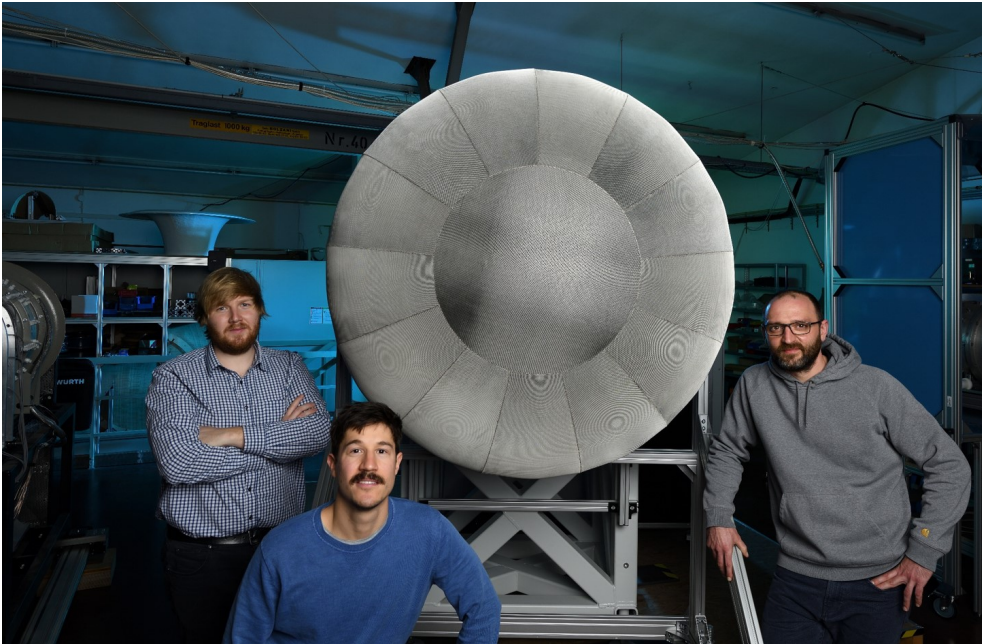


Figure 4.6.: Front view of the new ICD alongside with DLR colleagues. From left to right: Angelo Rudolphi, Luciano Caldas, Sebastian Kruck.

4.2. Aerodynamic instrumentation

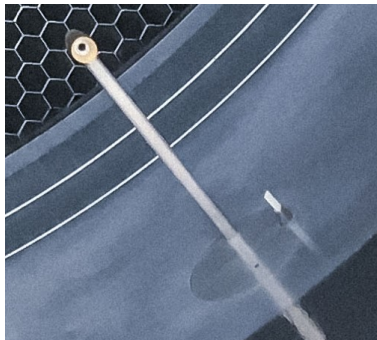
4.2.1. Essential aerodynamic instrumentation for the adjustment of fan operating point

Every time the test rig runs, the fan operating point has to be measured and adjusted to the target point. To do so, a few aerodynamic parameters have to be measured. These are:

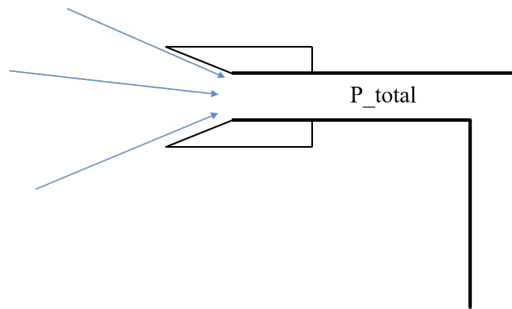
- *Meteorological parameters:* A weather station located inside the laboratory close to the test rig is used to measure the ambient pressure, room temperature, and air humidity. With these values, the air sound speed, air density, and air kinematic viscosity are calculated.
- *Static pressure:* Static pressure at measurement planes E0 and E6 (compare Fig. 4.2) are measured against the ambient pressure. The former combined with a pitot tube (explained next) allows the determination of the inlet flow speed, mass flow, and inlet pressure drop. One exemplary static pressure port can be seen in Fig. 4.7a. The tiny hole on the wall upstream of the pitot tube. The static pressure measured at the E6 plane permits the computation of the flow total pressure rise and therefore the fan pressure ratio. At each measurement plane, in total four pressure ports spaced by 90° are used to measure the static pressure. They are connected together

with the help of a tube. This produces an average static pressure over the four holes, reducing errors in the measurement.

- *Pitot tube:* A thin pitot tube is installed at the plane E0 approx. 50 mm away from the duct wall. A cone is installed on its inlet to allow the measurement of wider inflow angles, similar to a Kiel probe as shown in Fig. 4.7. By measuring the differential pressure with the help of static pressure ports on the wall, the precise determination of the inlet flow speed is possible.



(a) Inlet pitot tube. The temperature sensor is also seen on the right-hand side. The tiny hole seen upstream of the pitot tube refers to the static pressure port.



(b) Sketch of the cone used with the pitot tube to allow the measurement of broader inflow angles, similar to a Kiel probe.

Figure 4.7.: Pitot tube, static pressure port, and temperature probe installed at plane E0.

- *Total temperature at the inlet:* A PT100 temperature sensor is placed near the pitot tube in order to determine the temperature at the duct inlet. This temperature is used combined with the ambient temperature to characterize the inflow. The temperature sensor can be seen in Fig. 4.7a on the right-hand side of the pitot tube.

4.2.2. Pressure rakes

With the aim of evaluating the radial velocity profile of the inlet flow, pressure rakes were designed and constructed. Both the baseline and distorted inflow configurations were characterized by pressure rakes. In total, two rakes comprising 8 channels each were used: one shorter rake with higher resolution in the region close to the duct wall, and a second longer rake with roughly equally spaced ports. A photograph of both pressure rakes is shown on the bottom right-hand side of Fig. 4.8. The port positions for the short rake are (2, 6, 10, 15, 23, 45, 90, 135) mm away from the duct wall. For the longer rake they are found (15, 30, 50, 70, 90, 110, 135, 170) mm away from the duct wall.



Figure 4.8.: Photograph of the CRAFT inlet channel. View of the hot-wire measurement setup. Pressure rakes are shown on the bottom of the duct, whereas the two hot-wire probes on the top. The probes were mounted at plane E3.

The static pressure ports are located on the wall of the duct, at the same axial position as the pressure rakes, at 4 angular positions 90° apart and connected together with the help of a tube. The resulting differential pressure (total pressure minus static pressure = dynamic pressure, $p_t - p_s = p_d$) was measured by a multi-channel pressure scanner. The differential pressure: Static pressure at this measurement plane minus the ambient pressure ($p_s - p_{amb}$) was also captured. This allows retrieving all pressure information at the given measurement plane.

4.2.3. Hot-wire instrumentation

Two hot-wire probes were used in this test setup, each measuring two velocity components: one (u,v) probe, able to measure the axial and radial components and one (u,w) probe, able to measure the axial and circumferential components. Each probe is composed of two tungsten wire sensors of about 2.8 mm in length and $9\ \mu\text{m}$ in diameter to ensure great durability. Further details can be found in the references: Tapken et al. (2021b), Tapken et al. (2021a) and Meyer et al. (2019). Each probe was mounted in a radial traverse allowing the probe to travel up to 300 mm inside the channel. The probes were mounted 17° apart (equivalent to the stator vanes angular spacing) at the plane E3 as depicted in Fig. 4.8, on the top. For each measurement position, 10 seconds of data were acquired, sampled at $f_s = 192\ \text{kHz}$. For this study, hot-wire measurements were performed at plane E1 as a first assessment of the ICD performance, at plane E3 to generally characterize the inflow with and without inflow distortion, and at plane E5 to characterize the flow field and the rotor wakes.

4.3. Acoustic instrumentation

The CRAFT acoustic instrumentation in the inlet is composed of two arrays of sensors as shown in Fig. 4.9. The axial array AX1 consists of 30 equally spaced microphones placed 23.75 mm apart from each other. The farthest microphone is found at 1108 mm upstream of the rotor leading edge, whereas the nearest at 420 mm, relative to the same reference point. This array segment can be traversed in the azimuthal direction to spatially sample the sound field on the lateral surface of the duct. The ring array R1.2 consists of 59 equally spaced microphones and is mounted 300 mm upstream of the rotor leading edge. Both arrays are designed for in-duct sound fields with frequencies up to 6 kHz.

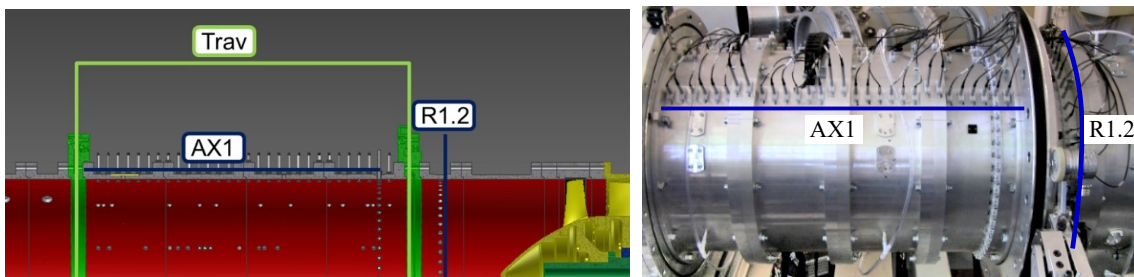


Figure 4.9.: Illustration and photograph of the axial and azimuthal microphone arrays mounted in the inlet of the CRAFT test rig.

More info about the array design is found in Tapken et al. (2021b) and Tapken et al. (2021a). The arrays were optimized for mode analysis techniques such as azimuthal mode decomposition, radial mode decomposition, and axial wave number decomposition. This arrangement enables the full decomposition of all azimuthal modes in the range up to $m = \pm 29$.

Condenser microphones of 6.35 mm (1/4 inch) diameter and 70 kHz bandwidth response are used. The microphones are flush mounted with the duct wall to avoid disturbances of the flow and the sound field. Acoustic data from all the microphones were acquired simultaneously at $f_s = 65.536 \text{ kHz}$ and the acquisition time was chosen to be 30 seconds. For measurements with traverse microphones, the same sampling frequency and acquisition time was used for each traverse position.

5. Baseline characterization of the CRAFT test rig.

WITH the aim of characterizing the baseline configuration of the CRAFT fan rig in the course of the rig commissioning, extensive measurements and analysis were performed. They are described in this chapter. Both the aerodynamic and aeroacoustic assessment are reported. The analyses are focused on the impact of the inflow control device (ICD) both on the flow aerodynamics as well as on the fan noise generation. These analyses are important not only to characterize the baseline configuration of the CRAFT fan rig (no inflow distortion), but also to assess the impact of the new ICD and its mechanisms on turbulence reduction and/or generation. For all analyses three different configurations were considered:

- Without ICD,
- with ICD, and
- with ICD and an additional honeycomb at plane E1.

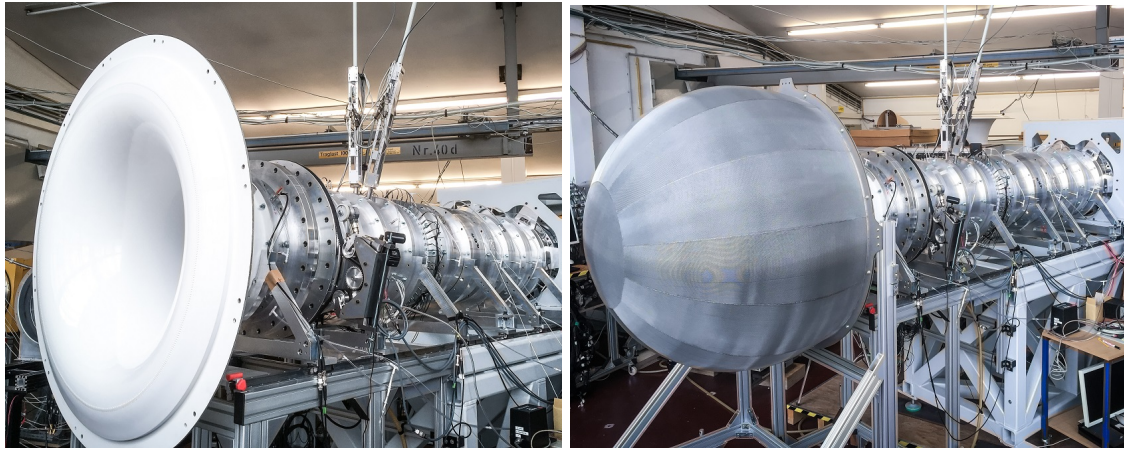
Photographs of the test rig with these three configurations are shown in Fig. 5.1.

The additional honeycomb was installed at the plane E1, as described in Chapter 4 and depicted in Fig. 4.2. It serves as flow straightener and as a support for e.g. distortion screens, as will be reported in Chapter 6.

5.1. Fan performance map

The fan performance map was assessed for the baseline configuration with ICD installed at the rig inlet. Three fan speeds were tested at the following corrected speeds: 4500 RPM (100% of the maximum speed), 3375 RPM (75%), and 2250 RPM (50%). The throttle position was adjusted from completely open exhaust and axially traversed towards the duct. The throttle was traversed in small steps and the fan operating point was measured for each throttle position. This procedure was repeated until the fan stalled, which for this rotor stator set typically occurs at a flow coefficient of approx. $\phi = 0.26$.

Fig. 5.2 shows the evaluated CRAFT fan performance map. Both fan speed and mass flow are corrected to the standard sea levels ($15^\circ C$ and $101.325 kPa$). The top x-axis displays the equivalent inlet axial Mach number. The corresponding fan speed of each curve is displayed near the curves. The blue dots refer to the flow coefficients, where typically aerodynamic and/or acoustic measurements are performed: $\phi = \{0.26; 0.28; 0.30; 0.33; 0.40\}$.



(a) Test rig without ICD.

(b) Test rig with ICD installed.



(c) Additional honeycomb installed at plane E1.

Figure 5.1.: Photographs of the CRAFT test rig configured for hot-wire measurement. The two traverse mechanisms mounted 17° apart at the plane E3 are seen downstream the inlet.

5.2. Inlet aerodynamics

5.2.1. Velocity flow profile at plane E1

The mean inflow velocity profile was measured with two total pressure rakes installed at the plane E1 together with the static pressure measured on the duct wall at the same plane. The rakes were traversed in the circumferential direction in order to assess circumferential homogeneity. Two fan speeds $\eta_c = \{2700; 4500\}$ RPM and four flow coefficients $\phi = \{0.28; 0.30; 0.33; 0.40\}$ were measured.

For each fan operation point, four angular positions were measured. One exception holds for the flow coefficient of $\phi = 0.33$, which was measured with a higher resolution of 12 angular positions. Results are shown in Fig. 5.3. The velocity profile for all tested fan

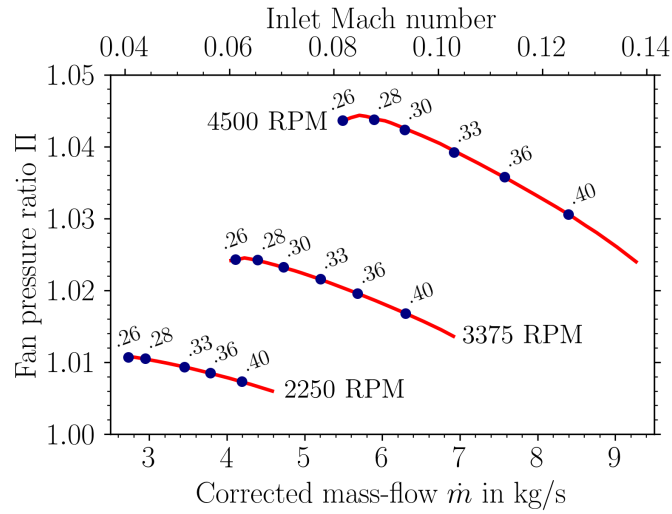


Figure 5.2.: CRAFT fan performance map for the baseline configuration with ICD. The blue dots refer to the flow coefficients (assigned along each point), where typically aerodynamic and/or acoustic measurements are performed.

operating points and flow coefficient revealed very similar shape. It should be noted that the data from every fan operating point are not averaged over the different circumferential positions. Instead, every curve corresponding to an angular position is plotted on top of each other. The fact that all curves overlap each other well is a hint of flow homogeneity over the circumference. At this measurement plane, the boundary layer is approx. 10 mm thick.

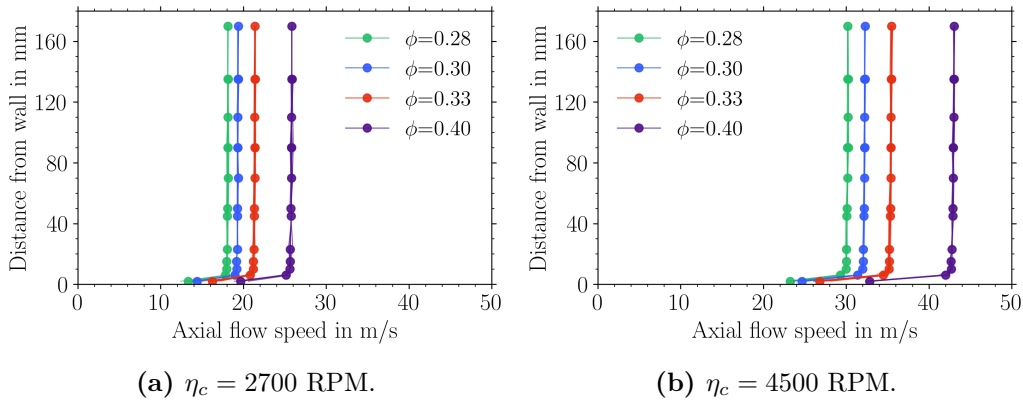


Figure 5.3.: Radial profile of the mean velocity measured at the plane E1 at several circumferential positions. Configuration with ICD. Two fan speeds and four fan flow coefficients are plotted.

5.2.2. Turbulence intensity analysis at plane E1 - Spatial homogeneity assessment

As discussed in Chapter 2, an important aspect for fan noise investigations is not only to establish low inflow turbulence levels, but also a homogeneous distribution over the duct

cross-section. The aim of this experiment was to assess the homogeneity of the turbulence intensity throughout the inlet duct cross-section. For that, hot-wire measurements were performed with a single (u,v) probe installed at plane E1. The (u,v) probe measures the axial and radial velocity components.

The hot-wire probe was traversed in radial and circumferential direction. This generated a regular mesh consisting of twelve circumferential by four radial positions. Due to space constraints to traverse the hot-wire probe completely 360° , no radial traverse was used. Instead, the different radial positions of the probe was manually adjusted at the four positions. The distribution of the turbulence intensity of the axial velocity component is depicted for the case without ICD in Fig. 5.4a and with ICD in Fig. 5.4b. Both refer to the fan operating point $\eta_c = 4500$ RPM, $\phi = 0.40$ and $\bar{U} \approx 43$ m/s. It should be noted that the red circle in these figures highlights the impact of the pitot tube (installed at plane E0, used to determine the flow speed in the inlet, compare Fig. 5.4c, as discussed in Section 4) on the turbulence field captured by the hot-wire probe. The comparison of both plots (figs. 5.4a and 5.4b) suggests a significant turbulence levels reduction and homogeneous distribution of the turbulence intensity when the ICD is installed on the rig's inlet. As a first try to detect any potential impact of the ICD ribs, the hot-wire measurements were performed with higher resolution (smaller angular step) at two radial positions, but no impact of the ribs in the flow could be observed. A dedicated study on that topic is reported in Section 5.2.8.

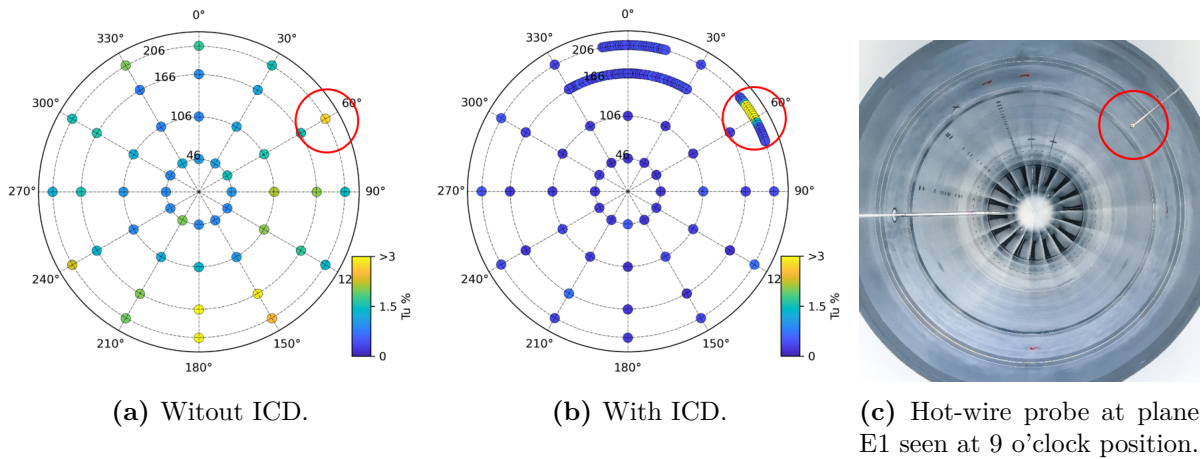


Figure 5.4.: Turbulence intensity plots of the axial velocity components measured at the plane E1. The hot-wire probe was traversed in radial and circumferential direction. The red circle shows the wake measured originated from the pitot tube upstream the hot-wire probe. Fan operating point: $\eta_c = 4500$ RPM, $\phi = 0.40$, and $\bar{U} \approx 43$ m/s.

5.2.3. Radial profile of the turbulence intensity and integral length scale at plane E3

A thorough analysis was performed with two hot-wire probes installed at plane E3. The two probes were installed 17° apart. In total, 25 radial positions were measured with the

help of a radial traverse at positions ranging from 1 mm to 180 mm relative to the duct wall. In order to estimate the turbulence intensity of each signal, its variance was estimated using Eq. 3.3.2, that means by integrating its turbulence spectrum. Each spectrum was obtained using the Welch method, utilizing the Hann window with 50% data block overlap. The block length selected generated an equivalent frequency resolution of $\Delta f = 11.7 \text{ Hz}$. The ILS was estimated by applying the low-frequency disturbance removal technique described in Section 3.1.1. The HIT assumption was taken to allow the use of eqs. 3.2.1 and 3.2.2 for the estimation of the ILS. Fig. 5.5 portrays the results for the fan operating point $\eta_c = 4500$ RPM, $\phi = 0.40$, and $\bar{U} \approx 43 \text{ m/s}$. In this figure, the top row refers to the turbulence intensity profiles, whereas the bottom row to the turbulence integral length scale profiles. The left-hand plots refer to the axial velocity component, whereas the right-hand plots to the radial velocity component. The following three test cases are analyzed: without ICD, with ICD, and with ICD and the additional honeycomb at plane E1.

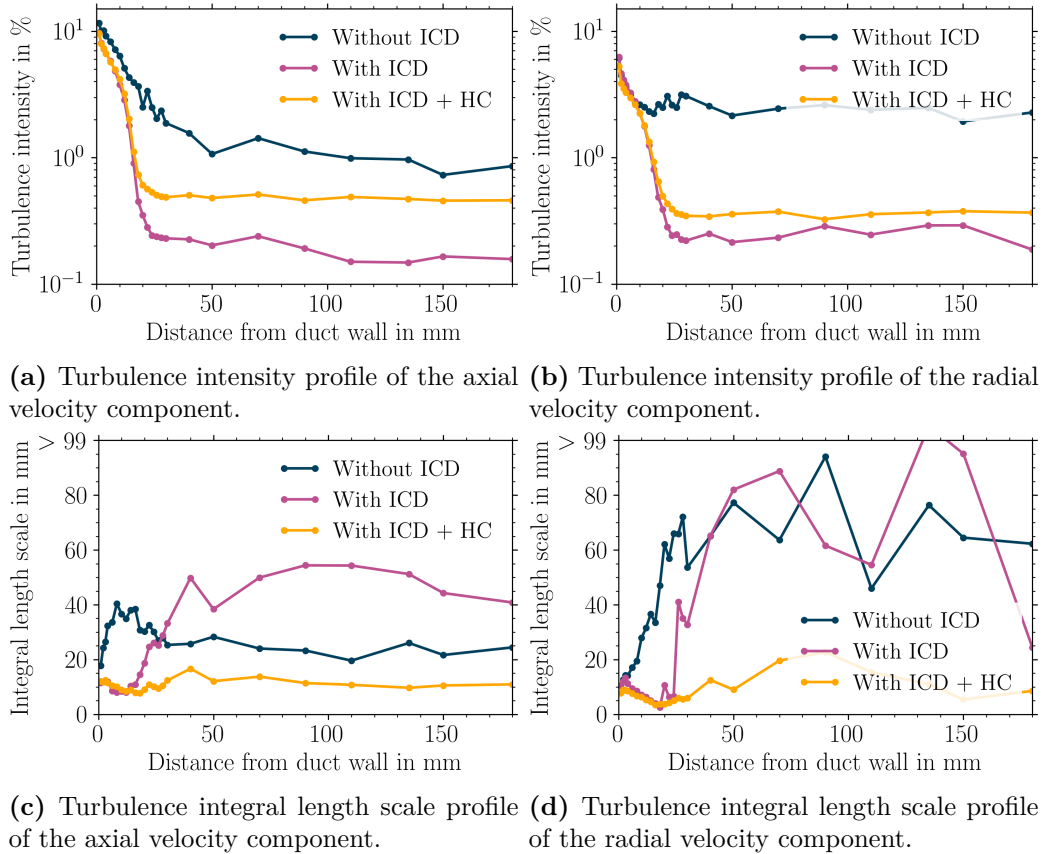


Figure 5.5.: Turbulence analysis along several radial positions. Measurements performed at plane E3. Fan operating point: $\eta_c = 4500$ RPM, $\phi = 0.40$, and $\bar{U} \approx 43 \text{ m/s}$.

When plotted in logarithmic scale, the turbulence intensity profile inside the boundary layer (up to approx. 25 mm away from the wall) seems to have two decay regimes. A less steep gradient is seen for small wall distances (from 0 mm to approx. 10 mm away from the wall), followed by a steeper slope for greater distances (from 10 mm to 20 mm, approx.). This is observed both for axial and radial velocity components. The turbulence

intensity profiles are smooth for the two test cases: with ICD (purple curve) and with ICD plus additional honeycomb (yellow curve). The presence of the honeycomb at plane E1 virtually does not impact the turbulent boundary layer profile. The turbulence levels with the additional honeycomb are slightly higher compared to the case without it. For the turbulence intensity profile outside the boundary layer, the additional honeycomb increased the turbulence intensity of the axial velocity component from approx. 0.15% to 0.5%. For the radial velocity component, this increase is less significant: from approx. 0.25% to 0.4%. For the case without ICD, the radial profile of the turbulence intensity is not only significantly higher at all measured points and for both velocity components, but its radial profile varies strongly from measured point to point. A turbulence reduction factor of approx. 10 was observed comparing the two cases with ICD with the case without it.

The turbulence integral length scale distribution has similar characteristics for both cases with ICD installed for points inside the turbulent boundary layer. For the case with ICD and honeycomb a small “bump” becomes visible for the radial velocity component at a distance of approx. 20 mm away from the duct wall (bottom-right plot in Fig. 5.5), characterizing a local increase in the integral length scale, followed by a reduction. This small bump seems to determine the transition from the wall turbulent boundary layer to the free-stream flow. The origin of this phenomenon is unknown. From this transition point, the properties of the integral length scale for the two cases with ICD start to diverge apart.

In the case with ICD and without honeycomb (purple curve in Fig. 5.5), the integral length scale profile raises rapidly for positions outside the boundary layer. This is observed for both velocity components. In order to better understand the physics behind that, a single point measured at 70 mm away from the duct wall was selected to be analyzed deeper. This is a measurement point outside of the wall boundary layer. Fig. 5.6 shows the spectra of both axial and radial velocity components for the three test cases. The turbulence intensity and integral length scale of each test configuration are assigned in the labels. The ILS were estimated under the HIT assumption and by averaging the turbulence spectra in the frequency band of $f < 100 \text{ Hz}$.

The spectra of both cases with ICD installed follow a similar shape for $f \lesssim 200 \text{ Hz}$. Above this frequency, the purple curve starts falling, whereas the orange curve follows a rough flat shape with a slightly negative slope. The difference between the two spectra is essentially the power content in the frequency band of $200 \text{ Hz} \lesssim f \lesssim 20 \text{ kHz}$. As discussed in Chapter 2, the integral length scale is associated to the most energetic eddies in a turbulent flow field (Hinze and B. J. Clark (1975) and Pope (2000)). For this particular test case, when the honeycomb is installed at plane E1 (orange curve in Fig. 5.6), besides breaking down big turbulence structures into smaller ones, additional turbulence is generated by

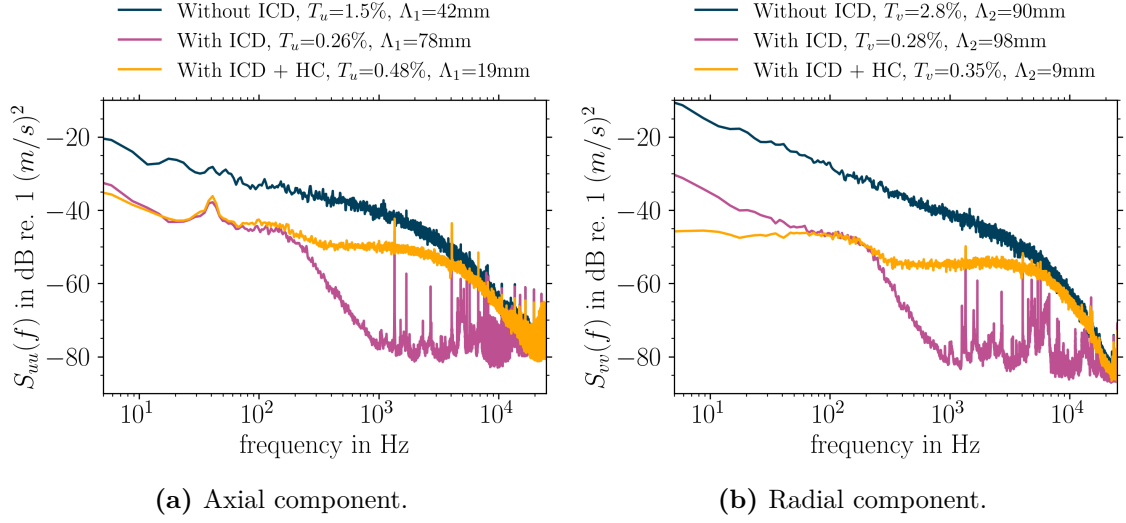


Figure 5.6.: PSD of the unsteady velocity data of the three configurations measured at a distance of 70 mm from the duct wall in the plane E3. Fan operating point: $\eta_c = 4500$ RPM, $\phi = 0.40$, and $\bar{U} \approx 43$ m/s.

the honeycomb itself. This additional power injected into the flow feed smaller eddies (at higher frequencies), making them the most energetic eddies in this test case.

For the case without honeycomb at E1 (purple curve), the considerable lower energy content of the smaller eddies ($f \gtrsim 200$ Hz) makes the big eddies (at lower frequencies) the dominant eddies in this flow field, even though their energy content is roughly the same compared to the case with the honeycomb at E1. Another way to look at this problem is through the equation used to compute the integral length scale under HIT hypothesis, as introduced in Chapter 2:

$$\Lambda_1 = \left[\frac{S_{uu}(f)U_0}{4u^2} \right]_{f \rightarrow 0}. \quad (2.3.11 \text{ revisited})$$

Looking again at Fig. 5.6a and comparing the orange and purple spectra, they both have similar values for $S_{uu}(f < 200 \text{ Hz})$, and comparable values for $S_{vv}(f < 200 \text{ Hz})$ in Fig. 5.6b. As the measurements were done at the same fan operating point, the axial flow speed U_0 is the same for both cases. A lower variance of the signal $u(t)$ described by $\overline{u^2}$ (lower turbulence levels) results in higher integral length scale. This explains why higher values of integral length scale is observed for the case ICD only when compared to the case ICD and additional honeycomb, when the low-frequency band of the turbulence PSD are similar.

Another possible reason is the poor performance of the ILS estimator under the circumstance of very low-turbulence levels. A hypothesis is that the HIT assumption no longer holds in this case, and therefore the ILS estimator might not be suitable anymore, what could lead to non representative ILS results. These hypotheses are made based on the

turbulence field measured and interpreted from the PSD of the unsteady velocity components. It is observed from several measurements that the turbulence PSD does not drop lower than $-80 \sim -90$ dB, which is believed to be approx. the noise floor of the hot-wire anemometry system. Inspecting Fig. 5.6 again, we see that the purple curve reaches this level already at $f \simeq 1$ kHz confirming that the measurable turbulent power in this case is found within the frequency band $0 \text{ Hz} < f < 1 \text{ kHz}$.

5.2.4. Deeper analysis of the low-frequency turbulence mechanisms

This section aims on shedding some light on the mechanisms behind the low-frequency turbulent power found in the measured data. The same data set as used in Fig. 5.6 was selected: measurement point at a distance of 70 mm from the duct wall, measurement plane E3. The radial velocity component was selected, as this component seems to be more sensitive to disturbances in the inflow.

The first analysis was obtained by estimating the variance of each signal by integrating its respective PSD following Eq. 3.3.2. The turbulence intensity was therefore obtained based on this variance. The key in this analysis was to vary the data block length (ensemble length), when processing the PSD using the Welch method. The block length was varied from the size of the entire data set $L=1.92 \times 10^6$ samples resulting in a frequency resolution of 0.1 Hz (10 s block size) up to $L = 1024$ samples, which produces a frequency resolution of 188 Hz (5.3 ms block size). When L is equal to the data set length, the use of Eq. 3.3.2 is equivalent to Eq. 3.3.1.

If the process is classified as stationary, the estimated variance does not depend on the data block length used to determine the PSD (Percival and Walden (1993), up from some certain minimum size). Fig. 5.7a shows the result of processing raw signals from the three test cases. For the case without ICD, the estimated turbulence intensity shows a fairly linear dependence (when both axes are in logarithmic scale, as in this plot) to the frequency resolution. For the case with ICD, a similar behaviour was found for $\Delta f > 10 \text{ Hz}$. When the additional honeycomb was installed, virtually no dependence was found on the data block length, indicating a good agreement of this signal with a stationary process.

Fig. 5.7b shows a similar analysis, but now after filtering each signal with a high-pass filter. The signals were filtered using a zero-phase filter by processing the data in both the forward and reverse direction. This is commonly named as “filtfilt”. A low-pass Butterworth digital filter of order 3 was designed with cut-off frequency f_c set to 150 Hz . The high-pass filtered content of each signal was obtained by subtracting the raw signal from the low-pass filtered one. This approach is in this case allowed due to the use of a zero-phase filter. We observe roughly no dependence of the estimated turbulence intensity on the data block length for each high-pass filtered signal. This suggests that the

low-frequency band $f < 150 \text{ Hz}$ of the signals are responsible for their non-stationarity behaviour.

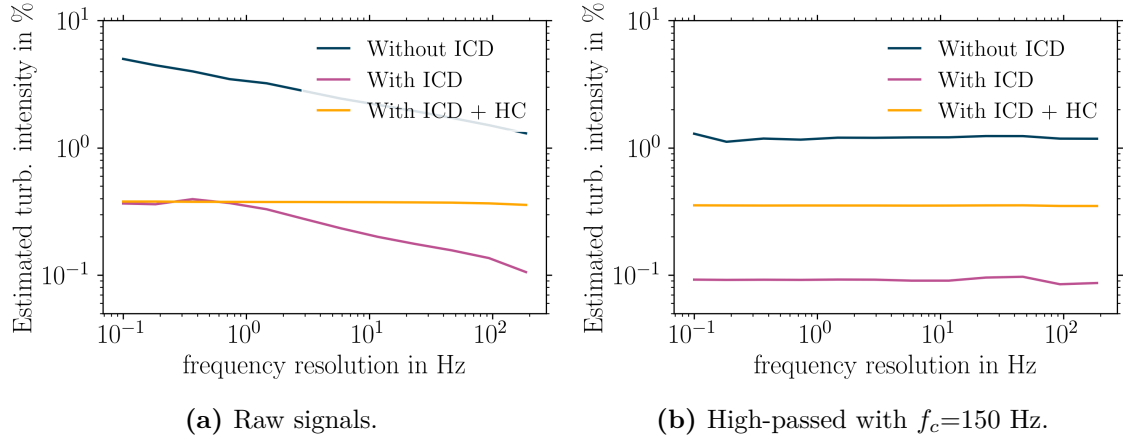


Figure 5.7.: Dependency analysis of the signal variance estimator against frequency resolution (or data block length) evaluated for a 10 seconds signal.

A second analysis was conducted by calculating the histogram of the three signal components: raw signal, low-pass filtered, and high-pass filtered. Each histogram was normalized by its total area. Results are shown in Fig. 5.8. The Fisher-Pearson coefficient of skewness (Kokoska and Zwillinger (2000)) g_1 of each curve is tabulated inside the label box. When the histogram is symmetric, e.g. a Gaussian curve (or bell curve), this coefficient is equal to zero.

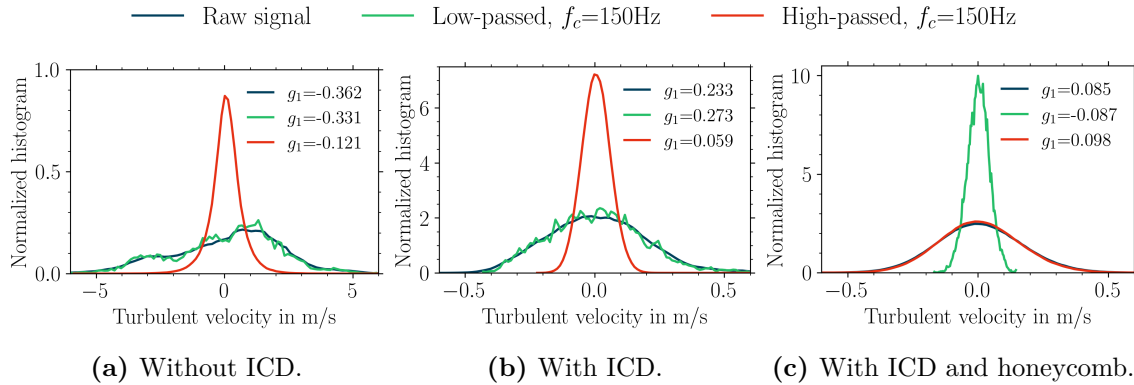


Figure 5.8.: Histogram of the radial velocity component for each frequency band and test configuration. The coefficient of skewness g_1 respective of each curve is indicated in the label box.

The results obtained for the test case without ICD is shown in Fig. 5.8a. The dark blue curve refers to the raw data (no filtering), green to the low-pass filtered, and red to the high-pass filtered data. The shape of the normalized histogram of the raw signal and the low-pass filtered are fairly similar. They are not symmetric as indicated by the skewness coefficient, nor similar to a Gaussian curve. The presence of the skewness (skewed left in this case) in these two histograms confirms the hypothesis of non-stationarity of the low-

frequency band of this signal. On the other hand, the high-pass filtered signal's histogram seems to be symmetric and similar to a Bell-curve.

In Fig. 5.8b, the results for the test case with ICD installed are quite different compared to the previous one. In both figs. 5.8a and 5.8b, the dark blue curves roughly follow the shape of the green ones. That means the power found in the frequency band $f < 150 \text{ Hz}$ is dominant in both data set. For the case with ICD, however, its width is narrower by a factor of approx. 10, and the skewness coefficient is also closer to zero (although not exactly zero). By inspecting the green and dark blue curves of Fig. 5.8b, it is noted that both histograms are closer to the shape of a Gaussian curve, than the ones in Fig. 5.8a.

The presence of skewness in the raw signals of both test cases with and without ICD agrees with the observed dependence of the estimated variance from the turbulent PSD with the data block size shown in Fig. 5.7. The non-stationarity of these signals has as consequence a variable variance of data ensemble selected from the data set. Furthermore, the ensemble variance is also dependent on its length. The problem faced by this observed non-stationarity impacts directly the estimation of turbulence parameters such as: turbulence intensity, turbulent kinetic energy, and the integral length scale. The dependency of the data block size leads to extra uncertainty and potential bias on the estimation of all these parameters.

When the additional honeycomb was installed (cf. Fig. 5.8c), an interesting behaviour is observed: The green histogram referred to the low-frequency band is now narrower than the raw signal's histogram. It is noticed on the one hand that the amplitude of the low-frequency fluctuations has indeed lower amplitude: roughly $\pm 0.1 \text{ m/s}$ comparing to approx. $\pm 0.5 \text{ m/s}$ for the case with ICD only. On the other hand, the high-frequency band has its amplitude increase for the case with additional honeycomb. By contrasting the raw signal of both cases with ICD (with and without additional honeycomb), we observe a similar range of amplitude for both signals, suggesting similar power levels. However, the shapes of the curves are slightly different. Without the additional honeycomb, a higher skewness coefficient is observed, which is due to the higher power content in the low-frequency band of this signal.

The honeycomb induces an additional pressure drop in the inlet of the rig. Indeed for the high speed test case with $\bar{U} = 43 \text{ m/s}$ the pressure drop due to the ICD lies approx. in the range of 10 to 20 Pa. For the same flow speed, the honeycomb induces a pressure drop in the order of a few hundred Pascals. It is believed that this additional pressure drop helps further eliminating the low-frequency content of the turbulence spectrum, similar again to a high-pass filter.

If a comparison to an electronic circuit may be drawn, it would be similar to the one depicted in Fig. 5.9. In this schematic, the pressure rise induced by the fan ΔP works

highlight is: it is not always possible to fully characterize statistically the measured data in terms of mean and variance, as in the case when the histogram of the measured data has the form of a Gaussian curve. Equivalently, it is often hard (perhaps impossible) to characterize a given turbulence field only in terms of turbulence intensity, integral length scale, and mean flow speed. We observed that even estimating the turbulence intensity can be problematic. The estimation of the integral length scale also becomes faulty due to the uncertainty in both estimating the turbulence intensity and the power in the low-frequency band of the spectrum.

5.2.5. Turbulence spectral assessment at plane E3

With the aim of inspecting the turbulence spectral shape of the turbulence field measured at plane E3, five radial measurement positions were selected from the data set introduced in Section 5.2.3. Fig. 5.10 depicts the results for each test configuration and the three velocity components. Two radial positions inside the boundary layer (1 mm and 8 mm, purple and red, respectively), one in the extremities of the boundary layer at 14 mm (blue), and two outside of it (28 mm and 110 mm, green and yellow, respectively) were selected. The fan operating point remains the same as previously.

For the majority of the plots, the initial decay of the turbulence spectrum follows approx. a typical $-5/3$ von Kármán slope. For $f \gtrsim 5 \text{ kHz}$ however, a steeper slope of the spectrum is observed in the experimental data. The origin of this phenomenon is not fully clear. One possible reason is the band-width limit of the hot-wire technique due to the wire diameter used ($9 \mu\text{m}$), as also reported by Caldas et al. (2021b). Another hypothesis is the beginning of the dissipation range of the turbulence at this frequency band, as reported by Santos et al. (2021).

For the test case without ICD, besides the expected higher turbulence intensity levels, it is worth mentioning the high power levels concentrated at the low-frequency band $f \lesssim 100 \text{ Hz}$ of all spectra and three velocity components. This is clearer observed when comparing this test case with the other two with ICD. This phenomena (extensively discussed in the last sections) is more pronounced for the transverse (radial and circumferential) velocity components. The spectral shape in the frequency band of $f \lesssim 1 \text{ kHz}$ is similar to a typical $1/f$ noise signature (Keshner (1982)). Looking at the spectra of the two measurement points inside the boundary layer (purple and red), the impact of the ICD is mostly noticed at this frequency band.

For the test case with the ICD, a noticeable impact on the turbulence spectral shape of the measurement points outside the boundary layer is observed. By comparing the plots on the left-hand side against the middle ones, the green and yellow curves reveal a remarkable power reduction at the low-frequency band of each PSD ($f \lesssim 100 \text{ Hz}$) for all three velocity components. This effect is more pronounced for the two transverse

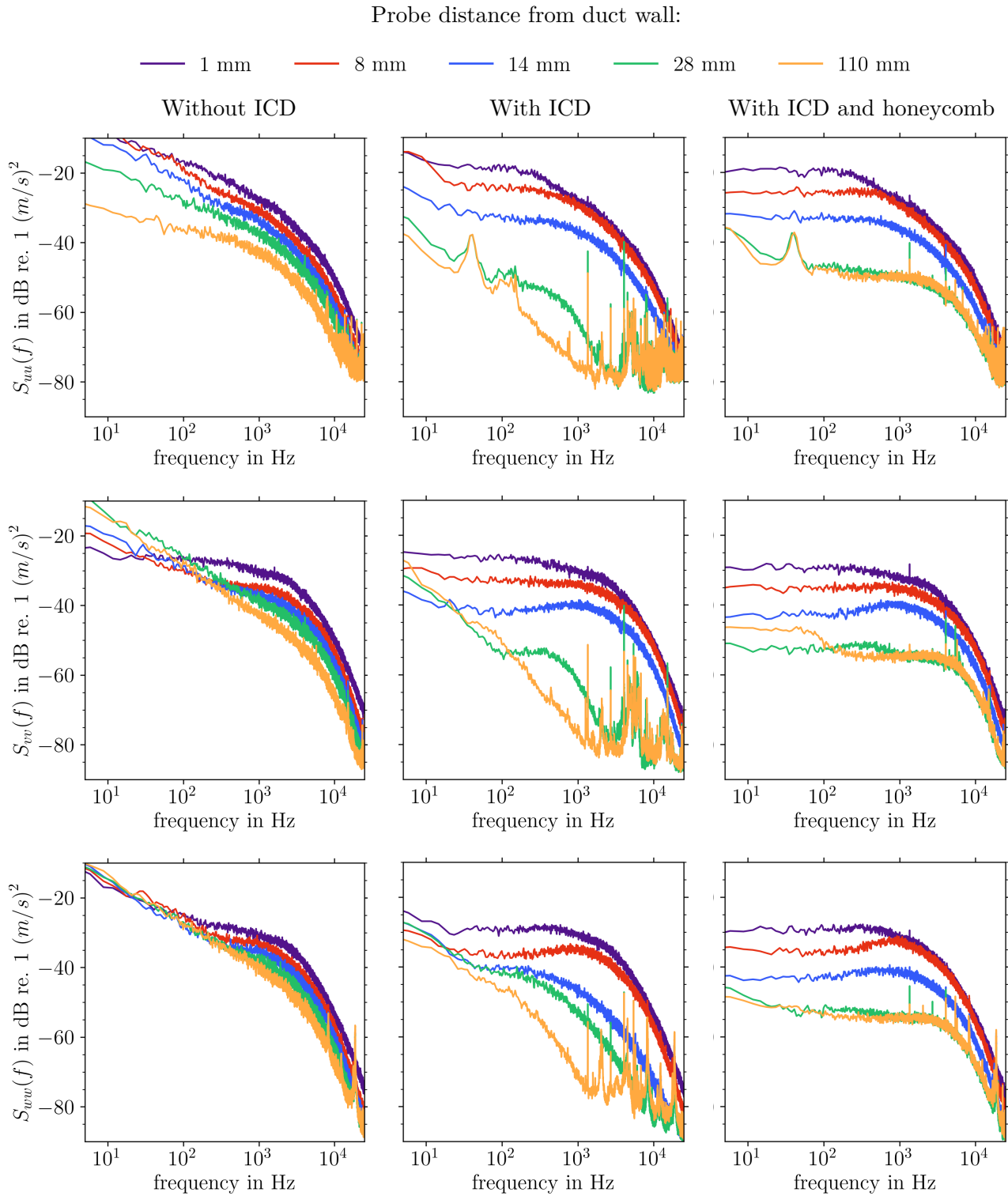


Figure 5.10.: Turbulence PSD of five different probe positions inside the channel. Three velocity components: Streamwise (top plots); radial (mid plots); circumferential (bottom plots) for the three test cases are shown. Fan operating point: $\eta_c = 4500$ RPM, $\phi = 0.40$, $\bar{U} \approx 43$ m/s.

components. The $1/f$ spectral shape in this frequency band is indeed associated not only with large length scales and turbulence ingestion, but especially with the operation condition in an indoor laboratory. The flow re-circulation inside the laboratory and the re-ingestion of turbulent flow coming from the exhaust set an unfavourable environment for low-turbulence ingestion experiments. Thanks to the ICD, not only the turbulence ingestion is remarkably reduced by breaking down big eddies and homogenizing the flow, but also the small pressure drop established by the ICD acts as a high-pass filter, reducing low-frequency oscillations from the inflow.

When the honeycomb is installed at the plane E1, a clear difference in all velocity component spectra is observed. As the honeycomb works not only as a flow straightener, but also as a turbulence generator Caldas et al. (2019b), a different turbulence spectral shape is observed for this case. Indeed, the measured velocity turbulent PSD are closer to the von Kármán model.

5.2.6. Radial profile of the Reynolds number based on the dissipation length scale (Taylor microscale) at plane E3

The Reynolds number based on the dissipation microscale was computed for each measurement point with the help of Eq. 2.3.17. Here, the dissipation microscale was estimated by Eq. 2.3.14 under the HIT assumption. Fig. 5.11 portrays the results for the three test cases: without ICD, with ICD, and with ICD and additional honeycomb. The axial and radial velocity components are investigated.

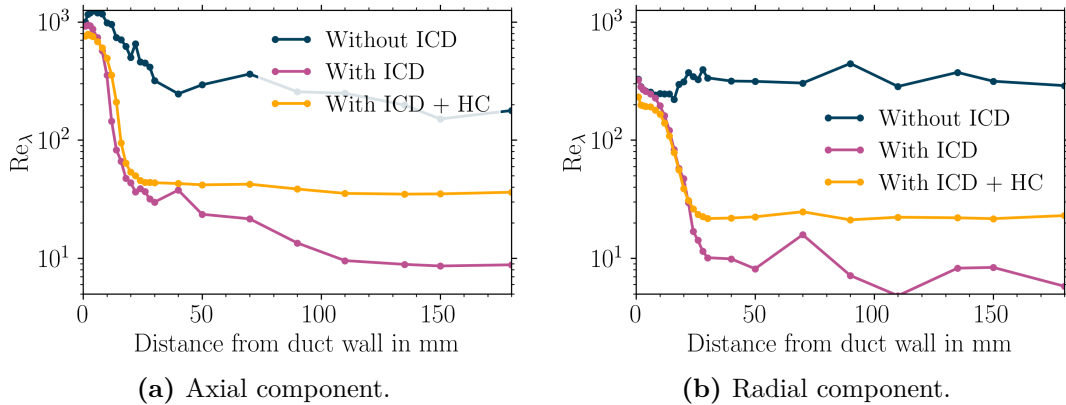


Figure 5.11.: Turbulence Reynolds number based on the dissipation length scale λ . Fan operating point: $\eta_c = 4500$ RPM, $\phi = 0.40$, and $\bar{U} \approx 43$ m/s.

It can be observed that without ICD (blue curves in Fig. 5.11) the Reynolds number for both velocity components are relatively high: $Re \gtrsim 200$. When the ICD is installed (purple and yellow curves in Fig. 5.11) a noticeable change in the shape of the turbulence Reynolds number inside the wall boundary layer is observed. For small distances to the duct wall ($\lesssim 10$ mm), the additional honeycomb (yellow curve in Fig. 5.11) reduced slightly the

turbulence Reynolds number when compared to the case with ICD only (purple curve in Fig. 5.11). This result complements the turbulence intensity profile shown in Fig. 5.5. Based only on that result, the boundary layer turbulence properties seem to be unaltered by the additional honeycomb.

Looking at the flow outside the wall boundary layer, the additional honeycomb increased the turbulence Reynolds number from roughly 10 to 40 (purple and yellow curve in Fig. 5.11). It is worth mentioning that these numbers are very low, characteristic for laminar flows (Pope (2000)). Important for acoustic measurements, as mentioned in Chapter 2, is a homogeneous inflow profile both in terms of mean flow speed profile and turbulence properties. In this case, we observe a fairly constant profile along the radius for the case with additional honeycomb (yellow curve in Fig. 5.11), what is desired for fan noise investigations.

5.2.7. Turbulence isotropy assessment at plane E3

Typically found in the literature, a rough isotropy assessment can be done by analyzing the turbulence intensity and integral length scale ratio between the longitudinal and transverse velocity components. This assessment was done for the radial and axial velocity components for the three test cases: without ICD, with ICD, and with ICD and additional honeycomb. Results are found in Fig. 5.12.

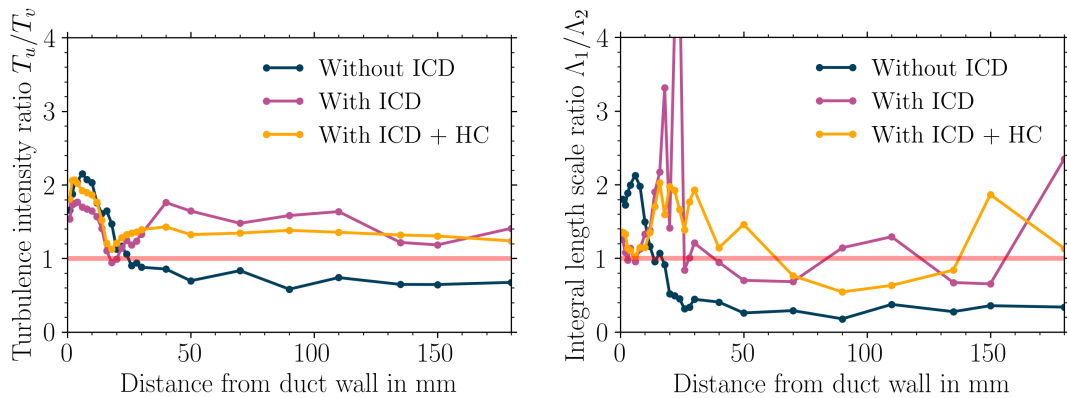


Figure 5.12.: Isotropy assessment by analyzing the ratio of the turbulence intensity and integral length scale of the radial and axial velocity components. The red line indicates the respective ratio in case of isotropy. Fan operating point: $\eta_c = 4500$ RPM, $\phi = 0.40$, and $\bar{U} \approx 43$ m/s.

The turbulence intensity ratio shows an interesting outcome. For all three test configurations and inside the wall boundary layer, the axial component has always more power than the radial one. This ratio reaches approx. a factor of 2 for some radial positions. The turbulence intensity ratio profile inside the boundary layer shows a consistent decaying behaviour for all three test cases reaching the value of approx. 1 at the boundary layer vicinity at approx. 20 mm. When the ICD is installed (purple and yellow curves

in Fig. 5.12) the curves start raising again for positions further away from the boundary layer. The ratio for both cases lies at roughly 1.5, indicating flow anisotropy. For the case without ICD, however, the turbulence intensity ratio continues to decrease, but in a flat slope. In this case, the radial component seems to have more power compared to the axial one, as the ratio is lower than unity.

As discussed in Chapter 2, the ILS ratio between longitudinal and transverse velocity components is two for isotropic flow. However, if the ILS is estimated under the HIT assumption and the flow is isotropic, both equations for longitudinal and transverse components lead to the same value. Therefore, in this case the ILS ratio for isotropic flows should be equal to unity. The test case without ICD compared to the two cases with ICD shows different behaviour inside the boundary layer. A higher ratio is found followed by a drop and, for the flow outside the boundary layer, the ratio stays relative constant value of $0.2 \sim 0.4$, indicating anisotropy.

For the cases with the ICD installed, the ILS ratio seems to oscillate in the vicinity of the boundary layer. This oscillation is more significant for the case with ICD only (purple curve in Fig. 5.12). For measurement points outside the boundary layer, the ILS ratio of both cases oscillates around unity. Again, this result indicate that the flow is not isotropic. However, a big discrepancy between the two velocity components is not observed.

5.2.8. Impact of the ICD ribs on the inflow turbulence

As discussed in Section 4.1.2, the ICD was built using 13 0.5 mm thick ribs serving as structural support for the honeycombs. Aiming to access the impact of these ribs on the ICD aerodynamics, the following measurement was performed: Two hot-wire probes were mounted on the duct at the plane E3 as shown in Fig. 5.13a, on the top. This duct section was connected to a circumferential traverse. The speed of the traverse mechanism was set to cover a range of roughly 80° within one minute. The acquisition time of the hot-wire system was also set to one minute. The hot-wire probes were set at an initial position of -40° , where 0° is at the top center as shown in Figs. 5.13a and 5.13b. The start movement of the traverse was synchronized with the hot-wire acquisition system. Hence, within the acquisition time, the hot-wire probes cover the span of three ribs from the ICD at -27.7° , 0° and 27.7° .

A rough estimation of the PSD in small time steps throughout the whole measurement time (or equivalently angular position) was possible with the help of the spectrogram technique (based on short-time discrete Fourier transform). The results for the test case with ICD and without honeycomb are displayed in Fig. 5.14. The fan operating point was set to $\eta_c = 4500$ RPM, $\phi = 0.40$, and $\bar{U} \approx 43$ m/s. The top plots show as black curves

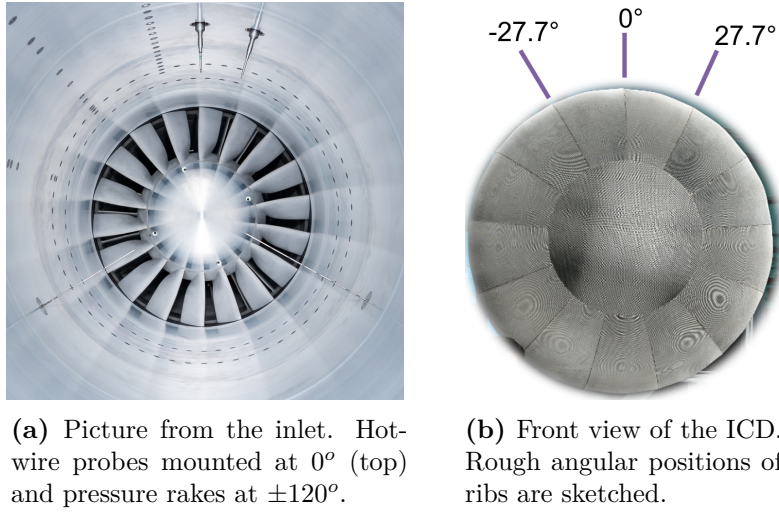


Figure 5.13.: Test setup used to assess the potential presence of ICD rib wakes in the inlet. The duct section, where the hot-wire probes are mounted, was traversed in the circumferential direction, clock-wise. Measurement plane is E3. Probes are mounted 17° apart.

the respective velocity component averaged in small time blocks and subtracted from the average value of the whole time series according to the following equation:

$$\bar{u}(k) = \frac{1}{N} \sum_{i=k-N/2}^{k+N/2} u(i) - \frac{1}{L} \sum_{i=0}^L u(i),$$

where $u(i)$ is a sample of the instantaneous velocity signal, L is the number of samples of the full signal length, and N the block size to be averaged. In this case N was set to a number of samples equivalent to 1.64 s. The red and thin curve in Fig. 5.14 stands for an estimate of the turbulence intensity of a short time obtained integrating every time step of the spectrogram with respect to the frequency axis. The average turbulence is shown as thick and dashed red line. It is important to remember that the movement of the hot-wire probes itself induces disturbances on the hot-wire elements, contributing to an increase of the turbulence intensity. The bottom plots are the spectrogram of the axial (probe 2) and radial (probe 1) velocity components, respectively.

As the probes rotate in the clock-wise direction, the probe 2 (showing the axial velocity component) detects first the wakes from the ribs, as it was mounted at 17° clock-wise from the probe 1 (showing the radial velocity component). A weak impact of the ribs was detected on the axial velocity component, as observed in Fig. 5.14a. The turbulence intensity (the red curve on the top plot) does not change significantly throughout the measurement time. The impact of the ribs is clearly seen on the radial component, compared to the axial component. The wakes from three ribs are clear and distinguishable from the free-flow. On top of Fig. 5.14b, the average radial velocity also indicates three valleys and three peaks. The increase in the turbulence intensity (the red curve) stays, however, lower than

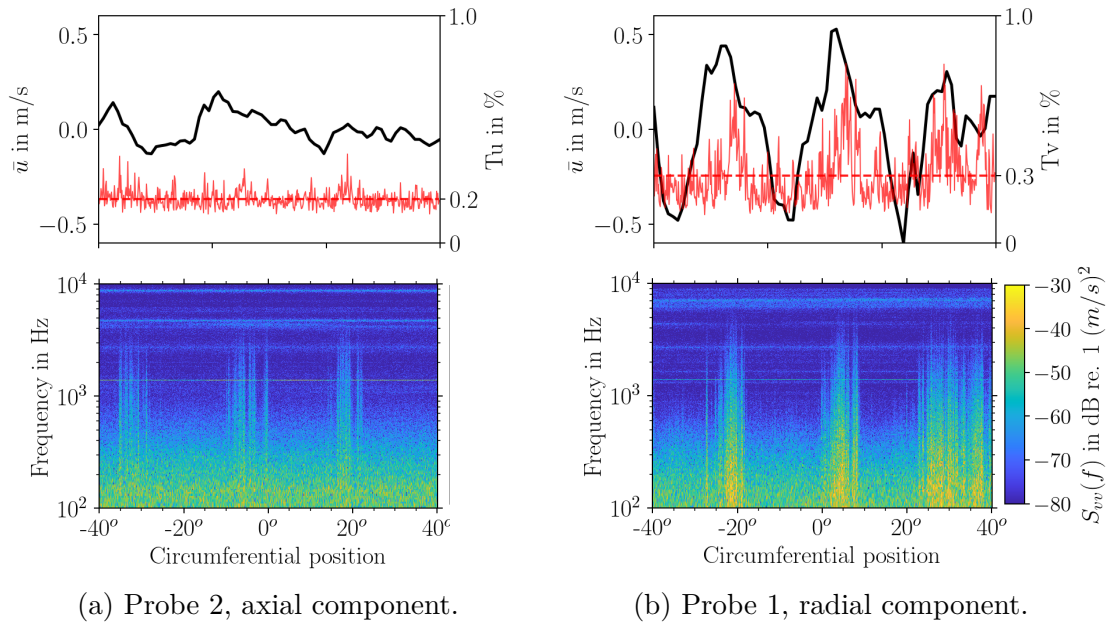


Figure 5.14.: Spectrogram of the hot-wire data for the case with ICD, without additional honeycomb, $\eta_c = 4500$ RPM, $\phi = 0.40$, and $\bar{U} \approx 43$ m/s. The velocity $\bar{u}(k)$ (plotted on top in black) refers to the same x-axis as the spectrogram. The red curve stands for the short time turbulence intensity obtained from the spectrogram. The dashed red line stands for the average turbulence intensity.

approx. 0.6 %. Note that due to the deceleration ramp of the circumferential traverse, the third wake in Fig. 5.14b appears to be wider than the other two.

With installed honeycomb at plane E1, however, compare Fig. 5.15, the turbulence was homogeneous throughout the whole measured angular span. The color map was kept constant for a better comparison to the case shown in Fig. 5.14. Furthermore, it is clear from these results that the turbulence intensity is also higher, when compared to Fig. 5.14 (the first has dark blue as dominant color, whereas the latter light green, which means around 15 dB higher levels). The turbulence intensity on the top plots also indicate more stable turbulence levels throughout the measurement time. Two possible explanations can be given: the turbulence generated by the honeycomb covers the turbulence from the rib wakes, making the flow homogeneous. The second possibility is that indeed the honeycomb eliminates the wakes from the ribs. A combination of both hypotheses seems plausible.

Fig. 5.16 displays the results for the case with ICD and no additional honeycomb, but for a lower fan speed: $\eta_c = 2250$ RPM, $\phi = 0.40$, and $\bar{U} \approx 25$ m/s. Interestingly, no discernible wakes from the ribs were measured by the hot-wires. On the other hand, the average velocity of the radial component (Fig. 5.16b) shows however three peaks. The turbulence intensity plot of the radial component also indicates an increase in the levels at roughly 0° . This might be associated with the ICD ribs. This result gives the hint that the inlet flow is potentially more homogeneous and free from wakes, when operating the

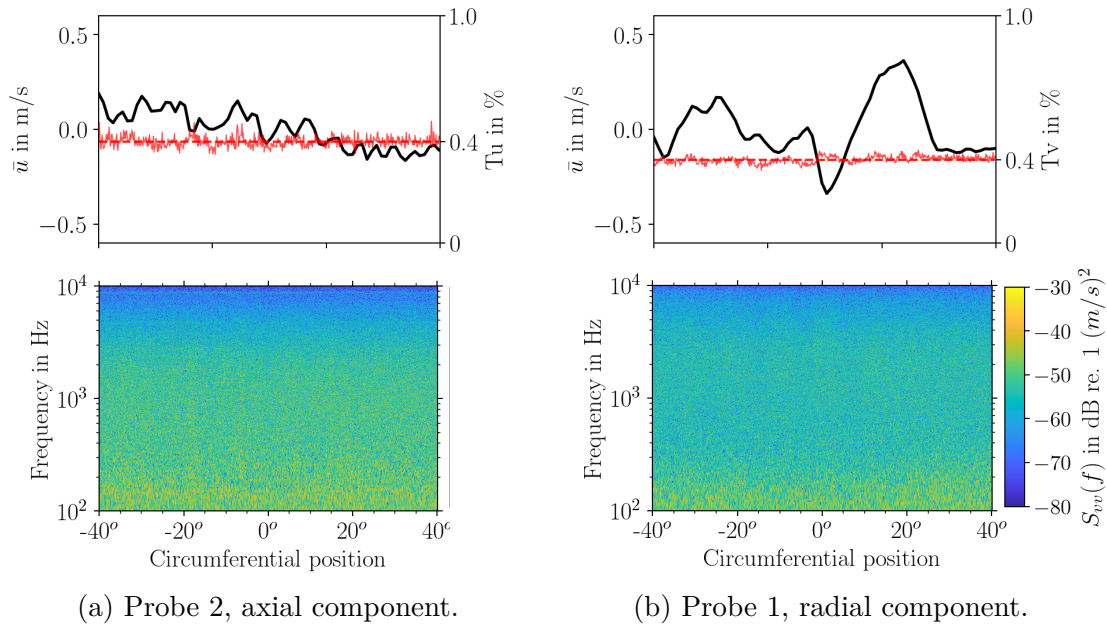


Figure 5.15.: Spectrogram of the hot-wire data for the case with ICD and honeycomb, $\eta_c = 4500$ RPM, $\phi = 0.40$, and $\bar{U} \approx 43$ m/s. The velocity $\bar{u}(k)$ (plotted on top in black) refers to the same x-axis as the spectrogram. The red curve stands for the short time turbulence intensity obtained from the spectrogram. The dashed red line stands for the average turbulence intensity.

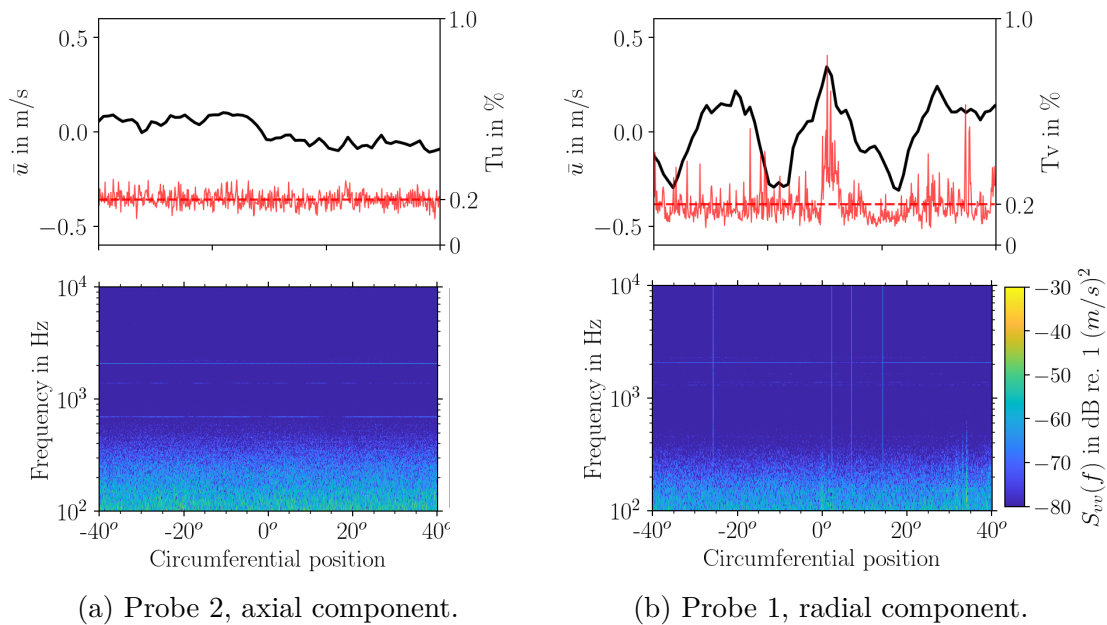


Figure 5.16.: Spectrogram of the hot-wire data for the case with ICD, without additional honeycomb, $\eta_c = 2250$ RPM, and $\bar{U} \approx 25$ m/s. The velocity $\bar{u}(k)$ (plotted on top in black) refers to the same x-axis as the spectrogram. The red curve stands for the short time turbulence intensity obtained from the spectrogram. The dashed red line stands for the average turbulence intensity.

CRAFT test rig at relatively low Mach numbers.

5.3. Interstage turbulence characterization at plane E5

5.3.1. Impact of the ICD on the turbulence field at plane E5

The impact of the ICD on the turbulence field measured downstream the fan was assessed by comparing the three test cases: without ICD, with ICD, and with ICD and additional honeycomb. All analyses are done for a constant fan speed of $\eta_c = 4500$ RPM. For the first analysis, the turbulence intensity distribution of both longitudinal and transverse components are plotted in figs. 5.17 and 5.18, respectively. The absence of the ICD impacts directly not only an increase in the background turbulence levels, but also the lack of homogeneity among the different radial positions measured. In other words, the turbulence statistics are not constant for every radial position, as for the two test cases with ICD. In figs. 5.17a and 5.18a, we observe rings with different shades of blue (lighter and darker), meaning different turbulence intensities at different radial measurement positions. It is worth mentioning that this unsteady behavior of the turbulence is undesired for acoustic measurements, as it leads in consequence to an unsteady acoustic behavior. Besides that, the rotor wakes are slightly wider for the case without ICD than for the two cases with ICD. It is important to remember that the wake width in this algorithm is computed based on the cyclic variance of the wakes, and not in the mean flow speed.

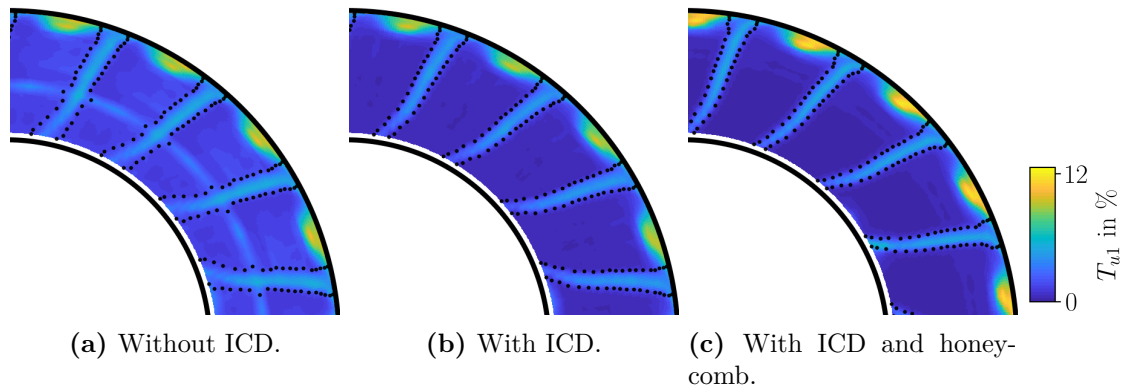


Figure 5.17.: Turbulence intensity distribution of the longitudinal velocity component T_{u1} . Fan operating point: $\eta_c = 4500$ RPM, $\phi = 0.33$.

By comparing the two test cases with ICD (without and with additional honeycomb), a visual inspection of the figs. 5.17b and 5.17c suggests slightly higher background turbulence levels for the former. For the latter, a stronger blade tip vortex is observed. The reason for that is unknown.

Fig. 5.19 shows the turbulence spectra of the longitudinal velocity component at a radial position equivalent to 55% of the blade height for the three test configurations. Fan operating point: $\eta_c = 4500$ RPM and $\phi = 0.33$. In Fig. 5.19a, the background turbulence spectrum (blue curve) surprisingly reveals that the low-frequency power content is still

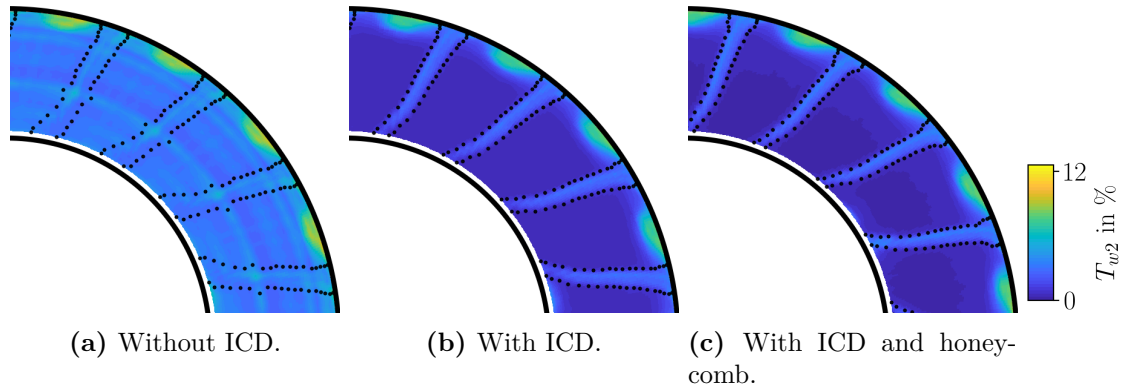


Figure 5.18.: Turbulence intensity distribution of the transverse velocity component T_{w2} . Fan operating point: $\eta_c = 4500$ RPM, $\phi = 0.33$.

present in the turbulence field downstream of the fan. This low-frequency power content is the same as discussed in the previous sections.

The configuration with ICD, as in Fig. 5.19b, shows some power content in the frequency band of $f < 100$ Hz, but considerably lower as compared to the case without ICD. Another relevant finding is that for the case with ICD (Fig. 5.19b), the raw spectrum (black curve) does not hint on low-frequency power content, as the dominant power comes from the rotor wakes. However, after separating the two domains and analyzing only the background flow turbulence data, the low-frequency power content becomes visible in the spectrum, but rather weak.

For the case with additional honeycomb, as in Fig. 5.19c, the background flow spectrum (blue curve) seems relatively flat in the low-frequency band. Furthermore, the wake spectra for both cases with ICD seem very similar without a visible impact of the additional honeycomb to their statistics.

A last analysis was performed by integrating the turbulence parameters over the radial axis with the help of Eq. 5.3.1 in order to obtain an average value for each fan operating point. Figs. 5.20 and 5.21 compile the results for all the three test configurations, fan speed $\eta_c = 4500$ RPM, and five fan flow coefficients. For the test case without ICD, no measurements were performed at $\phi = [0.30, 0.36]$. The first figure shows the average turbulence intensity, whereas the second refers to the integral length scale normalized by the blade chord length. In both figures, the left-hand side results refer to the rotor wakes, whereas on the right-hand side to the background flow.

In Fig. 5.20a, we observe a clear trend towards lower wake turbulence levels for higher flow coefficients. The test case with the ICD and no additional honeycomb delivered the lowest turbulence values for all flow coefficients. The additional honeycomb increased systematically and slightly these levels, with similar levels to the case without the ICD. For the lowest flow coefficient $\phi = 0.28$, however, the absence of the ICD produced the

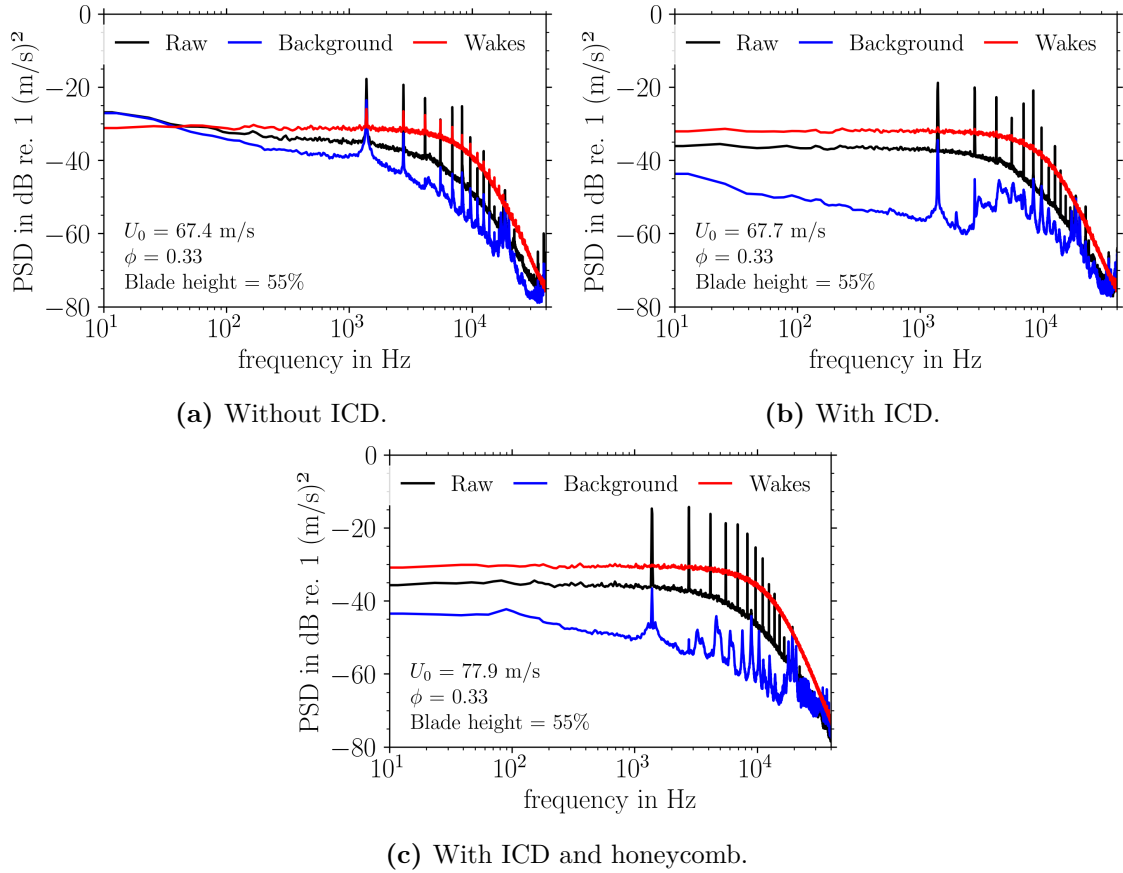


Figure 5.19.: Turbulence spectra of the longitudinal velocity component T_{u1} for the three test configurations. Fan operating point: $\eta_c = 4500$ RPM and $\phi = 0.33$.

highest wake turbulence levels. When looking at the background turbulence intensity profile in Fig. 5.20b, the two cases with the ICD delivered virtually identical values. As expected, without the ICD the background turbulence levels were approx. 1.5% higher than the two cases with ICD, corresponding to a factor of 2.

The wake ILS showed a weak dependence on the flow coefficient, as observed in Fig. 5.21a. In fact the wake ILS is directly related to the wake width (A. Moreau (2017)) and the reduction of the ILS observed with the increase of flow coefficient is likely due to the decrease of wake width, as seen in Fig. 5.25. A weak impact of the ICD on the wake ILS is observed. Virtually no difference is seen with and without the additional honeycomb. On the other hand, a greater impact of the test configuration is seen in the ILS of the background flow. The lowest values were produced by the test case with ICD and without additional honeycomb, followed by the addition of the honeycomb. A systematic increase of the ILS is observed with the increase of fan flow coefficient. The absence of ICD impacted on the highest background flow ILS values.

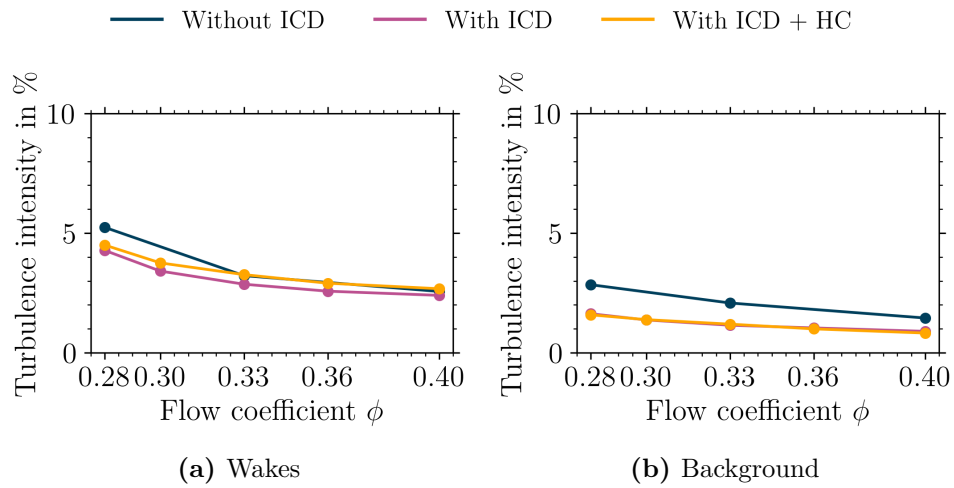


Figure 5.20.: Dependency of the turbulence intensity for five fan flow coefficients and three test configurations. Results for the longitudinal velocity component are shown. Fan speed: $\eta_c = 4500$ RPM.

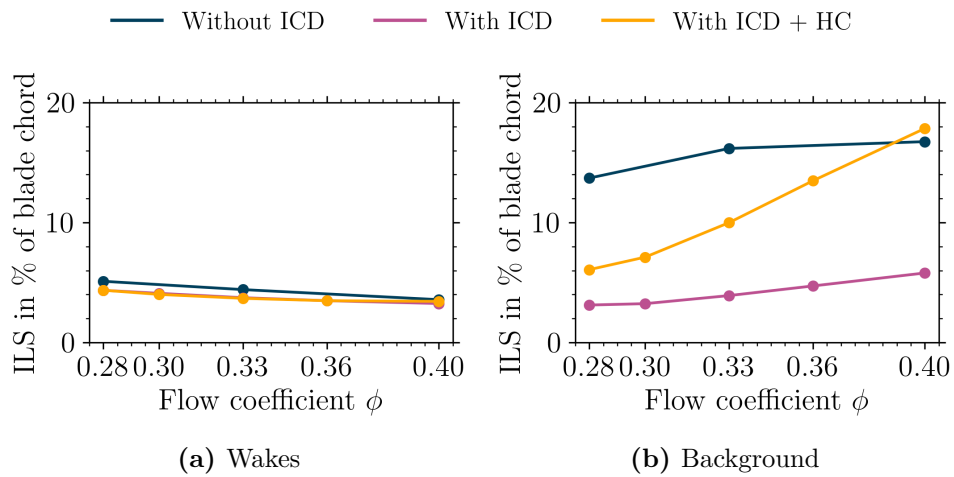


Figure 5.21.: Dependency of the ILS for five fan flow coefficients and three test configurations. Results for the longitudinal velocity component are shown. Fan speed: $\eta_c = 4500$ RPM.

5.3.2. Impact of the fan flow coefficient on the turbulence field for a constant fan speed

For the first analysis of the turbulence field downstream the fan, data were selected for a constant fan speed of $\eta_c = 4500$ RPM and three different flow coefficients: $\phi = [0.40, 0.33, 0.28]$. This produces an equivalent inlet Mach number flow velocity of approx. $M_{inlet} = [0.12, 0.10, 0.087]$, respectively. For $\phi = 0.40$, the fan produces a low total pressure rise and works more as a ventilator than as a compressor. The design point of this rotor-stator set, as discussed in Section 4, is at $\eta = 4500$ RPM and $\phi = 0.33$ (approx.). It was observed experimentally that this fan stalls at $\phi \approx 0.26$ with the given ambient conditions. The test configuration selected is with ICD and additional honeycomb.

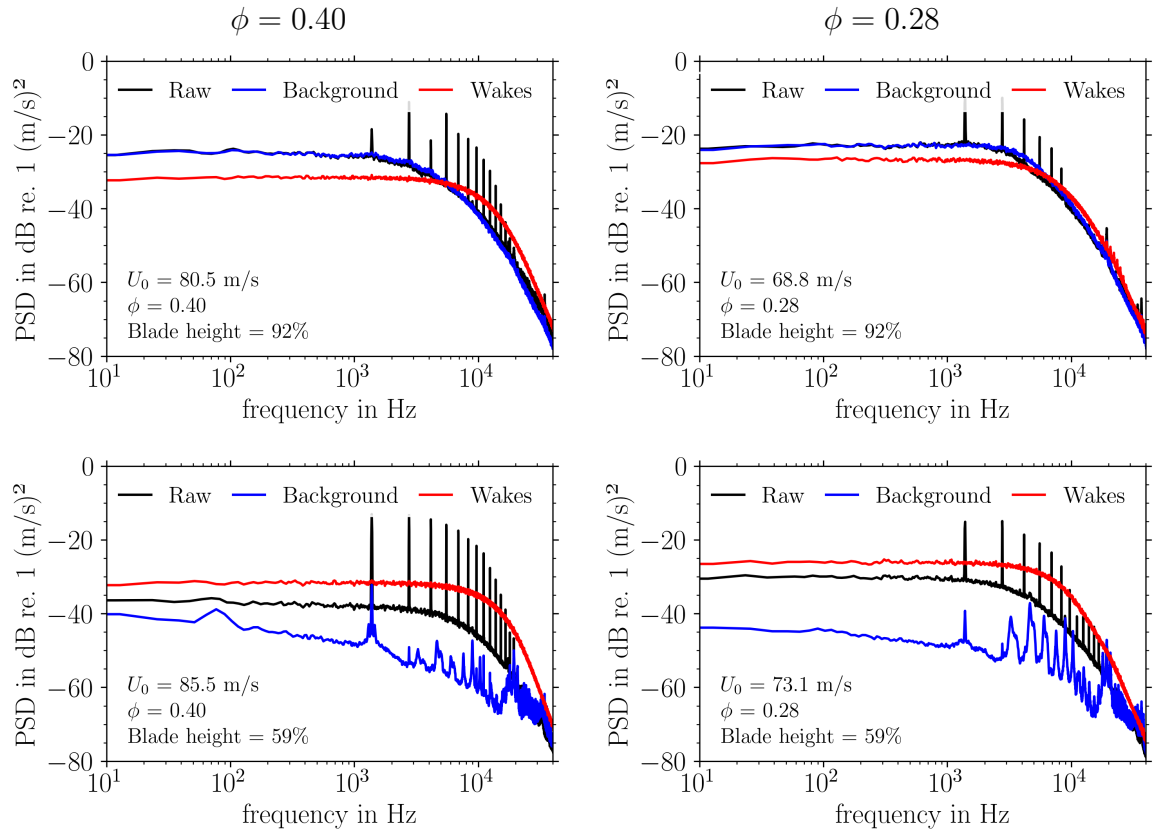


Figure 5.22.: PSD of the longitudinal velocity component of the raw signal (black), separated blade wakes (red), and background flow (blue). *Top and bottom:* Measurement points at 7 mm and 36 mm away from the outer casing (92% and 59% of blade span), respectively. *Left:* $\phi = 0.40$ and *right:* $\phi = 0.28$. All plots refer to the fan speed of $\eta_c = 4500$ RPM. Configuration with ICD and additional honeycomb.

The first analysis starts by inspecting the estimated turbulence PSD of the longitudinal velocity component measured at two radial positions and two fan operating points, as shown in Fig. 5.22. The top plots refer to a measurement point 7 mm away from the outer casing corresponding to 92% of the blade span. At this position, the background

turbulence (blue curve) levels are high due to the blade tip vortex. These values are even higher than the blade wake turbulence (red curve) itself. The black curve shows the PSD of the unsteady velocity signal, before the rotor wake separation technique has been applied. Tones are present in this PSD due to the periodic fluctuations associated to the velocity deficit from the rotor wakes, which are still contained in this signal. These periodic components are displayed in red in Fig. 3.10. Comparing the left-hand top plot against the right-hand top plot ($\phi = 0.40$ versus $\phi = 0.28$, respectively, both at $\eta_c = 4500$ RPM), virtually no difference is observed in the PSD level of the background flow. A higher incidence of tones is, however, seen for the higher flow coefficient case (left-hand plot). For the wake turbulence, though, the PSD shifts slightly up and to the right, which means an increase of the turbulence levels and a slight decrease in the integral length scale.

The bottom plots in Fig. 5.22 refer to a measurement position 36 mm away from the outer casing corresponding to 59% of the blade span. At this measurement position, the background turbulence levels are much lower compared to the total signal measured and the wakes turbulence. This is because most of the signal power measured is due to the rotor wakes. A noticeable increase in the wake turbulence levels is again observed for an increase in blade loading (reduction of flow coefficient). The background turbulence levels do not change considerably between these two operating points.

Fig. 5.23 shows the average phase-locked velocity of the longitudinal velocity component for a constant fan speed of $\eta_c = 4500$ RPM and for the three flow coefficients. It is worth mentioning that the hot-wire probes are fixed in a circumferential position and is able to radially traverse inside the channel. Due to the rotation of the fan upstream the hot-wire probes, it is possible to visualize the flow velocity distribution over the whole circumferential span, even though the probes are fixed. The black dots illustrate where the automatically detected border between blade wakes and background flow lies. A better view of this border will be provided in the next figures. The $B = 18$ radially distributed velocity deficit patterns associated with the rotor wakes in light blue color is clearly visible in all plots. The green-yellow color between the rotor wakes represent the background flow. A higher flow speed is observed in the region around the inner casing (fan hub). A deficit of velocity is also found in the region close to the outer casing, associated to its boundary layer and the blade tip vortex. Both the wake thickness and the tip vortex thickness are proportional to the blade loading, or inversely proportional to the flow coefficient.

Fig. 5.24 displays the turbulence intensity distribution of the longitudinal velocity component U_1 for the same fan operating points. In these plots, the low turbulence level region (dark blue) associated with the background flow is clearly distinguishable from the rotor wakes turbulence (light blue). The blades tip vortex (yellow spots near the outer casing and between every blade wake) is responsible for generating the highest turbulence levels measured. In this figure, the thickening of the tip vortex and blade wakes with the

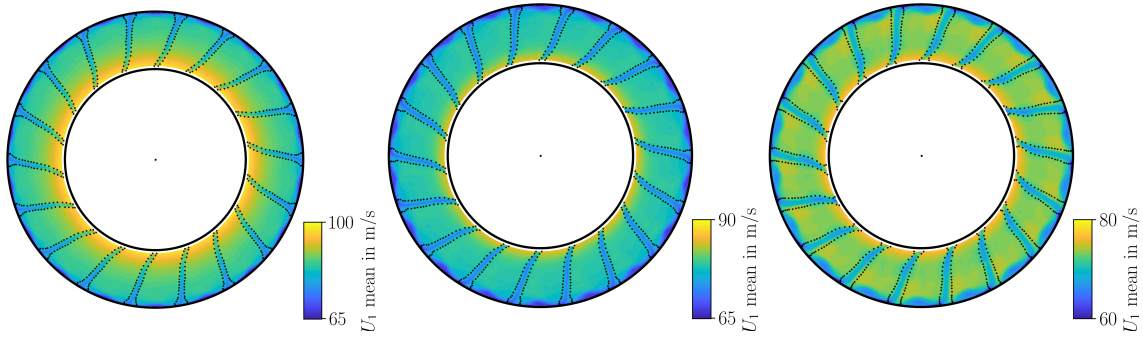


Figure 5.23.: Average phase-locked speed of the longitudinal velocity component U_1 . Fan operating point: $\eta_c = 4500$ RPM. *Left:* $\phi = 0.40$, *middle:* $\phi = 0.33$, and *right:* $\phi = 0.28$.

increase of blade loading (reduction of flow coefficient) is more evident. A closer look in the top-right quarter of each of the plots is shown in Fig. 5.25. In this figure, the black dots representing the detected border between blade wake and background flow are more discernible. Furthermore, the progressive change in wake thickness as well as the tip vortex are better visible. Interestingly, the turbulence intensity of the tip vortex seems to reach the highest values for $\phi = 0.33$, and not for $\phi = 0.28$ with the highest blade loading.

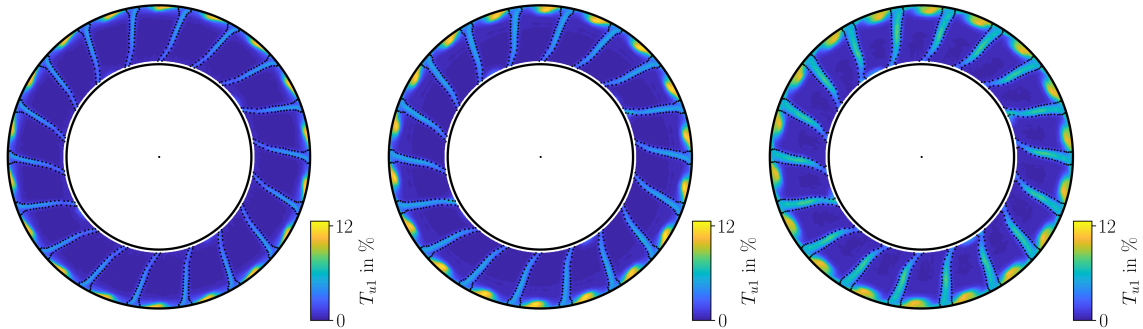


Figure 5.24.: Turbulence intensity of the longitudinal velocity component U_1 . Fan operating point: $\eta_c = 4500$ RPM. *Left:* $\phi = 0.40$, *middle:* $\phi = 0.33$, and *right:* $\phi = 0.28$.

Fig. 5.26 shows the turbulence intensity distribution of the transverse velocity component W_2 for the same fan operating points. The color mapping scale was kept the same (from 0% to 12.5%). Slightly lower turbulence levels are observed in the wake region. The tip vortex for this velocity component shows lower turbulence intensity values compared to the longitudinal component.

The radial distribution of the turbulence intensity as a function of the blade height is shown in Fig. 5.27. Both the rotor wakes and the background flow parameters are shown for both velocity components U_1 and W_2 . No noticeable difference is observed between the two fan operating points $\phi = 0.40$ and $\phi = 0.33$ in these plots. The increase in the tip vortex is, however, observed in the blue curves referring to the background flow. Outside this region, the background flow has roughly the same turbulence intensity values, which is one requirement (among others) for flow isotropy. The same does not hold for the blade

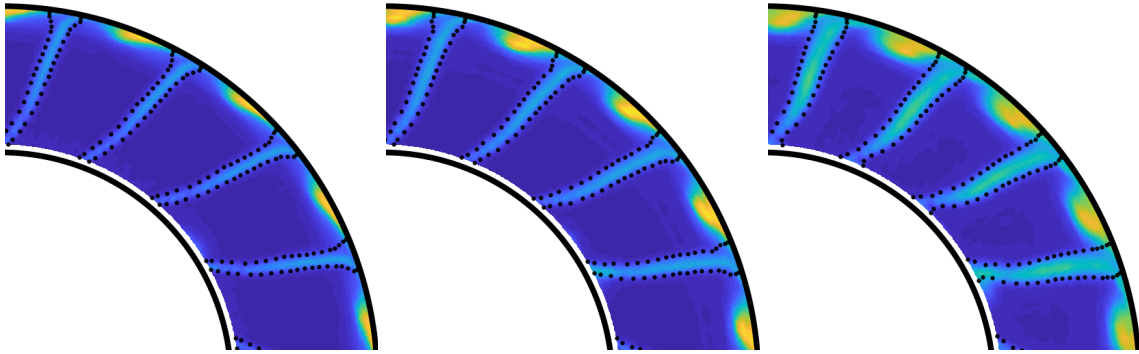


Figure 5.25.: Closeup in the top-right quarter of each plot of Fig. 5.24.

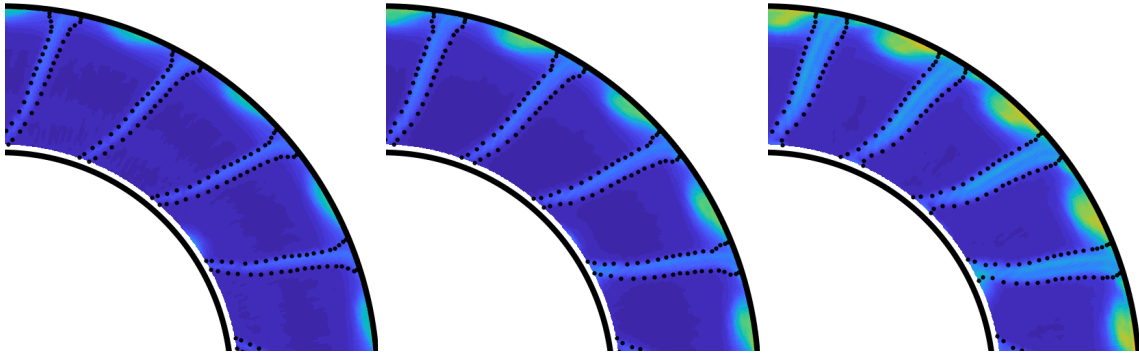


Figure 5.26.: Turbulence intensity of the transverse velocity component W_2 . For better visualization, a closeup in the top-right quarter is displayed. The color mapping scale remains the same as in Fig. 5.24. Fan operating point: $\eta_c = 4500$ RPM. *Left:* $\phi = 0.40$, *middle:* $\phi = 0.33$, and *right:* $\phi = 0.28$.

wake. Inside the rotor wakes, the turbulence intensity values of the longitudinal velocity component seem to be almost twice higher compared to the transverse one. The blade wakes properties did not change considerably between the two fan operating points.

For $\phi = 0.28$, however, besides a further growth of the tip vortex area, an overall increase in the turbulence intensity of the blade wakes over the whole blade span is observed. This result agrees with the observations from Evans (1975). A possible reason is that the suction side of the blades is near reaching stall, which happens at approx. $\phi = 0.26$. The lower the flow coefficient (i.e., higher blade loading) becomes, the closer to the leading edge the boundary layer transition from laminar to turbulent occurs in the blade suction side. Alongside with that, in this condition, flow separation can also occur at the blade trailing edge. A pronounced increase at 50% of blade height is noticed for the longitudinal component. This can be a hint for the first region of the blade to enter in stall condition, when the flow coefficient continues to shrink.

The radial distribution of the turbulence integral length scale (ILS) normalized by the blade chord length $C = 62$ mm as a function of the blade height is shown in Fig. 5.28.

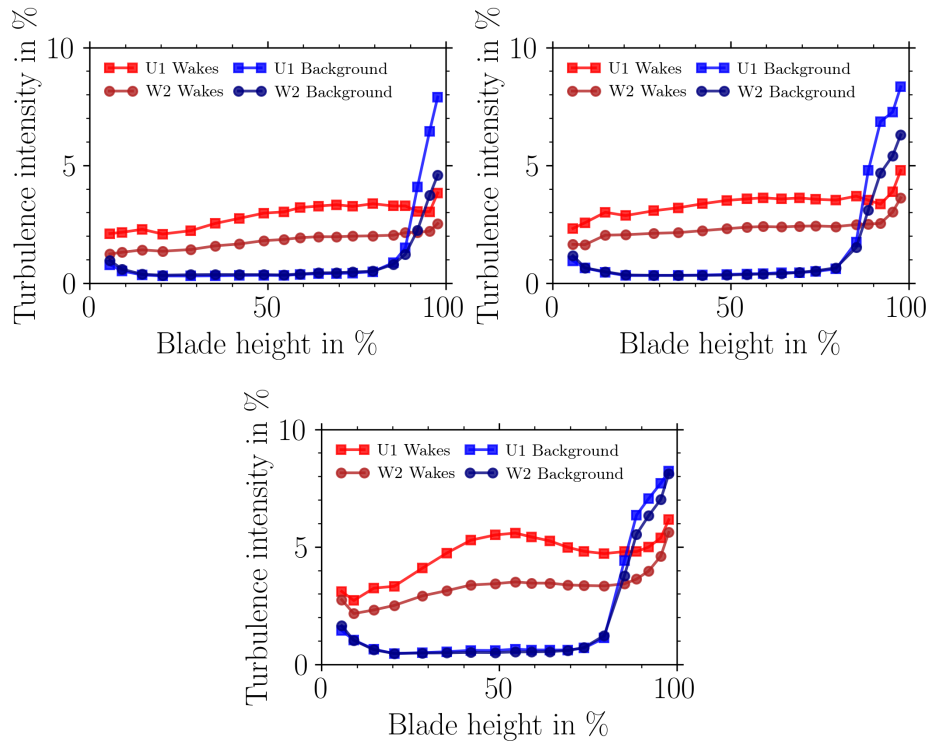


Figure 5.27.: Radial distribution of the turbulence intensity of both rotor wakes and background flow. Both velocity components are displayed U_1 and W_2 . Fan operating point: $\eta_c = 4500$ RPM. *Top-left:* $\phi = 0.40$, *top-right:* $\phi = 0.33$, and *bottom:* $\phi = 0.28$.

Again, both the rotor wakes and the background flow parameters are shown for both velocity components U_1 and W_2 . The ILS of the rotor wakes decreases slightly with the increase of the blade loading. The values stay in the range of approx. 3% to 7% of the blade chord length. The difference in the values of both velocity components of the rotor wakes seem to reduce with the increase of the blade loading. The transverse velocity component has higher values compared to the longitudinal one. This opposes with what was observed for the turbulence intensity in Fig. 5.27, where the longitudinal component always showed up greater values than the transverse one. At this point, the wake turbulence seem to have more energy in the longitudinal direction and shorter integral length scale compared to the transverse direction.

Two peaks are observed for radial positions close to the hub and outer casing for the dark blue curves of Fig. 5.28 referring to the transverse velocity component of the background flow. This is observed for all three flow coefficients. A hypothesis is that these peaks are associated to the two wall boundary layers: fan hub and outer casing. The ILS values of the background flow seem to reduce with increasing blade loading, especially for the longitudinal velocity component.

In order to get an overview of each parameter as a function of the flow coefficient, an

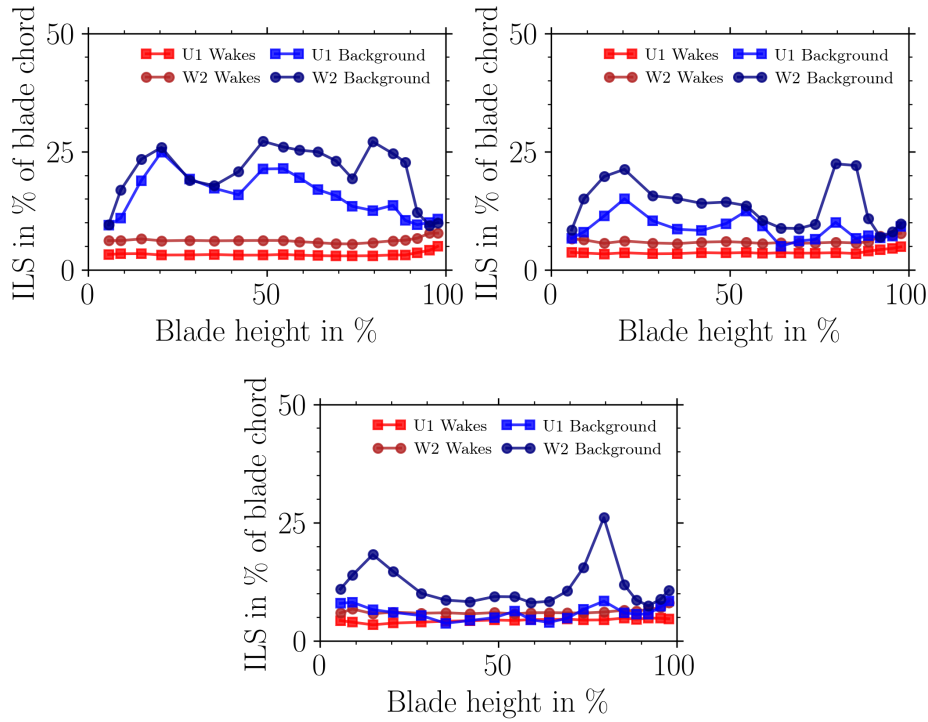


Figure 5.28.: Radial distribution of the integral length scale of both rotor wakes and background flow. Values are normalized by the blade chord length $C = 62$ mm. Both velocity components are displayed, U_1 and W_2 . Fan operating point: $\eta_c = 4500$ RPM. *Top-left:* $\phi = 0.40$, *top-right:* $\phi = 0.33$, and *bottom:* $\phi = 0.28$.

average over the measured span was calculated using

$$\bar{x} = \int_{r_1}^{r_2} x(r) dr / (r_2 - r_1), \quad (5.3.1)$$

where r is the radial position of the measurement and $x(r)$ is either the turbulence intensity or the integral length scale as a function of the radial position. r_1 and r_2 stand for the first and last evaluated radial positions, respectively. The average values for each flow coefficient are shown in Fig. 5.29 in addition to the flow coefficients 0.30 and 0.36. In this figure, the trends are clearer for both turbulence intensity and integral length scale. The increase in blade loading (reduction of flow coefficient) results in an increase of the turbulence intensity of both velocity components as well as in both the rotor wakes and the background flow regions. The increase in the turbulence intensity of the background flow, less pre-eminent than for the rotor wakes, is likely due to the increase of the rotor tip vortex effect.

For the integral length scale, however, different trends are observed. The increase in blade loading slightly increased the average integral length scale of the rotor wakes, but the opposite happened to the background flow. The reason for this phenomenon is not yet understood. One hypothesis is the proportional dependency of the length scales on the

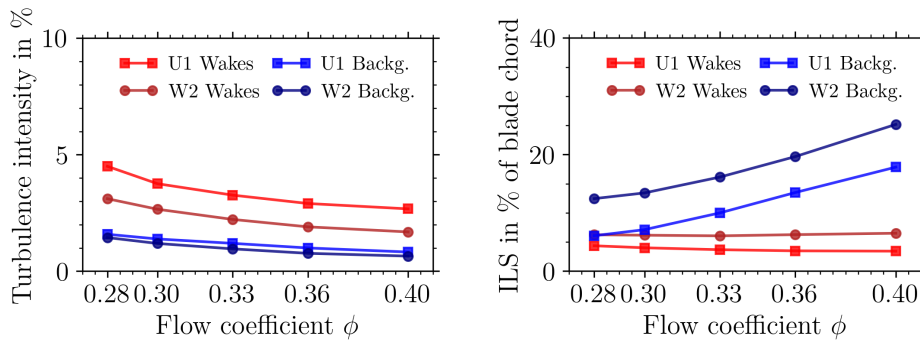


Figure 5.29.: Average values of the turbulence intensity (left plot) and of the integral length scale (right plot) over the blade span for three different flow coefficients. Fan speed: $\eta_c = 4500$ RPM.

averaged flow speed.

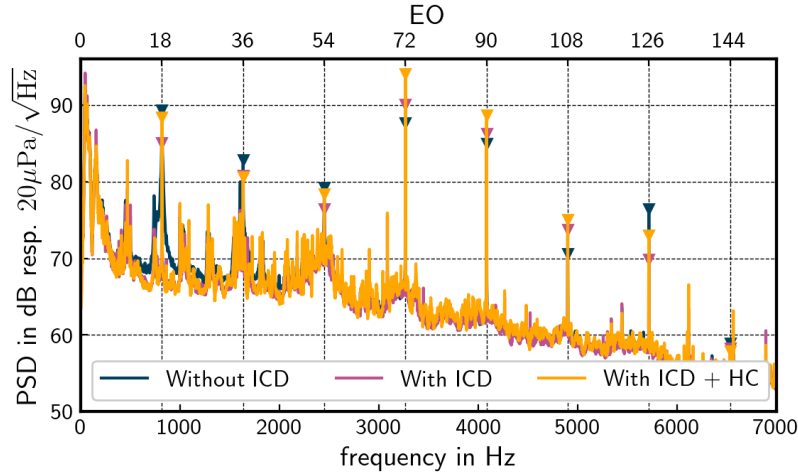
5.4. Inlet acoustic analyses

Acoustic data from the microphone ring array were first resampled with respect to the rotor shaft trigger using linear interpolation to produce 1024 samples per fan revolution. The use of adaptive resampling allows the reduction of the impact of rotor speed fluctuations over time on the fan tonal noise sources (Behn et al. (2018)). A cyclostationary analysis was subsequently performed to split the signals into rotor-coherent (tonal) and rotor-incoherent (broadband) signal constituents (Behn et al. (2018) and Grizewski et al. (2021)). For this purpose, the mean rotor-coherent spectrum is calculated by rotor-synchronous averaging of the FFT blocks. To determine the mean rotor-incoherent spectrum, from each of the individual FFT blocks the mean rotor-coherent spectrum is subtracted and then an averaging over the magnitude of the FFT blocks is performed.

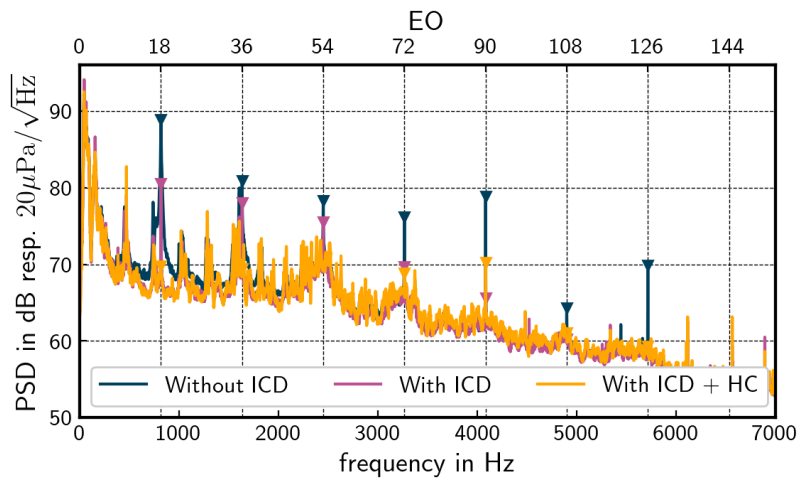
Besides the acoustic PSD analysis, the azimuthal mode decomposition technique was applied to both rotor-incoherent and coherent signals. The modal decomposition of broadband and tonal components was performed by solving a linear system of equations of cross-correlations between all microphone pairs as described by Grizewski et al. (2021) and typically used for such analysis. The solution is a cross-correlation matrix of the azimuthal modes with the squared mode amplitudes on its main diagonal.

The averaged auto-power spectra of all microphones in the ring array are depicted in Fig. 5.30a and 5.31a. It is worth mentioning that the boundary layer noise induced by the flow on the microphone membrane is still captured by them. They refer to the two operating points, which the aerodynamic measurement results presented in detail in the previous section. The auto-power spectra include both rotor-coherent and rotor-incoherent sound components excited by the fan. The rotor incoherent parts obtained by cyclostationary analysis are depicted in the Fig. 5.30b and 5.31b. The dark blue curves represent the

measurements without ICD, the purple curve with ICD, and the orange curve the case with ICD and the additional honeycomb installed at plane E1.



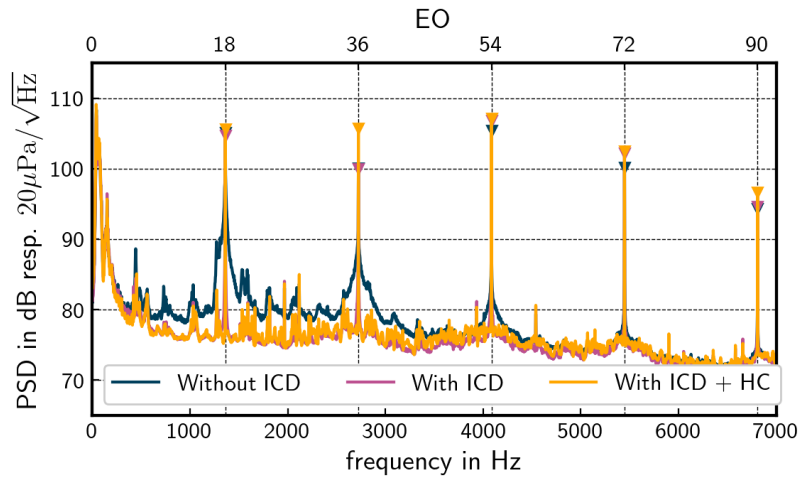
(a) Average auto-power spectrum.



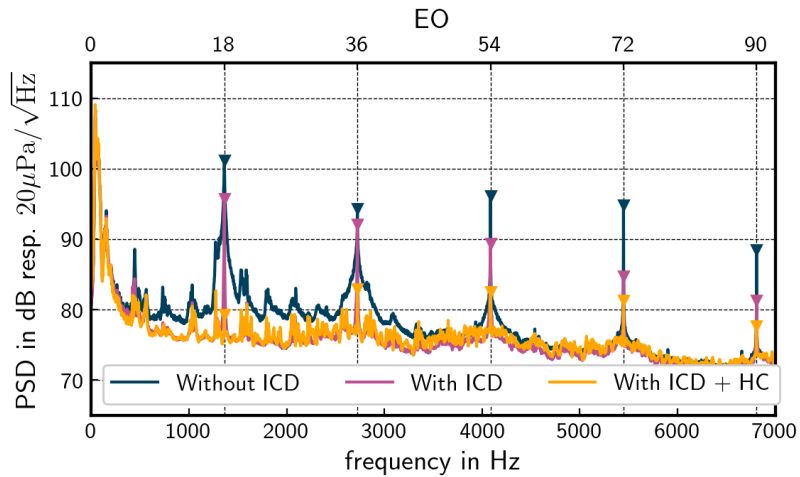
(b) Separated rotor-incoherent components.

Figure 5.30.: Averaged spectra for the three test cases: without ICD, with ICD, and with ICD and additional honeycomb. Fan operating point: $\eta_c = 2700$ RPM, $\phi = 0.28$.

Regarding the rotor-coherent components, under ideal spatially and temporally homogeneous flow at low fan speed 2700 RPM, the first three BPF tones are cut-off due to the selected blade numbers of the rotor and stator. However, in disturbed inflow conditions rotor-coherent blade tones are generated, predominantly due to the interaction of the inhomogeneous steady flow profile with the rotor. Indeed, in Fig. 5.30a, the first three BPFs are present in the spectrum for all three inlet configurations. For the case with ICD, however, these three tones have lower amplitude (roughly 5 dB) compared to the case without ICD. This is an evidence of the equalizing effect of the ICD. In contrast to the lower BPF harmonics, the tones at 4BPF to 6BPF are cut-on and even increase in amplitude when



(a) Average auto-power spectrum.



(b) Separated rotor-incoherent components.

Figure 5.31.: Averaged spectra for the three test cases: without ICD, with ICD, and with ICD and additional honeycomb. Fan operating point: $\eta_c = 4500$ RPM, $\phi = 0.40$.

the ICD is present. In this case, the more homogeneous the inflow is, the more stable are the sound sources located on the leading edges of the stator vanes. Stable in this context refers to their magnitude and phase, so that the constructive interference of the sound fields excited by the individual sources is increased. Similar findings were reported by Grizewski et al. (2021). At the higher rotor speed of $\eta_c = 4500$ RPM, all BPF tones are cut-on. The stabilizing effect of the ICD is noticeable in Fig. 5.31a, but the difference in the tone amplitudes is smaller.

Also for the rotor incoherent components, the reduction caused by the ICD can be clearly seen. Without the ICD, the interaction of the fan with the measured pronounced spatial and temporal inhomogeneities of the turbulent flow field leads to a level increase in the low to mid frequency band of the acoustic spectrum. In particular, a significant narrowband

level increase around the lower BPF harmonics (Atassi and Logue (2009)) is observed. This effect is also clearly observed in the azimuthal mode decomposition of the broadband components in Fig. 5.32. Another possible cause may be temporal fluctuations of the mean flow, which can lead to a projection of rotor-coherent components into rotor-incoherent components, see Schuster (2021). Such mean flow fluctuations are likely due to the test rig operation in the laboratory environment. The use of the ICD leads to a predominantly flat sound spectrum. This is due to the extensive homogenization of the turbulent structures and the reduction of the turbulence intensity, as presented in Section 5.2. The peaks at the BPF harmonics are now significantly narrower and have lower levels. They result primarily from the interaction of the turbulent rotor outflow with the stator. That the excited broadband noise level depends directly on the turbulence intensity is shown by further comparison with the configuration consisting of the ICD and the honeycomb. Compared to the ICD configuration, the turbulence levels outside the boundary layer have approx. doubled, cf. Fig. 5.10. At the lower speed, the noise components excited at the honeycomb are relatively more prominent and might mask the noise generated at the fan. Beyond that, the noise characteristics of the respective inlet configuration are very comparable with regard to the speed variation.

The haystacks around the BPF tones are clearly present in the acoustic PSD for the case without the ICD. Often found in the literature, the reason for this effect is attributed to turbulence ingestion (Preisser and Chestnutt (1984), Kobayashi and J. Groeneweg (1980), J. F. Groeneweg and Rice (1983) and Atassi and Logue (2009)). This explanation is, however, from the author's perspective too generic and does not explain the physics behind the phenomenon. My hypothesis is that its origin is strongly linked with the power present in the low-frequency band of the turbulence PSD, as discussed in Section 5.2.4, and reported by Caldas et al. (2021b). In Section 5.3.1, the impact of the inlet configuration on the flow turbulence characteristics downstream the fan is shown. For the test case without the ICD, a non-homogeneity of the turbulence distribution along the radius, as well as the low-frequency power in the turbulence spectrum at this axial position was observed. My hypothesis is that the haystacks around the BPF tones are a result of a modulation of the turbulence field by the periodic rotor wakes. The interaction of a random turbulent process with a deterministic process (periodic rotor wakes) results in this "hybrid" noise signal, a combination of tones and narrowband components around them.

For the fan speed of $\eta_c = 2700$ RPM the remaining narrowband components related to the BPF tones for the case with the ICD have significantly lower power in the rotor-incoherent spectrum (Fig. 5.30b) compared to the case without the ICD. For the $\eta_c = 4500$ RPM fan speed case, however, in Fig. 5.31b stronger remaining tones are observed. A possible explanation for this could be, as discussed in Section 5.2 with the help of Figs. 5.14 and 5.16, the more homogeneous inflow when the inflow velocity is lower. It is rather difficult to compare side-by-side the two operation points, as the flow coefficient are not the same for both cases. Therefore, a better inflow condition would allow more stable BPF tones,

which afterwards could be completely removed from the rotor-incoherent signal, with the help of a cyclostationary analysis. Schuster (2021) conducted an empirical analysis of the BPF tones stability of different fan test rigs under different inflow conditions. Further analysis on the impact of turbulence on the fluctuations of tone parameters can be found in this study. The peaks observed in Fig. 5.30 between BPFs, for example at EO 9 and 22 might be related to the cut-on mode zone. That means, new modes become cut-on at the respective frequencies, and can be easily excited. This is more evident for the higher fan speed case for EO = 6, 10, and 14 in Fig. 5.32. At these frequencies, a new azimuthal mode order becomes cut-on and therefore a sudden increase in power can be observed in the acoustic PSD, as additional modes are able to propagate in the flow channel.

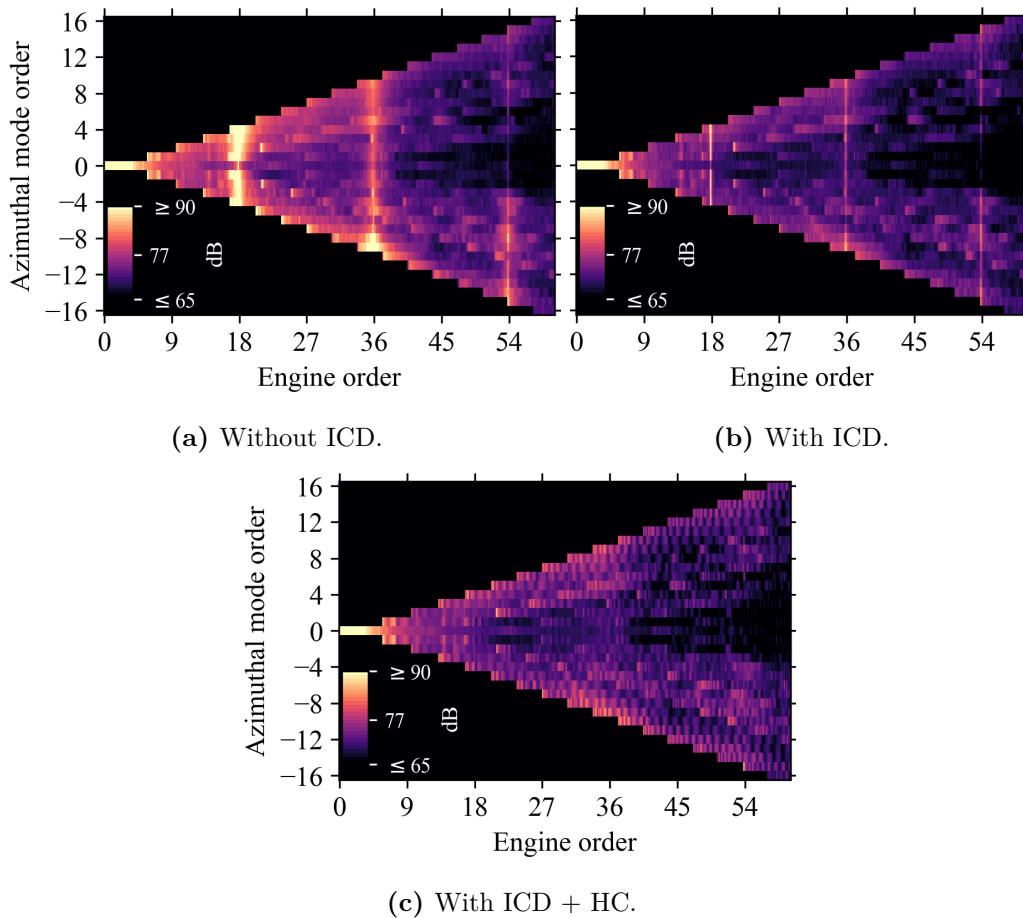


Figure 5.32.: Azimuthal mode analysis of the rotor-incoherent acoustic components for the three test configurations. Results are in decibels referred to $20 \mu Pa$. Fan operating point: $\eta_c = 4500$ RPM, $\phi = 0.40$.

It is clear in figs. 5.30b and 5.31b that most of the power concentrated in the BPF tones could be separated after the cyclostationary analysis for the case with the ICD and with ICD and the honeycomb at plane E1. The reason for that can be explained by the different inflow turbulence characteristics established by the additional honeycomb, as discussed along with Fig. 5.10. The lower power found in the low-frequency band of the turbulence

PSD, along with a more homogeneous inflow established, as shown in Fig. 5.15, is believed to be the more likely reason for the establishment of more stable BPF tones. For the same reason, the second BPF in Fig. 5.31a shows up a higher amplitude for the case with the ICD and the honeycomb at plane E1. Due to its stability, its energy concentrates more in a narrower band.

The azimuthal mode decomposition shown in Fig. 5.32 gives a further hint of the impact of the ICD on the broadband fan noise field. As discussed in Section 4.1, the ICD ribs excite cut-off modes, and therefore its signature would not be expected in the modal analysis. Furthermore, Section 5.2 revealed that no significant impact from the ICD ribs on the average axial velocity was measured by the hot-wire probes. Because of that, and that the ICD acts mainly in the turbulence field and homogenizing the flow, it was opted to perform the mode analysis in the broadband part of the signal, similar as reported by Grizewski et al. (2021). From Fig. 5.32, the impact of the ICD on the narrowband components around the BPF is clearly observed. No additional mode excitation is observed in Fig. 5.32b compared to Fig. 5.32a due to the ICD. This is confirmed by Fig. 5.32c, as the additional honeycomb completely removes the impact of the ICD ribs from the turbulence field. Interestingly, in Fig. 5.32a, we observe that modes in the transition from cut-off to cut-on are stronger excited, especially the negative ones (co-rotating with the rotor), likely due to the rotor shielding effect. This is not observed in Fig. 5.32b and Fig. 5.32c. This is one of the reasons for a higher broadband level PSD for the case without the ICD.

In order to analyze the stability of the first and second BPF tones for the three test configurations, a last investigation was performed. This analysis is based on short time azimuthal mode analysis, where the amplitude and phase of the dominant modes at the 1BPF and 2BPF tones are investigated. On the one hand, it is known that the more homogeneous and constant the inflow is, the more stable the tones are excited. On the other hand, the more stochastic the flow properties are, due to for example ingestion of turbulence, the more oscillations in these parameters are expected.

With the aim of analyzing the stability of the dominant modes regarding their phase and amplitude, an azimuthal mode analysis was performed again, but this time based on short time discrete Fourier transformation. A block length equivalent to 8 fan revolutions, or 106 *ms* and no data block overlap was applied to the resampled time series. The rectangular window was used for each data block as the analysis aimed on tones. Each microphone data block was discretely Fourier transformed and the complex values corresponding to the frequency bins of the first and second BPF were selected to be analyzed. The procedure to determine the modes amplitude and phase are identical to what was previously described.

Fig. 5.33 shows the results for the mode amplitude and phase in form of a polar plot. The three tested inlet configurations are shown: Without the ICD, with the ICD, and with the ICD and additional honeycomb. The top row refers to the first BPF, while bottom row

to the second BPF. Fan operating point: $\eta_c = 4500$ RPM, $\phi = 0.40$, and $\bar{U} \approx 43$ m/s. The Tyler-Sofrin interaction mode expected for the first BPF is $m = +3$ (18 rotor blades with negative¹ rotating direction and 21 stator vanes). As the modes $m = 0$ and $m = -3$ also showed up relevant power, they are also displayed in this analysis. The second BPF follows the same logic, where modes analyzed are $m = +6$, $m = 0$, and $m = -6$. In the scope of this study, no anechoic termination was applied to the outlet of the test rig. Thus, reflections and scattering effects are expected from the throttle and the three struts found downstream of the stator section.

It is evident in Fig. 5.33 that the ICD allows a more stable mode excitation in terms of amplitude and phase, when compared to the case without the ICD. The first BPF is the most affected by the ingested turbulence, whereas the second is more stable than the first, even for the case without the ICD. When the additional honeycomb was installed, a further improvement was observed. For this configuration, the amplitude and phase of modes are concentrated in an even smaller area, compared to the case with the ICD only. This is a consequence of a more stable and homogeneous inflow established by the combination of the ICD and the additional honeycomb.

¹The coordinate system used is when looking the fan from the inlet (rearwards), the fan rotates in the counter-clockwise direction, assumed to be negative. The circumferential angles of the microphones also reduce in the counter-clockwise direction. As consequence, negative spinning modes rotate in the same direction as the fan does.

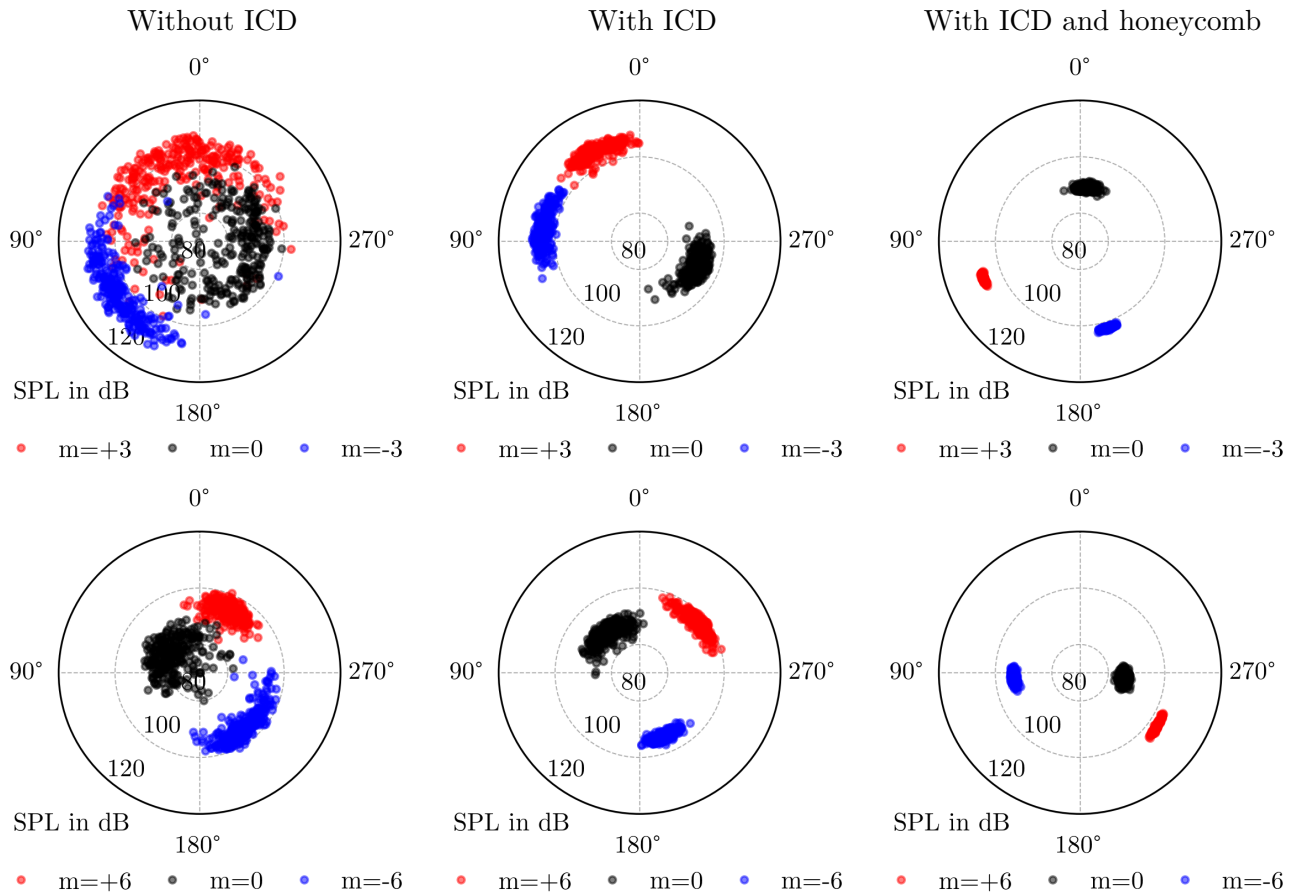


Figure 5.33.: Short time azimuthal mode analysis of the first and second BPF and the three tested inlet configurations: Without the ICD, with the ICD, and with the ICD and the additional honeycomb. The top row refers to the 1xBPF. The bottom row to the 2xBPF. Fan operating point: $\eta_c = 4500$ RPM, $\phi = 0.40$, and $\bar{U} \approx 43$ m/s. SPL levels are referred to $20\mu Pa$.

6. Measurements with variable fan inflow distortion

IN Chapter 1 the potential benefits of (highly) integrated propulsion systems to reduce aircraft fuel consumption by increasing flight efficiency were described. Numerous researches are found aiming on the assessment of the aerodynamic impact of inflow distortion on fan/compressor performance, such as Gunn and Hall (2014, 2019), Perovic et al. (2019) and Plas et al. (2007). However, the acoustic impact on fan noise of such inflow has not received much of attention, yet. This scenario started changing roughly in the last decade. The impact of inflow distortion in the fan noise generation was discussed in Chapter 2. In a nutshell, extra fan noise is generated from the interaction of the distorted inflow and turbulence with the rotating fan, in conjunction with the distorted rotor wakes and the stator (as depicted in Fig. 1.6 in Chapter 2, Silberhorn et al. (2019), Staggat (2021) and Staggat et al. (2019)).

To seek a better understanding of the inflow distortion impact on fan broadband noise generation, and especially the correlation between the inflow aerodynamic field (stationary and turbulence), the fan noise generation, a measurement campaign was conducted in the CRAFT fan test rig. Meshes and/or perforated plates (i.e., screens) are typically used to generate a total pressure distortion profile for aerodynamic performance investigation (Gunn and Hall (2014, 2019), Perovic et al. (2019) and Lucas (2013)). For acoustic investigations, however, the interaction of the mean inflow velocity profile is only responsible for the generation of tonal noise (Staggat (2021) and Staggat et al. (2019)). The turbulence characteristics of the distorted inflow in terms of Reynolds stresses (or the turbulent kinetic energy profile) and integral length scale are responsible for the fan broadband noise generation.

The analyses presented in this chapter had as goal not only addressing the fan noise emissions due to inflow distortion, but also evaluating the representativeness of the method used to generate specific distortion profiles for fan noise investigation. For this sort of investigation, specific velocity profiles have to be created. Additionally, a specific integral length scale and turbulence intensity distribution should also be generated, if the conditions of integrated engines shall be reproduced for acoustic investigations in a laboratory environment. In order to assess experimentally the aerodynamic parameters under distorted inflow condition, pressure rakes and hot-wire anemometry were installed downstream the distortion screens. The acoustic field was assessed by means of microphone arrays flush mounted in the duct wall. This chapter is based on the publications Caldas et al. (2022a) and Klähn et al. (2022a).

In the early stages of the project AGATA3S (which the present work was part of) initial investigation in the generation of flow distortion using screens and perforated plates were performed by Bremer (2018). In this study a 100 mm in diameter blower was used. The different screens and perforated plates were installed inside the channel for aerodynamic evaluation. Speeds up to $M = 0.25$ were tested. Hot-wire and total pressure probes were used for the aerodynamic measurements. This study focused in the generation of distortion profiles similar to in boundary layer ingestion fans in laboratory environment. A second preliminary study was performed by Caldas et al. (2019a) with the aim of evaluating the noise generated by the screens and perforated plates themselves. The same 100 mm diameter blower was used equipped with microphones. Measurements revealed that thick perforated plates (hole size dimension compared to the plate thickness) and a sharp leading edge can lead to the excitation of tonal noise sources. It was observed in this study, for a non-homogeneous velocity profile distribution and a given axial distance downstream the screen, the average sound pressure level captured by a microphone depends on its circumferential position relative to the velocity profile. Microphones placed in the velocity deficit region (low-flow speed) measured lower sound levels than to ones placed in higher-flow speed position.

6.1. Test rig configuration for inflow distortion (boundary layer ingestion - BLI) experiments

Thanks to the modularity of the CRAFT test rig, the inlet duct can be rearranged to allow measurements with distorted inflow. Fig. 6.1 shows a qualitative sketch of the test rig configuration for inflow distortion measurements, and on Fig. 6.2 a cross-section CAD drawing of the CRAFT test rig for the same measurement configuration. The aerodynamic distortion plane is found in the inlet at plane E1, right downstream the bell-mouth, labeled as “BLI” in Fig. 6.2. The flow distortion is generated with the help of perforated plates (or screens). A honeycomb (made out of stainless steel, 25.4 mm (1”) deep, hexagonal cell size of 6.25 mm (1/4”), and wall thickness of 0.2 mm, same shown in Chapter 5) was installed downstream of the screen to provide structural support and to guarantee flow straightness.

The distortion screens used are made of 1 mm thick aluminium perforated plates. The plates were cut in different sizes (height), generating more or less flow distortion by covering more or less the duct cross-section area. More detail about each screen configuration is given in the next section. The section containing the distortion screen and honeycomb is mounted in a circumferential traverse, allowing it to rotate 360° with the help of a servo motor. In Fig. 6.1, the dotted line further downstream of the honeycomb indicates, where aerodynamic measurements are performed: the plane E3, compare Fig. 6.2. On the top of Fig. 6.1, a rough sketch of how a generic normal Reynolds-stress and boundary layer profile along the duct diameter for a BLI configuration typically looks like is depicted. A

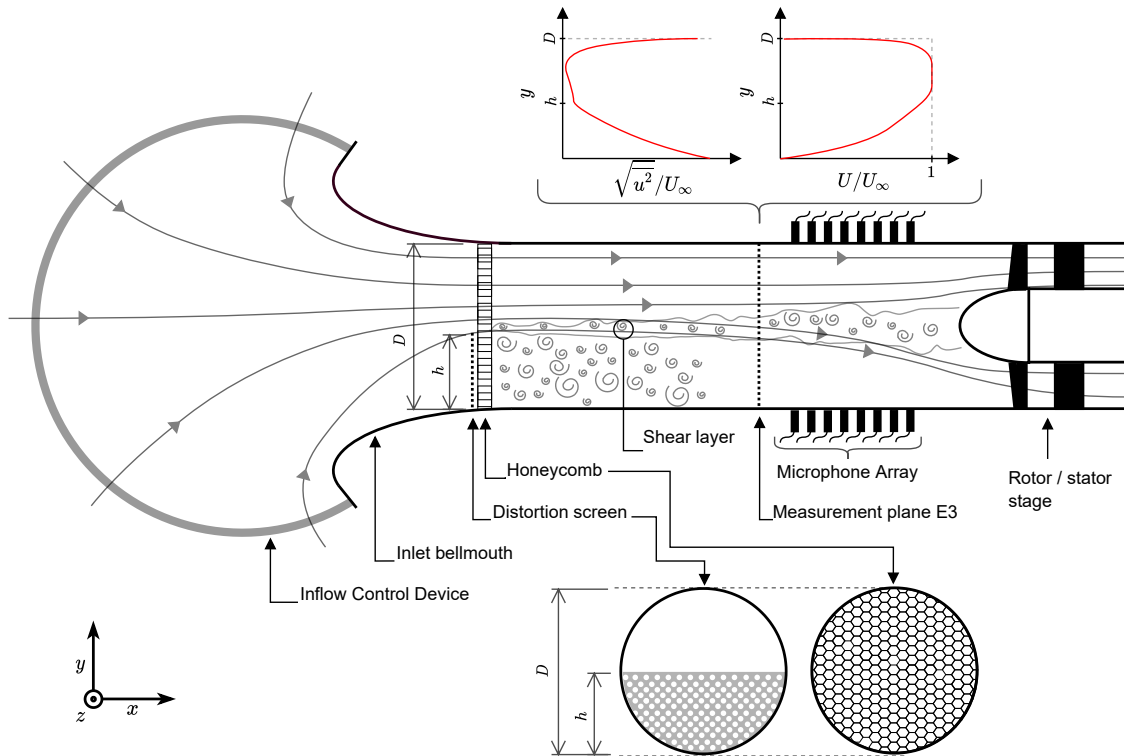


Figure 6.1.: Sketch of the CRAFT rig configured for inflow distortion experiments.

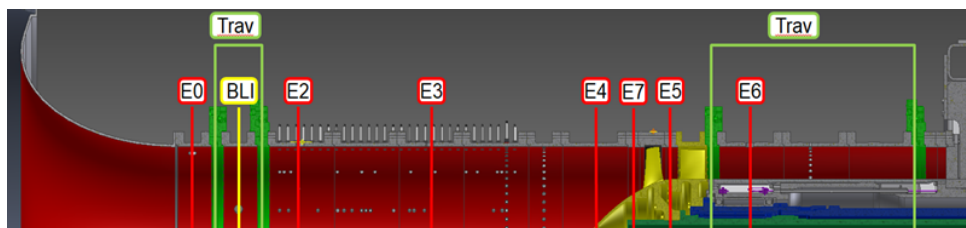


Figure 6.2.: Cross-section and measurement planes of the CRAFT test rig configured for inflow distortion experiments.

microphone array is also sketched and was used to assess the sound field emitted by the fan. Further downstream, the rotor-stator stage is depicted in black.

6.2. Test cases measured

Five test cases were measured in total. This includes the baseline configuration, which consists of the honeycomb alone installed in the channel, without distortion screen. Table 6.1 describes all configurations, as well as the sketch in Fig. 6.3.

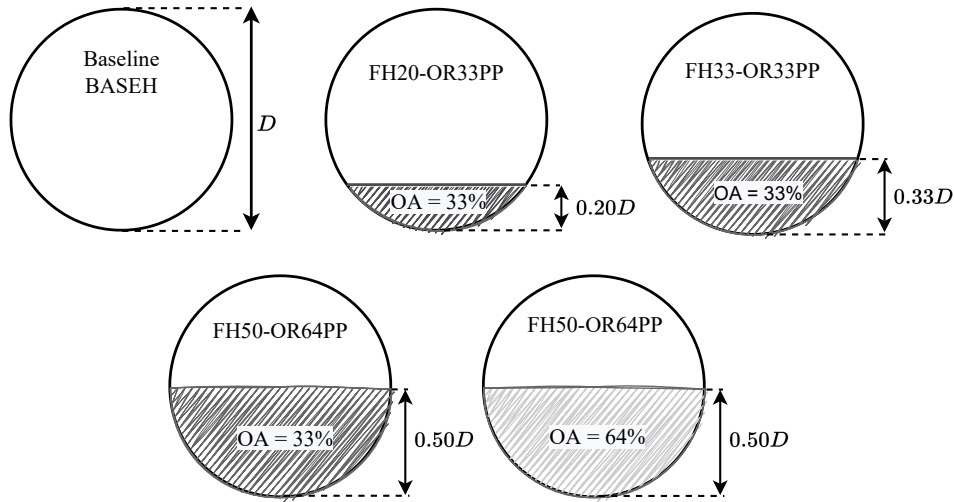


Figure 6.3.: Sketch of the distortion screens used.

Test case	Screen height, % of D	Screen height, mm	Screen open area, %
Baseline	-	-	-
FH20-OR33PP	20	91	33
FH33-OR33PP	33	150	33
FH50-OR33PP	50	227	33
FH50-OR64PP	20	227	64

Table 6.1.: Inflow distortion test cases.

A view from the rig's inlet is shown for each test case, see the photographs in Fig. 6.4. These perforated plates were selected from available materials and were not designed to generate a specific total pressure distribution as in Gunn and Hall (2014). As an initial study, the height of the screens were selected based visually and roughly on the height of distortion profiles observed in the references. The systematic variation of the screen height allowed the generation of more or less distorted velocity profiles for a fixed open area screen. This was made with the 33% OA screen, for which in total three different configurations were tested: FH20-OR33PP, FH33-OR33PP, and FH50-OR33PP. In this nomenclature FH stands for fence height, OR for open area ratio, and PP for perforated plate. A fourth screen with the same height as the highest from the previous set, but

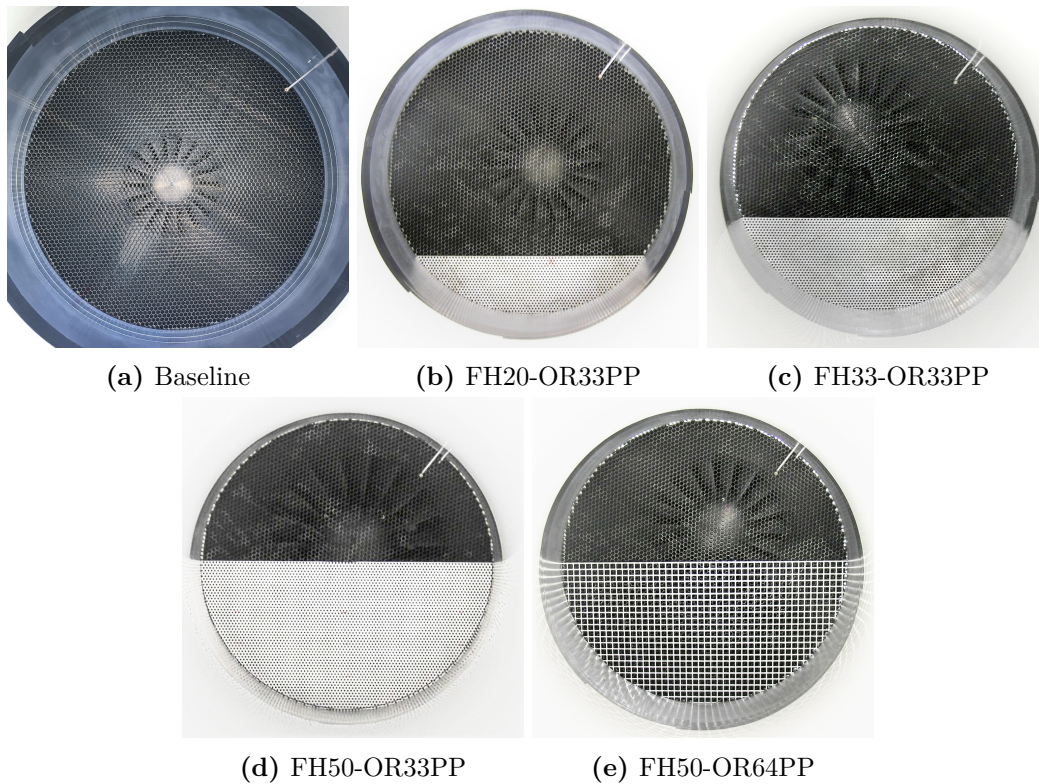


Figure 6.4.: Inflow distortion screens mounted on a honeycomb structure.

with 64% open area, was also selected, the FH50-OR64PP screen. This screen allows the comparison of the influence of a smaller velocity deficit in the flow profile, but approx. the same distorted area in the flow field.

6.3. Fan operation point adjustment

One important aspect of measurements with distorted inflow is the correct determination of the fan operating point. Due to the non-homogeneity of the flow velocity along the duct cross-section, the precise determination of the mass flow can no longer be assessed with a single pitot tube. An exception for that is if the pitot tube can be placed far enough upstream of the distortion device, hence avoiding its upstream effect. This was not possible in the current test setup due to space restrictions. Instead, a pressure rake (one, or multiple) combined with a circumferential traverse is necessary to allow a complete mapping of the duct cross-sections total pressure distribution downstream the distortion device. Once the whole area is measured, the mass flow can be determined by integrating the axial velocity as a function of r and θ , as in Eq. A.1.1. In the CRAFT test rig, a single pitot tube is placed at 100 mm upstream of the distortion plane and 50 mm downstream the bellmouth. It is used as reference for inlet flow velocity (or equivalently mass flow) measurements in uniform inflow conditions. For distorted inflow measurements, however, for a constant throttle position and fan speed, the flow velocity measured by the pitot

tube depends on its relative position to the distortion screen. This is because the pitot tube is only 100 mm upstream of the distortion plane, which is not enough to avoid its upstream impact on the streamlines. In order to overcome this problem, measurements were performed with two pressure rakes installed at plane E3 (see Fig. 6.2) and the pitot tube at the inlet. At several circumferential positions of the distortion plate were measured in order to estimate the mass flow. This process was performed for 4 different throttle positions. The estimated mass flow obtained using the pressure rakes for each throttle position could thus be correlated with the pressure measured by the pitot tube. In other words, the mass flow could be determined as a function of the pressure measured by the pitot tube (similar to a calibration curve, which was unique for each distortion screen), allowing a precise adjustment of the fan operating point using only the inlet pitot tube and the pressure rakes removed from the channel. Due to the disturbances caused by pressure rakes-induced wakes, the procedure aforementioned was a requirement for the acoustic measurements.

The aerodynamic analyses shown in this work refer to a fixed throttle position and fan speed. For this reason, as further shown in Table 6.1, the mean flow speed is slightly different depending on the study case, and therefore, different flow coefficients ϕ , which are slightly smaller for the BLI cases compared to the baseline configuration. For the aerodynamic result analysis this is not an issue, as the results are normalized by the mean flow velocity. For the acoustic experiments, indeed, the exact operation point was necessary to be adjusted, as noise emissions scale with the mean flow speed, more precisely, Klähn et al. (2022c) observed a scaling factor in the range of approx. $4 < \gamma < 5$ in the relation $P \propto M_{\text{tip}}^\gamma$ where P is the broadband sound power emission and M_{tip} the blade tip Mach number.

For the calculation of the corrected mass flow, as in Eq. A.2.10, the total pressure of the flow is taken into account. In a distorted inflow experiment, however, this pressure is not constant over the duct-cross section. The solution adopted in this work was to use the maximum total pressure captured by the total pressure rakes. This value represents the least distorted point in the flow or the point with least pressure drop along the rig's inlet. Hence, it is used as indication of an undisturbed flow condition. Analogously, in the case of an engine mounted on the fuselage of an aircraft, this pressure would be equivalent to the free-stream total pressure or the ambient pressure.

6.4. Aerodynamic and acoustic instrumentation

Total pressure measurements were performed with the help of two pressure rakes comprising 8 channels each, as described in Chapter 4. The two rakes were installed at the measurement plane E3, see Fig. 6.2. The distortion device was traversed in the circumferential direction in 2.5° steps, covering the whole 360° circumference. This resulted in

144 measurement points. Measurements with pressure rakes were performed at two fan operating points: $\eta_c = 2250$ RPM and $\eta_c = 4500$ RPM. For both cases, the throttle device was kept at a fixed position that produces a flow coefficient for $\eta_c = 4500$ RPM of approx. $\phi = 0.40$.

Two hot-wire probes were used in this test setup to assess all three velocity components. Each probe was mounted in a radial traverse, allowing the probe to travel up to 300 mm inside the channel. Both the hot-wire probes and the traverse mechanism were described in Chapter 4. The probes were mounted 17° apart at the plane E3 (Fig. 6.2). For each measurement position, 5 seconds of data were acquired sampled at $f_s = 192$ kHz. Measurements were performed at two operating points, similar to the pressure rake measurements. Radial sweeps from 2 mm to 300 mm (distance from the duct inner wall) containing in total 20 radial positions were performed.

As the hot-wire probes were mounted 17° apart in order to capture the turbulence field for the three velocity components using two probes, two circumferential positions of the distortion screen were needed for each fan operating point. The first run was done with the (u,v) probe travelling perpendicular to the distortion screen top edge. For the second run, the distortion screen was traversed by 17° , allowing the (u,w) probe to be at the same previous position of the (u,v) probe, relative to the distortion screen, perpendicular to the distortion screen top edge. This allowed the full assessment of the turbulence field of the three velocity components with two probes in the axis perpendicular to the screen height edge.

The microphone ring (R1.2) and axial (AX1) arrays were used for the acoustic measurements, as introduced in Chapter 4 and shown in Fig. 4.9. For the acoustic measurements, two fan speeds were tested: $\eta_c = 4500$ RPM and $\eta_c = 2250$ RPM, combined with five flow coefficients: $\phi = \{0.28, 0.30, 0.33, 0.36, 0.40\}$. For the precise adjustment of the fan operating point the mass flow (and therefore the flow coefficient) were adjusted following the procedure described in Section 6.3. For each fan operating point, 30 seconds of data were simultaneously acquired from all microphones at 65.536 kHz sampling rate.

6.5. Aerodynamic analyses

The results presented in this work refer to a fan operating point of: fan speed $\eta_c = 4500$ RPM, flow coefficient $\phi \approx 0.40$. A compilation of the most relevant stationary aerodynamic parameters is listed in Table 6.1. It is worth comparing the aerodynamic parameters like mean flow speed \bar{U} , the undisturbed flow speed U_∞ , and the Mach tip speed M_{tip} for each test case. The more pronounced the inflow distortion, for example with the screen FH50-OR33PP, the greater the discrepancy between these two velocities is. For this screen, most of the mass flow is concentrated at half of the duct, which is translated into high-flow speeds in one sector, and low-speeds in the other. The blade tip Mach number M_{tip}

shown was obtained by the resultant velocity vector formed by the circumferential velocity (ΩR) and the maximum axial speed U_∞ . The column showing ϕ (max, min) are a rough estimation of the two outermost flow coefficients experienced by the fan blades. Ideally, for a better understanding of the aerodynamic of the fan under distorted inflow conditions, it would be useful to compute precisely the variation in angle of attack experienced by the fan blades due inflow distortion for each tested case. However, the complexity of such effort is outside the scope this thesis. Instead, a rough estimation of the flow coefficient was computed for the two outermost flow velocity regions. The Eq. A.1.3 was used to compute the two flow coefficients. The highest ϕ is based on U_∞ , whereas the lowest on the lowest mean speed (outside the duct wall boundary layer) as shown in Fig. 6.5. As mentioned in Chapter 5, it is known from experiments that this fan stalls for $\phi \approx 0.26$. Therefore, flow coefficients bellow this number indicate potential local stall. In Table 6.1 this is observed for all 33% OA perforated plates. It is also worth mentioning, the increase in the difference between the max and min flow coefficients of each test configuration with the increase in the disturbance height.

Test case	\bar{U} , in m/s	U_∞ , in m/s	ϕ min, max	M_{tip}	δ_{99} , in mm	δ^* , in mm	θ	H
Baseline	42	44	0.40, 0.40	0.336	16	3.1	2.2	1.38
FH20-OR33PP	42	49	0.16, 0.45	0.341	212	67	32	2.12
FH33-OR33PP	41	55	0.18, 0.50	0.349	291	112	45	2.48
FH50-OR33PP	38	65	0.21, 0.60	0.363	357	173	59	2.93
FH50-OR64PP	40	50	0.30, 0.46	0.343	269	74	52	1.44

Table 6.1.: Aerodynamic characteristics of each test case. Fan operating point: fan speed $\eta_c = 4500$ RPM, flow coefficient $\phi \approx 0.40$. Parameters measured at plane E3, see Fig. 6.2.

With respect to the boundary layer thickness characterization, even though the δ_{99} -boundary layer is well appropriate for BLI test cases, when there is a free-flow around the object of study, as reported for wind-tunnel tests by Hickling et al. (2019), Gonzalez-Martino and Casalino (2019) and Morton (2012). For in-duct measurements, however, it does not seem to be very useful. In the first, measurements are often performed with constant free-stream velocity U_∞ , or in a parametric way on few different speeds. For fan experiments however, the mass flow (which is linked with the fan's thrust) is often the parameter to be kept constant among different configurations. Therefore, the average flow speed \bar{U} , which is a linear function of the mass flow, is preferred over U_∞ as the parametric magnitude.

Another relevant result is the comparison of the parameters obtained for screens FH50-OR33PP and FH50-OR64PP. Both screens share the same height, but different open area ratio. As consequence, the screen with higher blockage generated a 33% thicker δ_{99} boundary layer compared to the one with more open area. The displacement thickness δ^* was more than double for this test case comparison.

6.5.1. Velocity distribution profile

Results from the measurement performed with pressure rakes are displayed in terms of the local velocity $U(r, \theta)$ normalized by the free stream velocity U_∞ , shown in Fig. 6.5. The dashed lines show the height of each respective screen. The velocity deficit generated by the 33% open area screen is approx. 30% of the undisturbed flow. This represents a factor of approx. 3.

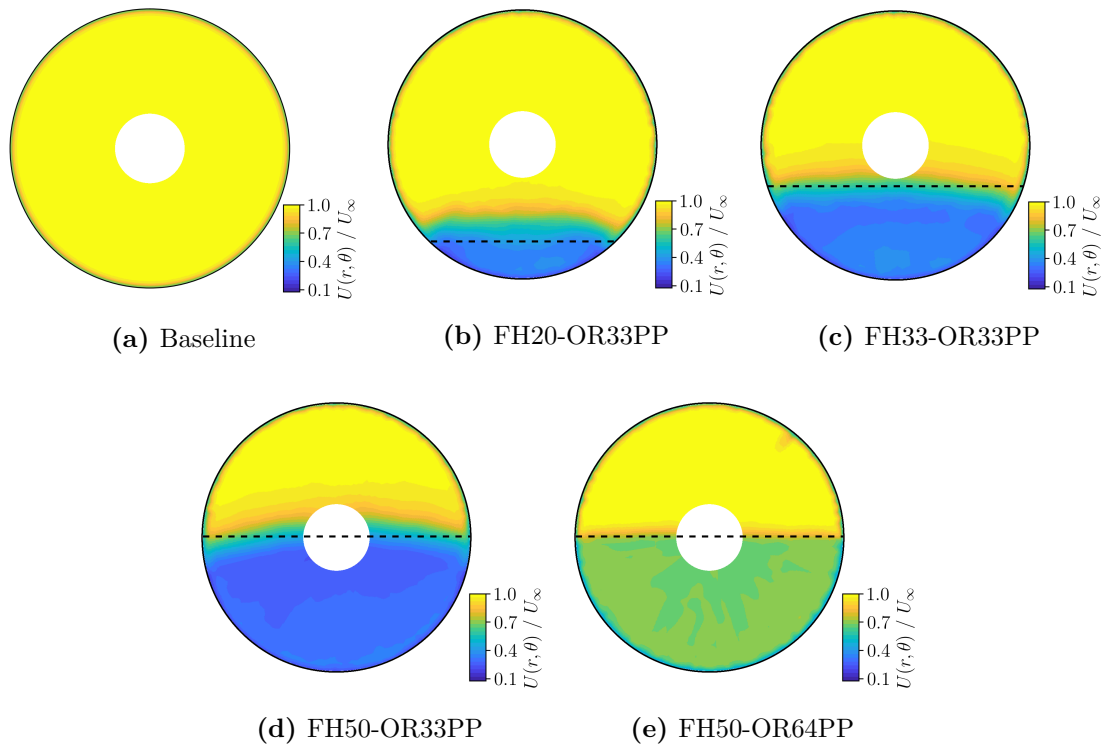
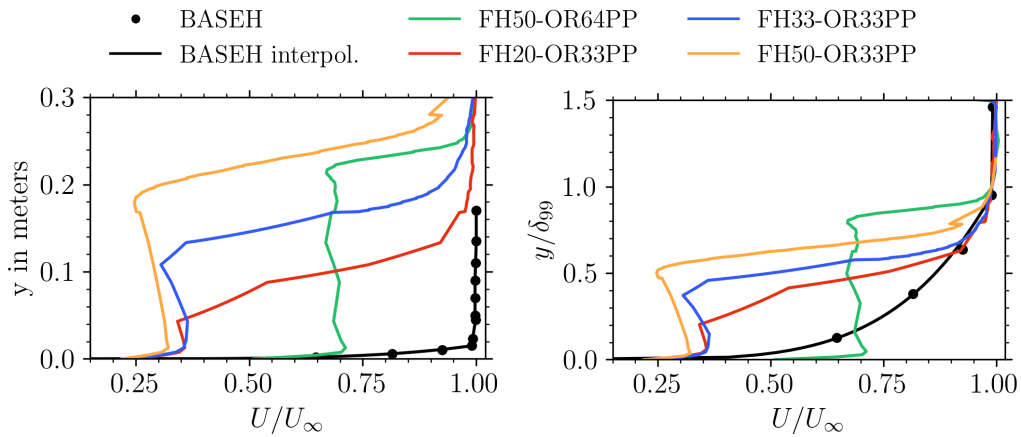


Figure 6.5.: Normalized mean axial velocity distribution measured with pressure rakes. Fan operating point: fan speed $\eta_c = 4500$ RPM, flow coefficient $\phi \approx 0.40$. The dashed line indicates the respective distortion screen height.

For the 33% open area screens, it is observed that the mean velocity inside the distorted area ranges from 20% to 40% of the mean free stream speed. Comparing results from the 33% open area screens with those from the 64% open area one, we observe that for the latter the transition area is straighter and sharper. Although the honeycomb placed right downstream the screen guarantees that the flow stream lines are straight and parallel, it is unclear whether the flow is absent of counter rotating vortices in the junction of edge of the screens, duct wall, and free stream. Gunn and Hall (2014) assessed the three-dimensionality of the flow in a similar experimental setup. In their work, however, this effect was reported at axial positions close to the fan, as a consequence of the flow redistribution forced by the rotating fan. The flow stream lines were assumed to be parallel to each other right downstream the distortion screen.

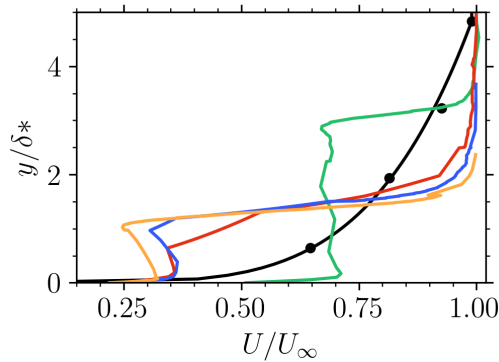
6.5.2. Boundary layer profile

The velocity profile along the diameter line perpendicular to the distortion screen top edge is plotted in Fig. 6.6. The velocity is normalized by the free stream velocity U_∞ . Fig. 6.6a shows the normalized velocity profile versus the normal distance from the duct wall. In this figure, the distance was not normalized and is shown in meters.



(a) Normalized velocity profile versus the normal wall distance in mm.

(b) Normalized velocity profile versus the normal wall distance normalized by the boundary layer thickness δ_{99} .



(c) Normalized velocity profile versus the normal wall distance normalized by the boundary layer displacement thickness δ^* .

Figure 6.6.: Boundary layer profile of all tested cases plotted with different wall distance normalization. Fan operating point: fan speed $\eta_c = 4500$ RPM, flow coefficient $\phi \approx 0.40$.

For the “BASEH” (baseline) test case two curves are shown: one with circles representing the measured data, and the solid line resulted from an interpolation. As only few points were measured inside the boundary layer for the baseline case (few ports available in the pressure rake used), for a more precise computation of parameters like displacement thickness and momentum thickness, an interpolation was necessary. The curve was interpolate inside the boundary layer ($y < 15$ mm) using a power-law velocity function

(Kudela (n.d.))

$$\frac{U(y)}{U_\infty} = \left(\frac{y}{\delta_{99}} \right)^{(1/n)}, \quad (6.5.1)$$

where n is a parameter to be adjusted in order to fit the velocity function $U(y)$ with the measurement data. With the tested input data, the parameter obtained was $n = 4.8$. According to this reference, for turbulent boundary layers this parameter is typically around $n = 7$.

In Fig. 6.6b, the normal distance from the wall is normalized with the δ_{99} -boundary layer thickness. The fitted data respective to the baseline case is better visible in this figure. We observe from this plot that the velocity profile from the screens with 33% OA do not group together, meaning the velocity profile does not scale with the δ_{99} -boundary layer thickness. Interestingly, the velocity profile of the plate FH50-OR64PP (green curve) stays fairly constant in the distorted region. This behaviour differs from the 33% OA screens. Another aspect to be noticed is the negative derivative of the velocity profile for the 33% OA screens in the region between the wall boundary layer and the screen edge shear layer. This behavior leads to two transition points in the pressure gradient signal. The first transition happens in the transition from duct wall boundary layer at approx. $y/\delta_{99} = 0.1$ or $y = 15 \text{ mm}$ (velocity start to decrease) and the second happens, when the velocity profile finds a local minimum and starts to rise again, at $y/\delta^* \approx 1$ in Fig. 6.6c.

Fig. 6.6c shows the same velocity profiles, but now the distance from the wall is normalized with the displacement thickness δ^* . It seems an appropriate boundary layer thickness normalization parameters, hence when used, the profiles generated by the 33% OA screens group all together.

6.5.3. Reynolds Stresses

The Reynolds stresses were assessed from the hot-wire data measured along the diameter line at the measurement plane E3. The power spectral density (auto- and cross-) of each velocity component obtained from the hot-wire anemometry was first computed. The Welch method (Percival and Walden (1993)) was used with Hann window type and 50% data block overlap. The window size produced a frequency resolution of 12 Hz. The normal and shear Reynolds stress were obtained with the help of Eqs. 2.3.8, 2.3.18, and 2.3.19, introduced in Section 2.3.3. Results computed for all test cases are depicted in Fig. 6.7. Note that the normalization velocity is the local mean speed U of every measurement point, and not U_∞ , as typically utilized in wind-tunnel tests. The results for the baseline case are shown with a different xy axis scale for better visualization, as the values are much lower than the BLI ones.

The curves shown in Fig. 6.7a for the baseline configuration agree well with those obtained from experimental as well as simulation data as in Hickling et al. (2019), Gonzalez-Martino

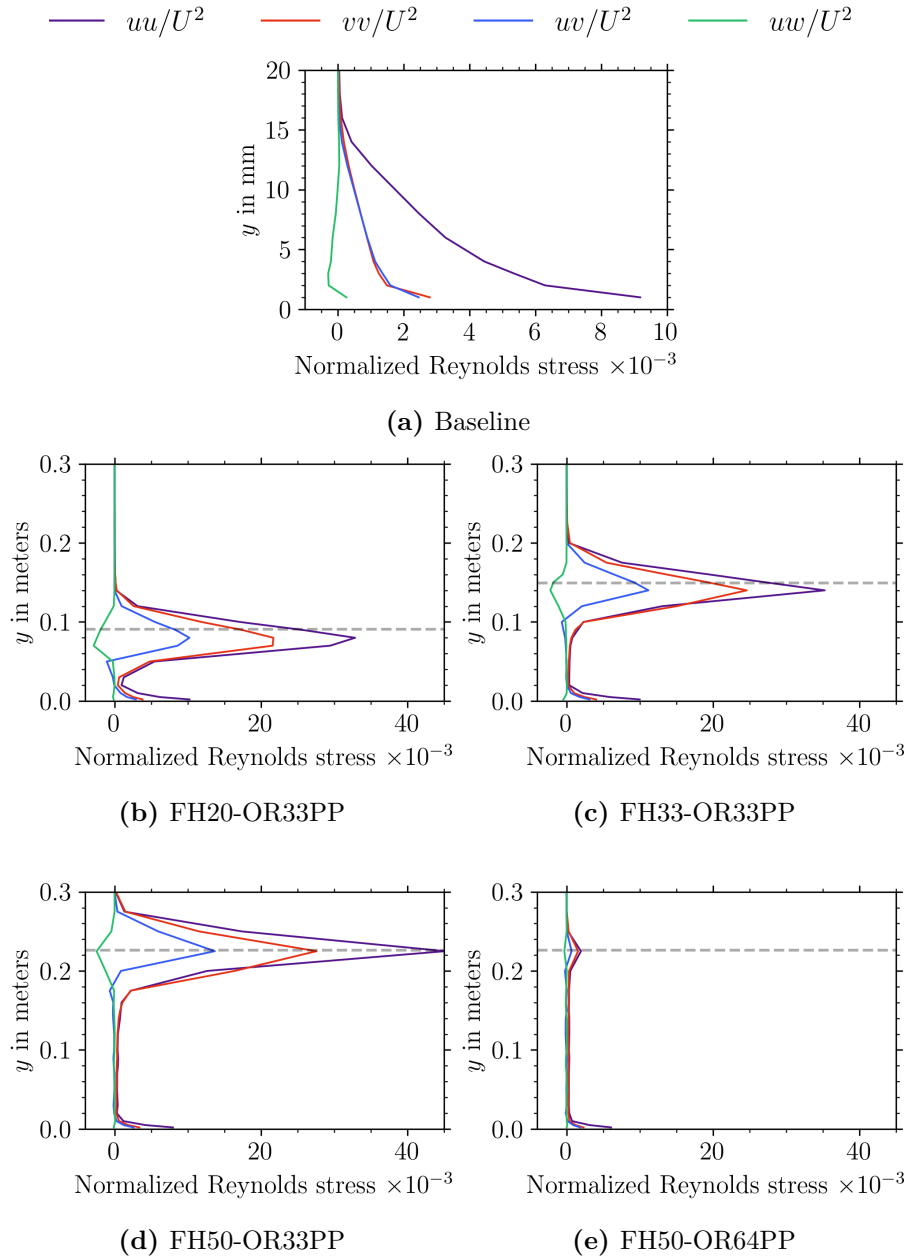


Figure 6.7.: Normalized normal and shear Reynolds stresses. Note that the normalization velocity is the local mean speed U and not U_∞ . Note also that the baseline plot (a) has different axes scaling. Fan operating point: fan speed $\eta_c = 4500$ RPM and flow coefficient $\phi \approx 0.40$. Dashed line indicates the respective distortion screen height.

and Casalino (2019), Morton (2012), Staggat (2021) and Staggat et al. (2019). The shear stress uv has values similar to the normal stress vv , which is a hint that the normal stress in the axial direction dominates in this flow field. For the four BLI configurations, a strong peak is observed for all Reynolds stresses at a radial position corresponding to the screen height. This is expected due to the shear layer created by the sharp transition from the screen to the free flow. The values reached in these peaks overcome the ones measured inside the wall boundary layer by a multiple of times. The screen with higher open area

(FH50-OR64PP) generated much less stresses in the shear layer compared to the other BLI test cases.

The stress levels inside the distorted flow region, outside the wall boundary layer and the shear layer are comparable to the levels in the free flow. In other words, despite of the velocity deficit in this region, the turbulence levels in this region are much lower than they would be expected inside a boundary layer, due to BLI. This leads to the conclusion that these screens are capable to generate a distorted mean velocity distribution, but do not increase considerably the flow turbulence levels.

6.5.4. Turbulence intensity and integral length scale

The turbulence integral length scale profile was computed from the hot-wire data for the same dataset as for the Reynolds stresses. The assumptions of “frozen turbulence” (Taylor condition) and HIT were taken, which means the equations introduced in Section 2.3.1 were used to compute the ILS. Fig. 6.8b shows the results for all test configurations for the axial (longitudinal) velocity component. Solid lines refer to the $\eta_c = 4500$ RPM test case, whereas the dashed lines to the $\eta_c = 2250$ RPM test case. The lower fan speed test case was added in this section for comparison against the higher fan speed. The ILS values were normalized by the rotor blade chord length $C = 62$ mm. This normalization is not linked to any turbulence generation mechanism. Instead of that, it is useful to give an idea of the coherence length of structures compared to the rotor chord length. This relationship information is relevant for the acoustic analysis, as the interaction of long turbulent structures with the rotating blades produces partly coherent noise sources (Staggat (2021) and Staggat et al. (2019)).

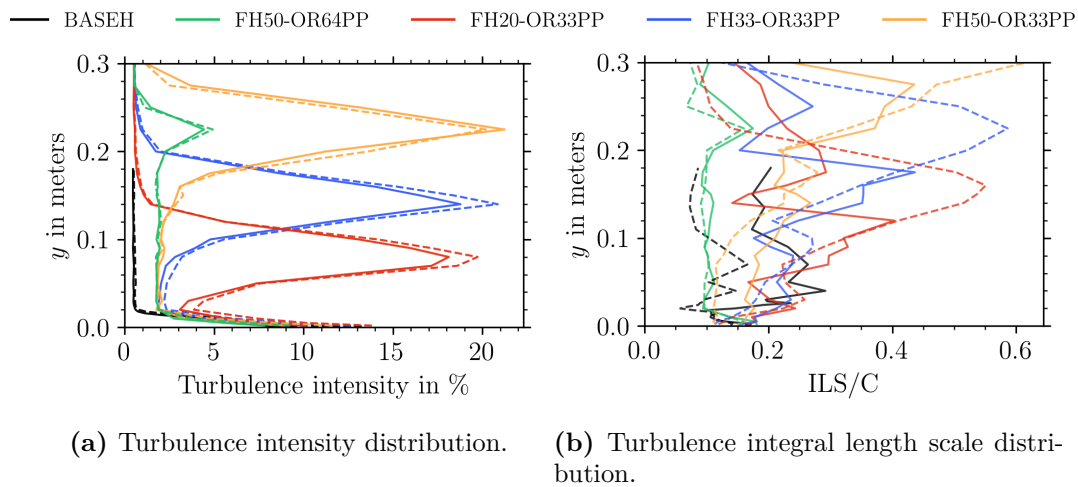


Figure 6.8.: Turbulence parameters of all screens tested plus the baseline test case. The axial velocity component is analyzed. Solid lines refer to the $\eta_c = 4500$ RPM test case, whereas the dashed lines to the $\eta_c = 2250$ RPM test case.

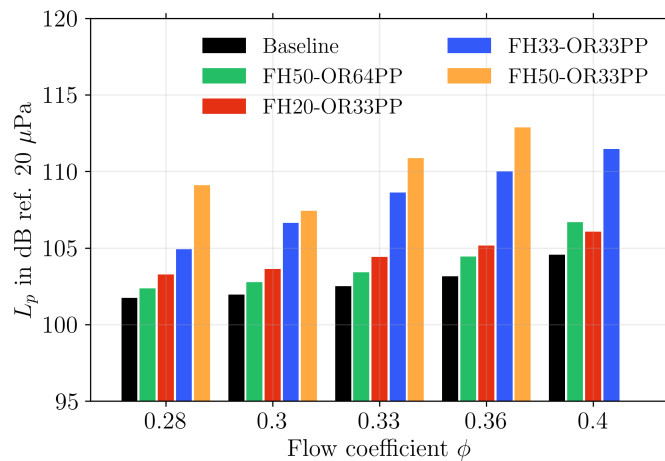
For the baseline test case (black curves), the values range from $0.1C$ to $0.3C$. The curves reach their minimum inside the boundary layer and raise quickly towards greater wall distances. No specific trend is observed. For the 33% OA screens, few common trends are observed: The ILS values of all these curves increase continuously until reaching the radial position respective to the shear layer, or roughly the screen height. At this radial position, a maximum of the ILS value is found. For greater radial positions, the ILS values fall abruptly towards an average value of $0.2C$. The turbulence intensity distribution on the left-hand side (Fig. 6.8a) gives a rough idea of the center of the shear layer, where the shear stress reaches its maximum. For the turbulence intensity distribution, results are weakly affected by the fan speed, or equivalently, the axial flow speed. However, interestingly, the ILS distribution seems to depend on the axial flow speed. For the high fan speed test case, the maximum of each curve (red, blue and orange) are found at lower radial positions compared to the lower fan speed test case. Furthermore, the radial position of these peaks do not coincide with their respective maximum in the turbulence intensity profile, i.e., roughly the screen height. The reason for that could be the dependency of the shear layer profile and thickness on the mean axial flow speed. The FH50-OR64PP screen (green curve) produced a roughly constant $0.1C$ ILS throughout the distorted region. Its shape virtually did not change comparing the two fan speeds. Similarly, at the screens' height a peak is observed, but less pronounced (of about $< 0.2C$ compared to $\approx 0.4C$ for the 33% OA screens). This screen produced the lowest ILS values.

6.6. Fan acoustic analyses

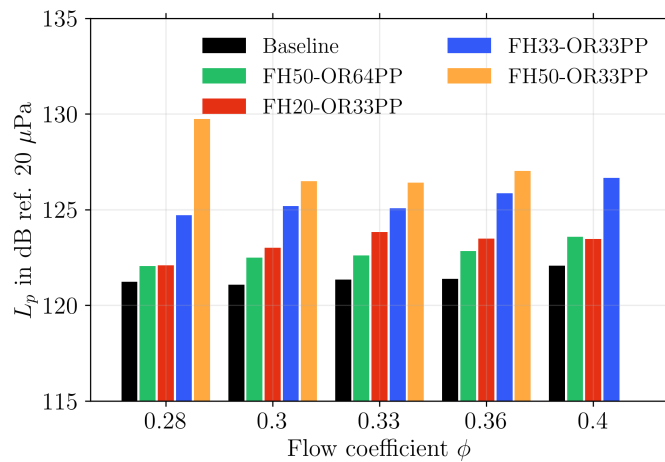
The acoustic analyses are based on the data measured by the microphone arrays installed on the inlet test section of the CRAFT fan rig as shown in Fig. 4.9. In this arrangement, the microphone arrays were installed downstream of the distortion screen plane. One issue resulting from this arrangement is the influence of the non-homogeneous flow field generated by the screens on the membrane of the microphones. A previous study with screens mounted in a duct channel and microphones flush mounted on the wall revealed that the sound pressure levels (broadband noise) captured by the microphones depend on their circumferential position relative to the screen (Caldas et al. (2019a)). It was observed that the microphones placed in the region subjected to lower axial flow speed captured slightly lower sound pressure levels than the ones placed in the region subject to higher flow speed. This is believed to be associated with the turbulence pressure fluctuation on the microphone membrane, as also reported by Bauers and Tapken (2012). A possible explanation for this phenomenon is that in the higher flow speed region, the boundary layer has a steeper gradient, what might excite higher turbulence levels compared to the region subject to lower axial velocity and therefore lower velocity gradient. For the CRAFT measurements with distortion screens, a similar effect was observed and it is reported in the following sections.

6.6.1. Overall SPL levels vs fan flow coefficient ϕ

An overview of the fan noise emissions due to inflow distortion is shown in Fig. 6.9. In order to compute the average sound pressure level (SPL, L_p) of each test case, first the PSD of each microphone from the R1.2 ring array was estimated. This PSD was averaged over all ring array microphones. This average PSD was in turn integrated to obtain the average SPL levels. Interestingly, the same trends are observed for both fan speeds. For $\eta_c = 2250$ RPM, a clear trend of increase in noise levels proportional to the flow coefficient is seen. An exception holds for the configuration FH50-OR33PP, which produces the most distorted flow. Regarding the test combination of this screen and the flow coefficient $\phi = 0.28$, we believe that, because of the low axial velocity inside the distorted flow region, flow separation might occur on the fan blades when they travel in the distorted flow region. This eventual local flow separation could explain the higher noise emissions detected for low flow coefficients.



(a) $\eta_c = 2250$ RPM.



(b) $\eta_c = 4500$ RPM.

Figure 6.9.: Comparison of the broadband sound pressure levels for all tested configurations as a function of the flow coefficient and two fan speeds.

The distortion screen FH50-OR64PP was, among the tested screens, the quietest configuration. In spite of its height, its higher open area produced a lower velocity deficit in the distorted region, as well as lower shear stresses as shown in Section 6.5. Due to these reasons, lower additional tonal and broadband fan noise were generated compared to the other screens. The screen FH20-OR33PP was the second quietest configuration. Despite of its lower height compared to the FH50-OR64PP screen, the FH20-OR33PP caused higher noise levels than the FH50-OR64PP. This is because of the higher turbulence levels generated in the flow shear layer (due to its lower open area ratio) and the lower flow velocity inside the distorted area.

Screens FH33-OR33PP and FH50-OR33PP have similar trends for the $\eta_c = 2250$ RPM test configuration: a progressive increase in SPL levels with the increase of the flow coefficient. The test case with $\phi = 0.40$ could not be achieved with the screen FH50-OR33PP due to its high pressure drop (high blockage). The strong velocity deficit generated by these screens as well as the great area comprising high turbulence levels due to the shear layer resulted in a remarkable increase in fan noise levels. For the test case $\eta_c = 2250$ RPM and $\phi = 0.33$, an increase of about 10 dB in the SPL level is observed due to the FH50-OR33PP screen.

6.6.2. R1.2 microphone ring array spectra vs angular position

For the sake of qualitatively analyzing the impact of the distortion screens in each individual microphone of the ring array, the spectrum of each array sensor as a function of its angular position is shown in Fig. 6.10, as reported by Klähn et al. (2022a). 0° refers to the top center, or the 12 o'clock position, when looking from the front towards the fan, as in Fig. 6.4. That means, 180° refers to the center underneath the distortion screens or the 6 o'clock position. The color scale was kept constant for all test cases, and for simplicity it is only once shown on the top of the baseline plot. The result for the baseline test case is depicted in Fig. 6.10a. For this configuration, within a certain tolerance margin, all spectra seem identical for the microphones in the ring array.

Regarding the tests with inflow distortion, however, this statement no longer holds true. Fig. 6.10b shows the microphone spectra for the screen FH20-OR33PP. In this plot, in the lower frequency band ($f/\text{BPF} \lesssim 1$) higher SPL were recorded by the microphones placed at approx. 140° and 220° . This angular position is equivalent to the height of the distortion screen. At this position, the shear layer generated by the screen meets the duct wall. As a consequence, the high shear stresses and turbulence levels generated induce high levels of pressure fluctuations on the microphone membrane. In other words, what we see is not expected to be fan noise related. Instead of that, it is due to pressure fluctuations resulting from the strong turbulence intensity (sometimes also called hydrodynamic pressure). The same effect is observed for all screens with 33% open area ratio. For tests with the screen

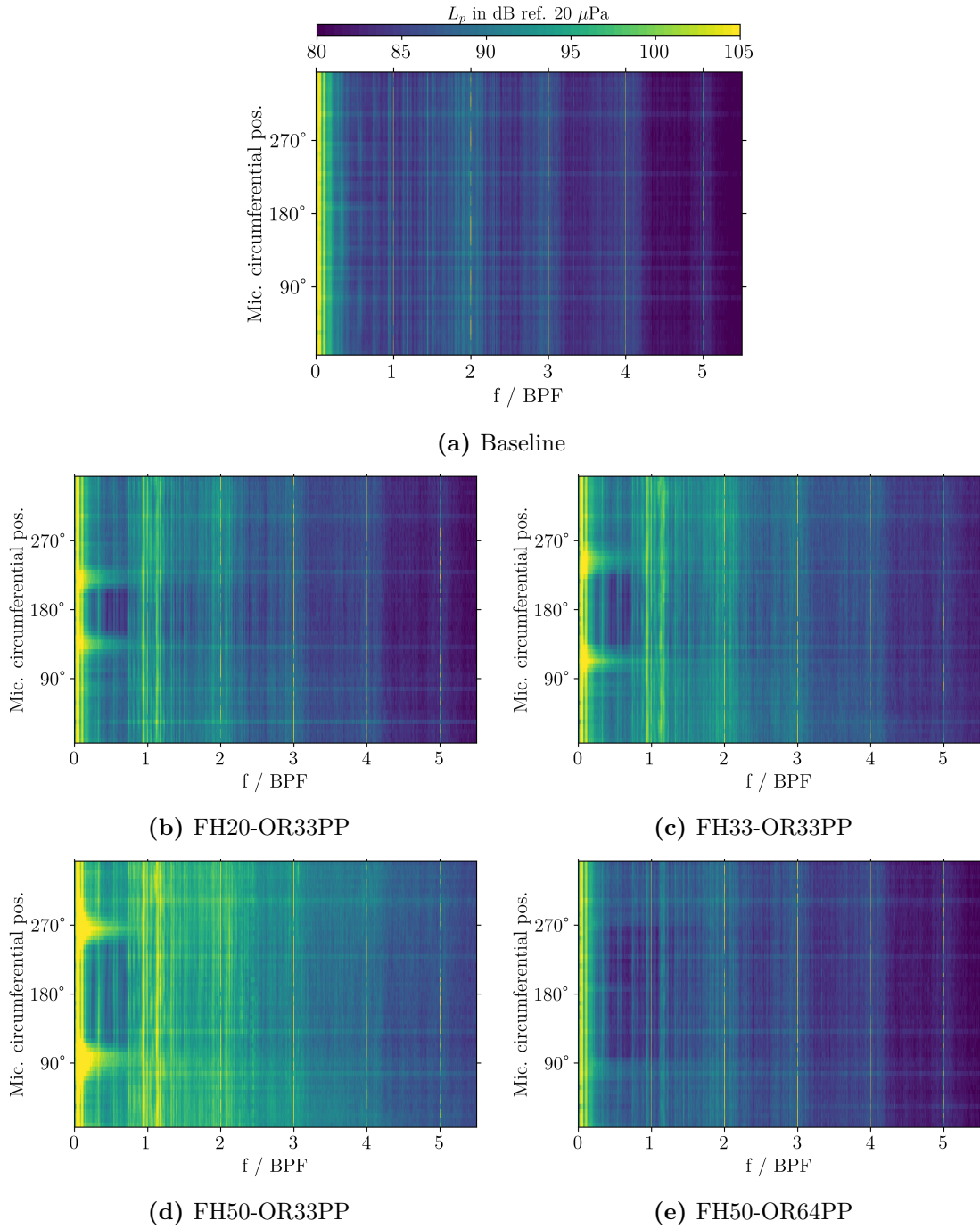


Figure 6.10.: Spectra of all 59 microphones from the R1.2 ring array as reported by Klähn et al. (2022a). Fan operating point: $\eta_c = 4500$ RPM and $\phi = 0.33$.

FH50-OR64PP, this effect is virtually not observed or rather very weak. Furthermore, the microphones placed inside the distorted flow region and outside the area equivalent to the screen height measured slightly lower SPL than the other ones. For instance, in Fig. 6.10b for the microphones placed in the region bounded by 140° , 200° , and $f/BPF \lesssim 1$, the dominant color seen is the dark blue, compared to green for the other microphones. A similar effect was observed in a previous study (Caldas et al. (2019a)).

Another relevant phenomenon to be highlighted from these plots is the increase in broadband levels around the first BPF ($f/BPF \simeq 1$). Especially for the 33% open area screens, strong narrowband components are observed in the frequency band around the first BPF. This effect was maximized by the screen FH50-OR33PP. A possible explanation for this is, on the one hand, the high turbulence levels found in the flow shear layer produced by this screen covers a higher duct area, when compared to the other 33% OA screens. Additionally, for a given mass flow, the higher the screen height is, the higher the velocity difference between the distorted and non-distorted regions become. For the 33% OA screens, the mean flow speed inside the distorted area is approx. 30% of the free-stream, as shown in Fig. 6.5. On the other hand, the increase in flow speed leads to an increase in the broadband rotor-stator interaction noise (Klähn et al. (2022c)). These facts help understanding the increase in broadband noise observed, especially in the frequency band mentioned, and why this effect is more pronounced for the screen FH50-OR33PP.

6.6.3. Sound power levels: Combined axial and azimuthal sensor array technique - CAAS

The combined use of both axial AX1 and ring R1.2 arrays allows a complete sound field mode breakdown of the broadband components into its radial and circumferential (azimuthal) mode constituents. A more detailed description of the technique can be found in Tapken et al. (2019, 2014). For simplicity, in this section we focus only on the baseline and the two distortion screens: FH20-OR33PP and FH50-OR33PP. Fig. 6.12 shows the results both as absolute sound power values (L_w), as also the difference against the baseline test case (ΔL_w) for the fan operating point $\eta_c = 4500$ RPM and $\phi = 0.33$, as reported by Klähn et al. (2022a). Results for the fan operating point $\eta_c = 2250$ RPM and $\phi = 0.33$ are shown in Fig. 6.11. The y -axis shows the circumferential mode order m , whereas the x -axis the engine order (frequency). All the radial mode orders are summed up for every (x, y) pair combination.

Figs. 6.11a and 6.12a portray the CAAS modal power breakdown for the baseline test case for the 50% and 100% fan speed, respectively. A clean and reasonably symmetric (up to $EO \simeq 40$) map is observed. The high power seen for m around zero and $EO > 80$ in Fig. 6.12a is due to the limit of the array in resolving high frequencies. For $EO > 40$, slightly more power concentrates in the negative spinning mode orders. The CRAFT fan rotates in the counter-clock wise direction (when looking from the front), which in the reference system used means negative spin direction. In our understanding, the noise sources located downstream of the rotor (for example rotor-stator interaction noise - RSI) propagating upstream has to travel through the rotor. For modes with same spinning direction (negative) this propagation occurs more efficiently. For positive mode order, however, this propagation occurs less efficiently and the rotor works in fact as a shield

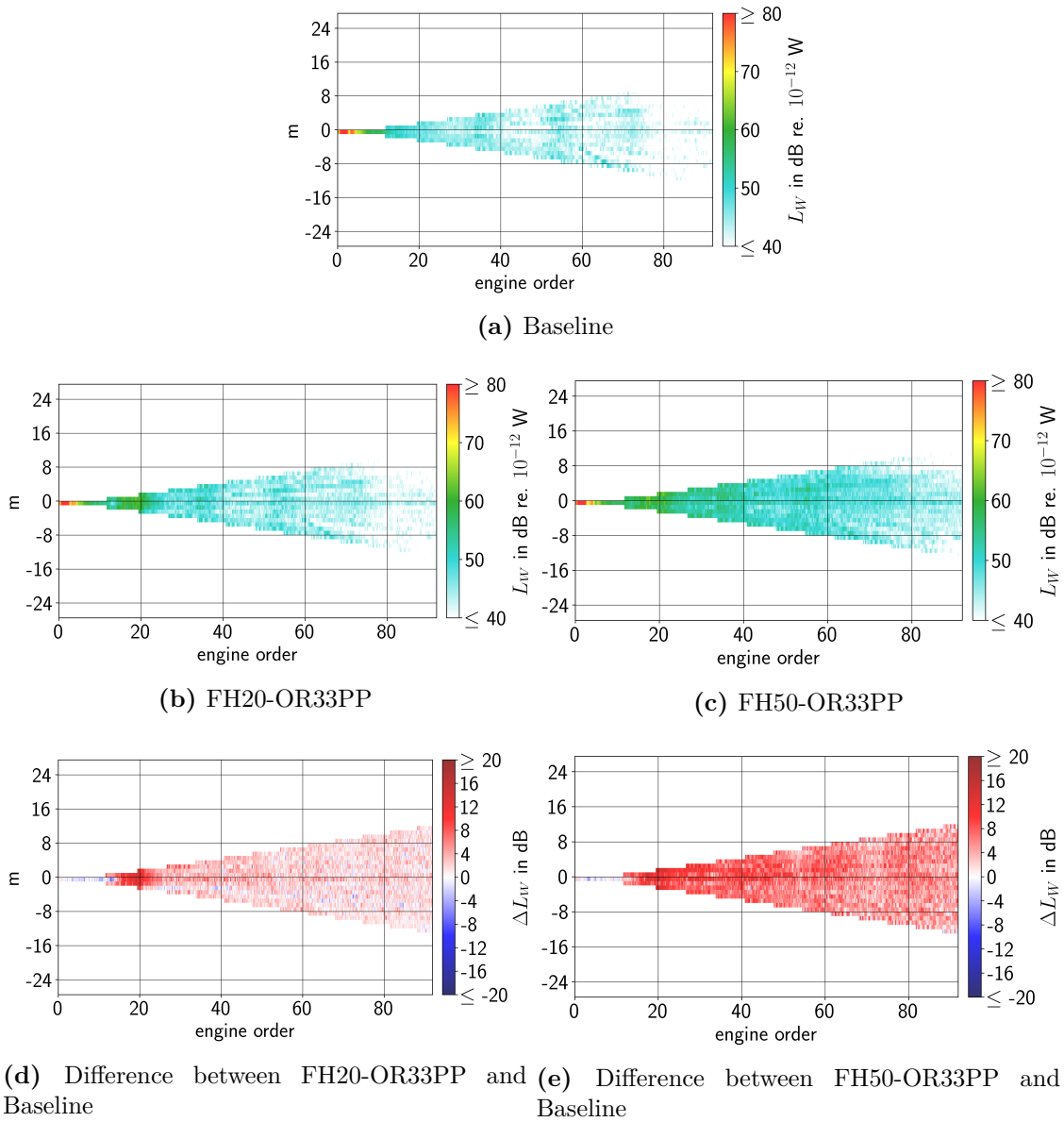


Figure 6.11.: CAAS broadband modal sound power level summed up over all upstream propagating radial modes. The baseline and the two distortion test cases are shown. Fan operating point: $\eta_c = 2250$ RPM, $\phi = 0.33$.

for these modes. This might explain the slightly higher power content in the negative circumferential modes part of this plot compared to the positive ones.

The first distorted test case displayed in Fig. 6.12b refers to the distortion screen FH20-OR33PP. By contrasting this figure against Fig. 6.12a, the increase in power mainly in the frequency band around $EO \simeq 20$ becomes evident. No mode was particularly over-excited. Instead, a broadband of modes had their power raised for this configuration. Fig. 6.12d shows the difference between figs. 6.12b and 6.12a, where this effect is highlighted. In Fig. 6.12d, it is clearer observed that modes in the cut-off border are excited for a broad range of frequencies. Due to the stochastic behavior of turbulence and its interaction

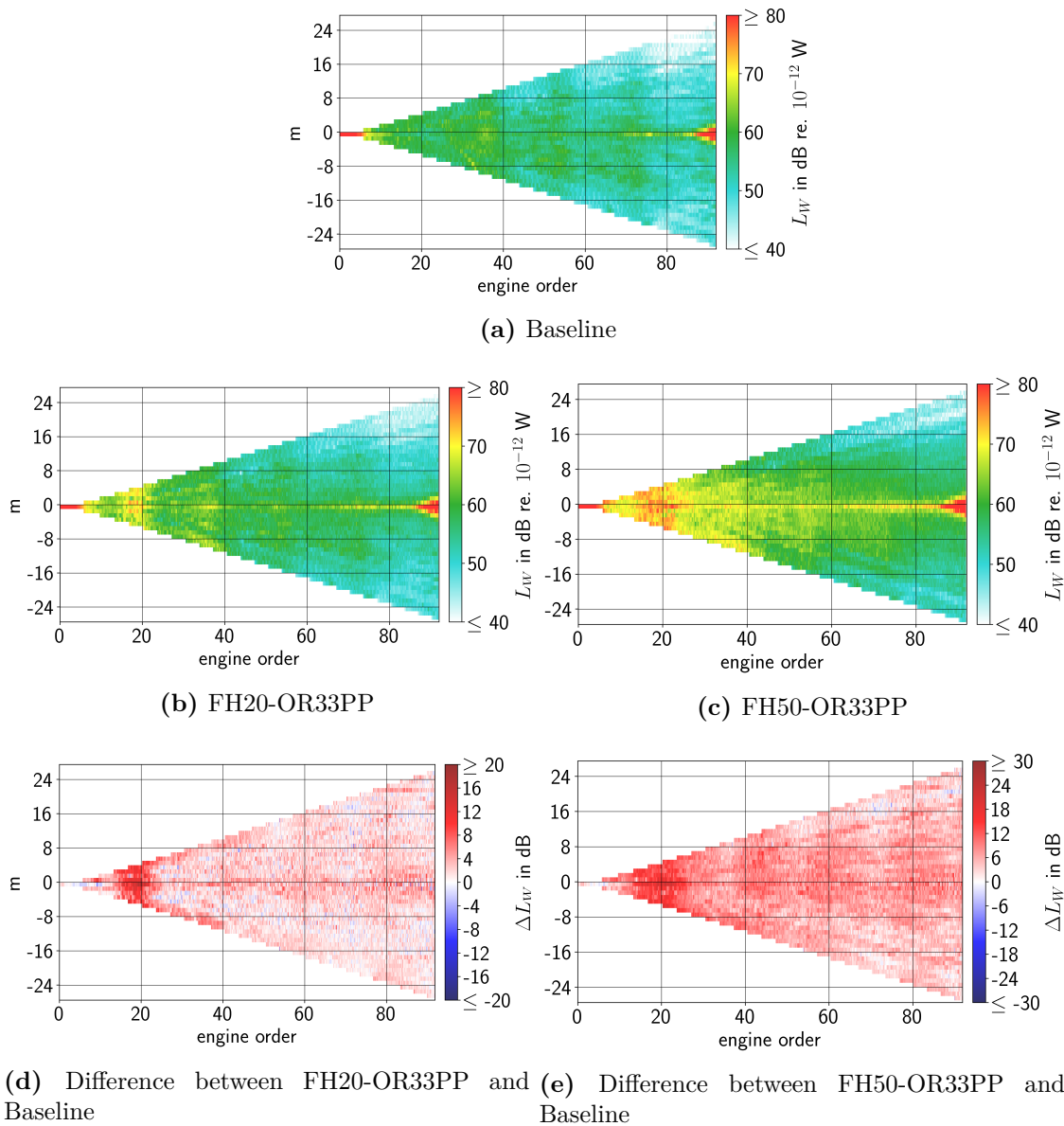


Figure 6.12.: CAAS broadband modal sound power level summed up over all upstream propagating radial modes. The baseline and the two distortion test cases are shown. Results extracted from Klähn et al. (2022a). Fan operating point: $\eta_c = 4500$ RPM, $\phi = 0.33$.

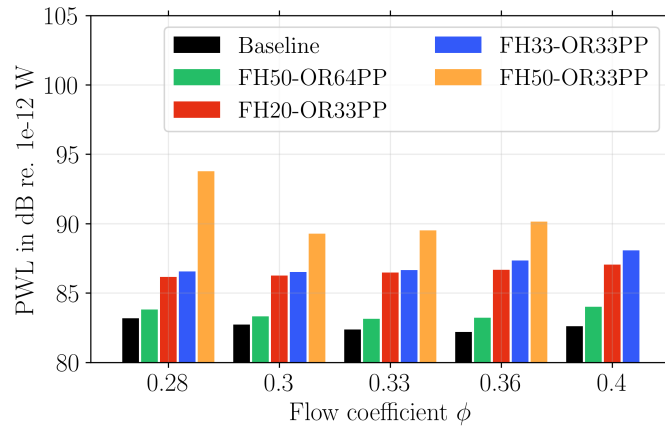
with the rotating blades, a broad range of modes are excited and no preference for a such structure is observed. This suggests the increase in the turbulence levels as the cause of the increase in sound power levels. Similar trends are found for the fan operating point $\eta_c = 2250$ RPM and $\phi = 0.33$, as in Fig. 6.11. Fig. 6.11d suggests that for the most of the additional sound power generated for this fan operating oping was in the frequency range around $EO \approx 20$, close to 1BPF.

Results with the test screen FH50-OR33PP follows the same trend, with a higher impact in the sound power generation due to the higher turbulence content in the inflow. In

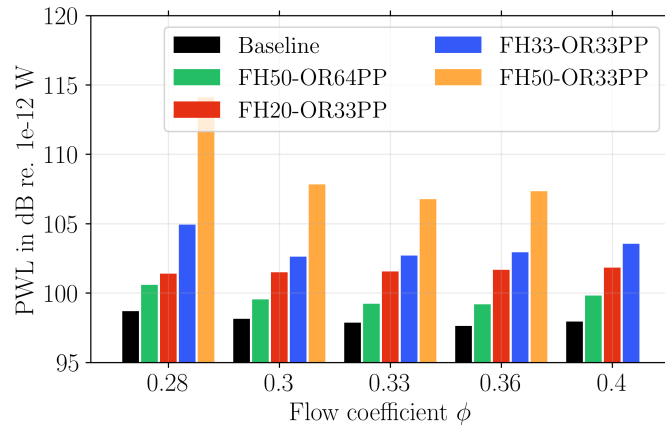
Figs. 6.12e and 6.11e, different than in Figs. 6.12d or 6.11d, the red color dominates the complete map. This indicates an increase in sound power levels over a broad range of modes. Again, no mode was particularly overexcited. In both figs. 6.12d, 6.12e, and 6.11d, an increase in sound power in the frequency band around $EO \simeq 20$ due to the interaction of the high turbulence content with the rotating fan blades is observed.

6.6.4. Overall sound power levels vs fan flow coefficient ϕ

The PWL were obtained by integrating the CAAS results for all fan flow coefficients and both fan speeds in the frequency range of $9 < EO < 81$. The use of these bounds is important to avoid the low-frequency noise content, believed to be related to reflections of the throttle at the rig's exhaust, and the high-frequency content due to the array and CAAS limitation. Fig. 6.13 exposes the results for all tested cases. Results were extracted from Klähn et al. (2022a).



(a) $\eta_c = 2250$ RPM.



(b) $\eta_c = 4500$ RPM.

Figure 6.13.: Comparison of the broadband sound power levels for all tested configurations as a function of the flow coefficient and two fan speeds. Results were extracted from Klähn et al. (2022a).

The baseline sound power level pattern exhibits for both fan speeds a slight U-shape, reaching its minimum for $\phi = 0.36$. This pattern is roughly identical for the test cases with screen FH50-OR64PP. For the test cases with 33% OA screen, however, slightly different trends are observed. For $\eta_c = 2250$ RPM, a continuous increase in the sound power levels with the increase in flow coefficient is observed. An exception holds for the screen FH50-OR33PP tested at $\phi = 0.28$. As said previously, it is believed that the fan blades operate partially stalled when they pass through the distorted flow region. The aerodynamics of the fan for this operating point was during the measurements, however, stable: the fan still produced a rise in total pressure and the operating point (average) was outside the stall margin for this fan. This effect is more evident for $\eta_c = 4500$ RPM, where the PWL compared to the other test cases is more prominent. Regarding this fan speed, the results for the screens FH33-OR33PP and FH50-OR33PP still show a roughly similar U-shape, with a minimum at $\phi = 0.33$. This behavior is not observed for the lower fan speed case.

In general words, not considering effects such as local stall, the trend in fan noise power emissions is proportional to the amount of turbulence ingested by the fan, as well as the difference in mean velocity comparing the distorted and non-distorted flow field.

6.6.5. Overall sound power levels trends: correlation with extrapolated aerodynamic data

With the aim of drawing a correlation between the overall fan sound power levels of each configuration with the ingested average turbulence power, the following is proposed: It is known and already observed that the fan broadband noise emissions scale with the level of turbulence ingested (A. Moreau (2017) and S. Moreau (2019)). In order to compute the turbulence levels over the duct cross-section, measurements over the whole section surface would be necessary. However, for the measurement dataset available, only the radial profile of the turbulence was accessible. The first attempt to draw this correlation was proposed by Klähn et al. (2022a,b). In this work, the peak of the turbulence intensity along the radial turbulence measurement axis combined with the distortion coefficient DC60 obtained from the pressure rakes was used. A trend was observed, but the use of these parameters was not sufficient to represent the turbulence behavior over the whole inlet cross-section. Here, a different approach is proposed by extrapolating the data available.

In order to roughly estimate the 2D turbulence distribution, the hot-wire measurement dataset performed in the radial direction was extrapolated over the whole duct cross-section. The assumptions taken were: the wall boundary layer turbulence profile is axisymmetric with reference to the axial axis and can be extrapolated for the whole cross-section. The turbulence profile measured perpendicular to each screen, as portrayed in Fig. 6.8a was assumed to be constant along the z axis, or parallel to the horizontal line when looking

from the inlet towards the screen. As also observed in this figure, the turbulence profile kept fairly constant for both inlet speeds tested. This last assumption is taken so that the turbulence variance can simply be estimated:

$$\overline{u^2}(r, \theta) = \left(T_u(r, \theta) \cdot U(r, \theta) \right)^2, \quad (6.6.1)$$

where the mean axial velocity distribution $U(r, \theta)$ is scaled according to the respective fan flow coefficient ϕ . The average value of $\overline{u^2}$ over the cross-section is given in the following steps.

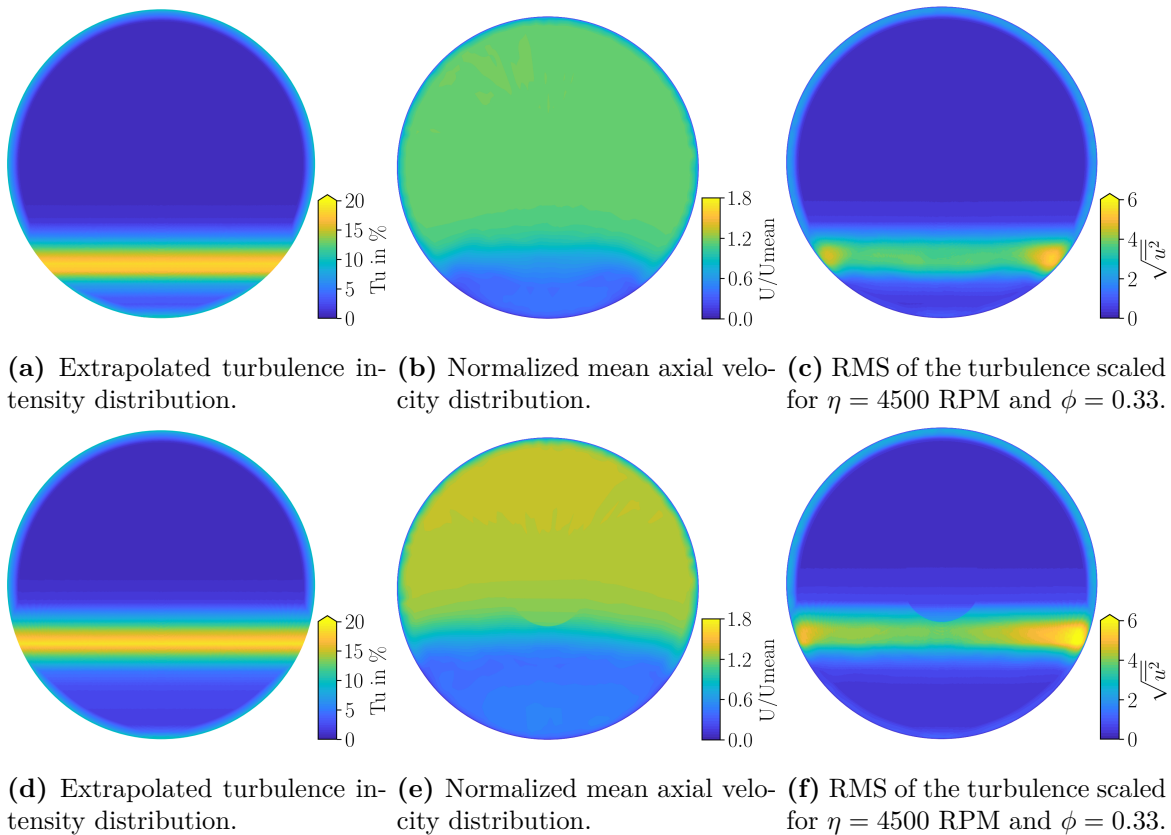


Figure 6.14.: Example of a 2D distribution of the extrapolated aerodynamic parameters computed for the screens FH20-OR33PP (top row) and FH33-OR33PP (bottom row).

An exemplary result for the screens FH20-OR33PP and FH33-OR33PP is depicted in Fig. 6.14. Data extrapolation was necessary for computing the mean axial velocity profile. The region delimited by $0 < r < 56$ mm could not be reached by the pressure rakes, as the longest rake was 170 mm long. This is shown as white disc in the middle of each plot of Fig. 6.5. The interpolation of this area was performed similarly to the hot-wire by assuming constancy along the z axis. Fig. 6.14b shows an exemplary result for the screen FH20-OR33PP and Fig. 6.14e for the FH33OR33 screen. The mean axial velocity was normalized with the overall mean velocity $U_{\text{mean}} = \overline{U}$ obtained by integrating the entire 2D map. The approximated velocity profile of each fan flow coefficient tested was

approximated by multiplying this normalized velocity distribution with the mean axial flow speed of each respective test case. The normalized turbulence variance is obtained by multiplying the 2D functions in Fig. 6.14a and Fig. 6.14b, and integrating them over the duct cross-section area according to:

$$\overline{u^2}_{\text{norm}} = \frac{1}{\pi R^2} \int_0^{2\pi} \int_0^R \left[T_u(r, \theta) \cdot \frac{U(r, \theta)}{\overline{U}} \right]^2 r dr d\theta, \quad (6.6.2)$$

where $\overline{u^2}_{\text{norm}}$ is the normalized variance that should be scaled up for all tested axial flow speeds. This is done by:

$$\begin{aligned} \overline{u^2} &= \overline{u^2}_{\text{norm}} \cdot \overline{U}^2 \\ &= \overline{u^2}_{\text{norm}} \cdot \left(\phi \frac{2\pi R \eta_c}{60} \right)^2. \end{aligned} \quad (6.6.3)$$

Fig. 6.15 finally shows the results for two fan speeds and five fan flow coefficients. A fairly linear behavior is observed as global trend as well as a good gathering of all curves. A few points referred to $\phi = 0.28$ do not follow the trend. They belong to the screen FH50-OR33PP. A possible reason for this abnormal behavior is a potential local stall in the rotor blades, when entering the region of high velocity deficit.

The points gathered in the region of low turbulence variance $\overline{u^2} < 0.5$ correspond to the baseline and to the FH50-OR64PP screen. In this region, the curves show up a slight steeper curvature, suggesting different sound power trends for lower $\overline{u^2}$. For higher average turbulence variance, a good linear trend is observed (not to forget the y -axis is in logarithmic scale), confirming a fairly linear relation of the average turbulence variance (proportional to the turbulent kinetic energy - TKE) and the overall fan sound power level emissions in decibel.

6.7. Representativeness of the distortion profile generated

The screens used in this work generated a distorted total pressure distribution representative for BLI of e.g. partially embedded aeroengines. With regards to the fan broadband noise generation mechanism, one important aspect is the characteristics of the turbulence field and its statistic parameters, such as the turbulence intensity and the integral length scale. As reported by Staggat (2021) and Staggat et al. (2019), these turbulence parameters play an important role in the noise generation of a rotating fan. There are few publications on the turbulence characteristics of the fan inflow in BLI configurations. Works such as Hickling et al. (2019), Gonzalez-Martino and Casalino (2019) and Morton (2012) presented experimental and/or CFD results for boundary layer ingestion experiments. Morton (2012) observed that for a turbulent boundary layer developing over a flat plate, for example, the Reynolds stress profiles decay monotonically with the increase

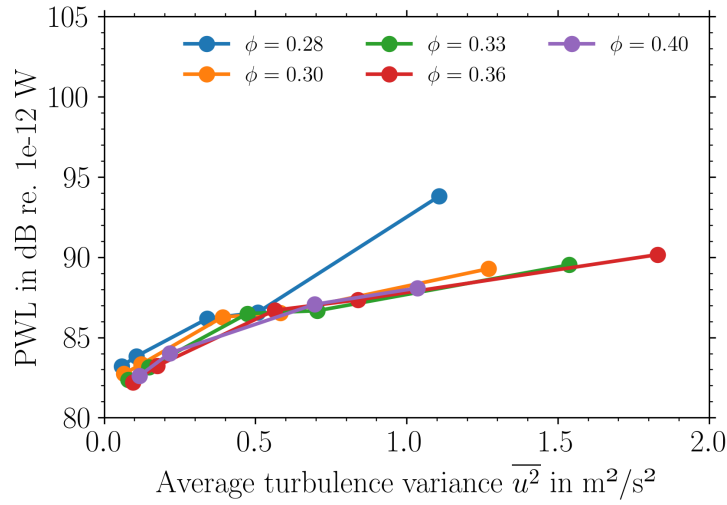
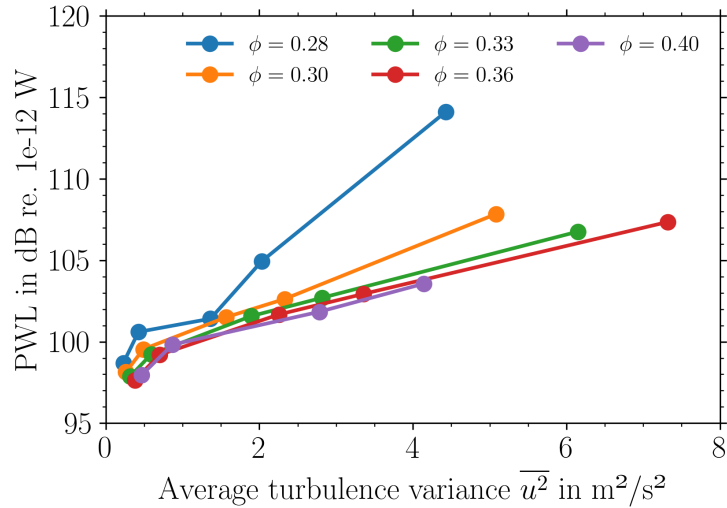
(a) $\eta_c = 2250$ RPM.(b) $\eta_c = 4500$ RPM.

Figure 6.15.: Overall fan sound power levels as a function of the average ingested turbulence power $\overline{u^2}$ for different fan flow coefficients and two fan speeds.

of the wall distance, just as measured for the baseline case shown in Fig. 6.7a. Similar finds are reported in Staggat (2021), Staggat et al. (2019), Hickling et al. (2019) and Gonzalez-Martino and Casalino (2019).

In the experiments performed in my thesis, however, as shown in Fig. 6.7, this behavior is observed only in the region close to the duct wall. On the basis of the available literature, it can be concluded so far that the Reynolds stresses in the region of the shear layer does not represent a typical BLI configuration. In spite of that, the test cases presented in the present work are valuable for noise emission investigations for distorted inflow.

6.8. Overall correlation among turbulence parameters

After analyzing a reasonable amount of turbulence data measured at the inlet of the CRAFT fan rig, the following and last analysis is performed. The results obtained within the frame of this thesis suggest a certain degree of correlation among integral length scale, turbulence intensity, and axial mean flow velocity. It was observed that for measurements inside the boundary layer, where the mean velocity is lower than in the free-stream, high turbulence intensity values are found with corresponding small integral length scales. For measurement points outside the boundary layer, on the other hand, signals with low turbulence intensity levels tend to have a large integral length scale.

In order to visualize this effect, Fig. 6.16 shows a scatter plot of all measurement data acquired in the inlet of the CRAFT test rig. For the estimation of the ILS the HIT assumption was taken. All three velocity components were considered as well as all test configurations: With the ICD, without the ICD, and with the ICD and the additional honeycomb and measurements with inflow distortion. Important to mention is that the y-axis in this plot is in logarithm scale. By observing this scatter plot, a rough shape of a $y = 1/x$ curve is formed by the points. On the one hand, this shape characteristic suggests that measurement points with high turbulence intensity levels are unlikely to have large integral length scales. On the other hand, measurement points with large integral length scales are unlikely to have high turbulence intensity. The colors in this scatter plot also suggest that measurement points at higher velocity tend to have lower turbulence intensity.

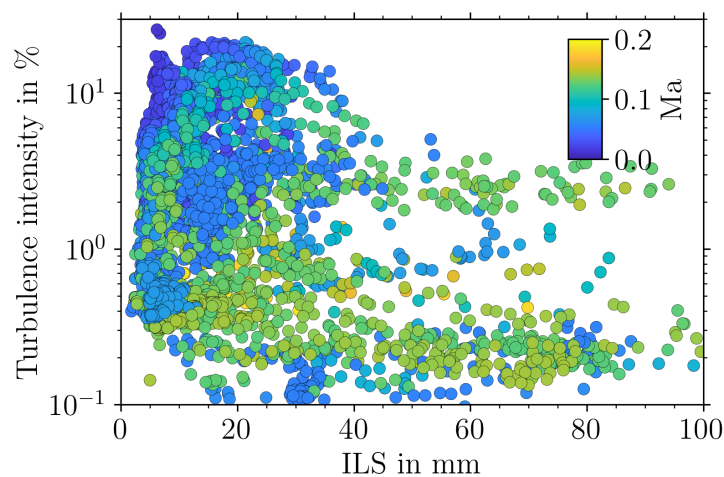


Figure 6.16.: Overall correlation between turbulence intensity, integral length scale, and axial Mach number.

7. Conclusions

THE overall aim of this work was the experimental characterization of the flow turbulence and its correlations and effect on fan noise emissions. For this investigation, the newly constructed low-speed fan test rig CRAFT was used as source of experimental data. Extensive aerodynamic and acoustic measurements were conducted and processed with both state of art, as well as with newly implemented analysis techniques.

For the purpose of establishing homogeneous inflow and low turbulence levels, a new Inlet Control Device (ICD) for the application of aeroacoustic tests was designed, built, and extensively tested. In addition to guidelines found in the literature, the design of the ICD was also supported by experiments to figure out the best material combination to be used, as reported in an early study. Based on the options found in the references and our capabilities, the use of flexible honeycomb combined with thin structural ribs and a thin wire mesh on both of its sides was chosen. Pressure rake measurements with the help of a circumferential traverse revealed that the combination of ICD and bellmouth, indeed, produces a homogeneous inflow. The axial flow velocity profile along the radial direction did not alter its shape for different fan operating points. The flow profile outside the boundary layer is flat and constant for all radial positions measured.

Hot-wire measurements confirmed the strong reduction of not only the turbulence intensity, but also its spatial non-homogeneity, when the ICD was installed. Measurements in the radial direction with two hot-wire probes made possible the characterization of the three velocity components (u, v, w). The ICD reduced noticeably the turbulence power content at the low-frequency band ($f < 100$ Hz) of the turbulence power spectral density (PSD), associated with large turbulence eddies. This effect was even more pronounced for the two transverse velocity components (radial and circumferential). Further improvements were found in this regard, when an additional honeycomb was installed at the measurement plane E1 between the inlet and the fan.

The use of the ICD established inlet turbulence levels for the axial velocity component in the order of 0.1% to 0.2% in the free stream, compared to around 1.5% to 2% without the ICD. A tenfold reduction was achieved. The additional honeycomb installed upstream of the fan (at the inlet downstream the bellmouth) increased this level from 0.1% to around 0.5% and reduced considerably the turbulence length scales. The large ILS estimated for the case with the ICD installed is possibly not representative. The reason for that is believed to be linked to the following hypotheses: the very low turbulence levels, the low

signal-to-noise ratio conditions, and the spectrum shape is not modelled by an isotropic model (the hypothesis stated is not met).

The aerodynamic impact of the ICD ribs in the flow was assessed with the help of a sweep measurement with hot-wires and the spectrogram tool. The wakes from these ribs were more noticeable in the transverse velocity components than in the axial component. The rib wakes were observed for the case with maximum flow speed $\bar{U} \approx 43$ m/s. When the honeycomb was installed at plane E1, though, no rib wake was detected. For the low-speed test case $\bar{U} \approx 25$ m/s and only the ICD installed (no additional honeycomb at the inlet), the analysis also did not reveal any wake in the flow measured.

With view on the turbulence field downstream the fan, a novel technique for the separation of turbulence parameters such as turbulence intensity (or the signal variance) and the integral length scale from the rotor wakes and the background flow was developed. The technique works in the time domain and is suitable for punctual velocity data measured behind a rotating fan, such as by means of hot-wire anemometry. The technique uses the cyclic variance of the unsteady velocity signal as input data to determine the two domain regions: blade wake and background flow. By applying suitable data tapers in the signal, the two processes are sorted out: blade wakes and background turbulence flow.

Aerodynamic data from the CRAFT fan test rig validated the developed algorithm. Its robustness allowed the separation of the blade tip vortex from the rotor wakes. The results were compared with another technique found in the literature and they are in agreement with other literature references. The width of the wakes and the tip vortex region increase with the blade loading. When analyzing the test configuration with the ICD and the additional honeycomb for 100% fan speed and for the highest fan loading analyzed, a significant increase in the rotor wake turbulence intensity was observed. The turbulence intensity of the longitudinal velocity component of the rotor wakes were considerably higher than the transverse component for all tested flow coefficients hence suggesting flow anisotropy. The radial profile of the turbulence integral length scale of the rotor wakes did not change considerably among the three analyzed flow coefficients. For the background flow, however, a consistent decrease in its values was observed with the reduction of the flow coefficient.

The impact of the three inlet configurations (without the ICD, with the ICD, and the with ICD and the additional honeycomb) on the turbulence downstream the fan was also assessed and analyzed. Not only higher turbulence levels for the case without the ICD compared to with the ICD was observed, but also a non-homogeneous radial distribution of the turbulence intensity for the former test configuration was detected. The use of the ICD at the inlet reduced the turbulence intensity of both the background flow and the rotor wakes. A systematic turbulence intensity reduction of both the rotor wakes and the background flow was observed with the increase of the flow coefficient for all test configurations. The analysis of the turbulence PSD of the separated domains (rotor wakes

and background flow) revealed the presence of high-power in the low-frequency band for the case without the ICD. This low-frequency power impacted only the background flow, and not the rotor wakes. For the case with the ICD and no additional honeycomb, the remaining low-frequency power in the turbulence PSD could be identified after the domain separation. Its power content was, however, weak.

Acoustic measurements revealed a small reduction in the blade passing frequency (BPF) tones due to the ICD for the higher fan speed case. The first BPF is cut-on at this fan speed. A remarkable reduction of the haystacks around the BPF tones was detected when the ICD was installed. This was confirmed by the azimuthal mode analysis of the broadband noise components. A hypothetical explanation for this is, due to the ICD, not only a better flow homogeneity (spatial and temporal) was established, but also a strong power reduction in the low-frequency band ($f < 100 \text{ Hz}$) of the turbulence PSD (associated with large turbulence eddies) was observed. For the lower fan speed configuration, the first three BPF tones are cut-off, however, they were still present in the acoustic PSD for all test configurations. For the case with the ICD, though, a reduction of approx. 5 dB on the first, second, and third BPF tone was observed. The azimuthal mode analysis revealed no additional excited fan modes due to the ICD. In the contrary, modes from the broadband PSD had their amplitude reduced by the use of the ICD, mostly the rotor co-rotating modes ($m < 0$) close to the cut-off zone.

The additional honeycomb in the inflow produced a slight increase in the fan acoustic broadband levels. This is believed to be linked to the slight increase in turbulence levels, when comparing to the case with the ICD only. When analyzing the acoustic rotor-incoherent component resulting from the cyclostationary analysis for the test case with additional honeycomb, the BPF tones could be completely separated from the broadband (rotor incoherent) PSD. A hypothesis is that this additional honeycomb allowed the fan to excite more stable BPF tones due to the establishment of a more homogeneous inflow (spatial and temporal) and the lower power content in the low-frequency band of the turbulence PSD. The use of an additional honeycomb inside the channel is an option to improve the flow homogeneity, important for fan acoustic investigations, with the penalty of a slight increase in the inflow turbulence levels.

Experiments with variable inflow distortion were performed in order to assess the correlation of the aerodynamic field with the fan noise emissions. Four distortion screens as experimental techniques to establish distorted inflow in combination with a honeycomb flow straightener plus one baseline configuration were tested. The acoustic field was captured by means of microphone arrays, whereas the aerodynamic field downstream the screens were acquired by means of pressure rakes and hot-wire anemometry. The screens successfully generated a distorted velocity field. It was observed that the screens with 33% open area screens generated a very low velocity magnitude (of approx. 30% of the free-stream speed) in the distorted region comparing to the region with no blockage. As

a result, flow separation might take place on the fan blades when traveling in the region of flow deficit. The turbulence measurements suggested a peak in all Reynolds stresses at the radial position equivalent to each screen height. This is associated to the shear layer created by the sharp transition of the screen to the free-flow. The screen with the highest open area (64%) generated the lowest shear layer stresses and the lowest turbulence integral length scales. The Reynolds stresses inside the wall-boundary layer were not altered by the screens. It was observed a peak in the ILS radial profile associated with the fence height, possibly due to the shear layer.

Acoustic measurements with distorted inflow revealed a remarkable increase in fan noise levels due to the ingestion of inflow distortion. One important aspect for this kind of acoustic measurements is the position of the microphones with respect to the distortion screen. The analysis of the spectra of all ring microphones revealed lower sound pressure levels for the sensors placed in the area where the velocity was lower (inside the distorted region). The microphones placed in the angular position equivalent to the screen height measured higher noise levels in the frequency band of $f < 1 \text{ BPF}$. This is due to the high turbulence levels found inside the shear layer generated by the screen. The azimuthal mode breakdown analysis revealed that no mode in particular was overexcited. Instead, the power of a broad range of modes was raised, suggesting the increase in turbulence ingestion as the reason for the fan sound power level increase. An approx. linear relation was found between the average turbulence variance ingested by the fan and the PWL in dB. The former was obtained by extrapolating the aerodynamic data available over the duct cross-section and for the different flow velocities.

The turbulence properties measured with distorted inflow profiles in this study are not similar to a boundary layer ingesting fan configuration. Nevertheless, the conducted experiments successfully generated inflow distortion test cases, which altered the fan broadband noise emissions and are useful for fan inflow distortion noise studies.

8. Recommendations for further research

As reported in the baseline assessment of the Inflow Control Device (ICD), a remarkable turbulence reduction and flow homogenization was observed due to the ICD. Regarding the inlet turbulence levels established, there is very little that can still be improved with a similar ICD concept. However, significant power in the low-frequency band of the turbulence spectrum for the test case with the ICD was still observed. I believe that this is due to the unfavourable condition, where the test rig operates: small and closed laboratory, which allows strong flow re-circulation in the room. One way to reduce this effect could be to increase the pressure drop at the rig inlet. This can be done by replacing the screens from one side of the ICD with another one with smaller open area. Another alternative is to install a honeycomb with thinner walls in the duct inlet. The honeycomb tested in the present work was made out of stainless-steel and has relatively thick walls (approx. 0.2 mm) compared to an aluminium honeycomb. Thinner walls generate less turbulence. This solution may also be combined with a high open-area screen placed upstream of this honeycomb (of around $>80\%$ open area and thin wires <0.1 mm to minimize the turbulence generation). Both solutions work on increasing the inlet pressure drop and stabilizing the flow better and reducing the turbulence low-frequency power, associated to large turbulence eddies. The advantage of the second solution over the first is the ease on installing this additional elements and allowing the fine tuning of screen and/or honeycomb specifications. The drawback of this solution is the potential acoustic reflections at the honeycomb. This effect was not assessed in this work. The first solution has the drawback of higher complexity and manufacturing time. Hot-wire measurement tests with different inlet pressure drops could answer the question regarding the correlation between the low-frequency power and the inlet pressure drop.

Alongside with that, further investigation and especially a thorough characterization of the low-frequency turbulence is recommended. This is because it has direct impact in the fan noise generation mechanisms. More precisely, in the interaction of the periodic tones with the stochastic turbulence, presumably linked to the hay-stacking spectral noise shape around the blade passing frequency (BPF) tones due to the power content in the large turbulence wave numbers (low-frequency). As reported, the low-frequency turbulence content seems to follow an expected inverse frequency ($1/f$ spectral shape) and has no stationary characteristics. Further tests to characterize this sort of turbulence can help figuring out its origin. Hot-wire measurements with longer data acquisition time (in the order of minutes) are necessary, as low-frequency frequency analyses require long data blocks to allow resolution in the low-frequency band.

Measurements with inflow distortion with the aim of reproducing the boundary layer ingestion conditions should consider ways to generate a specific turbulence profile in the region of the velocity deficit. Screens with lower open area discrepancy are recommended to avoid very large variations in the fan blades angle of attack, unless strictly desired. Turbulence generators shall also be considered to generate a more similar boundary layer turbulence profile within the distorted region. In fact, the different types of turbulence: wall boundary layer turbulence and free-stream turbulence have to be considered in the design of a boundary layer ingestion generator. An open question is how can a synthetic thicker boundary layer be generated in a (relatively) short duct, with all wall boundary layer characteristics (and not free-stream characteristics). Regarding the shear-stress generated by the screen open area transition, screens with a smooth and progressive open area variation would hopefully reduce or eliminate the strong shear layer problem and the peak in the associated Reynolds stresses, as well.

Bibliography

- ACARE (2010). *Beyond Vision 2020 (Towards 2050): A Background Document from ACARE*. Tech. rep. Advisory Council for Aeronautics Research in Europe (ACARE).
- Amiet, R. K. (1975). ‘Acoustic Radiation from an Airfoil in a Turbulent Stream’. In: *Journal of Sound and Vibration* 41.4, pp. 407–420.
- Antoni, J. (2007). ‘Cyclic spectral analysis in practice’. In: *Mechanical Systems and Signal Processing* 21, pp. 597–630.
- Antoni, J. (2009). ‘Cyclostationarity by examples’. In: *Mechanical Systems and Signal Processing* 23.4 (2009): 987–1036.
- Atassi, H. and M. Logue (2009). ‘Fan Broadband Noise in Anisotropic Turbulence’. In: *15th AIAA/CEAS Aeroacoustics Conference (30th AIAA Aeroacoustics Conference)*. URL: <https://arc.aiaa.org/doi/pdf/10.2514/6.2009-3148>.
- Batchelor, G. K. (1953). *The Theory of Homogeneous Turbulence*. Cambridge University Press, New York.
- Bauers, R. and U. Tapken (2012). ‘Separation of hydrodynamic perturbations in acoustic liner insertion loss measurements at a fan rig’. In: *18th AIAA/CEAS Aeroacoustics Conference (33rd AIAA Aeroacoustics Conference)*.
- Behn, M., B. Pardowitz and U. Tapken (2018). ‘Separation of Tonal and Broadband Noise Components by Cyclostationary Analysis of the Modal Sound Field in a Low-speed Fan Test Rig’. In: *International Conference of Fan Noise, Aerodynamics, Applications and Systems, 18-20 April 2018, Darmstadt, Germany, Paper No. 43*. URL: <https://www.fan2022.org/archives/fan2018/papers/paper-43.html>.
- Bertsch, L. (2013). ‘Noise Prediction within Conceptual Aircraft Design’. PhD Thesis. Technischen Universität Carolo-Wilhelmina zu Braunschweig.
- Bertsch, L., D. G. Simons and M. Snellen (2015). *Aircraft Noise: The major sources, modelling capabilities, and reduction possibilities*. Tech. rep. Deutsches Zentrum für Luft- und Raumfahrt (German Aerospace Center).
- Bräunling, W. J. G. (2004). *Flugzeugtriebwerke: Grundlagen, Aero-Thermodynamik, ideale und reale Kreisprozesse, Thermische Turbomaschinen, Komponenten, Emissionen und Systeme*. Springer-Verlag.
- Bremer, M. (2018). *Auslegung und Analyse von Siebkonstruktionen zur experimentellen Nachbildung von Grenzschichtinflüssen in einem Flugzeugtriebwerkeinlauf*. Bachelor thesis. Rheinisch-Westfälischen Technischen Hochschule Aachen.

- Butlera, R. J., A. R. Byerleyb, K. V. Treurenc and J. W. Baughn (2001). ‘The effect of turbulence intensity and length scale on low-pressure turbine blade aerodynamics’. In: *International journal of heat and fluid flow 22.2 (2001): 123-133*.
- Caldas, L., M. Behn and U. Tapken (2019a). ‘Experimental study of noise generation due to flow through perforated plates’. In: *DAGA Conference, Rostock, Germany, 18 - 21 March*.
- Caldas, L., L. Klähn, R. Meyer and U. Tapken (2022a). ‘Measurements of fan inflow distortion noise generation in a low speed fan - part I: aerodynamic analyses’. In: *28th AIAA/CEAS Aeroacoustics 2022 Conference June 14-17, Southampton, UK*. URL: <https://doi.org/10.2514/6.2022-2944>.
- Caldas, L., S. Kruck, L. Klähn, A. Rudolphi, R. Meyer, L. Enghardt and U. Tapken (2022b). ‘Construction and Assessment of an Inflow-Control-Device for a Low-Speed Aeroacoustic Fan Rig’. In: *AIAA Journal* 60.9, pp. 5299–5312. DOI: [doi/abs/10.2514/1.J061729](https://doi.org/10.2514/1.J061729).
- Caldas, L. and R. Meyer (2023). ‘New method to separate turbulence statistics of fan rotor wakes from background flow’. In: *Journal of Experiments in Fluids* 64.2, p. 32. DOI: [10.1007/s00348-023-03576-0](https://doi.org/10.1007/s00348-023-03576-0). URL: <https://doi.org/10.1007/s00348-023-03576-0>.
- Caldas, L., S. Oertwig, A. Rudolphi, R. Meyer, L. Enghardt and U. Tapken (2019b). ‘Development and assessment of an inflow control device and a bell-mouth for a low-speed aeroacoustic fan rig’. In: *25th AIAA/CEAS Aeroacoustics Conference*. URL: <https://arc.aiaa.org/doi/pdf/10.2514/6.2019-2713>.
- Caldas, L., C. A. Kissner, M. Behn, U. Tapken and R. Meyer (2021a). ‘Comparison of techniques for the estimation of flow parameters of fan inflow turbulence from noisy hot-wire data’. In: *AIAA AVIATION 2021 FORUM*.
- Caldas, L., C. Kissner, M. Behn, U. Tapken and R. Meyer (2021b). ‘Comparison of Techniques for the Estimation of Flow Parameters of Fan Inflow Turbulence from Noisy Hot-Wire Data’. In: *Fluids* 6.11, p. 372. ISSN: 2311-5521. URL: <https://www.mdpi.com/2311-5521/6/11/372>.
- Camp, T. R. and H. W. Shin (1995). ‘Turbulence intensity and length scale measurements in multistage compressors’. In: *J. Turbomach. January, 117(1): 38-46 (9 pages)*.
- Cattafesta, L., C. Bahr and J. Mathew (2010). ‘Fundamentals of wind-tunnel design’. In: *Encyclopedia of Aerospace Engineering: 1-10*. URL: <https://doi.org/10.1002/9780470686652.eae532>.
- Clark, I. A., R. H. Thomas and Y. Guo (2018). ‘Aircraft System Noise Assessment of the NASA D8 Subsonic Transport Concept’. In: *2018 AIAA/CEAS Aeroacoustics Conference*.
- Cocking, B. J. and R. B. Ginder (1977). ‘The effect of an inlet flow conditioner on fan distortion tones’. In: *AIAA 4th Aeroacoustics Conference, Atlanta, Georgia, Oct 3-5*.
- Conrad E. William, M. P. H. and J. E. McAulay (1955). *Effects of Inlet-Air-Flow Distortion on Steady-State Altitude Performance of an Axial-Flow Turbojet Engine*. Tech.

- rep. NATIONAL AERONAUTICS and SPACE ADMINISTRATION WASHINGTON DC.
- Cousins, W. T. (2004). ‘History, philosophy, physics, and future directions of aircraft propulsion system/inlet integration’. In: *Turbo Expo: Power for Land, Sea, and Air. Vol. 41677*.
- Denton, J. D. (1993). ‘Loss mechanisms in turbomachines’. In: *ASME 1993 International Gas Turbine and Aeroengine Congress and Exposition*. American Society of Mechanical Engineers, V002T14A001–V002T14A001.
- Dron, S. (2008). ‘Toward ACARE 2020: innovative engine architectures to achieve the environmental goals?’ In: *26th International Congress of The Aeronautical Sciences*.
- Envia, E. (2002). *Souce Diagnostic Test-Vane Unsteady Pressure Results*. Tech. rep. NASA, Technical Report No. TM-2002-211808.
- Envia, E. (2018). ‘Noise emissions from commercial aircraft’. In: *Green Aviation: Reduction of Environmental Impact Through Aircraft Technology and Alternative Fuels*. CRC Press, 3-24.
- Evans, R. L. (1975). ‘Turbulence and Unsteadiness Measurements Downstream of a Moving Blade Row’. In: *Journal of Engineering for Power, January, pp. 131–139*.
- Ganz (Mar. 31, 1981). ‘Inflow Turbulence Control Structure’. In: *Patent No 4,258,823*.
- Ganz, U. W. (1980). *Analytical Investigation of Fan Tone Noise Due to Ingested Atmospheric Turbulence*. NASA Contractor Report 3302. NASA.
- Ganz, U., S. Glegg and P. Joppa (1998). ‘Measurement and prediction of broadband fan noise’. In: *4th AIAA/CEAS aeroacoustics conference*.
- Giannakis, G. B., V. K. Madiseti and D. B. Williams (1998). ‘Digital Signal Processing Handbook’. In: Boca Raton, FL: CRC Press. Chap. Cyclostationary signal analysis.
- Glegg, S. A. L. (1993). ‘Broadband noise from ducted prop fans’. In: *15th AIAA Aeroacoustics Conference, Long Beach, CA, USA. AIAA 93-4402*.
- Gonzalez-Martino, I. and D. Casalino (2019). ‘Noise from a Rotor Ingesting a Turbulent Boundary Layer Using Very-Large Eddy Simulations’. In: *25th AIAA/CEAS Aeroacoustics Conference*.
- Grant, I. (1997). ‘Particle image velocimetry: a review’. In: *Proceedings of the Institution of Mechanical Engineers, Part C: Journal of Mechanical Engineering Science 211.1: 55-76*.
- Greitzer, E. M. et al. (2010). *N+3 aircraft concept designs and trade studies*. Tech. rep. NASA CR-2010-216794/vol2, NASA Glenn Research Center, Cleveland, Ohio, 44135.
- Grzewski, L., M. Behn, S. Funke and H. A. Siller (2021). ‘Cyclostationary Analysis of Fan Noise Influenced by an Inflow Control Device’. In: *AIAA Journal: Vol 59, No. 7*. URL: <https://arc.aiaa.org/doi/abs/10.2514/1.J059493>.
- Groeneweg, J. F. and E. J. Rice (1983). ‘Aircraft turbofan noise’. In: *Turbo Expo: Power for Land, Sea, and Air. Vol. 79559*. American Society of Mechanical Engineers. URL: <https://asmedigitalcollection.asme.org/GT/proceedings-abstract/GT1983/V005T14A003/234550>.

- Groth, J. and A. Johansson (1988). ‘Turbulence reduction by screens’. In: *Journal of Fluid Mechanics* 197, pp. 139–155.
- Gunn, E. and C. Hall (2014). ‘Aerodynamics of boundary layer ingesting fans’. In: *ASME Turbo Expo 2014: Turbine Technical Conference and Exposition*. American Society of Mechanical Engineers Digital Collection.
- (2019). ‘Nonaxisymmetric stator design for boundary layer ingesting fans’. In: *Journal of Turbomachinery* 141.7, p. 071010.
- Hanson, D. (2001). *Theory for broadband noise of rotor and stator cascades with inhomogeneous inflow turbulence including effects of lean and sweep*. Tech. rep. 2001-210762. NASA.
- Hanson, D. B. (1974). ‘Spectrum of rotor noise caused by atmospheric turbulence’. In: *The Journal of the Acoustical Society of America* 56.1, 110-126. URL: <https://asa.scitation.org/doi/abs/10.1121/1.1903241>.
- Hickling, C., N. A. Balantrapu, W. N. Alexander, A. J. Millican, W. J. Devenport and S. A. Glegg (2019). ‘Turbulence Ingestion into a Rotor at the Rear of an Axisymmetric Body’. In: *25th AIAA/CEAS Aeroacoustics Conference*.
- Hinze, J. O. and B. J. Clark (1975). *Turbulence*. McGraw-Hill series in mechanical engineering. ISBN: 0-07-029037-7.
- Homyak, L., J. G. McArdle and L. J. Heidelberg (1983). ‘A compact inflow control device for simulating flight fan noise’. In: *AIAA-83-0680, AIAA 8th Aeroacoustics Conference. April 11-13. Atlanta, Georgia*. URL: <https://arc.aiaa.org/doi/pdf/10.2514/6.1983-680>.
- Jurdic, V., P. Joseph and J. Antoni (2009). ‘Investigation of Rotor Wake Turbulence Through Cyclostationary Spectral Analysis’. In: *AIAA Journal, Vol. 47, No. 9, September 2009*.
- Kantola, R. A. and R. E. Warren (1978). *Basic research in fan source noise: Inlet distortion and turbulence noise*. Tech. rep. NASA-CR-159451.
- Karlos, A., C. C. Paruchuri, P. Joseph, V. Bahrs, W. Meyer R. Hage and E. Enghardt (2021). ‘Effects of probe vibration on hot wire turbulence measurement: A technique for its removal’. In: *AIAA AVIATION 2021 FORUM, August 2-6, 2021, VIRTUAL EVENT*. DOI: <https://doi.org/10.2514/6.2021-2213>.
- Kay, S. M. (1993). *Fundamentals of statistical signal processing*. Prentice Hall PTR.
- Keshner, M. S. (1982). ‘1/f Noise’. In: *Proceedings of the IEEE, VOL. 70, No. 3, MARCH*.
- Klähn, L., L. Caldas and U. Tapken (2022a). ‘Measurements of fan inflow distortion noise generation in a low speed fan - part II: acoustic analyses’. In: *28th AIAA/CEAS Aeroacoustics 2022 Conference, June 14-17, Southampton, UK*.
- Klähn, L., L. Caldas, R. Meyer, A. Rudolphi, A. Moreau and U. Tapken (2022b). ‘Experimentelle Untersuchung der Auswirkung von Einlaufstörungen auf die Aeroakustik einer Rotor-Stator-Konfiguration am Fan-Prüfstand CRAFT’. In: *Deutsche Gesellschaft für Luft- und Raumfahrt, DGLR-Publikationsdatenbank*.

- Klähn, L., A. Moreau, L. Caldas, R. Jaron and U. Tapken (June 2022c). ‘Advanced analysis of fan noise measurements supported by theoretical source models’. In: *International Journal of Aeroacoustics* 21.3-4, pp. 239–259. DOI: <https://doi.org/10.1177/1475472X221093703>.
- Kobayashi, H. and T. Torisaki (1986). ‘Experimental Study of Flight Effect on Fan Noise: 1st Report, A Study of Inflow Control Device for Simulating In-flight Fan Noise in Static Test’. In: *Bulletin of JSME* 29.251, pp. 1536–1543.
- Kobayashi, H. and J. Groeneweg (1980). ‘Effects of inflow distortion profiles on fan tone noise’. In: *AIAA Journal* 18.8, pp. 899–906. URL: <https://arc.aiaa.org/doi/pdf/10.2514/3.50832>.
- Köhler, W. (2012). ‘The influence of the TCS on the circumferential mode distribution in the inlet of a fan rig (UFFA)’. In: *Proceedings of ASME Turbo Expo: Power for Land, Sea, and Air, vol. 44748, pp. 1813-1822, GT2012, June 11-15, Copenhagen, Denmark*. URL: <https://doi.org/10.1115/GT2012-69762>.
- Kokoska, S. and D. Zwillinger (2000). *CRC Standard Probability and Statistics Tables and Formulae*. Chapman & Hall: New York. DOI: doi.org/10.1201/b16923.
- Kolmogorov, A. N. (1941). ‘The local structure of turbulence in incompressible viscous fluid for very large Reynolds numbers’. In: *Cr Acad. Sci. URSS* 30, pp. 301–305.
- Kudela, H. (n.d.). ‘Turbulent flow’. Lecture Notes on Fluid Mechanics. URL: http://www.itcmp.pwr.wroc.pl/~znmp/dydaktyka/fundam_FM/Lecture_no3_Turbulent_flow_Modelling.pdf.
- Kulkarni, V., N. Sahoo and S. D. Chavan (2011). ‘Simulation of honeycomb–screen combinations for turbulence management in a subsonic wind tunnel’. In: *Journal of wind engineering and industrial aerodynamics* 99.1, pp. 37–45.
- Lewalle, J. and D. E. Ashpis. (2004). *Estimation of time scales in unsteady flows in a turbomachinery rig*. Tech. rep. NASA/TM—2004-209452.
- Loew, R. A., J. T. Lauer, J. McAllister and D. L. Sutliff (2006). ‘THE ADVANCED NOISE CONTROL FAN’. In: *25th AIAA Aerodynamic Measurement Technology and Ground Testing Conference. 5 - 8 June, San Francisco, California*.
- Lucas, J. R., W. F. O’Brien and A. M. Ferrar (2014). ‘Effect of BLI-Type Inlet Distortion on Turbofan Engine Performance’. In: *ASME Turbo Expo 2014: Turbine Technical Conference and Exposition*. American Society of Mechanical Engineers Digital Collection.
- Lucas, J. R. (2013). ‘Effect of BLI-Type Inlet Distortion on Turbofan Engine Performance’. PhD Thesis. Virginia Tech.
- Madani, V. and T. Hynes (2009). ‘Boundary layer ingesting intakes: design and optimization’. In: *Proceedings of XIX International Symposium on Air Breathing Engines, Montreal, Canada, ISABE. Vol. 1346*.
- Majumdar, S. J. and N. Peake (1998). ‘Noise generation by the interaction between ingested turbulence and a rotating fan’. In: *Journal of Fluid Mechanics* 359, pp. 181–216.

- Mark, W. D. (1982a). ‘Methods for estimation of Bullen turbulence spectrum parameters’. In: *NASA-CR-165912*.
- Mark, W. D. (1981). ‘Characterization, Parameter Estimation, and Aircraft Response Statistics of Atmospheric Turbulence’. In: *NASA Contractor Report 3463*.
- (1982b). ‘Maximum Likelihood Estimation of Turbulence Spectrum Parameters’. In: *AIAA Journal, VOL. 22, NO. 1*.
- Martinez, B. R. J., L. Caldas, R. Cuenca, R. Lauterjung and P. C. J. Greco (2018). ‘Design of an instrumented stator vane for unsteady pressure measurements using mems microphones’. In: *31st Congress of the International Council of the Aeronautical Sciences, Belo Horizonte, Brazil, September 09-14*.
- Maunus, J., S. Grace, D. Sondak and V. Yakhot (2013). ‘Characteristics of Turbulence in a Turbofan Stage’. In: *Journal of turbomachinery, 135(2), p. 021024*.
- Mayle, R. E., K. Dullenkopf and A. Schulz (1997). ‘The turbulence that matters’. In: *International Gas Turbine & Aeroengine Congress & Exhibition. Orlando, Florida. June 2-5*.
- Mcardie, J., W. Jones, L. Heidelberg and L. Homyak (1980). ‘Comparison of several inflow control devices for flight simulation of fan tone noise using a JT15D-1 engine’. In: *AIAA-80-1025, 6th Aeroacoustics Conference, June 4-6, Hartford, Connecticut*.
- McMurtry, P. (2001). *Length and time scales in turbulent flows. Lecture notes on “ME 7960 Turbulence”*. Tech. rep. The University of Utah.
- Meillard, L., R. Schnell, R. Meyer and C. Voigt (2013). ‘Time resolved pressure and velocity measurements at the DLR UHBR-Fan and comparison with simulation data’. In: *62. Deutscher Luft- und Raumfahrtkongress, 10.-12. September 2013, Stuttgart, Germany*.
- Menegozzo, L. and E. Benini (2020). ‘Boundary Layer Ingestion Propulsion: A Review on Numerical Modeling’. In: *Journal of Engineering for Gas Turbines and Power 142.12*.
- Meyer, R., S. Hakansson, W. Hage and L. Enghardt (2019). ‘Instantaneous flow field measurements in the interstage section between a fan and the outlet guiding vanes at different axial positions.’ In: *Proceedings of the 13th European Conference on Turbomachinery Fluid Dynamics and Thermodynamics, Lausanne, Switzerland*. URL: <http://www.euroturbo.eu/paper/ETC2019-330.pdf>.
- Meyer, R., K. Knobloch and S. Hakansson (2015). ‘Hot-wire measurement in a Direct Driven high speed Turbo Fan (DDTF) Rig’. In: *ETC-11-256. 11th European Turbomachinery Conference; March 23-27, 2015, Madrid, Spain*.
- Meyer, R., U. Tapken, L. Klähn, M. Behn and A. Rudolphi (2022). ‘Experimentelle Untersuchung der Auswirkung von Grenzschichteinsaugung auf die Zuströmturbulenz und die Aeroakustik des gegenlüftigen Fan-Modells CRISPMulti’. In: *Deutscher Luft und Raumfahrt Kongress, 27-29 September, Dresden, Germany*.
- Moreau, A. (2017). ‘A unified analytical approach for the acoustic conceptual design of fans of modern aero-engines’. PhD Thesis. Technische Universität Berlin.
- Moreau, S. (2019). ‘Turbomachinery Noise Predictions: Present and Future’. In: *Acoustics 1.1, pp. 92–116. ISSN: 2624-599X. URL: https://www.mdpi.com/2624-599X/1/1/8*.

- Morton, M. (2012). ‘Rotor Inflow Noise Caused by a Boundary Layer: Inflow Measurements and Noise Predictions’. Master’s thesis. Faculty of the Virginia Polytechnic Institute.
- Moss, R. W. and M. L. G. Oldfield (1992). ‘Measurements of the effect of free-stream turbulence length scale on heat transfer’. In: *ASME 1992 International Gas Turbine and Aeroengine Congress and Exposition*.
- Murray, H. H., W. J. Devenport, W. N. Alexander, S. A. L. Glegg and W. Wisda (2018). ‘Aeroacoustics of a rotor ingesting a planar boundary layer at high thrust’. In: *Journal of Fluid Mechanics* 850, pp. 212–245. DOI: 10.1017/jfm.2018.438.
- Mydlarski, L. and W. Zellman (1996). ‘On the onset of high-Reynolds-number grid-generated wind tunnel turbulence’. In: *Journal of Fluid Mechanics* 320, pp. 331–368. DOI: 10.1017/S0022112096007562.
- Odier, N., F. Duchaine, L. Gicquel, G. Staffelbach, A. Thacker, N. García Rosa, G. Dufour and J. D. Muller (2018). ‘Evaluation of integral turbulence scale through the fan stage of a turbofan using hot wire anemometry and large eddy simulation’. In: *Proceedings of ASME Turbo Expo 2018, Turbomachinery Technical Conference and Exposition, GT2018. June 11-15, Oslo, Norway*.
- Percival, D. B. and A. T. Walden (1993). *Spectral analysis for physical applications*. Cambridge University Press.
- Perovic, D., C. A. Hall and E. Gunn (2019). ‘Stall Inception in a Boundary Layer Ingesting Fan’. In: *Journal of Turbomachinery* 141.9, p. 091007.
- Pestana, M. et al. (2017). ‘Aeroacoustics of an axial ducted low Mach-number stage: numerical and experimental investigation.’ In: *23rd AIAA/CEAS Aeroacoustics Conference*. URL: <https://doi.org/10.2514/6.2017-3215>.
- Phillips, C., R. Bandyopadhyay and D. J. McComas (2022). ‘Taylor Microscale and Effective Reynolds Number near the Sun from PSP’. In: *The Astrophysical Journal* 933.1, p. 33. URL: <https://doi.org/10.3847/1538-4357/ac713f>.
- Plas, A., D. Crichton, M. Sargeant, T. Hynes, E. Greitzer, C. Hall and V. Madani (2007). ‘Performance of a boundary layer ingesting (BLI) propulsion system’. In: *45th AIAA aerospace sciences meeting and exhibit*, p. 450.
- Pochkin, Y. and Y. Khaletskiy (2014). ‘Turbulence control screen impact on turbofan noise spectra in far sound field’. In: *The 21st International Congress on Sound and Vibration, 13-17 July, Beijing/China, ICSV 2014 (pp. 857-864)*.
- Podboy, G. G., M. J. Krupar, S. M. Helland and C. E. Hughes (2003). *Steady and Unsteady Flow Field Measurements Within a NASA 22-Inch Fan Model*. Tech. rep. NASA, Technical Report No. TM-2003-212329.
- Pope, S. B. (2000). *Turbulent Flows*. Cambridge University Press.
- Preisser, J. S. and D. Chestnutt (1984). ‘Flight effects on fan noise with static and wind-tunnel comparisons’. In: *Journal of aircraft* 21.7: 453-461. URL: <https://arc.aiaa.org/doi/pdf/10.2514/3.44993>.
- Richardson, L. F. (1922). *Weather prediction by numerical process*. Cambridge university press.

- Roach, P. E. (1987). 'The generation of nearly isotropic turbulence by means of grids'. In: *International Journal of Heat and Fluid Flow* 8.2, pp. 82–92.
- Rogers, D. and U. Ganz (1980). 'Aerodynamic assessment of methods to simulate flight inflow characteristics during static testing'. In: *AIAA-80-1023. 6th Aeroacoustics Conference, June 4-6, Hartford, Connecticut*.
- Santos, F. L. dos, L. Botero-Bolívar, C. H. Venner and L. D. de Santana (2021). 'Modelling the Dissipation Range of von Kármán Turbulence Spectrum'. In: *AIAA AVIATION 2021 FORUM*. URL: <https://arc.aiaa.org/doi/abs/10.2514/6.2021-2292>.
- Schulz, H. J. and W. Köhler (2011). 'UFFA – Universal Fan Facility for Acoustics - An Enhancement of Europe's Largest Aero Acoustic Test Facility for Aero Engine Fans'. In: *In INTER-NOISE and NOISE-CON Congress and Conference Proceedings (Vol. 2011, No. 2, pp. 4481-4500). Institute of Noise Control Engineering*.
- Schuster, W. (2021). 'Empirical Stability of Engine Tones Measured in Rig and Engine Testing'. In: *AIAA AVIATION 2021 FORUM*. URL: <https://arc.aiaa.org/doi/abs/10.2514/6.2021-2315>.
- Schuurman, R. (2022). *Embraer E190-E2 gets Chinese type certificate, Accessed in March-2023*. URL: <https://airinsight.com/embraer-e190-e2-gets-chinese-type-certificate/>.
- Sharland, I. J. (1964). 'Sources of noise in axial flow fans'. In: *Journal of Sound and Vibration* 1.3, pp. 302–322.
- Silberhorn, D., C. Hollmann, M. Mennicken, F. Wolters, F. Eichner and M. Staggat (2019). 'Overall Design and Assessment of Aircraft Concepts with Boundary Layer Ingesting Engines'. In: *Proceedings of the Deutscher Luft-und Raumfahrtkongress*.
- Staggat, M. (2021). 'Modellierung und Prognose des Grenzschicht-Rotor-Interaktionsschalls für integrierte Triebwerke'. PhD Thesis. Technische Universität Berlin.
- Staggat, M., A. Moreau and S. Guérin (2019). 'Analytical prediction of boundary layer ingestion noise for an integrated turbofan'. In: *Proceedings of the 26th International Congress on Sound and Vibration, ICSV 2019*.
- Sturm, M. (2015). 'Tonal Noise of Axial Fans Induced by Large-Scale Inflow Distortions'. PhD Thesis. Naturwissenschaftlich-Technischen Fakultät der Universität Siegen (University of Siegen).
- Sturm, M. and T. Carolus (2013). 'Impact of the large-scale environment on the tonal noise of axial fans'. In: *10th European Conference on Turbomachinery, Fluid Dynamics and Thermodynamics, 15-19 April - Lappeenranta, Finland*. URL: <https://journals.sagepub.com/doi/abs/10.1177/0957650913498082>.
- Sumner Miller, J. (1969). *Lesson 34. Resonance - Forced Vibrations - Demonstrations in Physics*. URL: <https://youtu.be/C-Bn70PpbrM>.
- Sutliff, D. (2019). *Advanced noise control fan: a 20-year retrospective of contributions to aeroacoustics research*. Tech. rep. NASA GRC-E-DAA-TN64107.
- Sutliff, D. L. (2018). 'Acoustic Directivity of the DGEN Aero-propulsion Research Turbofan at Multiple Farfield Array Locations'. In: *2018 AIAA/CEAS Aeroacoustics Con-*

- ference, June 25-29, Atlanta, Georgia. URL: <https://arc.aiaa.org/doi/pdf/10.2514/6.2018-3279>.
- Tapken, U. (2016). *Projektplan AGATA3s (Auswirkung von Grenzschichteinsaugung auf Triebwerkfans: Aerodynamik, Aeroelastik, Strukturmechanik und Akustik)*. Tech. rep. Deutsches Zentrum für Luft- und Raumfahrt.
- Tapken, U., M. Behn, M. Spitalny and B. Pardowitz (2019). ‘Radial mode breakdown of the ACAT1 fan broadband noise generation in the bypass duct using a sparse sensor array’. In: *25th AIAA/CEAS Aeroacoustics Conference. AIAA-2019-2525*.
- Tapken, U., L. Caldas, R. Meyer, M. Behn, L. Klähn, R. Jaron, A. Moreau, A. Rudolphi and L. Enghardt (2021a). ‘New test facility to investigate the noise generated by shrouded fans for small aircraft applications’. In: *DICUAM, 15-17 March, Delft, The Netherlands*.
- Tapken, U., D. Gutsche and L. Enghardt (2014). ‘Radial mode analysis of broadband noise in flow ducts using a combined axial and azimuthal sensor array’. In: *20th AIAA/CEAS Aeroacoustics Conference*. DOI: 10.2514/6.2014-3318.
- Tapken, U., T. Lengyel-Kampmann, J. Belz, A. Stürmer and T. Otten (2022). ‘Auswirkung von Grenzschichteinsaugung auf Triebwerkfans: Aerodynamik, Aeroelastik, Strukturmechanik und Akustik - Übersicht über das Projekt AGATA3S’. In: *Deutsche Gesellschaft für Luft- und Raumfahrt, DGLR-Publikationsdatenbank*.
- Tapken, U., L. Caldas, R. Meyer, M. Behn, L. Klähn, R. Jaron and A. Rudolphi (2021b). ‘Fan test rig for detailed investigation of noise generation mechanisms due to inflow disturbances’. In: *AIAA AVIATION 2021 FORUM, August 2-6, VIRTUAL EVENT*. URL: <https://arc.aiaa.org/doi/abs/10.2514/6.2021-2314>.
- Tennekes, H. and J. L. Lumley (1972). *A First Course in Turbulence*. The MIT Press.
- Thomas, R. H., C. L. Burley and E. D. Olson (2012). ‘Hybrid wing body aircraft system noise assessment with propulsion airframe aeroacoustic experiments’. In: *International Journal of Aeroacoustics* 11.3-4, pp. 369–409.
- Ting, D. (2016). *Basics of engineering turbulence*. Academic Press, Elsevier. ISBN: 978-0-12-803970-0.
- Tyler, J. M. and T. G. Sofrin (1962). ‘Axial flow compressor noise studies’. In: *Transactions of the society of automotive engineers, Vol. 70, 1962, pp. 309–332*. URL: <https://doi.org/10.4271/620532>.
- Wisda, D. M. (2015). ‘Noise from a Rotor Ingesting Inhomogeneous Turbulence’. Master’s thesis. Virginia Polytechnic Institute and State University.
- Wohlbrandt, A. (2017). ‘Stochastisches Verfahren zur Simulation von Breitbandschall in Triebwerkfans’. PhD Thesis. Technischen Universität Berlin.
- Zhang, Y., Z. Zhou, K. Wang and X. Li (2020). ‘Aerodynamic Characteristics of Different Airfoils under Varied Turbulence Intensities at Low Reynolds Numbers’. In: *Applied Sciences* 10.5. ISSN: 2076-3417. DOI: 10.3390/app10051706. URL: <https://www.mdpi.com/2076-3417/10/5/1706>.

A. Appendix

THE set of equations used in this work are shown in this section. References used are Bräunling (2004), Pope (2000) and Hinze and B. J. Clark (1975).

A.1. General aerodynamic equations

Mass flow

The average mass flow \dot{m} is calculated based on the spatial distribution of the mean axial velocity $U(r, \theta)$:

$$\dot{m} = \rho \int_0^{2\pi} \int_0^R U(r, \theta) r dr d\theta. \quad (\text{A.1.1})$$

Average axial flow speed

The average axial flow speed is computed based on the mass flow and the air density:

$$\bar{U} = \frac{\dot{m}}{\rho S}, \quad (\text{A.1.2})$$

where $S = \pi R^2$.

Flow coefficient

The flow coefficient ϕ describes the ratio of the inlet (or axial) Mach number M_{ax} and the rotor tip Mach number M_{tip} as

$$\phi = \frac{M_{ax}}{M_{tip}} = \frac{\bar{U}}{U_{tip}} = \frac{\bar{U}}{2\pi\omega R}, \quad (\text{A.1.3})$$

where U_{tip} is the tangential tip speed of the rotor, and consequently, $\omega = \eta_c/60$ is the fan rotation speed in Hz, and η_c the corrected fan speed in RPM. R is the fan radius.

Boundary layer displacement thickness

$$\delta^* = \int_0^\infty \left(1 - \frac{U(y)}{U_\infty}\right) dy, \quad (\text{A.1.4})$$

where $U(y)$ is the mean flow velocity as a function of the wall normal distance y .

Boundary layer momentum thickness

$$\theta = \int_0^\infty \frac{U(y)}{U_\infty} \left(1 - \frac{U(y)}{U_\infty}\right) dy, \quad (\text{A.1.5})$$

where $U(y)$ is the mean flow velocity as a function of the wall normal distance y .

Shape factor

The shape factor is defined as the ratio of the two boundary layer metrics: displacement thickness and momentum thickness:

$$H = \frac{\delta^*}{\theta}. \quad (\text{A.1.6})$$

A.2. Fan aerodynamic parameters**A.2.1. Total Temperature**

Comparable to the total pressure, the total temperature of a flow corresponds to the temperature measured at a stagnation point. At the stagnation point the fluid speed is zero and all kinetic energy has been converted to internal energy. An important aspect to mention is that the total temperature remains constant along the streamline leading to the stagnation point. The total temperature is given by Bräunling (2004) [Chapter 10, pg. 933]

$$T_t = T \left(\frac{p_t}{p_0} \right)^{\frac{\kappa-1}{\kappa}} \quad (\text{A.2.1})$$

where κ is a gas constant and for air it is equal to $\kappa = 1.4$, and T the static temperature. Equation A.2.1 can be rewritten as function of the Mach number by

$$T_t = T \left(1 + \frac{\kappa-1}{2} M^2 \right) \quad (\text{A.2.2})$$

A.2.2. Total Pressure Ratio

In a similar manner the total pressure p_t can be written as a function of the static pressure p_0 , the axial Mach number M by:

$$p_t = p_0 \left(1 + \frac{\kappa - 1}{2} M^2 \right)^{\frac{\kappa}{\kappa - 1}}. \quad (\text{A.2.3})$$

A.2.3. Corrected mass flow

If a fan (or compressor) is operated in two different days, let's say day (I) and (II) under different ambient conditions such as temperature and pressure, normalized parameters shall be used in order to establish comparable aerodynamic operating points. In order to compare the performance in these two different ambient conditions, the axial Mach number must be equal for day (I) and (II):

$$M_{x,I} = M_{x,II}, \quad (\text{A.2.4})$$

where the index x stands for the axial direction. With the help of the universal gases equation $\rho = p_0/RT$ and the definition of the Mach number we obtain:

$$M_x = \frac{u_x}{a} = \frac{u_x}{\sqrt{\kappa RT}} = \frac{\dot{m}/\rho \cdot A}{\sqrt{\kappa RT}} = \frac{\dot{m}\sqrt{\kappa RT}}{A \cdot p_0 \cdot \kappa}. \quad (\text{A.2.5})$$

Substituting Eq. A.2.5 into A.2.4 we obtain:

$$\frac{\dot{m}_I \sqrt{\kappa RT_I}}{A_I \cdot p_{0,I} \cdot \kappa} = \frac{\dot{m}_{II} \sqrt{\kappa RT_{II}}}{A_{II} \cdot p_{0,II} \cdot \kappa}. \quad (\text{A.2.6})$$

Under the conditions that the test rig geometry does not change, i.e., $A = A_I = A_{II}$, we obtain:

$$\frac{\dot{m}_I \sqrt{T_I}}{p_{0,I}} = \frac{\dot{m}_{II} \sqrt{T_{II}}}{p_{0,II}}. \quad (\text{A.2.7})$$

Substituting then the static parameters T_I , T_{II} , $p_{0,I}$ and $p_{0,II}$ by the given equations: A.2.2 and A.2.3

$$\frac{\dot{m}_I \sqrt{T_{t,I}}}{p_{0,I}} = \frac{\dot{m}_{II} \sqrt{T_{t,II}}}{p_{0,II}} \cdot \underbrace{\frac{A_I}{A_{II}}}_{=1} \cdot \underbrace{\left[\frac{1 + \frac{\kappa-1}{2} \cdot M_{x,II}^2}{1 + \frac{\kappa-1}{2} \cdot M_{x,I}^2} \right]^{\frac{1}{2} \cdot \frac{\kappa+1}{\kappa-1}}}_{=1} \quad (\text{A.2.8})$$

Due to the boundary condition established by Eq. A.2.4, the term inside the brackets in Eq. A.2.8 is equal to the unit, as well as the term $A_I/A_{II} = 1$. In this way Eq. A.2.7 reduces to :

$$\frac{\dot{m}_I \sqrt{T_{t,I}}}{p_{t,I}} = \frac{\dot{m}_{II} \sqrt{T_{t,II}}}{p_{t,II}} \quad (\text{A.2.9})$$

At this point one can define the corrected mass flow \dot{m}_c as a correction from the measured value by a reference value for temperature and pressure. In this work the reference used is the sea level standard levels: $T_{ref} = 288.15 \text{ K}$ and $p_{ref} = 101,325 \text{ Pa}$. Therefore, the corrected mass flow is given by

$$\dot{m}_c = \dot{m} \frac{p_{ref}}{p_t} \sqrt{\frac{T_t}{T_{ref}}}, \quad (\text{A.2.10})$$

The mass flow \dot{m} is the one measured in the test rig, as well as the total pressure p_t . The total temperature may be obtained with the help of Eq. A.2.2. With the use of Eq. A.2.10, the fan performance map can be evaluated with normalized parameters and thus independent to the variations of ambient conditions.

A.2.4. Corrected fan speed

If a fan (or compressor) is operated in two different days, let's say day (I) and (II) under different ambient conditions such as temperature and pressure, normalized parameters shall be used in order to establish comparable aerodynamic operating points. In order to compare the performance in these two different ambient conditions, the tangential (or tip, or circumferential) Mach number must be equal for day (I) and (II), i.e.

$$M_{t,I} = M_{t,II}, \quad (\text{A.2.11})$$

where the index t stands for the tangential (or tip) Mach number. Using again the Mach number definition together with the tangential speed of a rotating object:

$$M_t = \frac{u_{tip}}{a} = \frac{\omega r}{\sqrt{\kappa R T}} = \frac{\pi}{30} \cdot \frac{\eta r}{\sqrt{\kappa R T}}. \quad (\text{A.2.12})$$

Substituting then Eq. A.2.12 in Eq. A.2.11 it becomes:

$$\frac{\pi}{30} \cdot \frac{r_I \cdot \eta_I}{\sqrt{\kappa R T_I}} = \frac{\pi}{30} \cdot \frac{r_{II} \cdot \eta_{II}}{\sqrt{\kappa R T_{II}}}. \quad (\text{A.2.13})$$

As the geometry of the test rig does not change from day (I) to day (II), i.e., $r_I = r_{II}$, Eq. A.2.13 holds true only if:

$$\frac{\eta_I}{\sqrt{T_I}} = \frac{\eta_{II}}{\sqrt{T_{II}}}. \quad (\text{A.2.14})$$

Substituting then the static temperature from Eq. A.2.2 to Eq. A.2.14 we obtain:

$$\frac{\eta_I}{\sqrt{T_{t,I}}} \left[1 + \frac{\kappa - 1}{2} M_{t,I}^2 \right]^{\frac{1}{2}} = \frac{\eta_{II}}{\sqrt{T_{t,II}}} \left[1 + \frac{\kappa - 1}{2} M_{t,II}^2 \right]^{\frac{1}{2}}, \quad (\text{A.2.15})$$

which under the assumption from Eq. A.2.11 reduces to:

$$\frac{\eta_I}{\sqrt{T_{t,I}}} = \frac{\eta_{II}}{\sqrt{T_{t,II}}}. \quad (\text{A.2.16})$$

Assuming then one of the days as a reference measure, in this work the reference used is the sea level standard levels: $T_{ref} = 288.15 \text{ K}$ and $p_{ref} = 101,325 \text{ Pa}$. The corrected speed is therefore given by:

$$\eta_c = \eta \sqrt{\frac{T_{ref}}{T_t}}, \quad (\text{A.2.17})$$

where η is the measured fan speed during the experiment and T_t the total temperature in K .